

Numerical and Experimental Verification of Investment Casting Process

Materials and Manufacturing Academy: Advanced Materials and Manufacturing

Victoria Ursula Thomas

Academic Supervisors: Prof. N P Lavery and Prof. S G R Brown

Industrial Supervisor: Dr. S P Leyland



Submitted to Swansea University in fulfilment of
the requirements for the Degree of Doctor of Engineering



Faculty of Science and Engineering
Swansea University
Wales, United Kingdom
31st December 2022

Copyright: The Author, Victoria U. Thomas, 2023

Distributed under the terms of a Creative Commons Attribution 4.0 License (CC BY 4.0).

Abstract

Vacuum induction melting investment casting is a process used to produce metal components. The procedure comprises of induction melting of a billet under vacuum conditions, followed by direct pouring into a casting mould. Castings made by this method are prone to defects such as misrun, inclusions and porosity. In this work, the impact of piping defects within IN713C billets is examined, specifically their size and location on flow characteristics during pouring and defect occurrence in finished castings. Manufactured holes were introduced in concast billets as a controlled method of exploring the effect of piping on alloy pouring flow characteristics. Using a Design of Experiments approach, an L9 array of two-piece billets was used to investigate the impact of disc height, hole diameter and hole position. A bespoke vacuum induction melting chamber was designed and fabricated with viewing ports which enable non-contact temperature measurements and high-speed images to be recorded during the heating and pouring processes, respectively. The L9 array was reproduced in numerical models of electromagnetic induction heating, and thermal fluid flow during alloy pouring, created using the in-development EMAG module for ESI ProCAST. Thermal results from electromagnetics models were used as initial conditions for alloy pouring, and additional mould filling and solidification simulations.

The experimental data served as validation for numerical models and demonstrates that the modelling approach delivers representative results, while minimising computational demand. Knowledge of the temperature distribution within the billet from electromagnetic simulations is found to be key for accurate defect prediction. By interrogating defect criteria in post-processing, the impact of piping on defect occurrence is understood. Using a 15 mm disc, or ‘penny’, resulted in a reduction of defect instances, consistent with anecdotally reported improvements observed in the casting industry. Through this modelling, this is explained by reductions in the maximum alloy pouring temperature.

Declarations and Statements

This work has not previously been accepted in substance for any degree and is not being concurrently submitted in candidature for any degree.

Signed: 

Date: 31/12/22

This thesis is the result of my own investigations, except where otherwise stated.

Other sources are acknowledged by footnotes giving explicit references.

A bibliography is appended.

Signed: 

Date: 31/12/22

I hereby give consent for my thesis, if accepted, to be available for electronic sharing after expiry of a bar on access approved by the Swansea University.

Signed: 

Date: 31/12/22

The University's ethical procedures have been followed and, where appropriate, that ethical approval has been granted.

Signed: 

Date: 31/12/22

Contents

1	Introduction	1
1.1	Overview of Vacuum Investment Casting	1
1.2	The Research Problem	3
1.3	VIM-IC Modelling and Validation Literature Review	5
1.3.1	Modelling and Validation of VIM	8
1.3.2	Modelling and Validation of Casting Processes and Solidification .	11
1.3.3	VIM-IC Modelling and Validation Literature Summary	13
1.4	Thesis Objectives	15
2	Thermophysical Properties: Review and Experimentation	17
2.1	Thermophysical Properties: Review and Experimentation Overview . . .	17
2.2	Thermophysical Properties Review	18
2.3	Solidus, Liquidus and Latent Heat: DSC	25
2.3.1	Solidus, Liquidus and Latent Heat: DSC Overview	25
2.3.2	DSC Experiment Setup and Method	25
2.3.3	DSC Experiment Results	26
2.3.4	Solidus, Liquidus and Latent Heat: DSC Conclusion	27
2.4	Emissivity and E-Slope: Temperature Calibration	28
2.4.1	Emissivity and E-Slope: Temperature Calibration Overview . . .	28
2.4.2	Determining Borosilicate Glass Spectral Transmittance	30
2.4.3	E-Slope: Temperature Calibration Experiment Overview	31
2.4.4	E-Slope: Temperature Calibration Experiment Setup	32
2.4.5	E-Slope: Temperature Calibration Experiment Method	33
2.4.6	E-Slope: Temperature Calibration Experiment Results	34
2.4.7	E-Slope: Temperature Calibration Experiment Discussion	37
2.4.8	Emissivity: Temperature Calibration Experiment Overview	37
2.4.9	Thermal Imaging Camera: Calibration Experiment Setup	38
2.4.10	Thermal Imaging Camera: Calibration Experiment Method	39

2.4.11	Thermal Imaging Camera: Calibration Experiment Results	40
2.4.12	Thermal Imaging Camera: Calibration Experiment Discussion . .	41
2.4.13	Thermal Imaging Camera Calibration: Conclusion	41
2.5	Effective Thermal Diffusivity: LFA	42
2.5.1	Effective Thermal Diffusivity: LFA Overview	42
2.5.2	Effective Thermal Diffusivity: LFA Sample Preparation	45
2.5.3	Effective Thermal Diffusivity: LFA Experiment Setup and Method	47
2.5.4	Effective Thermal Diffusivity: LFA Experiment Results	48
2.5.5	Effective Thermal Diffusivity: LFA Experiment Discussion	49
2.5.6	Effective Thermal Diffusivity: LFA Experiment Conclusion	51
2.6	Thermophysical Properties: Review and Experimentation Conclusion . .	51
3	Small Scale Induction Melting and Modelling with COMSOL	53
3.1	Small Scale Induction Melting and Modelling with COMSOL Overview .	53
3.2	Small Scale Induction Melting Experiment	54
3.2.1	Small Scale Induction Melting: Experiment Setup and Method . .	54
3.2.2	Small Scale Induction Melting: Experiment Results	56
3.3	Small Scale Induction Modelling	58
3.3.1	Small Scale Induction Modelling: Governing Equations and Physics	58
3.3.2	Small Scale Induction Modelling: Geometry and Mesh	59
3.3.3	Small Scale Induction Modelling: Boundary Conditions	60
3.3.4	Small Scale Induction Modelling: Material Properties	61
3.3.5	Small Scale Induction Modelling: Fluid Flow	62
3.3.6	Small Scale Induction Modelling: Mesh Sensitivity	62
3.3.7	Small Scale Induction Modelling: Results	63
3.3.8	Small Scale Induction Modelling: Discussion	66
3.4	Small Scale Induction Melting and Modelling with COMSOL: Conclusion	67
4	VIM-IC and Pouring Experiments	69
4.1	VIM-IC and Pouring Experiments Overview	69
4.2	Molten Alloy Imaging Experiment	72
4.2.1	Molten Alloy Imaging Experiment Overview and Aims	72
4.2.2	Molten Alloy Imaging Experiment Setup	73
4.2.3	Molten Alloy Imaging Experiment Method	74
4.2.4	Molten Alloy Imaging Experiment Results	75
4.3	Initial Induction Melting Experiments	78
4.3.1	Induction Melting Experiment Overview and Aims	78
4.3.2	Induction Melting Experiment Setup	79

4.3.3	Induction Melting Experiment Method	81
4.3.4	Induction Melting Experiment Results	82
4.3.5	Fixed Thermal Imager Results	83
4.3.6	High Speed Camera Results	86
4.3.7	Velocity Measurements	88
4.4	VIM-IC Design of Experiments: L9 Array	94
4.4.1	Design Of Experiments: L9 Array Overview and Aims	94
4.4.2	Partial Factorial Design: L9 Array	95
4.4.3	Bespoke VIM Chamber	97
4.4.4	DOE: Alloy Preparation	98
4.4.5	DOE: L9 Array Experiment Setup	99
4.4.6	DOE: L9 Array Experiment Method	100
4.4.7	DOE: L9 Array IR Thermometer Results	101
4.4.8	ANOVA Analysis of IR Thermometer Results	102
4.4.9	DOE: L9 Array High Speed Camera Results	104
4.4.10	ANOVA Analysis of High Speed Camera Results	108
4.5	Induction Melting: Testing Process Parameters	113
4.5.1	Induction Melting: Testing Process Parameters Overview and Aims	113
4.5.2	Induction Melting: Testing Process Parameters Experiment Setup	115
4.5.3	Induction Melting: Testing Process Parameters Experiment Method	115
4.5.4	Induction Melting: Testing Process Parameters Experiment Results	116
4.6	VIM-IC and Pouring Experiments Discussion	123
4.7	VIM-IC Experiments Conclusion	128
5	Modelling VIM-IC: Induction Melting and Pouring	130
5.1	Modelling VIM-IC Overview	130
5.2	Modelling VIM-IC: ESI ProCAST EMAG Module Overview	131
5.3	Modelling VIM-IC: ESI ProCAST EMAG Module Governing Equations and Physics	132
5.4	Modelling VIM-IC: Material Properties	134
5.5	Modelling VIM-IC: Geometry and Mesh	136
5.5.1	Coil Test Section: Mesh Refinement Study	136
5.5.2	Modelling VIM-IC: Geometry and Mesh	139
5.6	Modelling VIM-IC: Materials and Boundary Conditions	141
5.7	Modelling VIM-IC: Simulation Parameters	141
5.8	Modelling VIM-IC: Results	142
5.9	Modelling VIM-IC: Discussion	146

5.10	Modelling VIM-IC: Conclusion	149
5.11	Modelling VIM-IC: DOE L9 Array Overview	150
5.12	Modelling VIM-IC: DOE L9 Array Geometry and Mesh	150
5.13	Modelling VIM-IC: DOE L9 Array Materials and Boundary Conditions .	152
5.14	Modelling VIM-IC: DOE L9 Array Simulation Parameters	158
5.15	Modelling VIM-IC: DOE L9 Array Results	158
5.16	Modelling VIM-IC: DOE L9 Array Discussion	162
5.17	Modelling VIM-IC: DOE L9 Array Simulation Results Conclusion	163
5.18	Modelling VIM-IC Pouring: DOE L9 Array Overview	164
5.19	Modelling VIM-IC Pouring: DOE L9 Array Governing Equations and Physics	165
5.20	Modelling VIM-IC Pouring: DOE L9 Array Geometry and Mesh	166
5.21	Modelling VIM-IC Pouring: DOE L9 Array Materials and Boundary Conditions	167
5.22	Modelling VIM-IC Pouring: DOE L9 Array Simulation Parameters	169
5.23	Modelling VIM-IC Pouring: DOE L9 Array Results	170
5.24	Modelling VIM-IC Pouring: DOE L9 Array ANOVA Analysis of Simulation Results	175
5.25	Modelling VIM-IC Pouring: Discussion	181
5.26	Modelling VIM-IC Pouring: Conclusion	189
5.27	Modelling VIM-IC: Conclusion	190
6	Modelling VIM-IC: Mould Filling, Solidification and Defect Prediction	191
6.1	Modelling VIM-IC Mould Filling and Solidification Overview	191
6.2	Modelling VIM-IC: Mould Preheat and Cooling	191
6.2.1	Modelling VIM-IC Mould Preheat and Cooling Overview	191
6.2.2	Modelling VIM-IC Mould Preheat and Cooling: Governing Equations and Physics	192
6.2.3	Modelling VIM-IC Mould Preheat and Cooling: Geometry and Mesh	193
6.2.4	Modelling VIM-IC Mould Preheat and Cooling: Materials and Boundary Conditions	195
6.2.5	Modelling VIM-IC Mould Preheat and Cooling: Simulation Parameters	197
6.2.6	Modelling VIM-IC Mould Preheat and Cooling: Results	198
6.2.7	Modelling VIM-IC Mould Preheat and Cooling: Discussion	198
6.2.8	Modelling VIM-IC Mould Preheat and Cooling: Conclusion	199
6.3	Modelling VIM-IC: Mould Filling, Solidification and Defect Prediction . .	200
6.3.1	Modelling VIM-IC: Mould Filling, Solidification and Defect Prediction Overview	200

6.3.2	Modelling VIM-IC: Mould Filling, Solidification and Defect Prediction Governing Equations and Physics	200
6.3.3	Modelling Mould Filling and Solidification: Geometry and Mesh .	201
6.3.4	Modelling Mould Filling and Solidification: Materials and Boundary Conditions	202
6.3.5	Modelling Mould Filling and Solidification: Simulation Parameters	203
6.3.6	Modelling Mould Filling and Solidification: Results and Discussion	204
6.3.7	Modelling Mould Filling and Solidification: Conclusion	212
6.4	Modelling VIM-IC Mould Filling and Solidification: Conclusion	213
7	Conclusion and Further Work	214

Acknowledgements

I could not have undertaken this journey without the support, guidance and encouragement of my supervisors: Prof. Nick Lavery, Prof. Steve Brown and Dr. Steve Leyland. I would like to express my deepest appreciation and gratitude for everything that you have done in support of me and my work. This project would not have been possible without you.

I would like to extend my sincere thanks to Ole Koeser and Ronan Cronin from ESI Group, who I have had the pleasure of collaborating with, and who have generously given their time and support. I am also grateful to members of the MACH1 research group, ASTUTE and my colleagues at Swansea University who have contributed their time and resources towards this project.

Many thanks to ESI Group for providing access to the ProCAST software which was used in this work. I would also like to give special thanks to my colleagues at Uni-Pol Group, who have gone above and beyond to assist me over the course of this project.

The author would like to acknowledge the Materials and Manufacturing Academy (M2A) funding from the European Social Fund via the Welsh Government (c80816) and Uni-Pol Group that has made this research possible.

Lastly, I would like to thank those who have supported me personally in this endeavour. Andrew, thank you for your endless amount of support, love and encouragement. Words cannot express my gratitude for all that you have done. Thank you to my family and friends, who have assisted in providing emotional support and keeping my spirits high. Finally, thank you to Alex and Mari. The practical support and kindness that you have shown me is something that I will always be grateful for. Thank you for keeping me moving forward.

List of Publications and Presentations

- Thomas V U, Leyland S P, Bennett R, Brown S G R, Lavery N P. *Effect of Inlet Velocities on Mould Filling in Investment Casting*. [Presentation] TMS 2018. Phoenix, USA. 12th March 2018.
- Thomas V U, Leyland S P, Brown S G R, Lavery N P. *Modelling Investment Casting Mould Filling Using Experimental Data*. [Presentation] EICF 2018. Porto, Portugal. 24th April 2018.
- Thomas V U, Yar M A, Cullen J C T, Mehraban S, Brown S G R, Lavery N P. Numerical Modelling and Validation of Induction Melting of IN713C for Investment Casting. In: *Proceedings of COMSOL Conference 2020 Europe, 14-15 October 2020, Online*.
- Thomas V U, Koeser O, Leyland S P, Brown S G R, Lavery N P. Extension of Investment Casting Process Simulation By Electromagnetic Modelling of the Pre-Process Step of Billet Induction Melting. In: Krane M, Kharicha A, Ward M (eds.) *Proceedings of the Liquid Metal Processing & Casting Conference 2022, 18-21 September 2022, Philadelphia, USA*. Pittsburgh, USA: The Minerals, Metals & Materials Society (TMS). p.173-182.

List of Figures

1.1	VIM combined with direct pouring into investment casting mould setup .	3
2.1	Temperature dependent thermal conductivity for studied materials. IN713C: Krajewski et al. [58], CompuTherm [56]*. Aluminosilicate Ceramic Fibre: ProCAST [20]. Zircon: ProCAST [20]. Mullite: ProCAST [20]. *Thermal conductivity is artificially increased steadily between solidus and liquidus temperatures, up to 1800 W/m·K at liquidus, in electromagnetic simulations to account for fluid flow not being modelled.	21
2.2	Temperature dependent density for studied materials. IN713C: CompuTherm [56], CompuTherm adjusted [56]*. Aluminosilicate Ceramic Fibre: ProCAST [20]. *Density is adjusted according to experimentally obtained solidus and liquidus temperatures.	21
2.3	Temperature dependent density for air: ProCAST [20].	22
2.4	Temperature dependent enthalpy for IN713C: CompuTherm [56], CompuTherm adjusted [56]* *Enthalpy is adjusted to experimentally obtained solidus and liquidus temperatures.	22
2.5	Temperature dependent specific heat capacity for studied materials. Aluminosilicate Ceramic Fibre: [20], Air: [20], Mullite: [20].	23
2.6	Temperature dependent Newtonian viscosity for IN713C [56].	23
2.7	Temperature dependent newtonian viscosity for air [20].	24
2.8	DSC internal diagram, recreated from [62]	26
2.9	DSC heating and cooling curves for IN713C	27
2.10	Spectral transmittance of 10 mm thick borosilicate glass from 200-2600 nm	30
2.11	Diagram of temperature calibration experimental setup	33
2.12	Photograph of optical pyrometer calibration experiment with glass	33
2.13	Graph showing observed differences between thermocouple and infrared thermometer readings, with and without glass	36

2.14	Thermal image of billet and thermocouple in box furnace experiment . . .	38
2.15	Thermal image of box furnace experiment obscured by glass	38
2.16	Thermal imaging camera calibration experimental setup	39
2.17	Graph showing observed differences between thermal imaging camera and thermocouple readings, without glass	40
2.18	Thermal image of a hot investment casting mould filled with alloy taken with Thermoview Pi20HT, showing a defined AOI	42
2.19	Diagram showing internal configuration of an LFA machine, recreated from [71]	43
2.20	Schematic of two contacting bodies in direct contact, with arrows showing heat flow	44
2.21	Temperature dependent effective thermal diffusivity in one-piece and two-piece IN713C samples, pyroceram reference samples, and obtained thermal diffusivity values of IN713C from the work of Krajewski et al. [58].	48
3.1	Small scale induction melting and optical pyrometer setup	55
3.2	Temperature reading and induction heater settings: heating	56
3.3	Temperature reading and induction heater settings: melting	57
3.4	2D axisymmetric model geometry and mesh	60
3.5	Mesh convergence study	63
3.6	Induction heating simulation results for varying effective heat transfer coefficients. Optical pyrometer data set starts at 385 °C, which is the equipment lowest detectable temperature.	64
3.7	Induction melting simulation results for varying effective heat transfer coefficients	64
3.8	Billet temperature profile from melting model, $t = 100$ s	65
3.9	Phase transition and electromagnetic stirring, with black representing fully solid alloy and white representing fully molten alloy. Red and yellow regions are representative of alloy in the mushy zone.	65
3.10	Velocity profile and electromagnetic stirring, with dark blue representing stationary alloy and red indicative of alloy moving at higher velocities. . .	66
3.11	Thermal imaging: industrial induction melting	67
4.1	X-ray of Trials 14 and 15 from Initial Induction Melting Experiments in Section 4.3, with visible internal piping along the billet centrelines	70
4.2	Crucible test section, clamped and suspended above alloy basin	73
4.3	High speed camera focused on crucible test section	73
4.4	Optimal image	75

4.5	Close up photograph of a welded joint between two billet halves	78
4.6	Billet faces without external piping (left) and with visible piping (right) .	78
4.7	Experimental setup with IR and high speed camera on tripods	80
4.8	IN713C billet loaded into ceramic crucible in the induction coil	80
4.9	Trial 10 piping on billet face	81
4.10	Trial 11 piping on billet face	81
4.11	Trial 12 piping on billet face	81
4.12	Trial 13 piping on billet face	81
4.13	IR image of nickel billet heated to temperature	83
4.14	IR image of molten metal during electromagnetic stirring	83
4.15	IR image of welded alloy melt behaviour, billet top piece turning	83
4.16	Example window of DTPi software for top plane temperature analysis of Trial 5	84
4.17	Table in Excel showing maximum alloy temperature from crucible top plane during electromagnetic stirring for solid billets	85
4.18	Trial 6 - Solid concast billet pour	87
4.19	Trial 7 - Two-piece billet pour, poorly welded	87
4.20	Trial 13 - Two-piece welded billet, hole on pour face	88
4.21	Trial 14 - 3.295 kg billet with internal piping	88
4.22	Magnitude, PIV and Vector Plots generated using PIV Fiji plug-in	89
4.23	MATLAB PIV Plots	90
4.24	MATLAB PIV Graph Plots, x and y shift in pixels per frame	91
4.25	Inlet velocities, y direction for Trial 2	92
4.26	Left to right: full image of PIV plot with velocity vectors, top half of pouring alloy image, bottom half of pouring alloy image	94
4.27	Disc Height PLs (left to right): PL1: 15 mm, PL2: 35 mm, PL3: 50 mm	96
4.28	Hole Diameter (left to right): PL1: 0 mm, PL2: 2 mm, PL3: 10 mm . . .	96
4.29	Hole Position (left to right): PL1: Bottom (B), PL2: Middle (M), PL3: Top (T)	97
4.30	Bespoke VIM chamber front view	98
4.31	Bespoke VIM chamber left side view	98
4.32	Bespoke VIM chamber rear view	98
4.33	PL1: 15 mm disc, 170 mm top billet piece	99
4.34	PL2: 35 mm disc, 150 mm top billet piece	99
4.35	PL3: 50 mm disc, 135 mm top billet piece	99
4.36	Billet pieces with 2 mm hole (left) and 10 mm diameter hole (right) . . .	99

4.37	Bespoke VIM chamber installed on site with IR thermometer above top viewing port and high speed camera focused on front viewing port	100
4.38	Trials 1a-1c: Top Billet Face Temperatures in Induction Heating and Melting	102
4.39	Time Between 880°C to Pour	103
4.40	Time Between 880°C to Solidus	103
4.41	Superheat Duration	104
4.42	Superheat Start Temp.	104
4.43	Pour Temp.	104
4.44	Maximum Recorded Temp.	104
4.45	Trial 4b end of pour small width	105
4.46	Trial 1c mid pour, large width	105
4.47	Trial 7a start of pour, small angle	106
4.48	Trial 3c end of pour, large angle	106
4.49	Trial 1a - First analysed image, n=0 with generated grid and velocity vectors	107
4.50	Trial 1a - Final analysed image, n=5 with generated grid and velocity vectors	107
4.51	Trial 1a - Image n=0 imposed upon n=5 showing shift between frames .	107
4.52	Trial 1a, start of pour: Average x and y velocities in cm/s for each row of dots in the grid generated on the flow surface	107
4.53	Pour Time	109
4.54	Flow Width: Start of Pour	109
4.55	Flow Width: Middle of Pour	110
4.56	Flow Width: End of Pour	110
4.57	Flow Angle: Start of Pour	111
4.58	Flow Angle: Middle of Pour	111
4.59	Flow Angle: End of Pour	111
4.60	Flow Vel Mag: Start of Pour	111
4.61	FlowVel Mag: Middle of Pour	112
4.62	Flow Vel Mag: End of Pour	112
4.63	Trials 1-5, top face temps	117
4.64	Trials 1-5, pouring temps	117
4.65	Trials 1-3, 6-10, top face temperatures	118
4.66	Trials 1-3, 6-10, pouring temperatures	118
4.67	Trials 4, 5, 11-14, top face temperatures	119
4.68	Trials 4, 5, 11-14, pouring temperatures	119
4.69	Trials 9, 10, 15, 16, top temps	120
4.70	Trials 9, 10, 15, 16, pour temps	120
4.71	Trials 1-3, 17-22, top face temperatures	121

4.72	Trials 1-3, 17-22, pouring temperatures	121
4.73	Trials 1-3, 23, 24, top face temperatures	122
4.74	Trials 1-3, 23, 24, pouring temperatures	123
4.75	One-piece billet, end of pour high speed camera image	124
4.76	Alloy leftover from a complete pour (left) vs. Run 6	125
4.77	Leftover alloy solidified in crucible outlet after pouring	125
5.1	Coarse coil mesh	136
5.2	Fine coil mesh	136
5.3	Coarsely meshed coil: B (real)	138
5.4	Finely meshed coil: B (real)	138
5.5	Coarsely meshed coil: Magnetic Energy Density	138
5.6	Finely meshed coil: Magnetic Energy Density	138
5.7	VIM geometry: tetra element 3D mesh cross section	140
5.8	VIM-IC Model: Magnetic Flux Density	142
5.9	VIM-IC Model: Magnetic Energy Density	142
5.10	VIM-IC Model: Joule Heat Density	142
5.11	VIM-IC Model: temperature in coil and crucible at pour point	142
5.12	Fraction solid: melt front progression in induction heating (left to right) .	143
5.13	Billet heated by induction for 50 seconds before generator switch off [94]	143
5.14	VIM-IC Model: Fraction solid distribution at pour point, cut off at $fs_{0.3}$ plot	143
5.15	VIM-IC induction heating model vs. experiment, top face temperatures during VIM	144
5.16	VIM-IC Model: Billet temperature distribution at pour point	145
5.17	No Split Billet Length Temperature Profile, Pour Point	145
5.18	VIM-IC Model: Billet temperature distribution at pour point	146
5.19	No Split Billet Bottom Face Temperature Profile, Pour Point	146
5.20	Fraction solid curve: solid to liquid state transition between solidus (1) and liquidus (0) temperatures [94]	146
5.21	3D render of copper induction coil	149
5.22	Run 3 tetra mesh featuring hole and slice volumes	151

5.23	Testing constant heat transfer coefficient values applied at split billet interface, at the time step at which the melting front meets the billet interface for Run 1	153
5.24	Pouring time step billet length temperature profile, one-piece billet vs. fixed heat transfer coefficient values applied at billet interface for Run 1 .	153
5.25	Temperature dependent heat transfer coefficient for split billet interface	154
5.26	Coincident interface condition for Run 1, 15 mm disc with no holes	154
5.27	Temperature along billet length for Runs 1, 4 and 7 (no holes) at the time step for which the melting front is located at the billet split interface . .	155
5.28	Coincident interface condition for top hole position configuration	156
5.29	Top hole position fraction solid distribution of melt front at interface point	156
5.30	Coincident interface condition for middle hole position configuration . . .	157
5.31	Middle hole position fraction solid distribution of melt front at interface point	157
5.32	Coincident interface condition for bottom hole position configuration . . .	157
5.33	Bottom hole position fraction solid distribution close to pour point . . .	157
5.34	Top billet face temperatures in VIM-IC induction heating simulations *Temperature curves for models for runs 6 and 8 were stopped at predicted pouring time steps and were not suitable for use as an initial condition for the ANOVA analysis of simulation results. This is further explained in Section 5.21.	159
5.35	Run 2 billet pour face fraction solid at pour, $fs_{0.3}$ and below cut off image	160
5.36	Run 4 billet pour face fraction solid at pour, $fs_{0.3}$ and below cut off image	160
5.37	Run 6 billet pour face fraction solid at pour, $fs_{0.3}$ and below cut off image	160
5.38	Run 8 billet pour face fraction solid at pour, $fs_{0.3}$ and below cut off image	160
5.39	Fraction solid distribution at pouring across billet diameter for Runs 1-9 *Simulations for models for runs 6 and 8 were stopped at predicted pouring time steps and were not suitable for use as an initial condition for the ANOVA analysis of simulation results. This is further explained in Section 5.21.	161
5.40	ANOVA Flow Width, Start of Pour, Simulations vs. Experiments	161
5.41	Magnetic Energy Density for Run 4, 35 mm disc with no holes	162

5.42	Section view of 3D tetra mesh for pouring simulation setup	167
5.43	Temperature dependent heat transfer coefficient between alloy and mould	168
5.44	Run 3, alloy pouring out of the crucible into an empty channel volume .	170
5.45	One-piece billet during pouring, billet and alloy volumes	170
5.46	Run 1, alloy pouring temperature with rayleigh plateau instability	171
5.47	Run 7, alloy temperature plot with further rayleigh plateau instability	171
5.48	Run 9, flow showing ‘corkscrew’ style flow perturbations	171
5.49	Run 9, flow showing ‘tree-like wire’ style flow pattern	171
5.50	One-piece billet fluid velocity, vena contracta and perturbations	172
5.51	Run 4 temperature plot with highly angled flow	172
5.52	End of pour flow temperature for Run 5	172
5.53	Run 1, leftover alloy solidifying at crucible outlet after crucible emptying	172
5.54	VIM-IC pouring models, temperature ingate plots at crucible outlet *Runs 6 and 8 not included as pouring could not be accurately modelled for these configurations.	173
5.55	VIM-IC pouring models, temperature ingate plots at crucible outlet *Runs 6 and 8 not included as pouring could not be accurately modelled for these configurations.	173
5.56	VIM-IC pouring models, velocity magnitude ingate plots at crucible outlet *Runs 6 and 8 not included as pouring could not be accurately modelled for these configurations.	174
5.57	VIM-IC pouring models, velocity magnitude ingate plots at crucible outlet *Runs 6 and 8 not included as pouring could not be accurately modelled for these configurations.	174
5.58	ANOVA Pour Time, Simulations vs. Experiments	176
5.59	ANOVA Flow Width Start of Pour, Simulations vs. Experiment	176
5.60	ANOVA Flow Width Mid Pour, Simulations vs. Experiments	177
5.61	ANOVA Flow Width End of Pour, Simulations vs. Experiments	178
5.62	ANOVA Flow Angle Start of Pour, Simulations vs. Experiments	178
5.63	ANOVA Flow Angle Mid Pour, Simulations vs. Experiments	179
5.64	ANOVA Flow Angle End of Pour, Simulations vs. Experiments	179
5.65	ANOVA Fluid Vel. Start of Pour, Simulations vs. Experiments	180
5.66	ANOVA Fluid Vel. Mid Pour, Simulations vs. Experiments	180

5.67	ANOVA Fluid Vel. End of Pour, Simulations vs. Experiments	181
5.68	Hypothesised billet portion pour order	184
6.1	Meshed investment casting tree geometry, sprue and wheel castings	193
6.2	Meshed investment casting shell mould created around crucible assembly	193
6.3	Crucible and mould assembly meshed with 3D tetra mesh and 2D tria based air enclosure mesh	195
6.4	Film coefficient transition from atmosphere conditions to vacuum, from furnace removal to alloy pouring point	196
6.5	Meshed investment casting shell mould and crucible, with region in which wrap boundary condition is applied in the blue region	196
6.6	Mould assembly temperature distribution at alloy pouring point, after preheating and cooling	198
6.7	Top view of shell mould after preheating and cooling, showing internal mould temperatures with crucible geometry hidden	198
6.8	Crucible, billet and mould assembly, 3D tetra mesh	201
6.9	Film coefficient transition from vacuum conditions to atmosphere, from alloy pouring point onwards	203
6.10	Mould design side view with numbered tiers	204
6.11	Mould design top view with numbered wheels	204
6.12	Casting with no misrun predicted	205
6.13	Casting with misrun predicted	205
6.14	Defect mapping: misrun	206
6.15	Shell region with no mould erosion predicted	208
6.16	Shell region with mould erosion predicted	208
6.17	Defect mapping: mould erosion	209
6.18	Casting with only internal shrinkage porosity predicted	209
6.19	Casting with surface level porosity predicted on blades	209
6.20	Defect mapping: surface level porosity	210
6.21	Defect mapping: internal porosity	210

List of Tables

2.1	Thermophysical properties for the studied materials	20
2.2	IN713C composition: alloy specification ranges and input composition values	25
2.3	Temperature difference observed between thermocouple and IR thermometer readings for trialled E-Slope values	35
2.4	Polishing sequences implemented to achieve different surface finishes. . .	46
2.5	Polishing sequences implemented to achieve different surface finishes . . .	47
3.1	Calculated penetration depths at known frequencies	60
3.2	Relative CPU time (1 absolute time unit = 8 hours) and average model mesh element quality for varying billet and crucible domain max. element sizes	62
4.1	Frame rate calculations	74
4.2	Determining Optimal Camera Settings	77
4.3	Induction melting trials overview	82
4.4	Table showing conversion of pixels per frame to metres per second	92
4.5	Testing the effect of frame step number on computed velocities	93
4.6	DOE table for experiments based on L9 array; three parameters at three levels	95
4.7	Testing process parameters trials overview	114
5.1	Electromagnetic properties for the studied materials	135

Definitions and Abbreviations

AC	Alternating current
AOI	Area of interest
CAD	Computer aided design
DC	Direct current
DOE	Design of experiments
DSC	Differential scanning calorimetry
EDM	Electrical discharge machine
FDM	Finite difference method
FEM	Finite element method
FPS	Frames per second
FVM	Finite volume method
fs	Fraction solid
HTC	Heat transfer coefficient
IN713C	Inconel 713C
IR	Infrared
LDV	Laser doppler velocimetry
LES	Large eddy simulation
LFA	Laser flash analyser
MHD	Magnetohydrodynamics
PIV	Particle image velocimetry
PL	Parameter level
PTV	Particle tracking velocimetry
TCC	Thermal contact conductance
TPV	Thermographic particle velocimetry
TRC	Thermal contact resistance
UDV	Ultrasound doppler velocimetry
VIM	Vacuum induction melting
VIM-IC	Vacuum induction melting investment casting

Chapter 1

Introduction

1.1 Overview of Vacuum Investment Casting

Induction melting involves the heating and subsequent melting of a metal, due to eddy currents in the metal workpiece which are induced by an alternating magnetic field. The alternating current (AC) produced by an induction coil results in a changing magnetic field in the surrounding area, with a frequency matching the coil AC. If an electrically conductive metal is placed within the induction coil loop, eddy currents of the same frequency of the coil current but in the opposing direction will be induced within it. The metal is inductively heated, largely due to the Joule effect [1]. The Joule effect, also referred to as Joule heating, occurs as a result of resistive losses during the movement of electrons associated with the eddy currents [2]. These losses are as a result of the electrical resistance of the metal workpiece [2].

In ferromagnetic materials, additional heating can occur due to the effects of magnetic hysteresis [2]. A ferromagnetic material behaves as a ferromagnetic system, i.e., as a cooperatively ordered system with long-range interaction in which a magnetic moment relies on its neighbours to create magnetic ordering [3]. It is made up of many small magnetic domains, where a magnetic domain can be defined as a region in which the magnetic moments of the individual atoms within the region are aligned with each other [4]. For a ferromagnetic system, magnetisation of the system occurs with the presence of a magnetic field. However, once the external magnetic field is removed, the magnetisation of the system does not return to zero [5]. This phenomenon is known as magnetic hysteresis. Remanence is a measure of the residual magnetic flux in the material when the external

magnetic field is zero [5]. Furthermore, coercivity is a measure of the field in the opposite direction which is required to return the magnetisation to zero after magnetic saturation [5]. This hysteresis can cause additional heating, which can be understood in a simplistic way as being as a result of friction between molecules or magnetic dipoles that change in orientation with the alternating field [2][6]. The energy required to reverse the orientation of the dipoles in the alternating field is dissipated as heat [2].

Magnetic hysteresis occurs up to the Curie temperature, which is the critical temperature above which a ferromagnetic system begins to behave as a paramagnetic system [7]. A paramagnetic material is comprised of many small domains which, without the application of an external magnetic field, are magnetised in random orientations, resulting in a total net zero magnetisation [3]. Under an external magnetic field, the domains within a paramagnetic system are weakly magnetised in the direction of the magnetic field. However, paramagnetic materials do not experience hysteresis, therefore additional heating through hysteresis losses does not occur.

Vacuum Induction Melting (VIM) is induction melting under vacuum conditions. Melting and casting the alloy in a vacuum can help to prevent entrapped air bubbles within the melt. It is also necessary for casting nickel based alloys, which contain highly oxidising elements. In this thesis, VIM is studied in the context of Vacuum Induction Melting Investment Casting (VIM-IC). Investment casting derives its name from the verb '*to invest*', which means to coat [8]. Creation of an investment casting mould involves coating an assembled wax component tree in a slurry made of a finely powdered mineral and binder. The finely powdered mineral used is often zircon, or aluminium silicate which also known as mullite. Stucco, a coarser mineral, is applied before the slurry dries. This process is repeated, forming successive layers which gradually accumulate and form a shell mould. An autoclave is used to remove wax from the shell, which is then fired in a furnace to strengthen the mould and remove any remnants of carbon from the lost wax. The shell mould is then filled with molten metal. After the metal has cooled, the casting is ready for shell removal.

The VIM-IC process involves VIM of an alloy billet, combined with direct pouring into an investment casting mould. An Inconel 713C (IN713C) nickel alloy billet is inserted into a ceramic fibre crucible attached to a shell mould. The loaded crucible is positioned within a copper induction coil. The coil is contained within a vacuum chamber, and the coil terminals are attached to a generator. The majority of the billet length is positioned within the coil, with a portion of the billet length extending below the bottom of the

1.2. THE RESEARCH PROBLEM

coil. The generator power sequence is initiated, producing an AC in the coil circuit. As a result, the billet experiences induction heating.

As the billet melts it begins electromagnetic stirring, due to the eddy currents produced by the AC. The crucible outlet is attached to a mould composed of zircon sand, mullite and vermiculite. The crucible is attached to the mould during the investment casting shelling process, by successive slurry dipping and stucco coating. This allows for direct pouring into the mould from the crucible. Once the remaining billet length below the coil has melted by conduction, the liquid metal will immediately drop from the crucible. Molten metal leaves the crucible and directly fills a runner system, creating casted components on an investment casting tree. Figure 1.1 shows the VIM-IC setup for the production of turbocharger turbine wheels. The shell is removed using strong vibrations, and remaining shell material is removed by methods such as shot blasting. Individual components are cut from the central sprue, and casted components are then post processed to remove any visible defects.

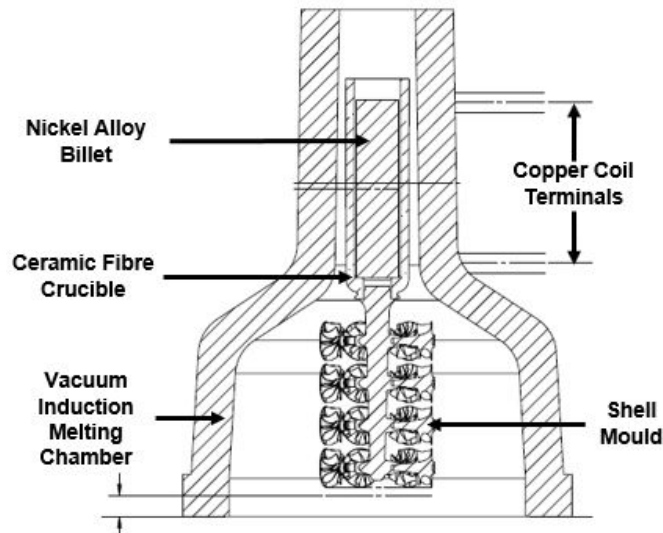


Figure 1.1: VIM combined with direct pouring into investment casting mould setup

1.2 The Research Problem

VIM-IC is chosen as a method for manufacturing precision components, where high quality surface finish is critical. It is often used for manufacturing components of which making a one-piece mould in situ would be challenging. Historically, investment casting of nickel based alloys has been prone to high scrap rates, which is a main factor causing this manufacturing method to be expensive. A combination of the frequency and severity of

1.2. THE RESEARCH PROBLEM

defect occurrence in the finished castings determines the overall scrap rate.

Three common defects that occur in the investment casting industry are porosity, misruns and inclusions. All three of these defect types can be triggered by a variety of sources, but one factor which unites them all is issues related to alloy temperature. Porosity can occur when alloy temperatures are low during filling and solidification, as insufficient feeding of the casting causes both internal and external porosity to form. Misruns can also be caused by alloy temperatures within the mushy zone temperature range during filling, as the alloy fails to fill the mould completely and due to solidification while filling. In the case of misruns, the alloy stops short of the extremities of the geometry in the mould cavity. Although not temperature related, misruns can also be caused by an increased internal pressure within the mould at the last point of filling. This can cause an inability of the shell to undergo the outgassing process, resulting in misruns. Finally, inclusions can be caused by excessively high alloy temperatures during filling. This is due to the relationship between fluid viscosity of the alloy and its temperature, with high temperature alloy increasing the risk of mould erosion. Mould erosion is the term used to describe when particles of refractory material, such as zircon, delaminate from the internal surface of a mould. Mould erosion is a result of high velocity fluid flow and turbulence behaviour during mould filling. This causes the refractory material to delaminate, which often manifests as an inclusion in the finished casting if it does not end up in the sprue. Due to a density difference between the inclusion particles and alloy, the particles float to the surface of the casting and can be detected by visual inspection.

However, mould erosion is not the sole cause of inclusions in finished castings. Inclusions can also be generated due to excessive electromagnetic stirring in the crucible. This excessive stirring can cause crucible material, such as aluminosilicate ceramic fibre, to be eroded from the crucible walls. This material is then pulled into the shell mould below as the alloy pours from the crucible into the mould, and can be detected as an inclusion in the finished casting. Both mould erosion and crucible erosion are caused by excessive velocities of molten metal during electromagnetic stirring and subsequent mould filling. Furthermore, there are other factors which can cause inclusions to occur. For example, poor assembly of the casting wax patterns onto the sprue wax pattern can create negative holes which are filled with ceramic. These holes are prone to being eroded by the molten alloy, and hence ceramic inclusions can be formed.

It is important to gain an understanding of the alloy temperatures and velocities during mould filling, as a result of VIM-IC. However, using standard industrial VIM-IC equipment,

it is not possible to determine the temperature distribution throughout a billet of alloy during induction heating. The standard VIM chamber only has a top viewing port, allowing visibility of the top of the billet during heating and melting. This does not provide an opportunity to measure the temperature of the alloy throughout the billet during VIM, or in pouring for mould filling. Even if the chamber was not opaque, the alloy pours directly into a mould attached to the crucible, which also does not allow temperatures of alloy to be measured or flow behaviour to be observed during pouring.

Computational modelling of VIM can be implemented to predict the temperature profile of alloy in this melting process, and the effect this has on casting defect occurrence in VIM-IC models. Computational modelling is a cost effective method of evaluating optimal operating conditions, as numerous parameter combinations can be tested without the costs associated with physical experiments. However, it is important to validate the temperature and flow characteristics generated by VIM-IC models with experimental data. A smaller array of experiments can be devised for model validation, to compare results and establish accuracy of the numerical models. Experiments can be designed to measure temperature and flow data during induction heating, melting and direct pouring, which can be used as model validation. Limits of acceptability for alloy condition can be determined for VIM using current operating conditions, to produce an acceptable pour temperature, flow pattern and velocity. Additional experiments will be used to determine material properties that are not available from existing literature.

1.3 VIM-IC Modelling and Validation Literature Review

Modelling the VIM-IC process requires an understanding to be developed of both the underlying physics involved and the equations governing the induction heating phenomena. To achieve this, it is not only important to examine the literature regarding induction melting physics, but also to review the existing studies which have been conducted on modelling induction melting. With the aim of understanding the effect of varying process parameters on the outcomes of casting defect rates, it is beneficial to consider software packages with the capability of predicting casting defects. The physics of the models herein are outlined and discussed in the relevant chapters.

Computational modelling of industrial processes allows for the testing of an infinite number of process parameter combinations. There is comparatively little associated

1.3. VIM-IC MODELLING AND VALIDATION LITERATURE REVIEW

cost compared to running physical trials for all of the possible permutations. The value of modelling industrial processes is increased further by experimental validation. This ensures that computational models are accurately predicting the physical behaviour which is observed in the real world and producing results which are valid. However, the value of modelling is not only in the ability to produce reasonable results, but also in the insight which it offers as to why certain behaviours are occurring. For example, by gaining an understanding of the physical mechanisms which cause differences in flow width, or changes in temperature, this knowledge can then be used to better inform process design without requiring an extensive number of further physical trials to be run.

Modelling the VIM-IC process involves the computation of multiple different multiphysics phenomena. Investment casted components often consist of complex geometries. The modelled materials have temperature dependent thermophysical material properties. To successfully model VIM-IC involves solving complex partial differential equations with applied boundary conditions to obtain solutions across the discretised geometrical domains. Due to the complexities involved in modelling VIM-IC, analytical solutions to these problems cannot be obtained. For this reason, numerical methods are used. These methods include Finite Difference Method (FDM), Finite Volume Method (FVM), Finite Element Method (FEM) and others [9][10]. For all of these methods, the overarching approach to tackling casting simulations follows four steps: creation of CAD for the riser and casting design, model setup including application of materials and boundary conditions, simulation computation, and post-processing of results [11].

In the investment casting industry, the design geometry for the desired casting is often provided by the customer in CAD format. However, establishing a suitable riser design for an investment casting tree mould often involves an iterative process in-house at the foundry. Various configurations are tested using a combination of simulation modelling and prototype design casting trials. Building the geometry of the casting tree can either be done from scratch, or by assembling casting geometries onto existing riser designs in the required form. A mesh is created, with appropriate levels of refinement to effectively depict the casting geometry.

Next, the designation of casting and mould volumes are defined with the appropriate materials. At this stage of the process, the relevant material properties and boundary conditions are applied. Depending on the required boundary conditions, techniques may be used to model an infinite ‘air’ domain. Thermophysical properties of materials may need measuring, where these properties do not exist in the literature. These material

properties may or may not need to be temperature dependent, dependent upon if it is important for the physics that is being modelled.

Numerical computation of the simulation is performed. This is the stage at which numerical methods such as FDM, FVM, or FEM are implemented. FDM involves the discretisation of a continuous domain, in which the dependent variables of partial differential equations are calculated at only the discrete nodes. The solutions at these nodes are approximated by solving a linear algebraic equation, in which the differential terms of the partial differential equation are converted into what is known as the finite-difference equation [12]. The benefits of FDM are that the solutions are stable, converge rapidly and provide a straightforward solution for solving partial differential equations [12]. However, the disadvantage of FDM is that complex surfaces are not created smoothly using an FDM mesh [13]. This can cause issues for the definition of boundary conditions at curved surfaces, for an FDM mesh which is not sufficiently refined. As an FDM mesh consists of these uniform cubic elements, the required mesh refinement level for a complex geometry with thin sections would be very high. Although methods to allow mesh adaptive techniques for FDM have been explored [14], including for the application of casting process simulation [15], this capability is not very widely available in commercial FDM casting software. FVM works on the basis of conservation of fluxes at the cell boundaries [16]. While FDM solves differential equations based on nodal relations, FVM discretises the governing equations in integral form [17]. According to Kolditz, there are two main advantages of FVM. The first is that conservation of quantities is enforced at a discretised level, allowing for accurate computations in the presence of strong gradients. The second is that FVM is well suited to complex geometries, as arbitrary meshes can be capitalised upon [17].

FEM satisfies the conditions of conservation implicitly. The spatial domain is divided into simple geometric triangular or quadrilateral elements. Across the domain of each element, the solution is approximated using weighted residual concepts to solve the partial differential equations [18]. There are many advantages to using FEM for the application of fluid dynamics. One of the main advantages is that FEM allows for an arbitrary domain subdivision to be implemented which is fully unstructured, serving as an approximation that is either equal or superior to those provided by FDM for self-adjoint problems [19]. There is a higher computational expense associated with implementing FEM compared to FDM and FVM, for modelling fluid flow in this application. As a result, the widespread use of FEM solvers in commercial casting software has mostly taken place in the last two decades, coinciding with improvements in computing power.

The final stage of the casting simulation procedure involves the post-processing of results. Useful information regarding mould filling and solidification behaviour can be obtained by interrogating images of the process at defined timesteps. Cut-off plots which allow for the given parameter to be displayed above, below or within the range of certain values allow for prediction of defect occurrence and severity. Numerical data regarding the evolution of a parameter such as temperature can be plotted over time for a given node, or alternatively profiles across a given geometry can be extracted and plotted for comparison. Commercially available casting softwares such as ESI ProCAST [20] allow for these types of results interrogation to be performed.

1.3.1 Modelling and Validation of VIM

The modelling of induction melting has been covered in existing literature, using a variety of different software packages to model the phenomena. Where possible, a simplified approach to modelling high frequency induction heating may be favoured [21]. However, the reduction of induction heating and melting systems to a simplified form is not always possible for generating useful data. In these cases, the use of software capable of modelling electromagnetics is required. One example of software used to model induction melting is the Magneto-Hydrodynamics (MHD) module in Ansys Fluent. It is capable of analysing electrically conductive fluid flow under the influence of a direct current (DC) or AC electromagnetic field [22]. The module allows the use of built-in functions or user-defined data files, and existing research shows that the add-on module has been used to model similar problems. In their study of molten steel, Wang *et al.* used Ansys Fluent to simulate fluid flow, solidification, and the motion and entrapment of non-metallic inclusions in a 3D computational model of steel undergoing induction melting [23]. The model was developed using a combination of Ansys, Fluent and MATLAB, with Ansys being used to compute the electromagnetic field. The electromagnetic data was then obtained from Ansys and written to a ‘MAG’ file, which was carried out by the MHD model in Fluent, using the software interface between Ansys and Fluent (MHD). The fluid flow behaviour of velocity vectors in during electromagnetic stirring was computed by the MHD module, using a ‘MAG’ file in Fluent. User defined files were also applied to the model. These files were written to account for the acceleration rate produced by the electromagnetic repulsion force, define the boundary condition, and to apply the condition for inclusions to enter the melt. Similarly, Yang *et al.* modelled induction melting of Ti-Al using Ansys to compute the electromagnetic field, and Fluent for the fluid flow and thermal calculations. The T- Ω method was used to solve Maxwell’s equations, which is described further in

the paper [24]. This case examined the ‘Cold Crucible Direct Solidification’ process of TiAl alloys. The time averaged velocity vectors of the flow field within the meniscus were predicted and created graphically.

In a research paper investigating the heat transfer process in electromagnetically driven flow within a vacuum induction furnace, Buliński *et al.* used Ansys to model the velocity vectors, alongside the temperature of the molten nickel [25]. Furthermore, Spitans *et al.* implemented a combination of Ansys Classic, Fluent and CFX-Post external coupling to develop a new method for a joined simulation of liquid metal flow, free surface dynamics and an electromagnetic field [26]. The model was specialised to include electromagnetic levitation and considered in three dimensions by applying $k-\omega$ ‘Shear Stress Transport’ or ‘Large Eddy Simulation’ (LES).

Spitans *et al.* also compared the results of their new method to other models, and conducted experiments taking measurements in both traditional and electromagnetic levitation induction furnaces. Their work proved capability of the model to calculate Lorentz force density, flow pattern and free surface dynamics in two dimensions. The model assumed that the electromagnetic field and eddy currents within the melt were of a harmonic nature, allowing the Lorentz force F^{Lorentz} to be separated into a steady and harmonic part that oscillates with double frequency. The harmonic contribution was considered negligible due to the inertia of the melt being much greater than the alternate electromagnetic field timescale. The model also deemed any secondary electromagnetic field generated due to flow as negligible compared to the induced field.

An LES turbulence model in Ansys Fluent was also used by Musaeva *et al.* to simulate melt flow in an induction crucible furnace under a low frequency pulsed Lorentz force [27]. In their work, they compared the effect on flow of applying a pulsed Lorentz force to flow produced by a continuously applied force. It is evident from these studies using Ansys to model induction melting, that the velocity vectors of metal during electromagnetic stirring and the free surface are able to be captured.

The work of Pericleous has been especially prevalent in the field of modelling MHD, particularly with regards to simulating the magnetic levitation of metals [28]. In a numerical study of the cold crucible melting process, experimental validation of a number of parameters was achieved [29]. This included measurements of the meniscus height relative to the top of the crucible, and temperature measurements throughout the melting and solidification of aluminium billets, using a thermocouple inserted into a drilled hole in the billet. An emphasis on modelling the meniscus dome shape has been a theme

throughout Pericleous' work, including in a study of cold crucible melting with bottom pouring nozzle with Bojarevics [30]. Experimental validation of the meniscus shape has also formed a part of Pericleous' work, which is seen in the work of others such as Buliński *et al.* [31]. The studies in this field by Pericleous, Bojarevics *et al.* were implemented using different numerical softwares, including SPHINX and Physica [28][29][30]. Meanwhile, other literature has explored the use of Ansys to model electromagnetic levitation melting [32][33].

COMSOL is a multiphysics solver known for its capabilities in coupling phenomena. In 2015, Bruyere of SIMTEC published an article on the COMSOL online blog describing a model of an induction furnace created using COMSOL Multiphysics software [34]. The model utilises the Induction Heating multiphysics interface within COMSOL, which automatically applies 'Magnetic Field' and 'Heat Transfer in Solids' physics interfaces to the component. In order to ensure a strong coupling, study steps of 'Frequency-Stationary' or 'Frequency-Transient' can be preselected. For these study steps, Ampere's law was solved for each time for a given frequency, followed by the thermal problem for a stationary or transient state. The model geometry was created in COMSOL and was assumed to be axisymmetric. This meant that the only non-zero component of the magnetic potential vector was perpendicular to the geometry plane. A 'Single-Turn Coil' condition was added to the copper surfaces to apply the electromagnetic source, while 'Coil Group' mode was used to apply the coil power due to excitation. This was selected to ensure the sum of voltages of all the turns was used to produce total coil power. This allowed the problem to become nonlinear, and COMSOL Multiphysics automatically applied related equations to calculate the correct power. The 'Surface-to-Surface' boundary condition was implemented as an approach for the thermal problem, with the 'Heat Transfer in Solids' physics interface by selecting the external boundaries of each component. The heat equation was only solved for solid parts, neglecting the effect of surrounding air. By taking the temperature of the molten metal to be homogeneous, surface tension and buoyancy effects can be neglected. This leaves only Lorentz forces in action, which is added as an extra term to the fluid momentum equation. In support of the use of the single-turn coil condition in COMSOL is the analytical and experimental validation of electromagnetic simulations by Kennedy *et al.* [35]. One of the conclusions drawn from their work was that single-turn domains were required for scenarios in which electromagnetic penetration depth was smaller than the diameter of the coil tubing.

A study by Hadad *et al.* used COMSOL to model VIM was to test the effect of adding a secondary heating coil to account for stepped diameter crucibles [36]. Their work also

involved the use of thermocouples to monitor temperature of the melt and crucible wall. Temperatures were compared for trials with the use of secondary heating coil, to those measured without the use of this additional coil. Equally, in their work to determine critical wire size for the application of a specific induction heating system, Prasad *et al.* used an infrared (IR) thermal imaging camera to experimentally validate molten metal temperatures obtained in their ABAQUS numerical model [37]. However, temperature validation is not the only aspect of induction melting that can be validated. Velocities of molten Wood's metal in a model induction furnace were measured using a potential probe by Umbrashko *et al.*, in validation of their LES-modelling of melt flow [38]. Similarly, the velocities of Wood's metal were obtained experimentally for comparison to computed velocities in a thesis by G. Nardo [39]. COMSOL was used to model an induction furnace, melting the metal at its low melting point of 72 °C. The approach taken in this work involved recording melt velocities using an Ultrasound Doppler Velocimetry (UDV) probe. The results were computed for different methods, including $k-\epsilon$, $k-\omega$ and Low-Re $k-\epsilon$ solutions. The study concluded that the Low-Re $k-\epsilon$ method most accurately described the fluid flow behaviour. Nardo *et al.* used both $k-\epsilon$ and $k-\omega$ solutions to compute the fluid flow vortexes in an induction furnace, complimented by experiments using an Ultrasound Doppler Velocimetry probe to determine the velocity profile within the melt. $k-\epsilon$ solution was considered the most straightforward way to predict location of vortexes within the molten metal flow. $k-\omega$ is more accurate near walls, allowing increased accuracy of turbulent viscosity on the fluid domain. However, the computational refinement for $k-\omega$ requires a good quality mesh structure. Although the meniscus and free surface of the alloy is not predicted in induction melting models using COMSOL software, the stirring due to the Lorentz force appears to be captured.

1.3.2 Modelling and Validation of Casting Processes and Solidification

Modelling the investment casting process allows for multiple design iterations to be tested, without undergoing the time consuming and costly process of producing and casting prototype models for each iteration. Furthermore, when testing the capability of a new mould design, large batch numbers must be produced in order to account for the unpredictability of VIM and any variability within the production process. Viable investment casting modelling avenues should allow for the import of CAD geometry, as complex geometry requests from customers are not uncommon.

To ensure the reliability of mould filling simulations, computed fluid flow behaviour should ideally be compared to experimental data on mould filling. By performing X-ray radiography of an aluminium casting, the progression of mould filling was captured in a series of images which were used as a benchmark for comparison to simulation results by Sirrell *et al.* [40]. Comprehensive details of the casting geometry and conditions were provided, which allowed for these experiments to serve as useful benchmarking data within the casting simulations field. Later work of Campbell with Hsu *et al.* revisited this X-ray radiography technique for aluminium gravity casting, tracking the movement of liquid metal for comparison to computational modelling of mould filling [41]. Another example of mould filling model validation for aluminium gravity castings is the work of Zhao *et al.* [42].

The prediction of defects in investment casted parts has been widely studied over the years, using a range of computational methods. The FDM software ‘ADSTEFAN’ was developed via an industry-university cooperative project in Japan in 1999. The capability of this software for modelling shrinkage porosity defects using a volume change model was tested by Takahashi *et al.*, comparing the simulation results to those of die casted components [43]. In their work on defect prediction, Bounds *et al.* implemented PHYSICA software to predict misruns, shrinkage macroporosity and pipe shrinkage using a pressure based criterion [44]. This approach involved using a family of finite volume unstructured mesh procedures, which were applied to address thermal elastoviscoplastic solid mechanics. Their work sought to couple the effects of free surface flow interacting with heat transfer and solidification, whereas at the time the convention was to base prediction of defects such as macroporosity by applying empirical relations to simulation results. Equally, there are many examples in the literature of the application of a fraction solid based criterion to predict casting defects [45][46]. Beyond its application as a modelling criterion to dictate the mobility of an alloy throughout the mushy zone temperatures, attempts to experimentally estimate values for critical fraction solid at which flow movement ceases were conducted by Mu *et al.* [47].

For studies centered around casting defect prediction, the confidence in simulation models is greatly strengthened by experimental validation [48]. Where possible, techniques such as placement of thermocouples within ceramic shells can provide a good basis for validation. This was implemented by Wang *et al.* to provide validation for simulation models [49]. In their work, FEM based casting software ProCAST was used to predict deformation and shrinkage results in investment castings, based on the displacement field of a wax pattern. The efficiency of running both casting simulations and validation

experiments to determine the critical process parameters causing defects can be greatly improved by devising a Design of Experiments (DOE) [50][51][52].

It is clear that a key benefit to modelling the casting process is the ability to optimise riser design to prevent defects from developing in castings [53]. However, the optimisation of riser designs to prevent defect prediction is not the only benefit which modelling casting processes can provide. Reduction of alloy wastage to increase the yield of a casting tree is also a key motivator for simulating the casting process, as demonstrated by Zhang *et al.* [54]. In many cases, defect prevalence will be balanced with the cost effectiveness of producing a mould. Although reliable castings can be produced by following the ten rules outlined by Campbell [55], riser designs resulting in the lowest scrap rate for castings may not always be the most cost effective approach due to alloy wastage in the riser design.

1.3.3 VIM-IC Modelling and Validation Literature Summary

The existing literature on modelling VIM spans a broad range of approaches to numerical modelling of the induction melting phenomena. From simplified FEM techniques to the application of software packages designed to model MHD and electromagnetics, the scope is wide for avenues to tackle this problem. The literature review covered the use of ABAQUS, ANSYS (Classic, Fluent, MHD, and Ansoft Maxwell), COMSOL, MATLAB, PHYSICA, SPHINX, amongst other methods, in modelling induction heating and melting. Experimental validation techniques for obtaining melt temperatures, flow velocities and meniscus shape were complimentary to the modelling for many of the studies in the literature. However, the author is not aware of measured temperature distributions throughout the alloy in experimental validation of induction heating and melting. The studied literature relied upon temperatures measured via thermocouples in a fixed location, or the top face temperatures in non contact temperature measurement.

Modelling of casting processes and defect prediction has been explored thoroughly in the existing literature, with the strongest studies supported by experimental validation for the numerical models. The literature review has spanned a number of software used for casting simulations. These include Adstefan, ANSYS, AUTOCAST - XI, Flow-3D, NOVA Flow&Solid, MAGMASOFT, PHYSICA, and ProCAST. Adopting a DOE approach to both simulations and experimentation is an efficient and effective approach for testing the impact of changing process parameters in the casting procedure.

Although this review of the current literature on the topics of modelling VIM-IC and experimental validation covered numerous software and modelling approaches, the selection

1.3. VIM-IC MODELLING AND VALIDATION LITERATURE REVIEW

of suitable modelling software for this thesis was restricted by availability and the feasibility of sourcing a given program or software. ANSYS and MATLAB are examples of programs which were readily available. Both ANSYS and MATLAB allowed for a high degree of flexibility in their programming capabilities. However, it should be noted that in the literature, MATLAB was not used as a standalone program for modelling induction melting and was used in combination with ANSYS and Fluent (MHD). Although ANSYS allowed for user defined functions to be implemented and a degree of programming flexibility, the MHD module was not readily available. Furthermore, the development of a solver within the MATLAB programming environment would add considerable complexity and extend beyond the scope of this project.

COMSOL Multiphysics software is a relatively simple but powerful tool for modelling coupled physics, which lends itself well to the multiphysics phenomena of induction melting. Its usability was a key factor in its selection, while also remaining a cost effective solution compared to acquiring the MHD module in Fluent. It is important to note the limitations of using COMSOL; with its simplicity, the complexity of the geometries which could be modelled was limited. The capability of the software to model larger scale or more complex scenarios was also restricted by the license type, which was for a local workstation as the cost of a license which allowed cluster computing was excessive in comparison.

ESI ProCAST software was available as a feasible option for modelling VIM later in the project. The opportunity to be involved in the development period of the electromagnetics ‘EM’ module allowed for modelling of industrial scale VIM, with the extension of casting models allowing for the whole VIM-IC process to be modelled in discretised stages. Use of ESI ProCAST software was also beneficial as its solvers were optimised for modelling casting processes and finding solutions to industrial casting problems. For maximum delivery of added value to industrial foundries, it was crucial that the software had built-in functions to predict casting defects, as a range of casting software packages existed, many of which were outlined in this literature review. This built-in casting centric functionality provided ease of results interpretation, to allow for process optimisation. It also helped to better inform foundries on how to improve mould designs, for the purpose of defect reduction and reduction of alloy wastage. Despite its many benefits, it is also important to acknowledge the limitations of using ESI ProCAST software. It is possible that simplifications were made to reduce computation time and the complexity of building casting models, in order to appeal to an industrial user base. Additionally, the requirement to discretise the physics of VIM in a separate model from casting with fluid flow and

solidification was a notable limitation. However, the goal of creating a predictive model for use in the casting industry, with computing requirements suitable for an industrial user base, was also a factor which limited computational demands.

1.4 Thesis Objectives

This thesis aims to investigate the effect of varying alloy condition and process parameters for VIM-IC, upon the prevalence of defects in turbocharger turbine wheel castings. Central to the project is computational modelling, covering all stages of the casting from VIM, to alloy pouring, filling and solidification. The modelling is underpinned by a series of experiments to determine fluid flow properties and alloy temperature. The objectives of this thesis are as follows:

- **[OB1]:** Create a VIM model capable of accurately predicting billet temperature distribution during induction heating, for practical usage in industry.
- **[OB2]:** Understand the heating, melting and pouring behaviour of IN713C in induction melting and subsequent pouring, in terms of alloy temperature and flow behaviour.
- **[OB3]:** Determine if the presence of piping, and its size and location, have an impact on flow characteristics and temperatures of alloy during pouring.
- **[OB4]:** Test the impact of using a solid ‘penny’ in VIM-IC, seeking to understand the science behind the anecdotal casting defect reductions observed when using it.
- **[OB5]:** Devise methodologies for modelling piping and thermal contact resistance between two-piece billets in VIM thermal only models without fluid flow activated.
- **[OB6]:** Create a reliable model for predicting mould filling and solidification in VIM-IC, which accurately captures defect occurrence in finished castings.

Experimental techniques should be employed to determine the following:

- Solidus, liquidus and latent heat of fusion for IN713C alloy.
- E-Slope and emissivity values for IN713C, to enable accurate non-contact temperature measurements.
- Transmittance of borosilicate glass to enable accurate non-contact temperature measurements through the viewing port of a bespoke VIM chamber.

1.4. *THESIS OBJECTIVES*

- The effect of contact thermal resistance on heat transfer through a two-piece sample, compared to a one-piece sample.
- Temperature profiles of IN713C billets during induction heating, melting and pouring.
- Pour time, flow angle, flow width and fluid velocities of alloy leaving a crucible in a VIM-IC industrial setup.

Chapter 2

Thermophysical Properties: Review and Experimentation

2.1 Thermophysical Properties: Review and Experimentation Overview

Thermophysical properties of alloys in computational modelling are required for the accurate prediction of heating and solidification behaviour, in both induction melting and subsequent mould filling models. Thermophysical properties required for these models include thermal conductivity, density, enthalpy, specific heat capacity, solidus and liquidus temperatures, Newtonian viscosity, latent heat of fusion and emissivity. Whilst these properties are sometimes found in existing literature for a selection of common alloys, there are an extensive number of alloys for which this data is not available, including IN713C. Therefore, this chapter summarises the thermophysical data obtained for IN713C and the experimental methods used to obtain these properties. This includes the use of Differential Scanning Calorimetry (DSC) and a Laser Flash Analyser (LFA). Determination of an appropriate ‘E-slope’ setting in reference to temperature dependent emissivity, and a fixed emissivity value, is explored for the practical application of non contact temperature measurement and thermal imaging equipment calibration. Finally, the concept of ‘effective thermal diffusivity’ is investigated, by testing the impact of contact layer effect on heating two-piece samples.

2.2 Thermophysical Properties Review

Thermophysical properties of the studied materials in this work are shown in Table 2.1. Constant and temperature dependent values have been obtained from a variety of sources, including existing literature, data generated by CompuTherm software [56], and the ESI ProCAST built-in materials database [20]. Thermophysical properties for many of the studied materials were estimated to be constant values. This allowed for simplification of the models, where temperature dependent material data was less crucial to the correct modelling of the physics involved. Where temperature dependent thermophysical property data was used, a figure plotting the data for a given temperature range is referenced.

The built-in CompuTherm Ni software module used in ESI ProCAST software to determine the thermophysical properties of IN713C. This package allows for temperature dependent material property data to be generated. The material property generation software uses the back diffusion method, alongside thermodynamic calculations, to determine thermophysical properties of an alloy based upon alloy composition. The term ‘back diffusion method’ refers to the approach implemented to predict the solidification path of an alloy. It differs from the Scheil model, which “assumes that the solute diffusion in the solid phases is small enough to be considered negligible and that diffusion in the liquid is rapid enough to assume that diffusion is complete” [57]. The back diffusion method assumes that there is finite diffusion in the solid, with solidification occurring under non-equilibrium conditions [57]. The back diffusion is a function of cooling rate, and its assumption of non-equilibrium conditions during solidification is more realistic for practical situations. To calculate the properties in this IN713C material property data file, a cooling rate of 1 K/s was applied for the back diffusion method. The accuracy of both the back diffusion method and CompuTherm thermodynamic database in generating accurate temperature dependent thermophysical properties of alloys was proven by Guo *et al.* [57]. All thermophysical data computed using CompuTherm Ni software was based upon the input alloy composition listed in Table 2.2. The back diffusion method was not used to calculate electromagnetic properties of IN713C.

Figure 2.1 shows a close correlation between the experimentally determined thermal conductivity values for IN713C from Krajewski *et al.* [58], compared to the values generated using CompuTherm Ni. Experimentally obtaining thermophysical properties within the solidus to liquidus temperature range for nickel based superalloys is a challenge. Therefore, CompuTherm Ni is a useful tool for determining thermophysical property data in this range. Figure 2.2 shows the CompuTherm generated temperature dependent

2.2. THERMOPHYSICAL PROPERTIES REVIEW

density for IN713C. However, due to the different solidus and liquidus values for IN713C which were experimentally obtained in Section 2.3, this temperature dependent density curve was adjusted according to the experimental solidus and liquidus temperatures. These temperatures are 1331.9 °C and 1389.3 °C respectively, which were close to the values obtained by Przeliorz *et al.* [59] and can be seen in Table 2.1. The temperature dependent density of air is shown in Figure 2.3, which was taken from ProCAST materials database.

Using CompuTherm Ni software, the enthalpy of IN713C was plotted in Figure 2.4. Values for enthalpy were also adjusted for the experimentally measured solidus and liquidus temperatures from DSC experiments.

In Table 2.1 and Figures 2.1-2.7, where multiple values or sources are cited for a given material, the value(s) and source in bold text is the value which was used in numerical models. Furthermore, where asterisks are noted in the table and associated figures, this indicates that a footnote is present in the relevant figure.

The value of ' 1×10^{-12} W/m·K' was input as thermal conductivity of air for the models involving electromagnetics. This value is used instead of zero, as the software is not able to process zero values for material properties. Of course, in reality the thermal conductivity of air is not zero. However, modelling the heating of the surrounding air volume was not important for simulating the VIM-IC industrial process.

For temperatures outside of the plotted temperature ranges in Figures 2.1-2.7, the ESI ProCAST software uses a constant value for the given thermophysical property, which corresponds to the defined value at the closest given temperature point. Although this approach is unlikely to be an accurate representation of thermophysical material properties of IN713C outside of the defined temperature ranges, extrapolation of the graphs based on data within the defined ranges would not guarantee a better approximation. If greater accuracy is required for thermophysical properties outside of the defined temperature ranges, experiments would need to be conducted to determine the values. However, this can be challenging due to the difficulties associated with experimental determination of alloy thermophysical properties in the molten state.

The artificial increase of the thermal conductivity values above solidus is implemented to account for electromagnetic stirring during electromagnetic modelling, where fluid flow is not explicitly modelled. The reason for artificially increasing these values above solidus is further discussed in Sections 3.3.4 and 5.4.

2.2. THERMOPHYSICAL PROPERTIES REVIEW

Material	Thermal Conductivity (W/m·K)	Density (kg/m ³)	Enthalpy (kJ/kg)	Specific Heat (kJ/kgK)	Solidus and Liquidus (°C)	Newtonian Viscosity (Pa·s)
IN713C	Figure 2.1 [58], [56]*	Figure 2.2 [56], [56]*	Figure 2.4 [56]	N/A	1226, 1340 [56] 1307, 1391 [59] 1260, 1288 [60]	Figure 2.6 [56]
Copper	387.6 [20]	8978 [20]	N/A	0.381 [20]	N/A	N/A
Aluminosilicate Ceramic Fibre	Figure 2.1 [20]	Figure 2.2 [20]	N/A	Figure 2.5 [20]	N/A	N/A
Air	1×10^{-12}	Figure 2.3 [20]	N/A	Figure 2.5 [20]	N/A	Figure 2.7 [20]
Zircon	Figure 2.1 [20]	4560 [20]	N/A	0.754 [20]	N/A	N/A
Mullite	Figure 2.1 [20]	3150 [20]	N/A	Figure 2.5 [20]	N/A	N/A
Vermiculite	0.065 [20]	140 [20]	N/A	1 [20]	N/A	N/A

Table 2.1: Thermophysical properties for the studied materials

2.2. THERMOPHYSICAL PROPERTIES REVIEW

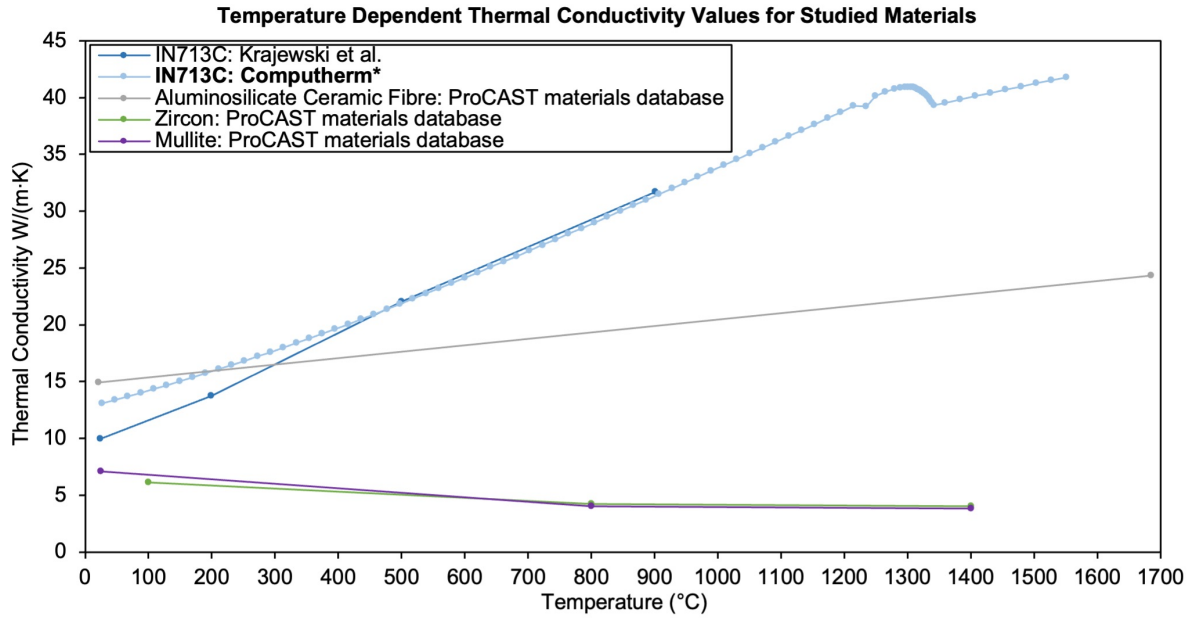


Figure 2.1: Temperature dependent thermal conductivity for studied materials. IN713C: Krajewski et al. [58], **CompuTherm** [56]*. Aluminosilicate Ceramic Fibre: ProCAST [20]. Zircon: ProCAST [20]. Mullite: ProCAST [20]. *Thermal conductivity is artificially increased steadily between solidus and liquidus temperatures, up to 1800 W/m·K at liquidus, in electromagnetic simulations to account for fluid flow not being modelled.

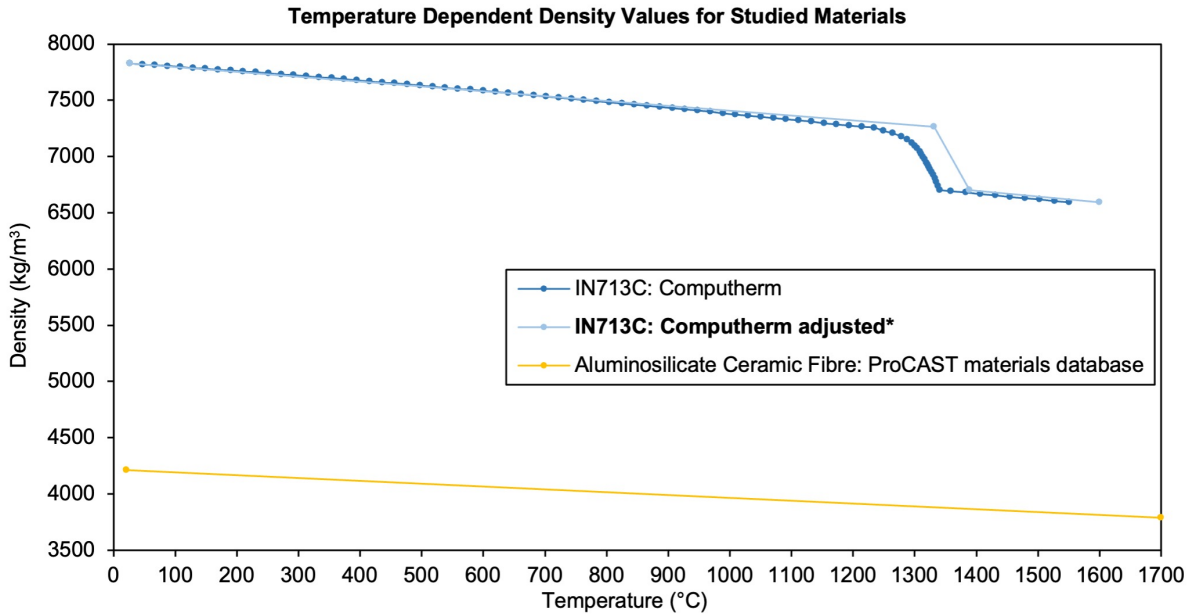


Figure 2.2: Temperature dependent density for studied materials. IN713C: CompuTherm [56], **CompuTherm adjusted** [56]*. Aluminosilicate Ceramic Fibre: ProCAST [20].

*Density is adjusted according to experimentally obtained solidus and liquidus temperatures.

2.2. THERMOPHYSICAL PROPERTIES REVIEW

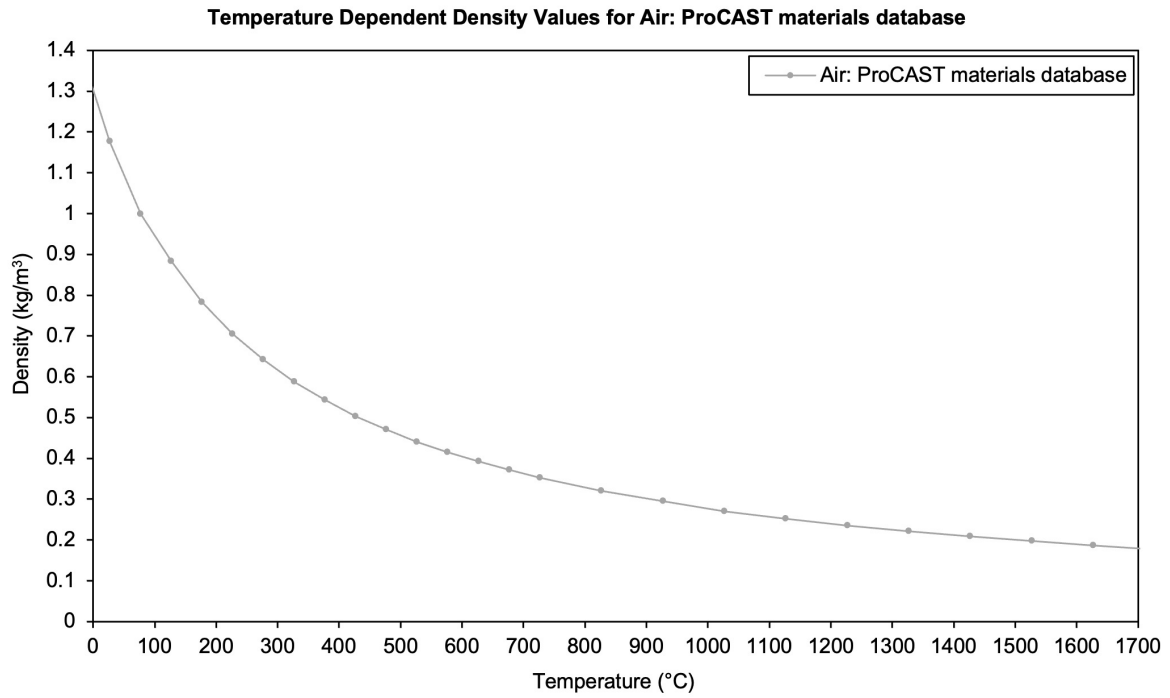


Figure 2.3: Temperature dependent density for air: ProCAST [20].

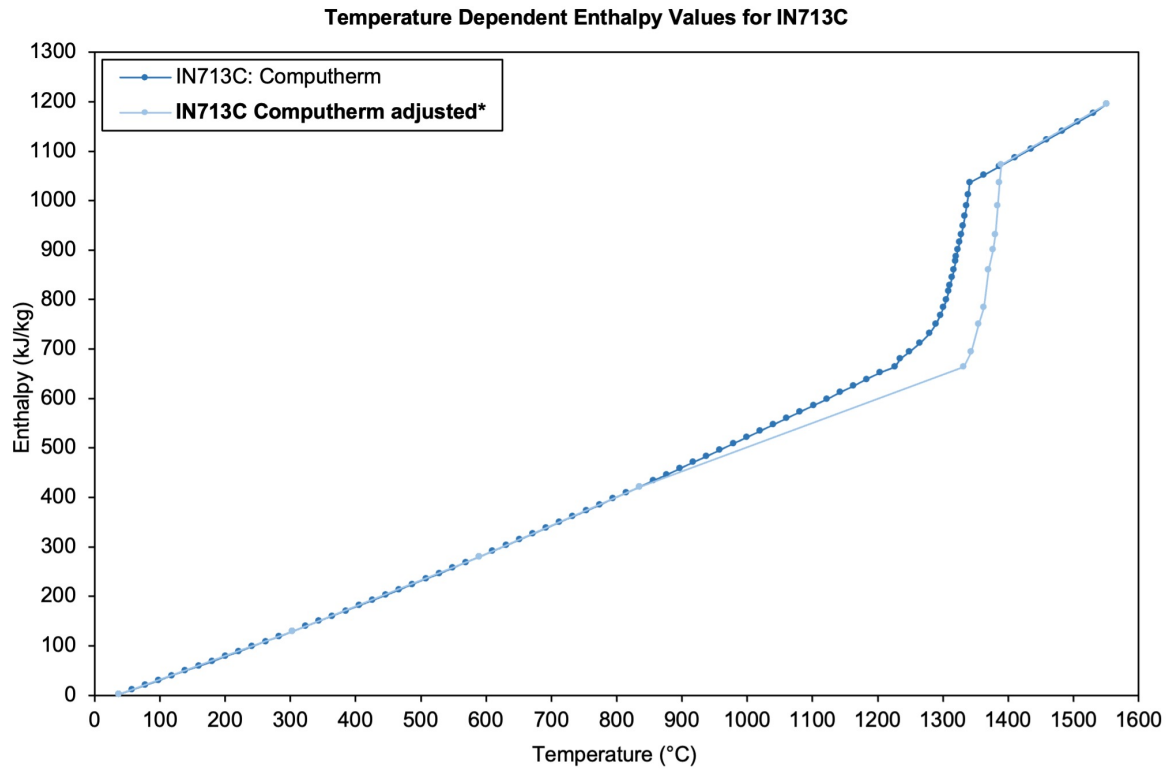


Figure 2.4: Temperature dependent enthalpy for IN713C: CompuTherm [56], **CompuTherm adjusted** [56]*

*Enthalpy is adjusted to experimentally obtained solidus and liquidus temperatures.

2.2. THERMOPHYSICAL PROPERTIES REVIEW

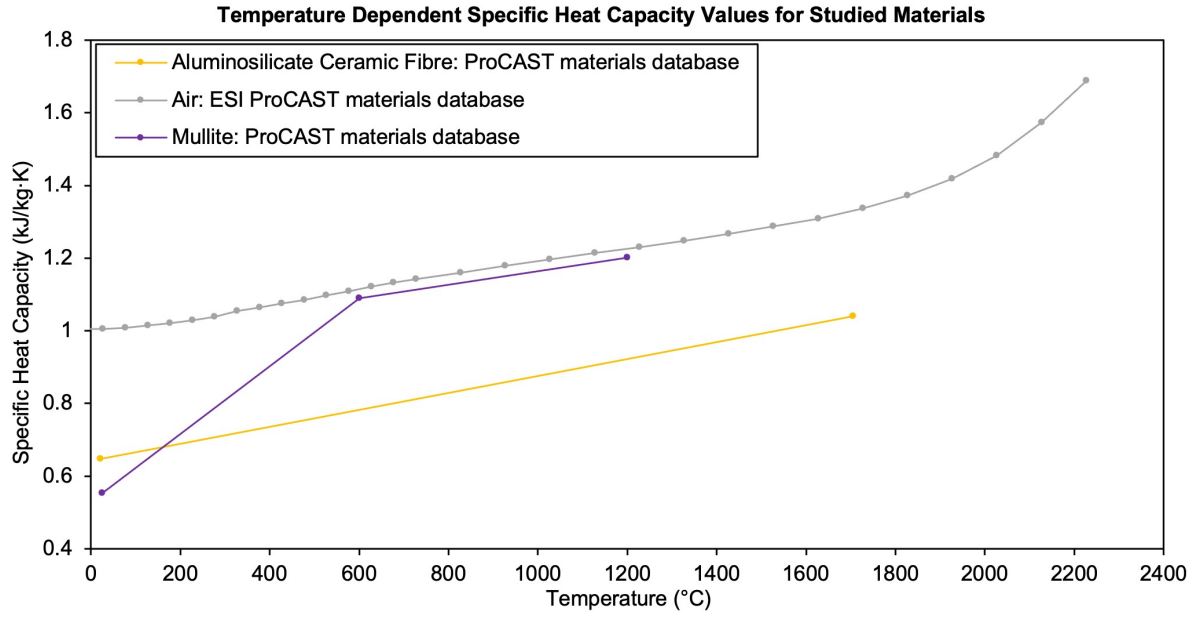


Figure 2.5: Temperature dependent specific heat capacity for studied materials. Aluminosilicate Ceramic Fibre: [20], Air: [20], Mullite: [20].

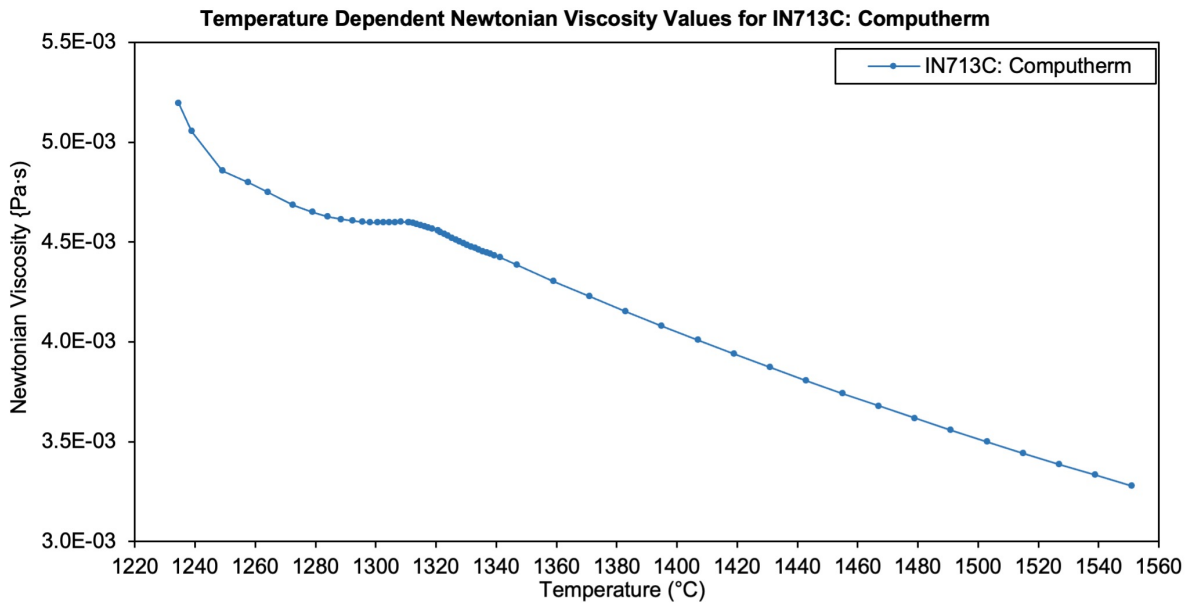


Figure 2.6: Temperature dependent Newtonian viscosity for IN713C [56].

Figure 2.5 shows the temperature dependent specific heat capacity values, plotted for aluminosilicate ceramic fibre, air and mullite. These values were obtained from the ProCAST materials database. Figures 2.6 and 2.7 show the temperature dependent Newtonian viscosity for IN713C and air respectively. Newtonian viscosity in CompuTherm was calculated using a pair-wise mixture model, based upon an extensive database for

2.2. THERMOPHYSICAL PROPERTIES REVIEW

calculating thermophysical properties, as outlined in the paper by Guo *et al.* [57]. Values for IN713C were generated using CompuTherm Ni, whereas the values for air were obtained from the ProCAST materials database.

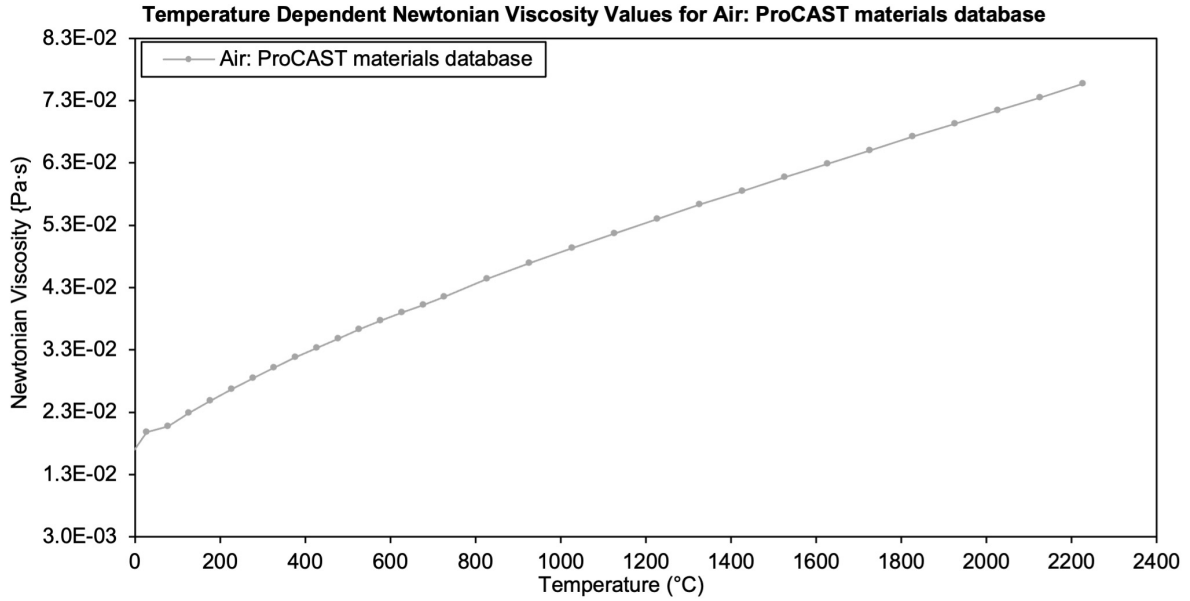


Figure 2.7: Temperature dependent newtonian viscosity for air [20].

Many of the generated thermophysical property values and those found in the ESI ProCAST material database were within the expected ranges when compared to the data in existing literature, where available. However, when comparing the CompuTherm Ni generated solidus and liquidus temperature values to the those stated by the Nickel Institute [60], there were significant differences between these values. Table 2.2 shows the composition data used as an input for IN713C material properties to be generated using CompuTherm Ni.

As the solidus and liquidus temperatures are dependent upon the specifics of the alloy composition, and the solidus and liquidus values for IN713C varied widely in the literature, the need for conducting tests to determine these values for a sample of IN713C was identified. Furthermore, the latent heat of fusion for IN713C could not be found in existing literature, requiring this parameter to also be measured experimentally.

Additionally, E-Slope and emissivity values for a metal are highly dependent upon a number of factors, which requires these parameters to be measured experimentally to ensure that the values are accurate for the given scenario.

2.3. SOLIDUS, LIQUIDUS AND LATENT HEAT: DSC

Element	AMS 5391 Specification Range (%)	Input Alloy Composition (%)
C	0.08 - 0.20	0.13
Si	0.5 max.	0.04
Mn	0.25 max.	0.01
P	Not specified	0.01
Al	5.50 - 6.50	6.00
B	0.005 - 0.015	0.01
Co	Not specified	0.13
Cr	12-14	13.00
Cu	0.5 max.	0.05
Fe	2.5 max.	0.14
Mo	3.8-5.2	4.10
Nb	Nb + Ta = 1.8 - 2.8	2.10
Ni	bal	bal
Ti	0.5 - 1.0	0.75
Zr	0.05 - 0.15	0.13

Table 2.2: IN713C composition: alloy specification ranges and input composition values

2.3 Solidus, Liquidus and Latent Heat: DSC

2.3.1 Solidus, Liquidus and Latent Heat: DSC Overview

Differential Scanning Calorimetry (DSC) is a thermal analysis technique, where thermal analysis is defined as ‘a group of techniques in which a physical property of a substance is measured as a function of temperature while the substance is subjected to a controlled temperature program’ [61]. It measures heat flows and temperatures for exothermic and endothermic transitions. Conducting DSC experiments prior to induction melting was useful for determining the temperature at which the sample was fully molten, while phase change temperature transition interval and latent heat of fusion were important parameters for use in the numerical model. The DSC acquires this data by employing thermocouples to detect heat flow differences between a sample inside an alumina crucible, and an empty reference crucible.

2.3.2 DSC Experiment Setup and Method

A DSC 404 F1 Pegasus High-Temperature machine was used to establish the phase transformations, solidus and liquidus temperatures, and latent heat of fusion of IN713C.

2.3. SOLIDUS, LIQUIDUS AND LATENT HEAT: DSC

A diagram of the internal DSC setup is shown in Figure 2.8, which is a recreated version of Figure 22 in the thesis of J C T Cullen [62]. An initial cycle was conducted with an empty crucible on the platinum head alongside the reference crucible. This allowed for any corrections to be made, forming a baseline for the following experiments. Once this corrective run was complete, a sample of IN713C was subjected to cyclic heating and cooling in the DSC under nitrogen gas. The sample was heated to 1500 °C at a rate of 20 K/min, held in an isothermal state for five minutes, and cooled to 50 °C at a rate of 20 K/min. This process was repeated three times. These DSC experiments were conducted with the assistance of Dr. Shahin Mehraban, Swansea University.

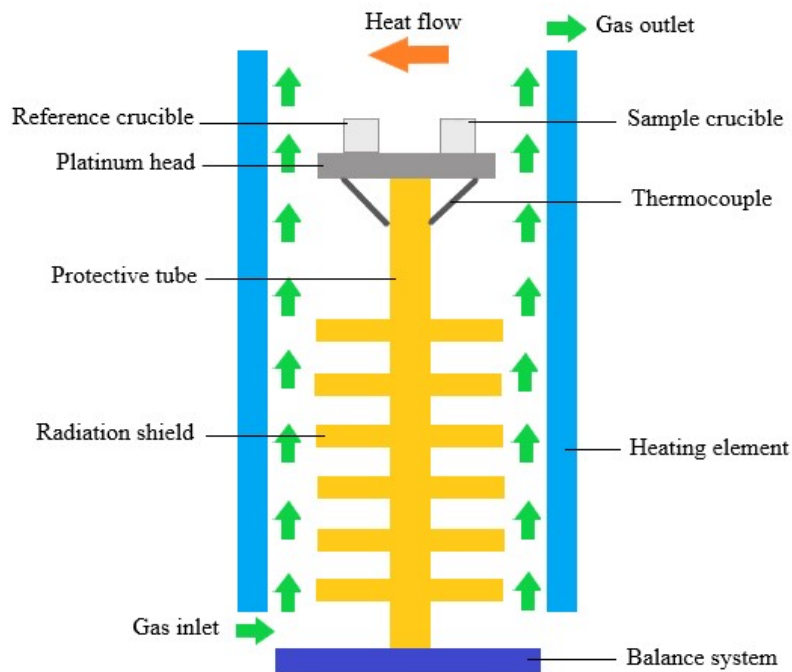


Figure 2.8: DSC internal diagram, recreated from [62]

2.3.3 DSC Experiment Results

Analysis of the DSC signal with respect to temperature allowed for solidus and liquidus temperatures to be determined from reading the temperatures at the onset and end of the signal curve peaks. Dr. Jonathan Cullen, Swansea University assisted with results analysis.

For nickel based superalloys, it is customary to use the peak onsets from the heating curve to read solidus and liquidus temperatures [63]. The heating cycle was repeated three times, as measurements from a third cycle are considered to be the most accurate. DSC signal with respect to temperature for the third heating cycle are shown in Figure 2.9. Solidus

2.3. SOLIDUS, LIQUIDUS AND LATENT HEAT: DSC

temperature can be identified as the first deviation from the baseline of the heating curve, shown in red. Liquidus temperature can be defined at the point of return to the baseline upon heating. From the heating curve, solidus temperature is 1389.3 °C and liquidus temperature is 1331.9 °C. The temperature transition interval and latent heat of fusion were 57.4 K and 333 kJ/kg respectively. Peaks are recorded at lower values on the cooling curve, which is a result of the undercooling effect [64].

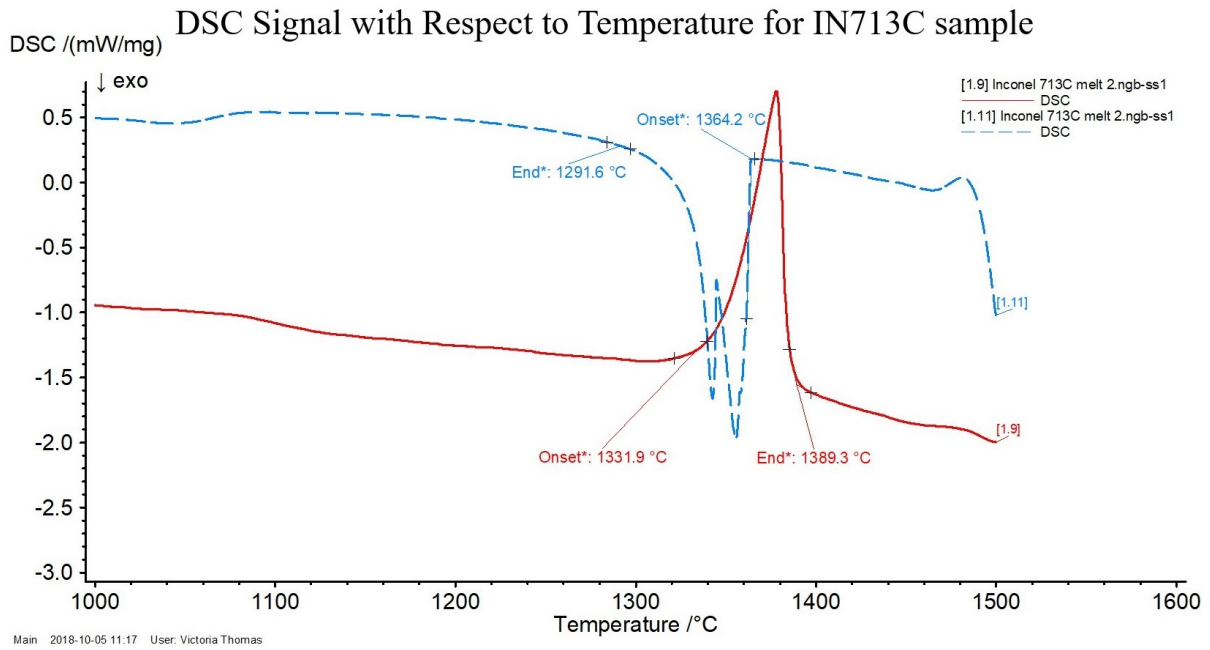


Figure 2.9: DSC heating and cooling curves for IN713C

2.3.4 Solidus, Liquidus and Latent Heat: DSC Conclusion

By performing three heat cycles of an IN713C sample, it was possible to determine the solidus, liquidus and latent heat of fusion for this alloy. These values can be applied to a computational model to aid the accurate prediction of heating and flow behaviour, as it allows for the definition of the alloy mushy zone region. It is important to note that the start and end points of peaks are subjective, which is a limitation that can cause variability in the accuracy of solidus and liquidus temperature definition.

2.4 Emissivity and E-Slope: Temperature Calibration

2.4.1 Emissivity and E-Slope: Temperature Calibration Overview

Emissivity, denoted as ' ϵ ', is defined as the ratio of energy emitted from a material surface to that radiated from a blackbody [65]. A blackbody is a perfect emitter, with a value of $\epsilon=1$. As it is a ratio, ϵ is a dimensionless number between 0 and 1, where a surface with $\epsilon=0$ is a perfect reflector. The energy radiated from a surface is temperature, wavelength (λ) and directionally dependent [65]. It is also affected by surface characteristics. Variations in surface characteristics, such as whether a surface is polished or rough, oxidised or unoxidised, can greatly affect the emissivity of a metallic surface. For example, a polished copper surface may possess an emissivity of $\epsilon=0.03$. In contrast, a heavily oxidised copper surface can display an emissivity of $\epsilon=0.7$ [66].

Pyrometers, which are also known as infrared (IR) thermometers, are a type of non-contact temperature measurement equipment. Non-contact temperature measurement can be an effective tool for measuring temperatures, in situations where use of contact thermocouples is impractical or impossible. Further advantages of using non-contact IR thermometry include speed, lack of interference and the capability of measuring temperatures up to 3000 °C [67]. However, accurate measurement of surface temperatures using non-contact measurement equipment requires input parameters to be defined correctly. An input parameter which has a large impact on the measured temperature is the emissivity value.

The emissivity value of the surface of an IN713C sample is potentially subject to great variability. Changing temperature, wavelength and the potential for oxidisation presents a significant challenge for the accurate measurement of alloy surface temperature. Basic pyrometers, with only one thermal sensor, rely upon an accurate emissivity value input for the correct surface temperature to be determined. However, this is often difficult to obtain and is unlikely to be a fixed value across a large temperature range. To overcome this issue, it is possible to use a pyrometer which contains two thermal sensors, also known as a 'two-colour' or ratio pyrometer.

Two-colour pyrometers use two one-colour pyrometers in the same system, operating at two different wavelengths, to detect the IR radiation from the same measurement target. In this case, 'colours' refers to different wavebands. The theory behind two-colour

pyrometers is that if the radiation is measured at two separate wavelengths, the ratio between the intensities can be solved to obtain temperature. By manipulating Planck's law mathematically, once temperature has been solved for, ϵ can be cancelled out. This is only true if the surface emissivity is of equal value at different wavelengths.

If the first thermal sensor is operating on Channel or 'Colour' 1 with wavelength λ_1 , and the second sensor is operating on Colour 2 with wavelength λ_2 , the measured temperature T_m can be calculated as follows [67]:

$$\frac{1}{T_m} = \frac{1}{T_t} + \frac{\lambda_1 \lambda_2}{c_2(\lambda_2 - \lambda_1)} \ln \left(\frac{\epsilon_2}{\epsilon_1} \right) \quad (2.1)$$

where T_t is the target temperature, c_2 is the second radiation constant in $\mu\text{m K}$, ϵ_1 is the emissivity at the wavelength of Colour 1, and ϵ_2 is the emissivity at the wavelength of Colour 2. If $\epsilon_1 = \epsilon_2$, the second term on the right hand side of the equation is zero.

However, this does not work for molten metals, as $\epsilon_1 \neq \epsilon_2$ for different wavelengths. Therefore, an adjustment constant value 'E-Slope' is required to rectify the signal ratio. This adjustment constant corrects the ratio by correcting the instrument indication, in accounting for the unequal emissivities in Colour 1 and Colour 2. The value of E-slope can be determined by calibrating the pyrometer reading with a thermocouple measurement.

Using a two-colour pyrometer instead of a one-colour pyrometer has other advantages, including the ability to account for signal attenuation. This ability is useful in industrial applications, where the signal from the measurement target can be reduced by the presence of dirt or smoke in the line of sight.

A two-colour IR thermometer was required to measure the surface temperature of IN713C during in-situ industrial VIM-IC experiments. An Endurance 1RL F2 two-colour IR thermometer with a temperature measurement range of 800-1800 °C was selected and used for this application due to its suitable properties. For example, in addition to the benefits of being a two-colour pyrometer, it also has the capability to account for temperature measurement through a piece of borosilicate glass in a VIM-IC chamber viewing port. The unit accounts for the glass by allowing an input value for spectral transmittance to be entered.

In order to perform accurate temperature measurements of IN713C in a bespoke VIM-IC chamber, it was important to determine the correct E-slope value by comparing IR thermometer measurements with contact thermocouple measurements over a range of temperatures. The spectral transmittance of the 10 mm thick piece of borosilicate glass

which was used on the top viewing port of the bespoke VIM-IC chamber was also required in the range of 750-1100 nm. This is due to the first thermal sensor of the IR thermometer operating in the range of 750-1100 nm, and the second sensor operating in the range of 950-1100 nm.

For scenarios in which there is an advantage to understanding the temperature distribution over a given area, a thermal imaging camera can be utilised. A Raytek Pi20 fixed thermal imager, capable of measuring temperatures from 200-2000 °C, was used in conditions where temperature distribution over a region was of interest. Temperature calibration experiments comparing the maximum measured temperature within an ‘Area of Interest’ (AOI) to the reading from a contact thermocouple were also conducted.

2.4.2 Determining Borosilicate Glass Spectral Transmittance

To determine what percentage of radiation was transmitted through the 10 mm thick piece of borosilicate glass, the spectral transmittance was measured over the wavelength range of 200-3300 nm. The measurements, shown in Figure 2.10, were performed using a Perkin Elmer Lambda 950 UV-Visible-NIR spectrophotometer. These measurements were performed with the assistance of Amirah Way, Swansea University.

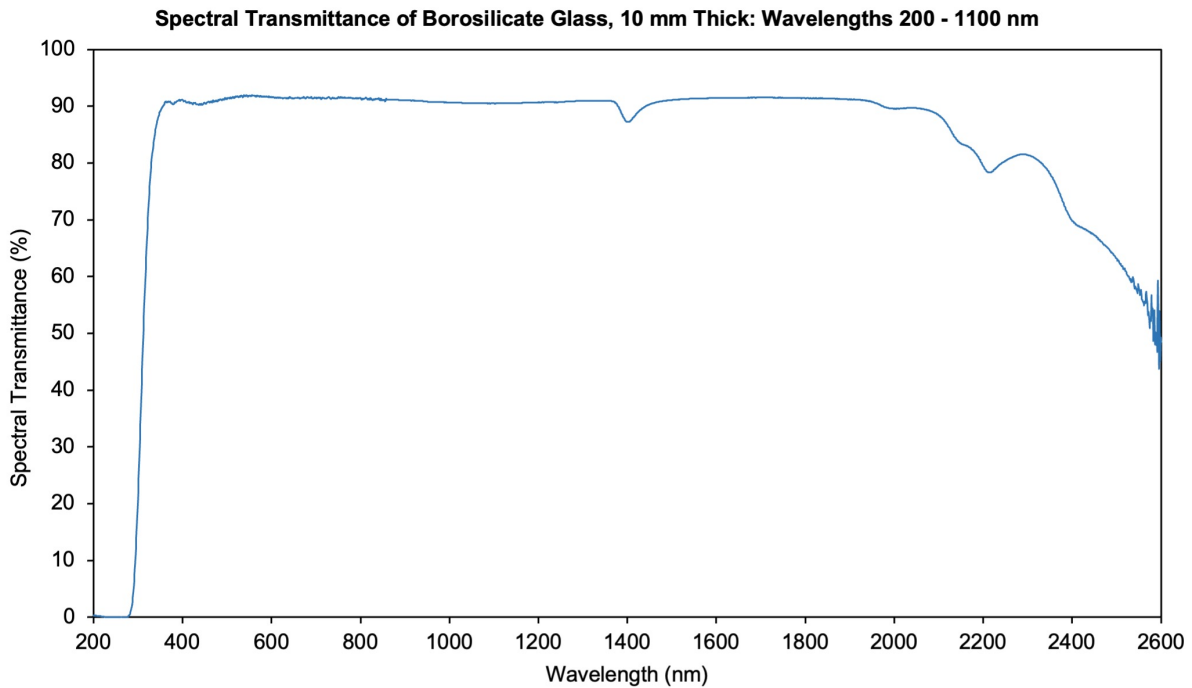


Figure 2.10: Spectral transmittance of 10 mm thick borosilicate glass from 200-2600 nm

Above 2600 nm, the signal to noise ratio of the data drops significantly, resulting in inaccurate transmittance values. The data in this region is therefore omitted. The IR thermometer operates in two overlapping spectral bands covering a total wavelength range of 750-1100 nm. Across this wavelength range, the spectral transmittance of the borosilicate glass remains very constant, with an average value of 91 %. Due to the minimal fluctuations in transmittance over this range, using a constant transmittance value of 0.91 for the IR thermometer was appropriate.

2.4.3 E-Slope: Temperature Calibration Experiment Overview

Calibration experiments were conducted to determine the correct E-slope correction ratio value to apply to temperature measurements of IN713C determined by the two-colour IR thermometer. The IN713C sample was heated using a box furnace up to 1100 °C. This upper temperature limit for the experiment ensured that the sample was kept below the mushy zone, as the experimental setup in the box furnace did not allow for the alloy to become molten. IR thermometer temperature measurements of the sample were compared to temperatures values measured using a contact thermocouple. The E-slope input value was adjusted until the closest temperature values to the measurements from the contact thermocouple were achieved.

Multiple thermocouple contact configurations were explored before the optimal position was found, which involved positioning the thermocouple tip within a groove. A groove was cut into the curved face of the cylindrical billet piece, to allow the N-type thermocouple tip to be held in place to measure the surface temperature. The thermocouple was passed through a port in the back of the box furnace and connected to a data logger. Although the thermocouple was not inserted into the billet face for which the surface temperature was to be measured by the IR thermometer, this was the best solution given the results of the other configurations. In this case, if the billet is assumed to be heated uniformly, the temperature measurement recorded by the thermocouple in this configuration can be considered as accurate. This setup produced the most consistent results, with the least fluctuation in temperature measurements upon opening the furnace door.

Two types of wire contact thermocouples were considered for use in this experiment: K-type and N-type. K-type wire thermocouples are often used for high temperature applications. However, the limitation of the available K-type thermocouple was that its upper temperature limit would restrict sample heating to 900 °C. As the bottom accurate temperature reading of the IR thermometer was 800 °C, this temperature limited K-type

thermocouple would not have allowed for a large temperature range to be tested.

N-type thermocouples are also suitable for high temperature applications. Moreover, the advantage of using an N-type thermocouple instead of a K-type for this experiment is that N-type thermocouples experience less drift in oxidising atmospheres. This was important, as due to the setup of the box furnace experiment, oxidation of the sample billet was unavoidable.

The experiment was repeated with the use of 10 mm thick borosilicate glass in the line of sight, to ensure that the transmittance value was correctly accounting for the percentage of radiation transmitted through the glass. This was the same viewing glass piece that was selected for use in the top viewing port of the bespoke VIM-IC chamber.

In the VIM-IC industrial experiments, the top billet face was to be positioned in the chamber at a distance of 432 mm from the external surface of the top viewing port. As the minimum focal distance of the IR thermometer is 600 mm, the minimum distance between the viewing port external surface and infrared thermometer lens was 168 mm.

2.4.4 E-Slope: Temperature Calibration Experiment Setup

A prepared 50 mm long, 50 mm diameter IN713C billet sample was placed inside a Nabertherm box furnace. The sample had a groove cut into the billet curved face, to allow for an N-type wire thermocouple tip to be positioned inside. The wire thermocouple was passed through a port in the back of the furnace and was connected to a data logger, which was connected to a computer for data transfer. The Endurance IR thermometer was bolted to a jack stage marked with tape for alignment, to ensure that the billet piece target measurement face and the IR thermometer lens were parallel. The jack stage was positioned to provide a distance of 600 mm from the billet target measurement face to the IR thermometer lens.

The distance ratio for the infrared thermometer is 100:1. Therefore at a 600 mm distance from the measurement target, the diameter of the target spot size is 6 mm. The infrared thermometer lens was focused according to the instructions in the manual, to account for the effect of parallax. A spirit level was used to ensure the flatness of the jack stage and to check that the IR thermometer was perpendicular to the platform and target measurement billet face. The IR thermometer was connected to a computer to allow data transfer via the associated software, DataTemp Multidrop. Figure 2.11 is a diagram of the setup for this calibration experiment.

2.4. EMISSIVITY AND E-SLOPE: TEMPERATURE CALIBRATION

Ideally, this experiment would have been conducted in a non-oxidising setting, with equipment which allowed the temperature to be more precisely controlled. Temperature data from the thermocouple and IR thermometer would also have been tested up to the liquidus temperature of IN713C. However, due to equipment availability and logistical reasons, this was not possible. Consequently, the calculation of E-Slope for IN713C in a non-oxidising environment could not be determined by temperature calibration.

The experiment was later repeated, including the use of a borosilicate glass piece. A 10 mm thick borosilicate glass piece was positioned at a distance of 432 mm from the front face of the billet. The glass piece was held in place using a clamp stand, resting on the surface of an additional jack stage. The jack stage was marked tape for alignment, to ensure that the glass piece was parallel to both the billet piece target measurement face and the IR thermometer lens. Figure 2.12 is a photograph of the experimental setup, including the glass piece, clamp stand and additional jack stage.

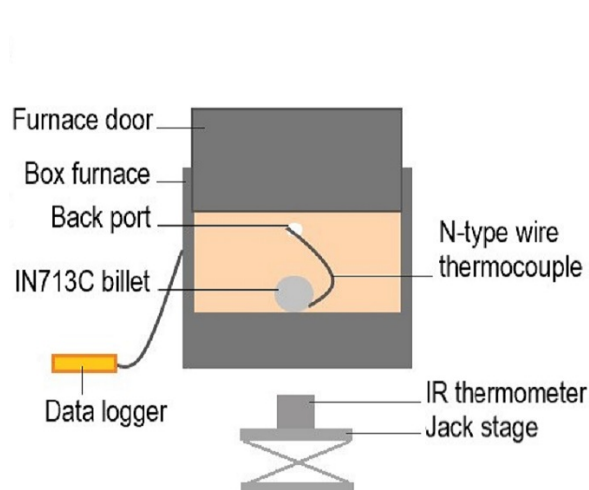


Figure 2.11: Diagram of temperature calibration experimental setup

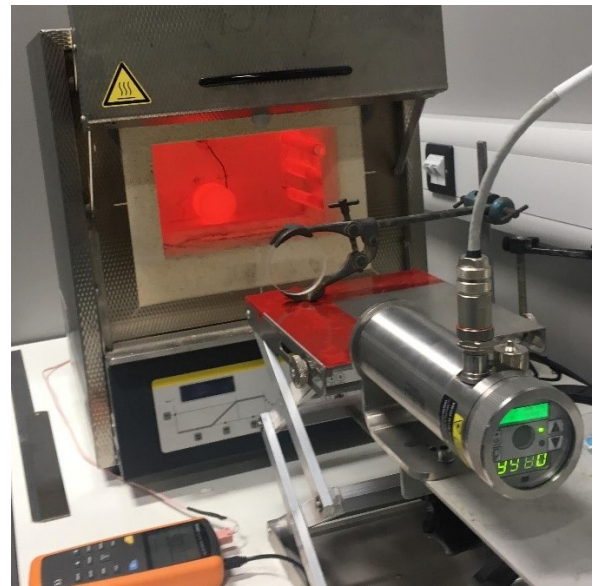


Figure 2.12: Photograph of optical pyrometer calibration experiment with glass

2.4.5 E-Slope: Temperature Calibration Experiment Method

Once the experiment was set up correctly, the box furnace was heated up to a temperature of 860°C, to ensure that the IR thermometer was operating comfortably above its lower temperature measurement range for testing E-Slope value. An initial test value of E-Slope for the unit was set to '1' within DataTemp Multidrop software. This estimated value of E-Slope was chosen for the initial test due to information in the IR thermometer manual,

2.4. EMISSIVITY AND E-SLOPE: TEMPERATURE CALIBRATION

which states that the E-Slope for oxidised Nickel can be estimated to be ‘1’. Temperature readings were taken by opening the furnace door, which allowed the IR thermometer to read the temperature of the target measurement spot, which was focused on the billet front face. IR thermometer measurements were recorded, alongside thermocouple temperature readings taken at the same time. At measured thermocouple temperatures of 858.6-869.7 °C, various slope settings were trialled and the difference between the IR thermometer reading for the given E-Slope value and thermocouple reading was compared. Once the optimal value of E-Slope was confirmed, the furnace temperature was adjusted to achieve heating of the billet in 20 °C intervals, from 760-1100 °C according to the thermocouple temperature readings. Each time the door was open, the thermocouple was confirmed to be held in the correct position before closing the door. To ensure that data points were taken at regular intervals, thermocouple readings for each 20 °C interval were kept within ± 3 °C of the target temperature. Temperature readings were recorded at each interval. This interval heating experiment was repeated three times for the given temperature range. The experiment was also repeated with the use of borosilicate glass, to ensure that the measured transmittance value was correct. The transmittance value was set using DataTemp Multidrop software, which allowed for input settings to be changed on the unit. The experiment including the glass piece was also repeated three times for a temperature range of 760-1100 °C, in 20 °C intervals.

2.4.6 E-Slope: Temperature Calibration Experiment Results

The recorded temperature differences in IR thermometer reading and thermocouple reading for a range of E-Slope values was tested for a temperature range of 858.6-869.7°C. The tested E-Slope values and the resultant absolute values of temperature deviation can be seen in Table 2.3. The E-Slope setting which produced the smallest temperature differences between the thermocouple reading and IR thermometer reading was a slope setting of ‘1’.

Figure 2.13 shows the average IR thermometer and thermocouple readings, with and without glass. Each data set represents the average value of readings from the three experiment repetitions. The blue line represents the average IR reading for which the target is obscured by glass, while the orange line represents the average for the given temperature interval without glass. Green and yellow lines represent the averaged reading from the thermocouple with and without glass respectively, at every temperature interval. For each measurement, was ensured that the thermocouple readings were within ± 3 °C of the 20 °C interval noted on the ‘Target Temperature’ axis.

2.4. EMISSIVITY AND E-SLOPE: TEMPERATURE CALIBRATION

E-Slope Value	Temperature Difference °C
1.110	123.7
1.060	73.7
1.040	55.6
1.035	52.1
1.030	45.8
1.010	24.7
1.005	16.5
1.000	11.4
0.995	110

Table 2.3: Temperature difference observed between thermocouple and IR thermometer readings for trialled E-Slope values

Lowest and highest values of any three readings for each given interval are represented by the whisker plots on each of the averaged data points. Broken and dotted lines are representative of upper and lower limits respectively of the IR thermometer and thermocouple, according to manufacturer specifications for both measurement devices.

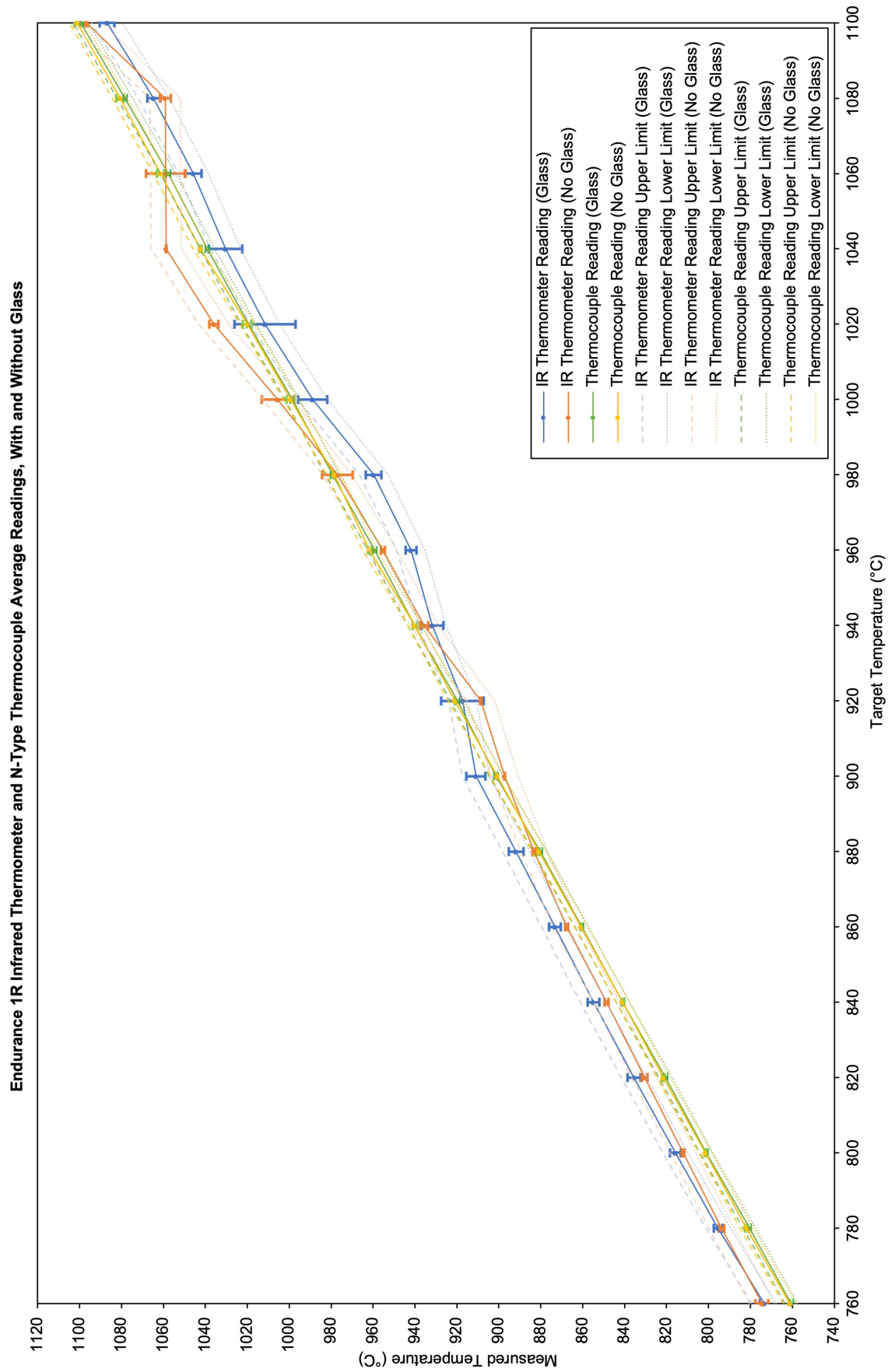


Figure 2.13: Graph showing observed differences between thermocouple and infrared thermometer readings, with and without glass

2.4.7 E-Slope: Temperature Calibration Experiment

Discussion

By examining the raw data set for temperature measurement comparisons with glass, it is evident that the temperature range of 900-940 °C is the interval in which the IR thermometer temperature offset compared to thermocouple reading transitions from a positive offset to a negative one. The maximum recorded positive offset was 18.6 °C, with the temperature range of 780-820 °C most prone to positive offset error.

This temperature difference within the temperature range of 780-820 °C is reasonable, considering that the bottom of the accurate temperature measurement range of the IR thermometer in two-colour mode is 800 °C. The maximum negative offset was -25.2 °C, with the region of 980-1020 °C most susceptible to negative offset. Although the reading accuracy of the IR thermometer was tested both with and without glass, it was the value of the reading with glass which was most important for the VIM-IC experiments. These experiments would involve borosilicate glass obscuring the measurement target, as a sealed chamber was required to achieve vacuum levels.

In a VIM-IC chamber, a non-oxidising environment for the metal is created. This would likely change the required E-Slope corrective value. According to the manual for the IR thermometer, oxidised pure Nickel shares the same emissivity and E-Slope values as IN713C. In this manual, un-oxidised pure Nickel is stated to have an E-Slope value of 1.06 [68]. Therefore, as oxidised IN713C had the same E-Slope value as oxidised pure Nickel, the assumption was made that the E-Slope value of unoxidised IN713C was 1.06. Due to the satisfactory temperature measurement values of the IR thermometer with glass when accounting for transmittance, it could be deduced that the transmittance value of 0.91 for the borosilicate glass piece was correct.

2.4.8 Emissivity: Temperature Calibration Experiment

Overview

To measure the temperature distribution across a region of interest, a thermal imaging camera was used in both induction melting and mould cooling temperature measurement experiments. Although the use of a fixed emissivity value for an alloy across different wavebands is not accurate, this was a limitation of the thermal imaging camera; a varying emissivity value could not be dictated. Determination of a fixed emissivity value for the thermal imaging camera to use, to measure the temperature of IN713C between

2.4. EMISSIVITY AND E-SLOPE: TEMPERATURE CALIBRATION

200-1100 °C was achieved by using the same calibration approach as the method used for determining E-Slope for the IR thermometer. An IN713C billet sample was heated using a box furnace. Measured temperatures from wire thermocouples were compared to the maximum temperature recorded using the AOI tool on the thermal imaging camera for a fixed emissivity value. According to the Endurance IR thermometer manual, the estimated emissivity of oxidised nickel is estimated to fall within the range of 0.8-0.9 [68]. Therefore, 0.85 was used as an initial test value of emissivity for the sample.

The thermal imaging camera could only be used for in air experiments and not in the VIM-IC experiments. This is due to the obscuration of the IN713C billet surface by a viewing glass, as it was required to allow the chamber to reach the given vacuum pressure level. As the ThermoView Pi20HT operates in the spectral region of 8000-14,000 nm, no signal could be detected due to the presence of the glass. Figure 2.14 shows the billet and thermocouple with surface temperature readings captured by the thermal imaging camera. The obscuration of the billet by the glass piece can be seen in Figure 2.15. From this, it can be deduced that radiation is not transmitted through the borosilicate glass in this wavelength range.

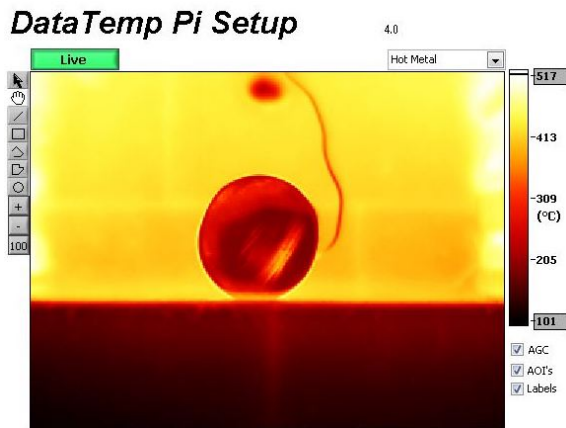


Figure 2.14: Thermal image of billet and thermocouple in box furnace experiment

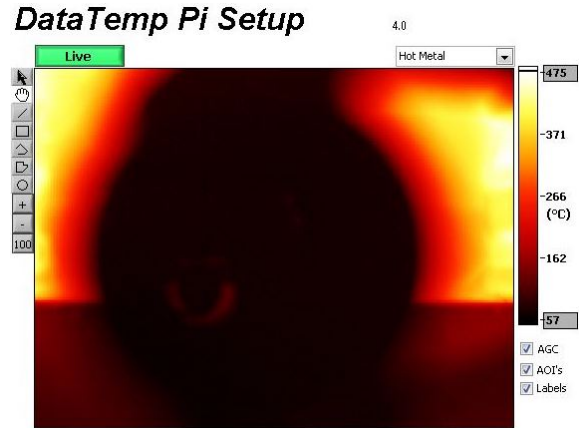


Figure 2.15: Thermal image of box furnace experiment obscured by glass

2.4.9 Thermal Imaging Camera: Calibration Experiment Setup

A prepared 50 mm long, 50 mm diameter IN713C billet sample was placed inside a Nabertherm box furnace. The sample had a groove cut into the billet curved face, to allow for an N-type wire thermocouple tip to be positioned inside. The wire thermocouple was

2.4. EMISSIVITY AND E-SLOPE: TEMPERATURE CALIBRATION

passed through a port in the back of the furnace and was connected to a data logger. The ThermoView Pi20HT was bolted to a jack stage marked with tape for alignment, to ensure that the billet piece target measurement face and the camera lens were parallel. The jack stage was positioned to provide a distance of 600 mm from the billet target measurement face to the IR thermometer lens. The minimum focal distance of the thermal imaging camera is 300 mm, but a distance of 600 mm was chosen for consistency with the IR thermometer calibration experiment.

The thermal imaging camera lens was connected to a computer. The lens was focused by twisting the lens collar according to the instructions in the manual until a sharp, focused image quality was visible via Raytek DataTempPi, which is the associated software with the thermal imaging camera. A spirit level was used to ensure the flatness of the jack stage and to check that the camera was perpendicular to the platform and target measurement billet face. A photograph of the setup for this calibration experiment can be seen in Figure 2.16.

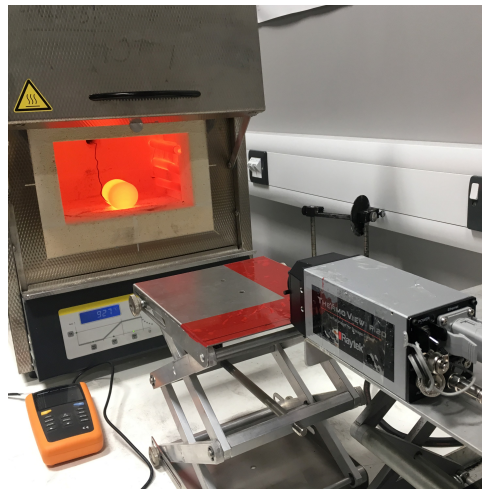


Figure 2.16: Thermal imaging camera calibration experimental setup

2.4.10 Thermal Imaging Camera: Calibration Experiment Method

Once the experiment was set up correctly, the box furnace was heated to a temperature of 200 °C. The emissivity value for the target measurement surface was set to ‘0.85’ within Raytek DataTempPi software. To ensure accurate temperatures were recorded, despite the distance to spot size ratio of 406:1, the AOI tool was used to obtain maximum temperature readings across the billet face. The AOI was set to the full billet face which

was positioned in the centre of the thermal imaging window. Assigning a large area as the AOI allowed for the small spot size to be taken into account.

Temperature readings were taken by opening the furnace door, which allowed the thermal imaging camera to read the temperatures within the AOI, which captured the whole billet front face. Maximum temperature readings across the AOI were recorded, alongside thermocouple temperature readings taken at the same time. The furnace temperature was adjusted to achieve heating of the billet in 100 °C intervals, from 200-1100 °C ± 5 °C according to the thermocouple reading at the given interval. Temperature readings were recorded at each interval. Each time the door was open, the thermocouple was confirmed to be held in the correct position before closing the door. This interval heating experiment was repeated three times for the given temperature range.

2.4.11 Thermal Imaging Camera: Calibration Experiment Results

Over the given temperature range, maximum negative offset was -32.3 °C and maximum positive offset was 32.1 °C. This can be seen in Figure 2.17.

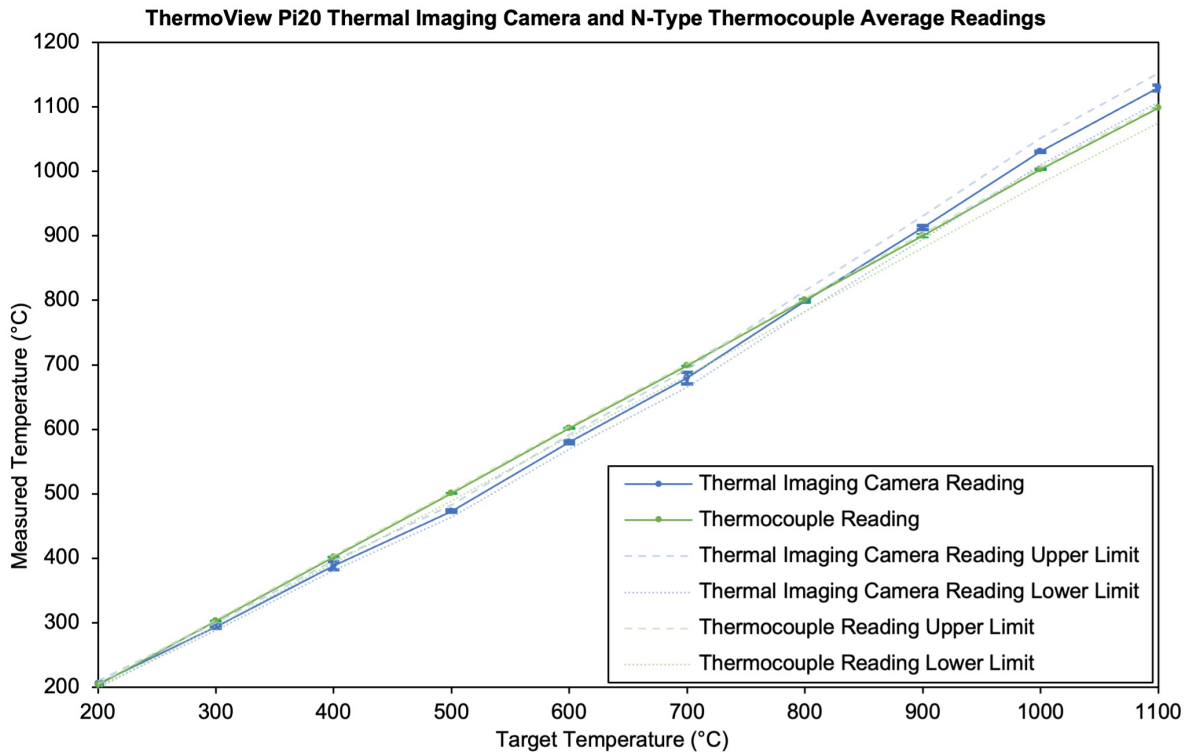


Figure 2.17: Graph showing observed differences between thermal imaging camera and thermocouple readings, without glass

The system accuracy of the thermal imaging camera was stated as subject to a variation of whichever is greatest out of $\pm 2\%$ of the reading, or $\pm 2^\circ\text{C}$. Despite the maximum positive and negative recorded offsets lying outside of this tolerance range, this can be expected. The thermal imaging camera relies upon a static emissivity value, which ultimately cannot be applied over such a wide temperature range due to the nature of molten metals. However, the accuracy of readings within $\pm 32.3^\circ\text{C}$ up to 1100°C is within an acceptable range for this type of temperature distribution measurement tool.

2.4.12 Thermal Imaging Camera: Calibration Experiment Discussion

It is important to note that as the thermal imaging camera requires a fixed emissivity input value, surface temperature measurements of IN713C did not account for potential emissivity value changes across different wavelength ranges. However, for the temperature measurements in the tested range of $200\text{--}1100^\circ\text{C}$, the discrepancies in thermal imaging camera readings compared to the values recorded by the contact thermocouple were of an acceptable magnitude. Ideally, the sample would have been heated to a molten state, with temperature measurements up to the liquidus temperature of IN713C. However, due to equipment availability and logistical reasons, this was not possible.

2.4.13 Thermal Imaging Camera Calibration: Conclusion

Thermal imaging cameras are useful for generating an overall understanding of temperature distribution across the surface of an object. Once the emissivity of a material across a temperature range of interest has been confirmed via calibration experiments, an acceptable temperature reading can be obtained. An emissivity value of 0.85 produces results within an acceptable temperature range of the measured thermocouple values, for a temperature range of $200\text{--}1100^\circ\text{C}$.

The thermal imaging camera could be a valuable tool for various industrial applications, including measuring the temperature distribution across the surface of a mould. An example of this can be seen in Figure 2.18, which also shows an assigned AOI for exporting temperature data from this region over time.

Equipment in the spectral range of $8000\text{--}14,000\text{ nm}$, such as the ThermoView Pi20HT, will lack the capability to receive temperature data when the target is obscured by most types of glass. To overcome this issue for industrial experiments in vacuum conditions, the creation of VIM-IC chamber viewing ports manufactured from special IR-transmissive

materials such as germanium, Amtir or zinc selenide would allow IR energy to be received by the thermal camera. However, this was not feasible in this situation, as the cost of these specialist types of glass is significant.

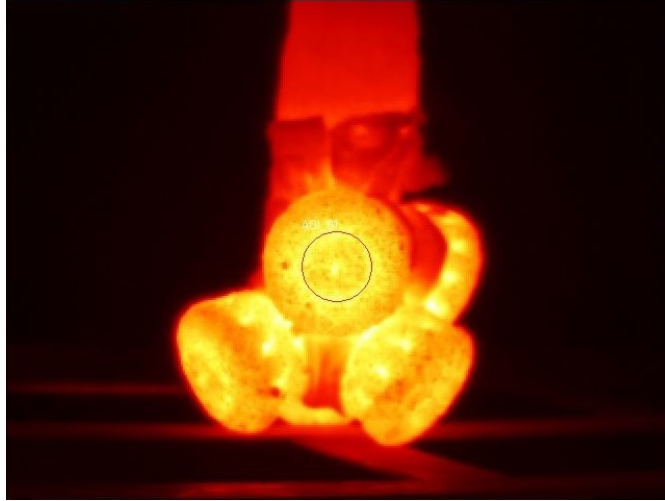


Figure 2.18: Thermal image of a hot investment casting mould filled with alloy taken with Thermoview Pi20HT, showing a defined AOI

2.5 Effective Thermal Diffusivity: LFA

2.5.1 Effective Thermal Diffusivity: LFA Overview

One of the process parameters as part of the industrial process which this work seeks to understand is the effect of the number of billet pieces used in VIM-IC. Often, the use of only one piece of the required alloy mass is used in the casting process when loading the crucible. However, it is not uncommon for two pieces of alloy to be used instead of one singular piece, to provide the required total charge mass for the casting. Further to this, in the investment casting industry it has been anecdotally understood that the use of a ‘penny’ can reduce the number of recorded defects per casting tree, which improves the overall yield. The penny is a thin disc of alloy which is inserted in the bottom of a crucible, with the rest of the alloy stacked on top. It is theorised that the total charge above the penny melts first before the rest of the charge.

Heat transfer between two bodies in contact will be subject to a temperature discontinuity at the interface. Thermal contact conductance (TCC) is the parameter that quantifies conductive heat flow across the interface of two contacting bodies [69]. In contrast, thermal contact resistance (TCR) is the inverse of TCC. It is hypothesised that the

2.5. EFFECTIVE THERMAL DIFFUSIVITY: LFA

effect of TCR at the contact interface between billet pieces, or the billet piece and the penny, is the cause of potential differences observed in heat transfer across two billet pieces compared to one billet piece of the same mass under the same melting conditions. This work seeks to develop an understanding of the impact of TCR for two IN713C faces in contact, and if the use of a penny or multiple billet pieces instead of one singular billet impacts measurable VIM-IC process outcomes.

A Laser Flash Analyser (LFA) machine was used to compare the measured thermal diffusivity for both one-piece and two-piece samples of the same total dimensions. The laser flash analysis method was developed in 1961 by Parker *et al.* [70]. The method was used to determine thermal diffusivity by pulsing a high intensity, short pulse of light on to the front surface of a thermally insulated sample coated in camphor black. The temperature of the rear surface of the sample was measured using a thermocouple and recorded by an oscilloscope and camera. By interrogating the shape of the temperature curve with respect to time, it is possible to determine the thermal diffusivity of the sample. Figure 2.19 is a diagram of the typical internal configuration of an LFA machine, which is a recreated version of ‘Figure 1’ from an article by Cheng *et al.* [71].

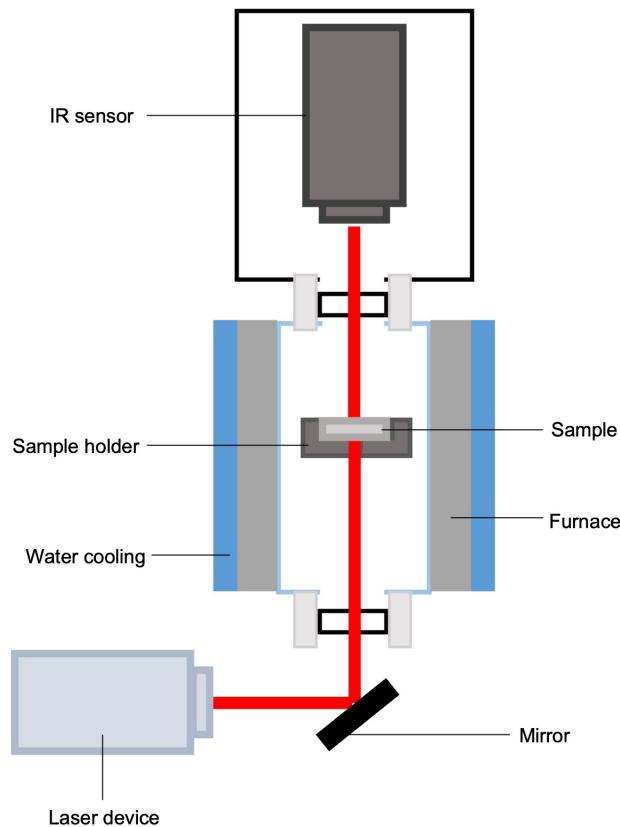


Figure 2.19: Diagram showing internal configuration of an LFA machine, recreated from [71]

2.5. EFFECTIVE THERMAL DIFFUSIVITY: LFA

Thermal diffusivity is the rate at which temperature spreads through a material, and can be measured in mm^2/s . LFA experiments testing thermophysical properties of selected Inconels, including IN713C, were conducted by Krajewski *et al.* [58]. However, in their work, the LFA experiments to determine thermophysical properties of IN713C were only conducted for one-piece samples. In this chapter, the value of an ‘effective thermal diffusivity’ for a two-piece layered system was obtained. The aim was to determine the impact of contact resistance between two IN713C pieces in contact, upon the heat transfer rate from the front sample surface to the rear surface. Values for ‘effective thermal diffusivity’ would be compared to the thermal diffusivity of the tested one-piece samples. The thermal diffusivity for one-piece samples were also compared to those found in the literature by Krajewski *et al.* [58].

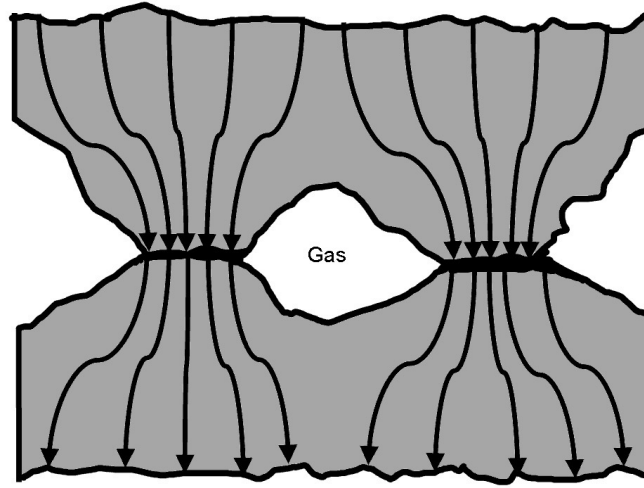


Figure 2.20: Schematic of two contacting bodies in direct contact, with arrows showing heat flow

A further objective of this experiment was to examine the effect of surface roughness on ‘effective thermal diffusivity’ in two-piece layered samples. In their work examining the effect of surface roughness on TCC between the surfaces of stainless steels, Dou *et al.* found that for the same applied pressure, an increased surface roughness resulted in a lower TCC [72]. When two surfaces are non-conforming and rough, the actual contact area between the two faces is substantially smaller than the nominal contact surface area. This results in a significant thermal resistance, due to heat transfer at the interface taking place across the smaller contact areas and through micro-gaps filled with air [73]. Figure 1(a) from an article by Grujicic *et al.* [73] has been recreated, as shown in Figure 2.20. This schematic demonstrates the lower regions of contact and air gaps observed between two non-conforming, rough surfaces. Heat flow across the interface is represented by the directional arrows. However, it is important to note that depending on the temperature

2.5. EFFECTIVE THERMAL DIFFUSIVITY: LFA

and the gas, there may be very high velocity recirculation which acts to transfer heat within the gap. This can, conversely, lead to lowering the effective thermal resistance in these instances.

Although the impact of surface roughness on TCC is well documented in literature, including the studies performed by Dou *et al.* on stainless steel [72], the effect of surface roughness on TCC for IN713C is not documented. Furthermore, many of the studies in existing literature involved the use of an applied pressure upon the layered samples. In this experiment to determine ‘effective thermal diffusivity’, there is no externally applied pressure between the two layer sample. This is a good representation of the industrial scenario of two billets stacked upon each other, with no externally applied pressure.

The two-piece LFA samples were prepared with varying levels of surface roughness on the two faces in contact. These samples were created to test the effect of surface roughness upon the measured ‘effective thermal diffusivity’ for heat transfer between the two IN713C sample layers. The thermal diffusivity measurements were taken by firing multiple laser pulse shots at the front face of the sample, with the measured thermal response on the rear face detected by an IR sensor. These thermal diffusivity values were compared to those of one-piece samples, to determine the difference in ‘effective thermal diffusivity’ between a one-piece and two-piece layered sample.

2.5.2 Effective Thermal Diffusivity: LFA Sample Preparation

Discs of IN713C alloy, with a diameter of 12.5 mm, were created from 50 mm diameter IN713C bar stock. These samples were created using a wire electrical discharge machine (EDM). Five sample sets were created, of which two were one-piece samples, and three were two-piece layered samples.

Preparing the contact surfaces of the sample pairs for layered samples with a uniform surface roughness for both surfaces in contact was achieved by mounting the samples in pairs. The samples were mounted using a Buehler SimpliMet XPS1 Mounting System, using resin to create the mounts. Once the sample pairs were mounted, they were polished using a Buehler EcoMet 250 Pro grinder-polisher machine. By applying a different sequence of polishing pads for each sample type, it was possible to achieve varying surface roughness by abrading the samples for a set amount of time, in a specified polishing direction with a given plate force. The details of the polishing sequences performed for the faces in contact of the samples named ‘Two-piece layered: DGD (Diamond Grinding Disc) finish’ and ‘Two-piece layered: Mirror finish’ are shown in Table 2.4. ‘Compound’

2.5. EFFECTIVE THERMAL DIFFUSIVITY: LFA

refers to the addition of either water or a fluid mixture containing abrasive particles of a given diameter in microns. The compound was applied to the sample using a dispensing system. ‘Rotation’ refers to the direction of sample rotation, relative to the rotation of the polishing pad. ‘Comp’ means that they are rotating in the same direction, while ‘Contra’ refers to rotation of the sample in the opposite direction to the pad rotation. Pads with a magnetic backing were applied directly to the aluminium platen with a magnet attached. Before and after the use of each pad, the pad and polisher platen system were rinsed and cleaned to remove any residue.

Sample Type	Pad	Time (mins)	Compound	Rotation	Force (lbs)
DGD finish	DGD	5	Water	Comp	5
Mirror finish	DGD	5	Water	Comp	5
	Hercules (H)	5	9 μm	Comp	5
	Ultrapad	10	9 μm	Contra	5
	Trident	10	6 μm	Contra	5
	Microfloc	10	1 μm	Comp	2

Table 2.4: Polishing sequences implemented to achieve different surface finishes.

Once the polishing sequences were complete, the samples were removed from their mounts using a compact press. Any remaining resin was removed from the samples, and the surface roughnesses of the polished faces were then measured using a Mitutoyo Surftest SJ-210 contact profilometer. To measure the surface roughness of each sample surface, it was important to firmly fix both the drive unit and the sample in place. This prevented the drive unit from deviating during measurement. It was also crucial to ensure that the contact between the sample surface and profilometer stylus was proper, and parallel to the measurement surface.

Surface roughness Ra and Rz measurements across each sample surface were taken three times, with the averaged values in microns for each surface listed in Table 2.5. In this case, Ra represents the average roughness of the metal sample surface across the tested surface length, by measuring the deviation of peaks and troughs of the surface height relative to the mean surface height line. Rz is a measure of the distance between the highest peak and lowest trough surface height, measured across the tested surface length.

In Table 2.5, ‘RRS’ is roughness reference sample, ‘IBS’ is the industrial billet sample, with ‘WC’ and ‘AC’ short for with cut and across cut respectively. ‘EDM’ represents the two-piece layered samples with unpolished faces cut by electrical discharge machine.

2.5. EFFECTIVE THERMAL DIFFUSIVITY: LFA

‘DGD’ represents the two-piece layered sample polished with only the DGD polishing pad, and ‘Mirror’ refers to the two-piece layered sample with a mirror finish on the two contact faces.

Parameter/Sample	RRS	IBS		EDM		DGD		Mirror	
		WC	AC	P1	P2	P1	P2	P1	P2
Average Ra (μm)	3.099	1.606	3.579	2.884	3.135	0.318	0.312	0.016	0.018
Average Rz (μm)	9.780	8.212	20.97	17.06	16.85	2.460	2.548	0.142	0.155
Thickness (mm)	N/A	N/A		3.870		2.864		2.330	

Table 2.5: Polishing sequences implemented to achieve different surface finishes

For each sample pairing, the two faces to be in contact in the LFA layered experiments are numbered separately. The surface roughness of a standard cut industry billet is also listed, alongside the surface roughness of the samples cut by wire EDM, and surface roughness values for a known reference sample. An unpolished layered sample was also tested in the LFA experiments, which was left with the surface finished achieved from its creation by the wire EDM. Samples are listed in order of surface roughness, with the ‘Two-piece layered: Mirror finish’ samples possessing the smoothest surface finish. The measuring speed used for the profilometer measurements was 0.5 mm/s.

In addition to surface roughnesses, the disc thicknesses of both the one-piece and two-piece samples are listed in Table 2.5, where thickness was measured using a micrometer. The two-piece layered samples were created by stacking the two pieces on top of each other, with the polished faces meeting together at the contact interface where applicable. For the two-piece samples, the measured thicknesses in Table 2.5 are the total thickness of two layers combined. Both one-piece samples and two-piece layered samples were coated with graphite to reduce reflection and increase laser energy absorption. For the two-piece samples, only the outer surfaces of these stacked samples were coated with graphite.

2.5.3 Effective Thermal Diffusivity: LFA Experiment Setup and Method

A NETZSCH LFA 457 LFA machine was used to determine thermal diffusivity of both one-piece and two-piece samples. The prepared samples were inserted into a three position sample holder. Two samples were inserted into the holder, alongside a Pyrocera 9606 reference standard sample. The measurement heating range was set to 50-1000 °C in

2.5. EFFECTIVE THERMAL DIFFUSIVITY: LFA

50 °C increments. Five laser pulse shots were applied at each temperature. The individual thermal diffusivity results for each shot were measured, and the average value was recorded. All samples, including the two-piece layered samples, were treated as one-piece samples by the system. This was to ensure that the effect on thermal diffusivity of the thermal contact resistance at the interfaces could be measured, obtaining ‘effective thermal diffusivity’ values for the two-piece layered systems. Two runs of the experiment were completed, as this was required for the thermal diffusivities of all samples to be obtained. All measurements were performed in an argon atmosphere. These LFA experiments were conducted with the assistance of Dr. Shahin Mehraban, Swansea University.

2.5.4 Effective Thermal Diffusivity: LFA Experiment Results

For the investigated temperature range, the measured effective thermal diffusivities of the one-piece and two-piece IN713C samples, and the Pyroceram 9606 reference sample for each of the experimental runs are plotted in Figure 2.21.

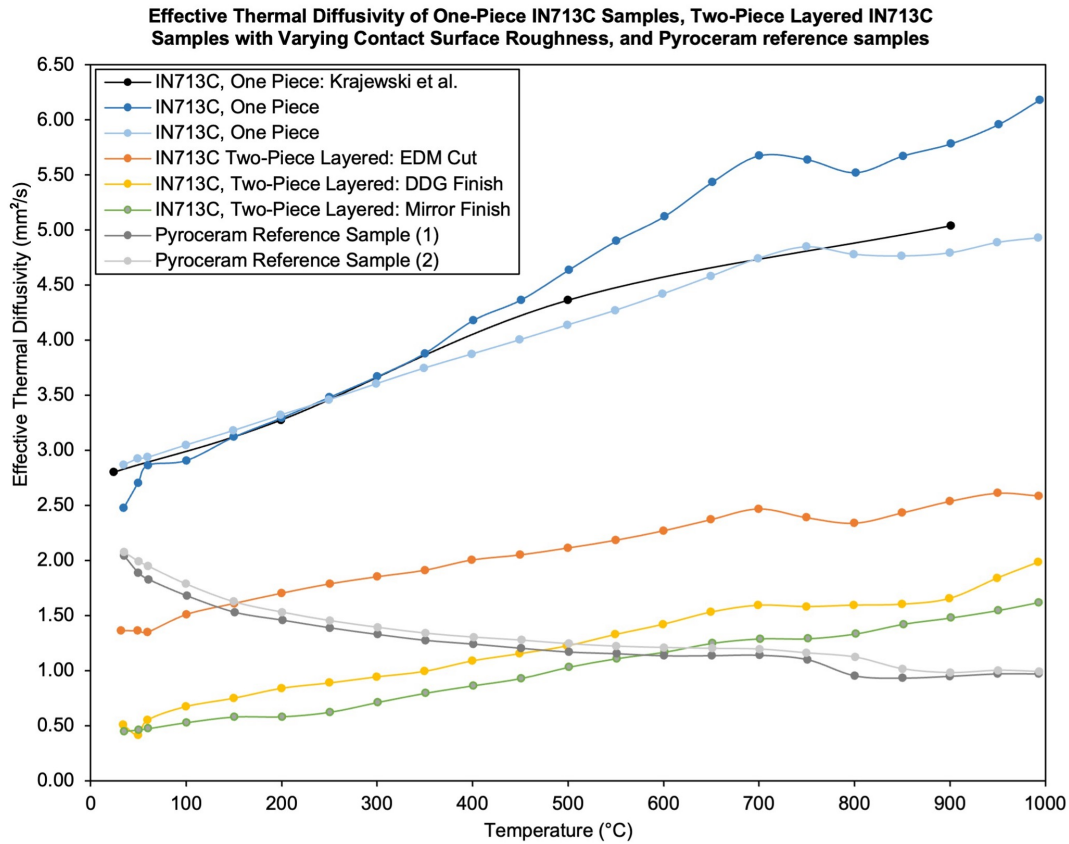


Figure 2.21: Temperature dependent effective thermal diffusivity in one-piece and two-piece IN713C samples, pyroceram reference samples, and obtained thermal diffusivity values of IN713C from the work of Krajewski et al. [58].

Thermal diffusivity values for IN713C obtained by Krajewski *et al.* [58] are also included in Figure 2.21 for comparison to the obtained values for the one-piece samples. The measured thermal diffusivity values of the Pyroceram 9606 reference sample closely matched the measured thermal diffusivity values of the reference sample provided by NETZSCH, throughout the temperature measurement range for each of the experimental runs. By comparing the measured thermal diffusivity values across the temperature range, it is evident that the thermal diffusivity values obtained by Krajewski *et al.* match the values of thermal diffusivity experimentally obtained for one-piece IN713C samples from the LFA experiments. Reviewing the data in Figure 2.21, there is a clear difference between the effective thermal diffusivity of a one-piece IN713C samples, compared to the measured effective thermal diffusivity of a two-piece layered system.

2.5.5 Effective Thermal Diffusivity: LFA Experiment Discussion

As previously mentioned, in theory and according to the existing literature on the effect of surface roughness on thermal diffusivity, two smoother surfaces should allow greater surface contact between the faces in contact, compared to two rougher samples. However, other experiments in the literature which have tested the effect of surface roughness on thermal diffusivity were conducted with a significant applied pressure pushing the two sample pieces together. The use of an applied pressure would ensure that there is a better contact between the two sample faces. In industry, there are no externally applied forces holding two pieces in contact within the crucible. Therefore, although the LFA experiment without an externally applied pressure is representative of the industrial setup, this differs from the methodology of previous literature studies which tested the effect of surface roughness on effective thermal diffusivity for layered samples.

Additionally, the theory behind the effect of surface roughness on thermal diffusivity assumes that the two surfaces in contact are parallel to each other. In the event that the surfaces are not perfectly parallel, there may be large areas of the surfaces which are not in contact. Although the samples were cut to size as accurately as possible using wire EDM, from this and the additional polishing steps it is not possible to guarantee that the two surfaces will be perfectly parallel. Therefore, it was not possible to guarantee that the contact area between the two surfaces would be larger for the smoother samples.

From Figure 2.21, the effective thermal diffusivity is significantly reduced for a two-piece layered sample, compared to a one-piece sample. Examining the differences in thermal

2.5. *EFFECTIVE THERMAL DIFFUSIVITY: LFA*

diffusivity for the two different one-piece samples, the recorded differences in thermal diffusivity readings for the two samples at temperatures exceeding 400 °C are larger than the the recorded differences seen between the two-piece layered DGD finish and mirror finish samples. For this reason, it is not possible from this experiment to determine the effect of surface roughness on effective thermal diffusivity, when observable differences were recorded for the two one-piece samples. The existence of these observed differences for two of the same type of one-piece sample, combined with the lack of an externally applied pressure, means that the effect of surface roughness cannot be determined from these test results. However, it is clear from the data obtained in these experiments that a clear difference in effective thermal diffusivity of a two-piece layered sample is observed, compared to one-piece samples of IN713C. This difference is a result of the thermal contact resistance at the interface between two pieces.

In the industrial VIM-IC process, the billets are not cut exactly flat to ensure parallelism of the two faces in contact. For two-piece billets which are used to create the combined total mass which is required for the casting, the piece lengths used are offcuts. To ensure exact parallelism between billet faces in contact would be both cost prohibitive and impractical due to the time required to achieve this. The main outcome of this experiment is the observation that the effective thermal diffusivity of two-piece layered samples is much lower. Although it would be interesting to understand the effect of surface roughness on effective thermal diffusivity for layered samples or two-piece billets, it is not necessarily relevant or the main factor which would influence the effective thermal diffusivity for the industrial application.

A penny vs. two-piece billet in casting has differences: the penny interfaces sits outside of the region in which the electromagnetic forces are acting, whereas a two-piece billet has an interface which sits within the region of the electromagnetic force acting upon it. An additional factor which could impact the effect of a thermal contact interface, is the location of the interface relative to the electromagnetic heating region. If the interface between the two billet pieces lies within the electromagnetic heating region of the coil, this could potentially have a different effect on the heating at the interface, compared to if this interface exists below the coil heating region where only conduction is active. A contact interface below the heating region occurs when a penny is used in casting.

The true impact of effective thermal diffusivity in the industrial setup, particularly with regards to an interface located within the electromagnetic heating region, cannot be tested for quantitative data using the LFA to conduct these experiments. The effective thermal

2.6. THERMOPHYSICAL PROPERTIES: REVIEW AND EXPERIMENTATION CONCLUSION

diffusivity in the industrial setup would also likely vary for each instance of VIM-IC, due to differences in billet face parallelism and surface roughness. Therefore, the main outcome of this experiment is the observation that a two-piece layered system results in a significantly lower effective thermal diffusivity compared to a one-piece sample.

The effect of a thermal contact resistance must be modelled in the simulations. It is also important to seek an understanding of the effect that a thermal contact interface has on flow characteristics during pouring. The effect of using two billet pieces and the position of this interface relative to the overall length of the billet is tested in the L9 array of industrial VIM-IC experiments in Chapter 4. Simulation results were compared to the experimental data to understand the real world impact of thermal contact resistance on alloy pouring and casting defect prevalence.

2.5.6 Effective Thermal Diffusivity: LFA Experiment Conclusion

From these experiments, it is evident that thermal contact resistance decreases effective thermal diffusivity for a two-piece layered sample compared to the measured values for one-piece samples. This effect occurs as a result of the reduced contact area for the two billet faces due to air gaps, which is not only a product of surface roughness, but could also be due to non-conforming contact faces which may not be exactly parallel or planar. With the understanding that thermal diffusivity is affected with the presence of a contact interface, this effect will be accounted for in the numerical models.

2.6 Thermophysical Properties: Review and Experimentation Conclusion

In this chapter, the key thermophysical properties that are needed to correctly model the VIM-IC industrial process are identified and defined. Experiments were performed to calibrate the IR thermometer and thermal imaging camera, resulting in identification of the required input values for accurate temperature measurement. Available temperature dependent thermophysical properties were collated from literature. IN713C material properties were derived using CompuTherm for nickel based superalloys, based on the input alloy composition. Solidus, liquidus and latent heat values for IN713C, and thermal diffusivity values for one- and two-piece samples were measured experimentally. Where otherwise not available or measurable, properties were estimated and defined based upon

guidance and best practice from ESI Group. The information presented in this chapter provides both quantitative data, and qualitative data which serves to build an understanding of the physics involved in numerical modelling of two-piece billets. These thermophysical properties will be used in the subsequent chapters for accurate experimental temperature measurement and modelling of the VIM-IC process [**OB1**, **OB2**].

Chapter 3

Small Scale Induction Melting and Modelling with COMSOL

3.1 Small Scale Induction Melting and Modelling with COMSOL Overview

An understanding of induction heating and melting is invaluable in determining the effect of process variables upon the quality of the finished castings. Numerical modelling of the induction heating and melting process is vital in developing this understanding. Data on measured temperatures of an IN713C billet in a small scale induction melting experiment during heating and cooling cycles were recorded using an optical pyrometer. The billet was heated and melted using an induction coil, followed by cooling as the coil power was switched off. This cycle was repeated, with heating and cooling curves plotted with respect to time. The ability to accurately model the heating, melting, and cooling of an IN713C billet on a smaller scale, provides a solid foundation for modelling VIM-IC on a larger industrial scale. Development of an experimentally validated, accurate induction melting model paves the way to a greater understanding of the VIM process for the application of component production in the automotive and aerospace industries. The principles from this small scale model can be applied to a larger scale model, providing an effective tool to investigate the effect of variables such as alloy condition on the quality and yield of finished castings.

COMSOL Multiphysics, a Finite Element Method (FEM) software, was used to model the

3.2. SMALL SCALE INDUCTION MELTING EXPERIMENT

induction heating, melting, and cooling which was experimentally observed in the billet. The COMSOL AC/DC module was used to implement the induction coil, producing the electromagnetic field in a 2D axisymmetric Frequency-Transient study. Phase Change Material functionality was used to map the progression of alloy phase change throughout the heating, melting and cooling cycles. Melting temperature, phase transition interval and latent heat of fusion for IN713C were determined using data from a Differential Scanning Calorimeter (DSC), as discussed in Section 2.2. Emissivity of IN713C was required for the numerical model, and obtained experimentally as shown in Section 2.3. Temperature results from the conductive heat transfer models were compared to experimentally obtained temperature data during heating, melting and cooling cycles. A model including Fluid Flow functionality, using a Low Reynolds number k - ϵ turbulence model, was used to model the effect of eddy currents. The time-averaged Lorentz force was applied to the fluid to drive the molten metal in electromagnetic stirring. A source term, F , was prescribed to dampen the velocity at the phase-change interface, so that velocities produced by solution of the momentum equations were inhibited for alloy in a solid state. Velocity profiles generated due to electromagnetic stirring provided qualitative information for the eddy currents, and a model with phase change and fluid flow will be developed upon in further work. The author would like to acknowledge the COMSOL technical support team for their assistance with this project. The work in this chapter was published in a conference proceedings paper by Thomas *et al.* [74]. The figures presented herein are reused from this publication.

3.2 Small Scale Induction Melting Experiment

3.2.1 Small Scale Induction Melting: Experiment Setup and Method

A 20 mm long, 12 mm diameter IN713C billet was heated in a ceramic crucible using an EasyHeat 0224FF CE 2.4 kW induction heater, in an argon environment inside a Saffron Scientific Equipment anaerobic glove box. The billet was inserted into the crucible and placed on a boron nitride plate. The plate was adjusted to a height which allows the crucible to sit within the coil using a jack stage. Temperature of the top billet face was measured using an Optris CTlaser 2MH CF3 optical pyrometer, which is capable of measuring temperatures in the range of 385-1600 °C. The optical pyrometer was fixed above the sample as shown in the experimental setup diagram, Figure 3.1. An alignment

3.2. SMALL SCALE INDUCTION MELTING EXPERIMENT

laser ensured that the top face of the billet was being measured by the optical pyrometer. Initial heating and melting experiments were conducted to determine the best current set points to use. The small scale induction experiments were conducted with the assistance of Dr. Jonathan Cullen and Dr. Mazher Yar. A heating experiment involved heating the billet to over 900 °C, by setting the induction heater current to 100.1 A. As billet temperature started to plateau, the current was increased to 140.4 A. Once it reached a maximum temperature of 944.1 °C, the current was set to zero. The sample was allowed to cool until it reached the bottom of the optical pyrometer temperature measurement range.

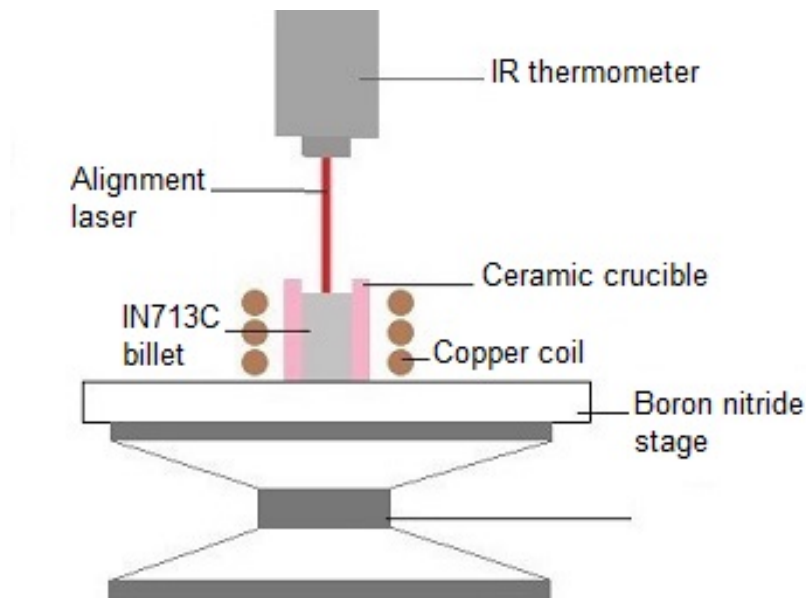


Figure 3.1: Small scale induction melting and optical pyrometer setup

Induction melting of the billet for a fixed high current required thermal cycling of the sample in the crucible, to prevent crucible breakage due to thermal shock. After initial thermal cycling, induction melting of the billet was achieved by setting the induction heater current to 280.1 A. The current was held at this value until the billet reached a maximum temperature of 1372.9 °C. Once the sample was observed to be molten, the current was set to zero. The sample was allowed to cool until it reached the bottom of the optical pyrometer temperature measurement range.

For both heating and melting experiments, the optical pyrometer emissivity value was fixed at 1.00. Emissivity was set to this value, as the dimensions and setup of the measurement target were such that it could be approximated as a blackbody for purpose of temperature measurement, where the emissivity of a blackbody is 1.00.

3.2. SMALL SCALE INDUCTION MELTING EXPERIMENT

3.2.2 Small Scale Induction Melting: Experiment Results

Temperature data from optical pyrometer measurements for the induction heating and melting experiments are shown in Figures 3.2 and 3.3 respectively. The optical pyrometer system accuracy is $\pm(0.3\%T_{\text{meas}}+2)^{\circ}\text{C}$, where T_{meas} is the measured temperature. Current, frequency and power settings for the induction heater were recorded for both heating and melting experiments, and are also shown in the graphs.

It is evident from examining the induction heating experiment graph, Figure 3.2, that once the top billet face temperature reaches around 600°C , it has reached a plateau for the given power setting. The increase in power allows the temperature to be taken up to over 900°C . Once this new temperature has been achieved, the power and current are switched off.

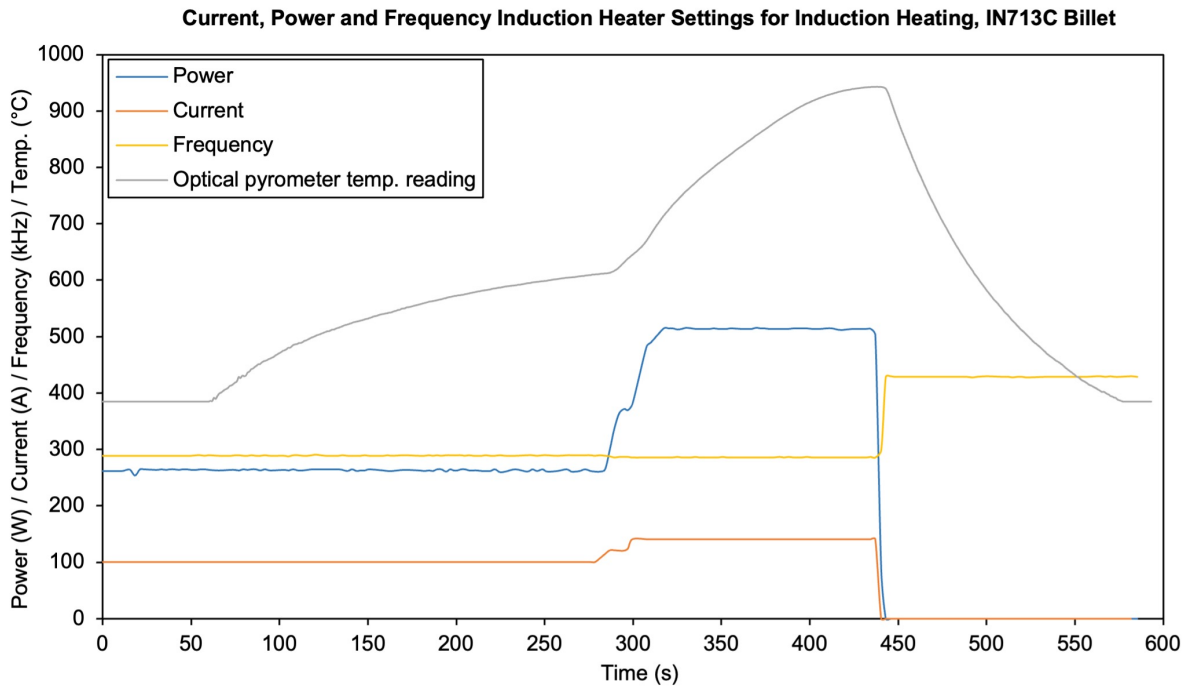


Figure 3.2: Temperature reading and induction heater settings: heating

Figure 3.3 shows the billet top face temperature with respect to current, frequency and power of the generator unit for an induction melting experiment. The power is kept constant at around 2 kW for the entirety of this experiment. Finally, once a molten state has been achieved, the power and current are switched off.

There is a plateau in the heating curve at around 1250°C . This may be indicative of melting. However, during this measurement, a small spot on the top face of the billet is

3.2. SMALL SCALE INDUCTION MELTING EXPERIMENT

being measured by the optical pyrometer. As the centre (vertically) of the billet melts first the top surface may still be solid, whilst underneath there is molten metal that is stirring under strong eddy currents. So, the optical pyrometer will not always be measuring the same spot. Therefore it cannot be concluded that this plateau is associated with melting as it could be related to measuring the temperature at different points on the top surface of the billet being measured.

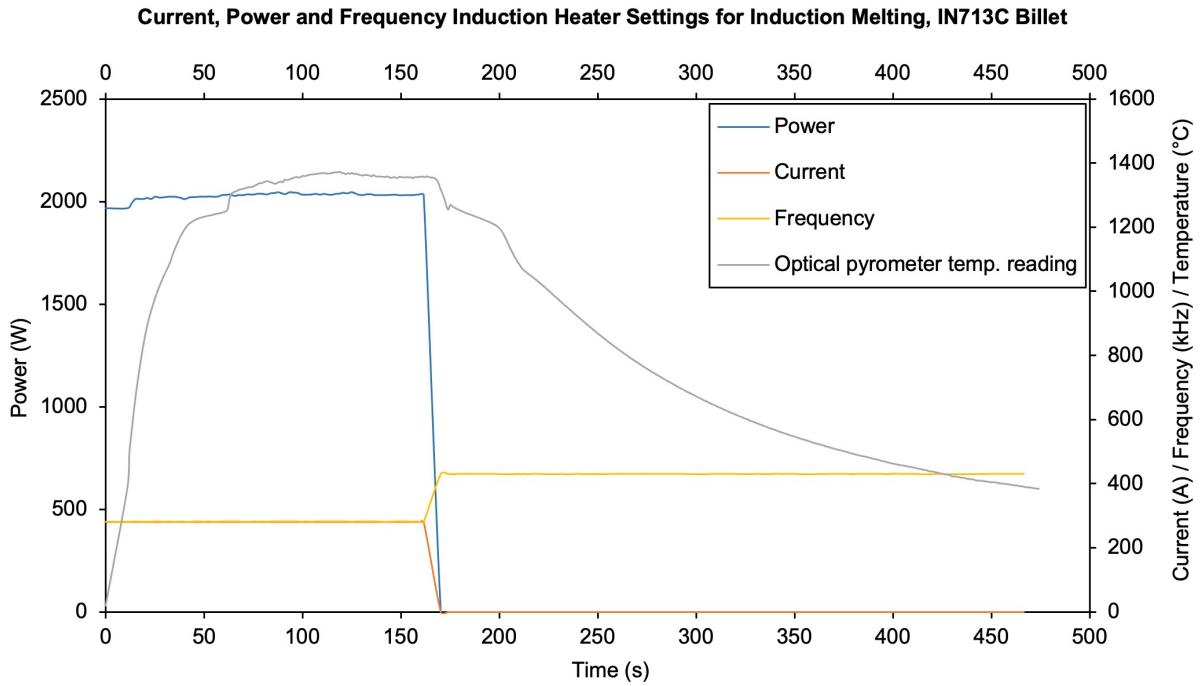


Figure 3.3: Temperature reading and induction heater settings: melting

In the case that this plateau is related to melting, it is within the range of solidus and liquidus values reported in the literature. Although the experimentally obtained solidus and liquidus values from the DSC experiment were used as the values in the modelling, it is important to note that in the literature, the liquidus value varies from 1288-1391 °C. Equally, the solidus value ranges from 1226 – 1307 °C in the literature; see Table 2.1. This large variation in reported mushy zone temperatures could be due to differences in elemental compositions, as there are ranges of acceptable alloy weight percentages for elements in the IN713C specification. For the experiments within this thesis, IN713C was provided from several different batches, and so the composition and the mushy zone temperatures may vary. This is standard within the industry and may explain reported potential differences in the solidus and liquidus temperature values.

3.3 Small Scale Induction Modelling

3.3.1 Small Scale Induction Modelling: Governing Equations and Physics

The ‘Electromagnetic Heating’ Multiphysics interface was applied, involving a combination of the ‘Magnetic Fields’ and ‘Heat Transfer in Solids’ physics nodes. A fully coupled solver approach was adopted, for a Frequency-Transient model. A transient magnetic field is produced by applying an AC to a coil, which induces eddy currents in nearby electrically conductive materials according to Maxwell’s equations. These equations describe the relationship between fundamental electromagnetic quantities [75]. Maxwell-Ampere’s law for general time-varying fields can be written as:

$$\nabla \times \mathbf{H} = \mathbf{J} + \frac{\partial \mathbf{D}}{\partial t} \quad (3.1)$$

where \mathbf{H} is magnetic field intensity, \mathbf{J} is current density, and \mathbf{D} is electric displacement or electric flux density. Faraday’s law can be written as:

$$\nabla \times \mathbf{E} = -\frac{\partial \mathbf{B}}{\partial t} \quad (3.2)$$

where \mathbf{E} is electric field intensity and \mathbf{B} is magnetic flux density. (3.3) is the electric form of Gauss’ law, where ρ is electric charge density. (3.4) is Gauss’ law in the magnetic form.

$$\nabla \cdot \mathbf{D} = \rho \quad (3.3)$$

$$\nabla \cdot \mathbf{B} = 0 \quad (3.4)$$

Heat generation from induced currents in the electrically conductive material due to the Joule effect can be described by the following equation, where P is power, I denotes current and R is resistance:

$$P = I^2 R \quad (3.5)$$

The Lorentz force vector can be accurately calculated for an electrically conductive material, and added as a source term to the fluid momentum equation:

$$\mathbf{F}^{\text{Lorentz}} = \mathbf{J} \times \mathbf{B} \quad (3.6)$$

Skin depth is also an important factor in modelling penetration of a magnetic field within an electrically conductive material. Penetration depth decreases as frequency of the AC increases, as shown in (3.7) [76]:

$$\delta = \frac{1}{\sqrt{\pi f \mu \sigma}} \quad (3.7)$$

where δ is skin depth in metres, f is frequency of the alternating current in Hz, μ is absolute permeability in H/m, and σ is electrical conductivity in S/m.

‘Phase Change Material’ functionality was used in models both with and without fluid flow, to input the relevant parameters regarding material phase change. However, for the model including fluid flow the ‘Nonisothermal Flow’ Multiphysics interface was applied for the fluid flow model, employing a k- ϵ turbulence model. Materials undergoing phase change with a ‘mushy’ region have a temperature transition interval over which the phase change takes place. Activation of velocities across the mushy region can be modelled by setting permeability as a function of porosity. A damping source term, F , was applied:

$$F_{r,z} = -\frac{(1-\lambda)^2}{\lambda^3 + q} C(u, w) \quad (3.8)$$

where λ is the liquid phase volume fraction, C is a physics dependent large constant to produce damping, and q is a sufficiently small constant to avoid division by zero. u and w are the fluid velocity components in two directions for the 2D model. (3.8) was taken from the method of modelling convection-diffusion for mushy region phase change problems using a fixed grid approach by Voller *et al.* [77]. For the qualitative model with fluid flow, C was set to 1600 kg/m³s and q was equal to 0.001. These values were chosen to replicate parameters in the referenced paper.

3.3.2 Small Scale Induction Modelling: Geometry and Mesh

The model geometry was comprised of several domains, using a 2D axisymmetric approach. An infinite elements domain was applied around the outside of the argon domain. Figure 3.4 shows the model geometry with labelled domains for the billet, coil, ceramic crucible and argon, alongside the mesh configuration.

3.3. SMALL SCALE INDUCTION MODELLING

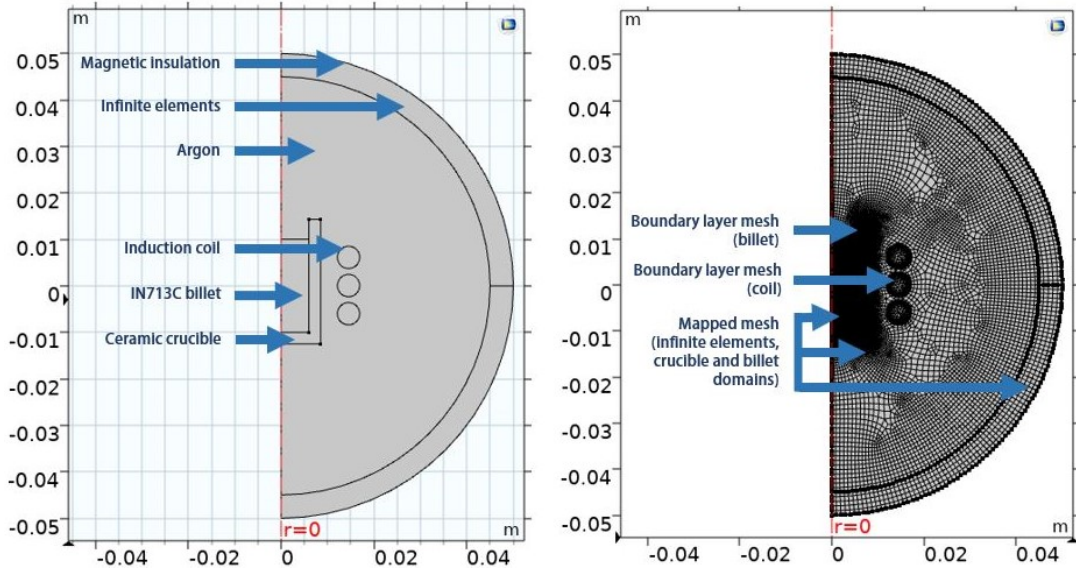


Figure 3.4: 2D axisymmetric model geometry and mesh

A mapped mesh with quad elements was applied to the infinite elements, crucible and billet domains. A free quad mesh was applied to the argon domain. Triangular elements covered the centre of the coil domains, with boundary layers on the boundaries of the billet and coil domains. The boundary layer mesh type was applied to ensure that a sufficient number of elements covered the total skin depth. Convention dictates that a minimum of four elements should cover the skin depth [78]. Therefore, five elements were applied across the calculated skin depth for each conductor material. The calculated skin depths for copper and IN713C at the frequencies recorded from the induction heater are listed in Table 3.1. Skin depths for the known frequencies determined the size of boundary layers.

Material	Frequency (kHz)	Skin Depth (mm)
Copper	282	0.12237
	429	0.09922
IN713C	282	1.13767
	429	0.92238

Table 3.1: Calculated penetration depths at known frequencies

3.3.3 Small Scale Induction Modelling: Boundary Conditions

Magnetic insulation is a homogeneous Dirichlet boundary condition, which fixes the field variable which is being solved for as zero at the boundary [79]. The magnetic insulation was applied to the outside of the infinite elements domain, to ensure that it was far

3.3. SMALL SCALE INDUCTION MODELLING

away enough from the induction coil and billet such that the solution was unaffected, and boundary conditions could be applied. The infinite elements domain was applied as a method for limiting the size of the argon domain, by applying coordinate scaling to an outer virtual domains layer. The three turn coil was represented by the COMSOL Coil feature from the AC/DC module, applied to the three circular domains. The ‘Single conductor’ option was used, modelling the solid regions as a ‘Coil group’. The current of the coil corresponded to the integral of the current density on a cross section. As the current varied with time for the induction heating model, it was defined as a time dependent piecewise cubic interpolation. ‘Surface-to-Ambient Radiation’ was applied to the billet top face, with the experimentally obtained surface emissivity of 0.85. An effective heat transfer coefficient was applied to all crucible surfaces exposed to the surrounding argon, as a ‘Heat Flux’. This artificially high effective heat transfer coefficient accounted for heat losses due to natural convection, radiative and other sources. Values between 50 - 5,000 W/m²K were tested in the model to determine which value most effectively captured sample cooling rate.

3.3.4 Small Scale Induction Modelling: Material Properties

Temperature dependent material properties for IN713C were available in the materials library of COMSOL Multiphysics software. These temperature dependent relationships were described by piecewise functions over a given temperature range. Outside of the function range, COMSOL sets the properties to a constant value at the lower and upper ends of the piecewise function by default. The main model discussed in this paper used only conductive heat transfer without a fluid flow component, not accounting for natural convection.

An artificially high value of effective thermal conductivity was employed at the melting point to account for the lack of fluid flow liquid phase transition. The artificially high effective thermal conductivity value accounts for a high rate of transport of momentum, as electromagnetic stirring generates strong fluctuating velocities with a very strong convection [80]. In addition, an artificially high specific heat capacity value was employed at melting point to account for phase change in a model without fluid flow. The liquidus temperature, temperature transition interval and latent heat of fusion were required by the Phase Change Material functionality. Values for these material properties were taken from DSC data.

3.3.5 Small Scale Induction Modelling: Fluid Flow

Quantitative temperature data was obtained from the solely heat conductive models in this paper. However, a qualitative model, for examining the behaviour of fluid flow as it initiates in an apple core pattern and stirs under electromagnetic forces, was developed. This model used a Frequency Domain study step to provide consistent initial conditions before deploying a time dependent Frequency Transient model. The Frequency Transient model used a segregated solver approach. Two types of ‘Volume Force’ were applied to the billet region of the model including fluid flow. A ‘Solid’ force, accounting for velocity damping in the solid and mushy regions, was applied by (3.8) as described in subsection 3.1.2. To account for buoyancy in the liquid metal, gravity was taken into account. A ‘Magnetic’ force was also applied by multiplying the parameters ‘mf.Fltzavr’ and ‘mf.Fltzavz’ by the COMSOL parameter for liquid phase. This allowed the Lorentz time averaged magnetic force to drive the movement of the molten metal in electromagnetic stirring. A condition of ‘No slip’ was applied to the crucible walls, with a pressure point constraint of 0 Pa applied to the bottom inner corner of the crucible. The billet top face was defined as an outlet with a pressure of 1 atm.

3.3.6 Small Scale Induction Modelling: Mesh Sensitivity

Electromagnetic heating was only active in the billet domain, with heat transfer modelled in both the billet and crucible. For this reason, the mesh sensitivity study was performed in the billet and crucible domains as the thermal problem was only solved in these areas. To measure the average temperature of the billet top face, a boundary probe was applied.

The mesh convergence study was conducted for the model replicating induction melting, as this covered a wider range of temperatures. A standard approach was used, reducing element sizes until results convergence was observed.

Element Length (mm)	CPU time	Element Quality
0.1	2.46	0.9596
0.2	1	0.9316
0.3	0.56	0.9241

Table 3.2: Relative CPU time (1 absolute time unit = 8 hours) and average model mesh element quality for varying billet and crucible domain max. element sizes

Study results are shown in Figure 3.5, with maximum element lengths of 0.1-0.3 mm. An

3.3. SMALL SCALE INDUCTION MODELLING

adaptive timestepping scheme was adopted, which allowed the software to automatically adjust the size of the timestep to remain within the relative tolerance of 0.01. The ‘Nonlinear controller’ option was selected, to account for the nonlinearity of the physics of this problem. CPU time relative to an element size of 0.2 mm and average mesh element quality for each element size is listed in Table 3.2. Results were converged to a satisfactory level for an element length of 0.2 mm. However, despite being 2.46 times more computationally expensive than a maximum element length of 0.2 mm, total CPU time for 0.1 mm was acceptable. Therefore, for maximum accuracy all further results in this paper have been generated using maximum element length of 0.1 mm within the billet and crucible domains.

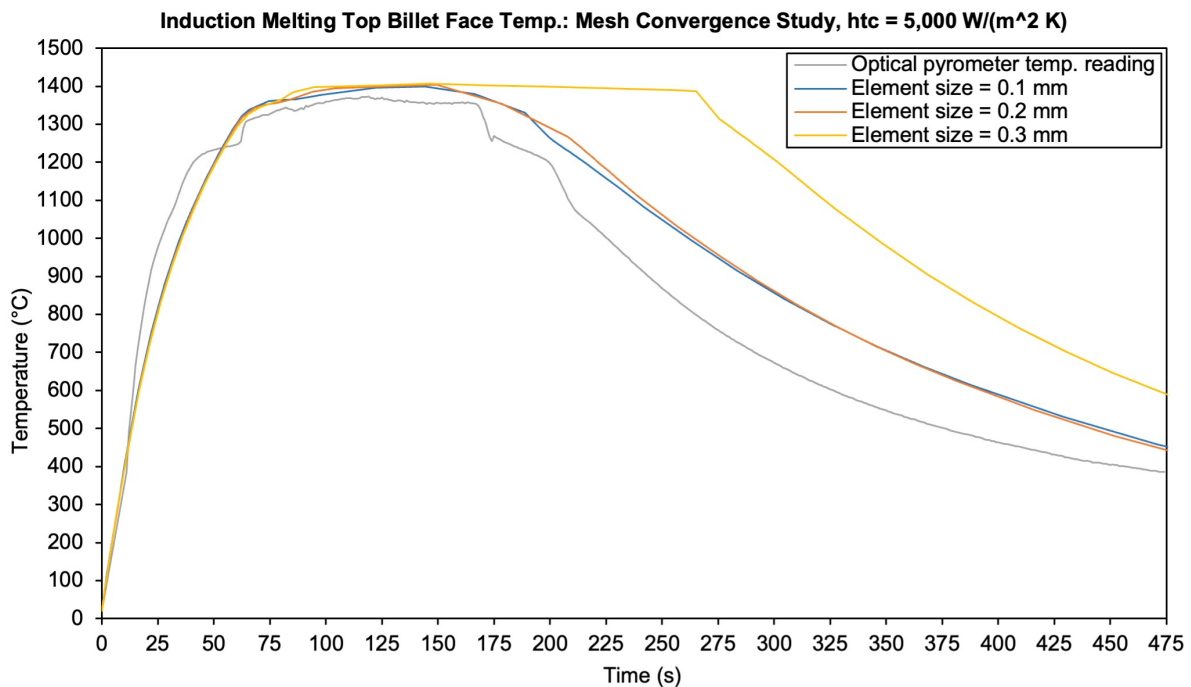


Figure 3.5: Mesh convergence study

3.3.7 Small Scale Induction Modelling: Results

Induction heating and melting models for the solely heat conductive models were run for varying effective heat transfer coefficients, shown in Figures 3.6 and 3.7 respectively. With increasing values of effective heat transfer coefficient, the top billet face temperatures tend towards convergence in Figure 3.7.

3.3. SMALL SCALE INDUCTION MODELLING

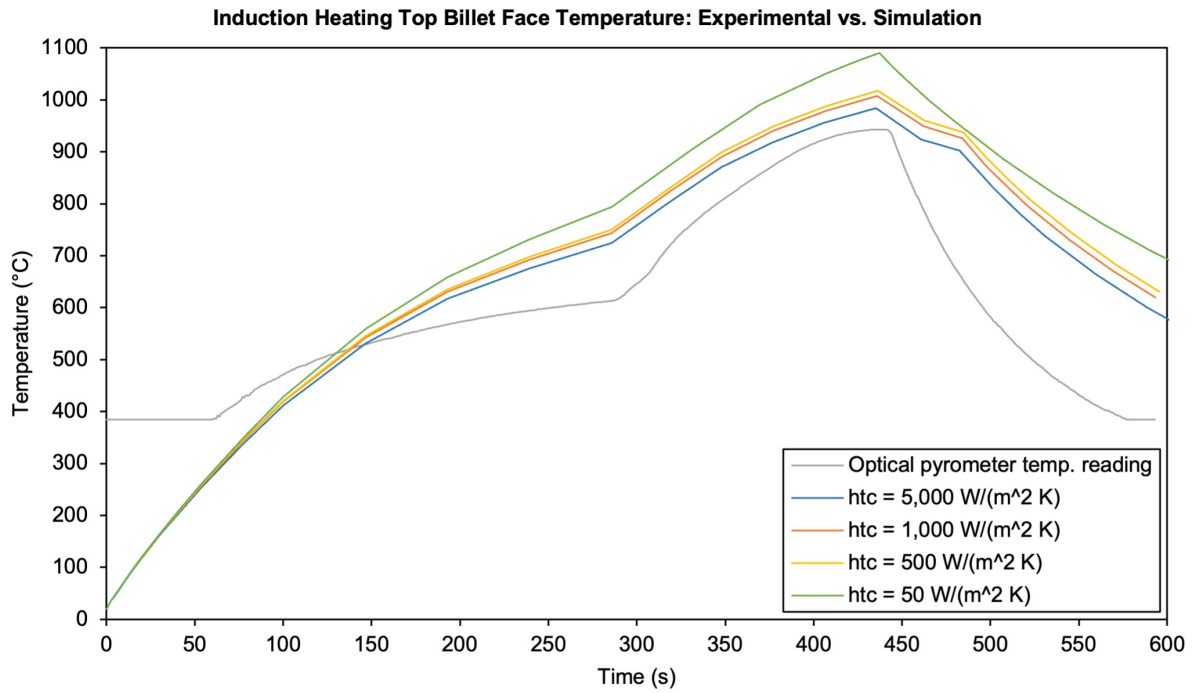


Figure 3.6: Induction heating simulation results for varying effective heat transfer coefficients. Optical pyrometer data set starts at 385 °C, which is the equipment lowest detectable temperature.

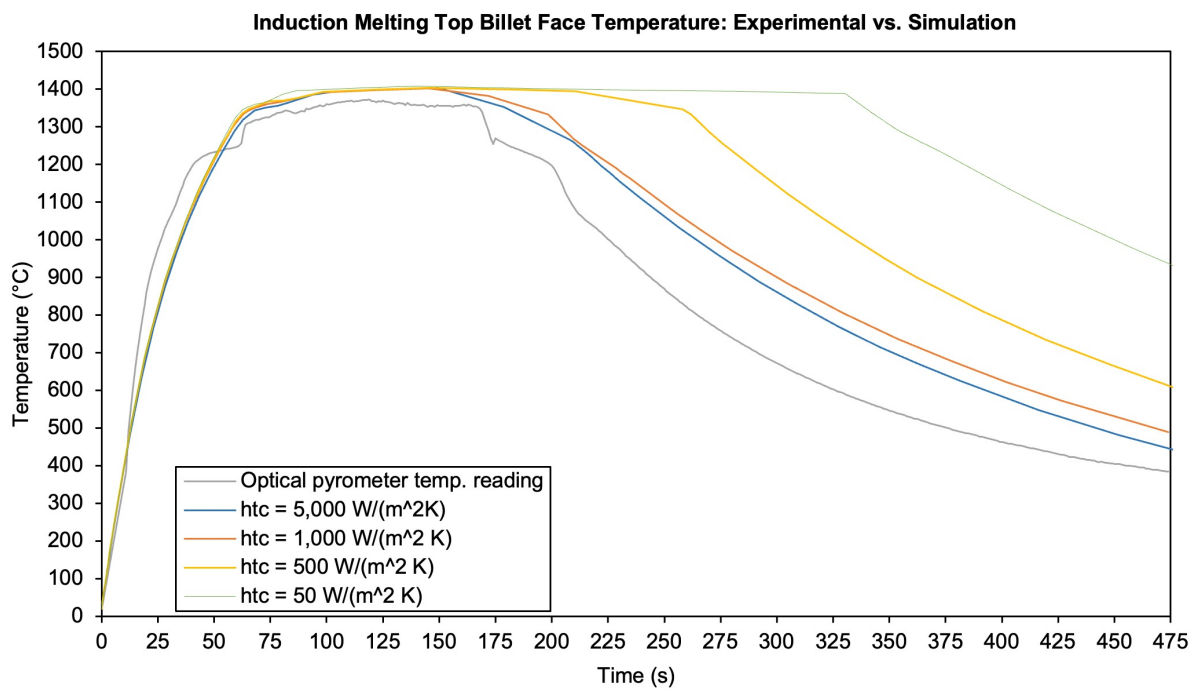


Figure 3.7: Induction melting simulation results for varying effective heat transfer coefficients

3.3. SMALL SCALE INDUCTION MODELLING

However, the temperature values do not exactly match the measured temperature reading curve. The cause of this is likely to be the use of a generalised heat transfer coefficient, as this is not a perfect substitution for modelling heat losses during cooling. Figure 3.8 shows the thermal profile of the billet at $t = 100$ s from the melting model, for a run where effective heat transfer coefficient was set as $5000 \text{ W/m}^2\text{K}$.

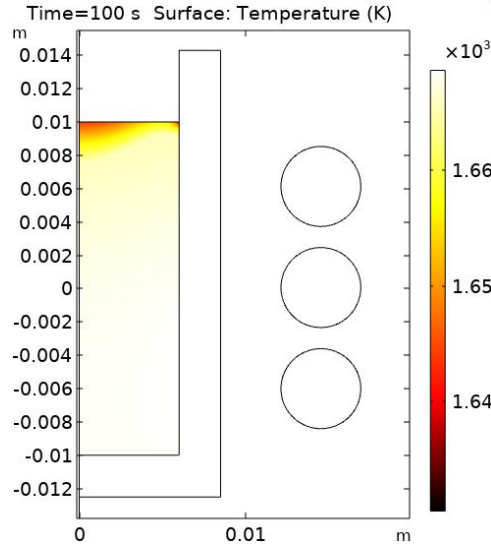


Figure 3.8: Billet temperature profile from melting model, $t = 100$ s

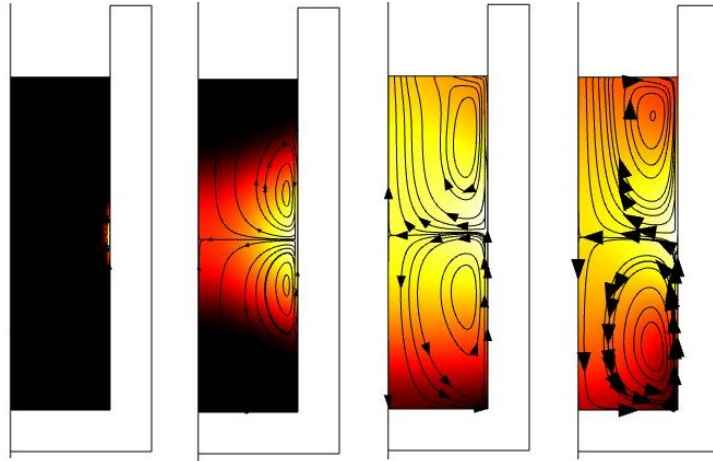


Figure 3.9: Phase transition and electromagnetic stirring, with black representing fully solid alloy and white representing fully molten alloy. Red and yellow regions are representative of alloy in the mushy zone.

For the qualitative fluid flow model, phase change transition and fluid flow driven by the Lorentz time averaged force can be seen in Figure 3.9, where black represents 100 % solid

3.3. SMALL SCALE INDUCTION MODELLING

alloy and white represents fully molten alloy, with red and yellow regions representative of the mushy zone. Magnitude controlled density streamlines are plotted of the alloy velocity, showing the velocity of the molten metal stirring within the crucible as it emerges at the liquid phase initiation site. Figure 3.10 shows the billet at identical timesteps with the same alloy velocity streamline plot, with a ‘jet’ colour bar velocity profile plotted across the billet domain surface. In this ‘jet’ colour bar profile, dark blue represents stationary and low velocity alloy, with red representing higher velocity values.

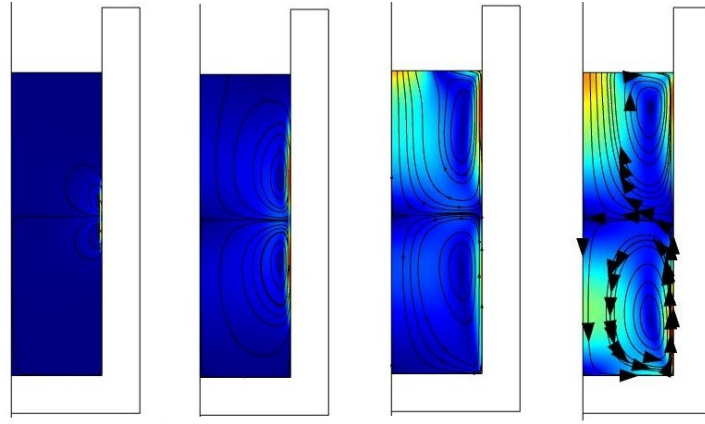


Figure 3.10: Velocity profile and electromagnetic stirring, with dark blue representing stationary alloy and red indicative of alloy moving at higher velocities.

3.3.8 Small Scale Induction Modelling: Discussion

For both heating and melting models, an effective heat transfer coefficient of $5\,000\text{ W/m}^2\text{K}$ produced results which most closely matched the experimental results. Varying the values of effective heat transfer coefficient had a greater effect on cooling of the billet than heating. The temperature plot in Figure 3.8 showed that at $t = 100\text{ s}$, the centre part of the top piece of the billet remains cooler than the rest of the billet domain surface. It is known from the physics of induction melting that the top centre part of the billet remains solid until last, which is shown in Figure 3.11. This image was taken from a thermal imaging video which was recorded in an industrial setting, where the billet temperature is lower in darker regions. In Figure 3.11, the central top billet piece has remained a lower temperature than its surroundings, while it undergoes stirring. This shows that the heat conductive model accurately reflected the physics that would be expected during induction melting. Examining the velocity profile of the molten alloy in Figure 3.10, the velocity is higher at the top part of the crucible wall compared to the billet centre. This can be seen from the higher density of velocity streamlines at the crucible top edge,

3.4. SMALL SCALE INDUCTION MELTING AND MODELLING WITH COMSOL: CONCLUSION

compared to in the centre. Therefore, it follows that the solid part of the billet would be eroded near the crucible wall before melting in the centre.

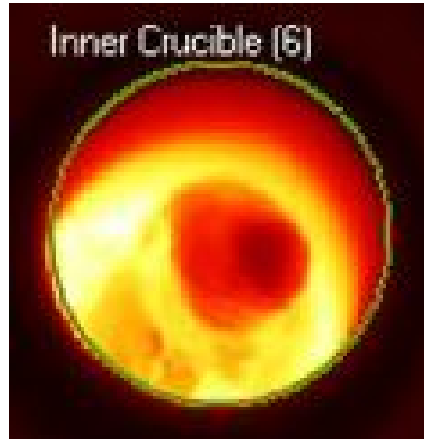


Figure 3.11: Thermal imaging: industrial induction melting

There are a number of factors which could contribute towards a difference between experimental and numerical results. Despite adopting effective material properties to account for strong convection, physics of the fluid flow were not modelled. Furthermore, various input parameters required for the model were not readily available or incomplete, such as temperature dependent material properties. Use of effective material properties and heat transfer coefficient are methods of model adjustment. This influences the output to reflect measured data, which could introduce error. Experimentally obtained temperature measurements are taken at a specific measurement spot, whereas the numerical result was an average temperature of the billet top face. Finally, a level of results discrepancy could be due to equipment sensitivity, which is inevitable.

3.4 Small Scale Induction Melting and Modelling with COMSOL: Conclusion

COMSOL functions as a simple but powerful tool to model multiphysics scenarios, and can predict the thermal behaviour of an IN713C billet in a relatively quick time frame. The billet top face temperature in a heat conductive model is in agreement with the experimental results, to a reasonable degree. This partially fulfils [OB2], albeit on a smaller scale. Due to the nature of this setup, alloy pouring is not studied in this chapter.

Use of an effective thermal conductivity and effective specific heat capacity can account for rapid thermal transfer from a model, including convective fluid flow and eddy currents.

3.4. SMALL SCALE INDUCTION MELTING AND MODELLING WITH COMSOL: CONCLUSION

Similarly, an artificially high effective heat transfer coefficient is helpful in modelling generalised heat losses. The proven effectiveness of these techniques contributes towards the development of [OB1]. A model including fluid flow and convection was suitable for qualitative assessment of the velocity profile.

However, to effectively simulate the industrial process, ideally a model is needed which can accurately predict temperature distribution throughout the alloy at the pouring time step. This is required to understand how process parameters must be adjusted to better inform the manufacturing process. To achieve this, mould filling must be modelled so that the impact of different billet temperature profiles on mould filling behaviour and final casting quality can be tested.

Chapter 4

VIM-IC and Pouring Experiments

4.1 VIM-IC and Pouring Experiments Overview

Piping, also known as solidification shrinkage of metals, is a naturally occurring defect in billets which are used in VIM casting. It is formed during the billet manufacturing process at the alloy supplier. Piping refers to the internal shrinkage porosity which can be found down the centre line of billets. Occasionally, piping is visible externally on the billet face, which is the case when the billet has been cut in the region of the internal piping. If the billet is not cut to size within the piping region, it is not possible to determine if internal piping exists without performing an X-ray.

It is anecdotally known within the VIM casting industry that if piping exists in the billet used for melting, it can cause a higher incidence rate of defects within the finished casting. In an effort to avoid these defects caused by piping, there are measures which can be taken in the casting process. Firstly, continuous casted billets, known as ‘concast’ billets, can be used instead of standard billets. In the continuous casting process, metal is used to feed the internally contracting metal in the centre of the billet. This works to reduce the occurrence of piping within the solidified billets. However, despite using the feeder metal, piping can and does still exist on occasion in concast billets. An X-ray of two concast IN713C billets can be seen in Figure 4.1. Internal piping is present, represented by the dark lines within the billets, down the centre line.

It is also known within the VIM industry that casting with piping on or close to the billet pour face is especially problematic, producing poor castings with higher incidences of defects. The ‘pour face’ is the billet face which sits in the bottom of the crucible. It is

4.1. VIM-IC AND POURING EXPERIMENTS OVERVIEW

the face from which molten metal pours during mould filling. To avoid the known issues associated with piping on the billet pour face, it is standard practice in many foundries to use a ‘solid end’ or ‘penny’ in the base of the crucible. This refers to a thin casted disc of the chosen alloy, which has no internal or external porosity. The purpose of this is to prevent the presence of piping on or in close proximity to the pour face.

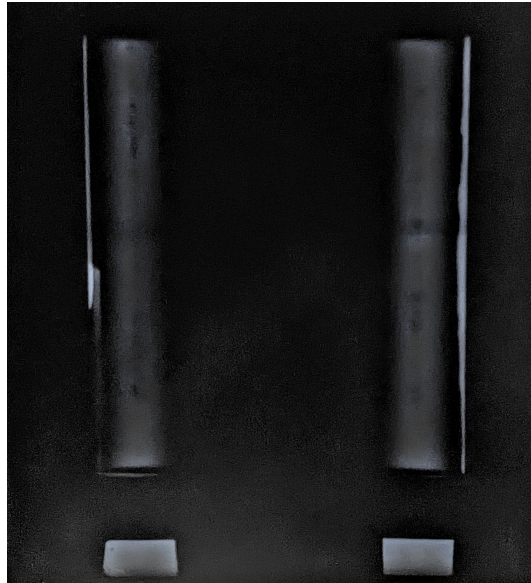


Figure 4.1: X-ray of Trials 14 and 15 from Initial Induction Melting Experiments in Section 4.3, with visible internal piping along the billet centrelines

However, the mechanism causing higher defect rates when piping is close to the pouring face is not fully understood. This is largely due to the inability to view metal flowing internally within the mould as part of the standard industry process. The purpose of these industrial experiments was to understand the effect of the existence of piping within billets, piping size and location on the pouring flow characteristics and alloy temperature during heating and melting. The temperatures of alloy during mould filling, fluid velocities at the crucible outlet and flow direction were assessed to determine the potential effects of piping on casting quality.

In this chapter, experiments are conducted to determine the effects of the presence of piping, piping size and piping location on the pouring alloy characteristics. It is important to understand how flow characteristics are affected by changes in these parameters, and also the effect that different flow characteristics have on defect occurrence in castings. Once the effect of piping size and location on unfavourable pouring behaviour is understood, the required measures to prevent this can be defined. Understanding melting and pouring

4.1. VIM-IC AND POURING EXPERIMENTS OVERVIEW

behaviour is vital for producing defect-free castings. The author would like to acknowledge Dr. Steve Leyland for supporting the industrial experiments in this chapter and the ASTUTE research group, Swansea University, for providing use of the high speed camera.

Herein, industrial induction melting experiments are conducted using a bespoke VIM chamber, with viewing ports on the top and side of the chamber to allow both temperature measurement and images of alloy during pouring to be captured. An IR thermometer is used to measure billet top face temperature during the heating and melting process. A high speed camera is positioned at the crucible exit to capture images of molten metal leaving the crucible. Conducting these experiments is not only useful to determine the isolated effects of various piping parameters on pouring behaviour, but it also serves as data for the validation of induction melting computational models.

To obtain useful images for velocity tracking of distinguishable features on the pouring alloy, initial experiments are required to determine the most effective high speed camera settings to use for capturing trackable features in molten metal. Once the optimal camera settings are determined, initial induction melting experiments are conducted to test the effect of piping formed in the billet manufacturing process. The initial experiments also test two-piece billets which are welded together.

After running these experiments, it becomes evident that naturally occurring piping is difficult to quantify. It is very difficult to determine the effect of piping location and size using naturally occurring piping, as repeatability of such tests is limited due to the naturally varying size and location of internal porosity within billets. Additionally, all billets would require X-rays to determine if piping was present, and if so, the size and location.

From this, the need for a set of experiments to reliably quantify the effect of piping size and location is identified. A Design of Experiments (DOE) L9 array of induction melting experiments is devised. The array consists of two-piece billets, all of the same total length when stacked. The billet parameters that are tested include disc height (length of the bottom piece in a two-piece billet sample), diameter of manufactured piping, and piping location relative to the pour face. The effect of varying these parameters on billet temperature in heating and melting, plus the pouring flow pattern and fluid velocities at the crucible exit is tested. This is later replicated in induction heating simulations (see Chapter 5) and compared to the effects seen in the DOE experiments.

Finally, further temperature measurement experiments testing the effect of varying billet masses, number of billet pieces, varying generator power and billet position within the coil

on heating and pouring temperatures are conducted. For these experiments, a second IR thermometer is acquired to enable both the alloy temperature during heating and pouring to be measured.

4.2 Molten Alloy Imaging Experiment

4.2.1 Molten Alloy Imaging Experiment Overview and Aims

Primitive alloy heating and pouring experiments were conducted at the Polycast site in Warsash, UK. There were two main objectives for conducting these experiments. The first objective was to determine optimal camera settings to allow identifiable features to be tracked on the free surface of the pouring alloy in high speed camera images. The second objective was to ascertain if refractory particles of a different emissivity, which were added to the molten alloy in the crucible, could be tracked using a thermal imaging camera to perform Thermographic Particle Velocimetry (TPV) of the alloy during electromagnetic stirring. The concept for this was derived from the work of Charogiannis *et al.* In their work, TPV was employed to achieve simultaneous temperature and velocity measurements. This was achieved with the introduction of particles which possessed a different emissivity to the surrounding fluid domain [81]. The experimental setup of Charogiannis *et al.* consisted of an IR camera mounted above a petri dish. The petri dish was placed on top of a heater, to allow for the flow to be heated and stirred. Implementing TPV, the interfacial temperature, Particle Image Velocimetry (PIV) and Particle Tracking Velocimetry (PTV) measurements were recorded. As described by Qureshi *et al.*, the primary difference between PIV and PTV is that ‘PIV measures average displacement of a cluster of particles in the interrogation window’, compared to PTV which tracks the motion of individual particles [82]. In their work, vortical flow was observed during stirring, showing the velocity vectors of the heated stirred flow in the petri dish.

For this experiment, nickel based alloy Inconel 657 was melted in a crucible in an open air environment. Refractory particles were added to the melt so that TPV, PIV or PTV could be attempted, as they possessed a different emissivity to the molten alloy.

Frames recorded by the thermal imaging camera and high speed camera were reviewed to determine if TPV in electromagnetic stirring and PIV in pouring via a crucible outlet could reliably be determined by using image processing software. The aims of this high speed camera settings experiment were as follows:

- Track particles of a different emissivity to alloy in electromagnetic stirring for TPV.

4.2. MOLTEN ALLOY IMAGING EXPERIMENT

- Capture images on a high speed camera of molten metal leaving a crucible with trackable features to perform PIV.
- Determine optimal high speed camera settings to capture distinguishable features on the free surface of the alloy during pouring.

4.2.2 Molten Alloy Imaging Experiment Setup

A ceramic crucible test section was held in place by a fixture on a clamp stand, which was protected from molten alloy by Kaowool fibre blanket. The crucible outlet was positioned at a height of 25 cm above the base of a vessel for catching the molten Inconel 657 alloy, as shown in Figure 4.2. Refractory particles were also used to protect the surrounding environment from molten alloy which could escape the alloy basin. A Photron FASTCAM SA4 high speed camera, which is a monochrome 12bit camera with a CMOS image sensor, was fixed to a tripod and set up at a distance of 2 m from the crucible test section, as shown in Figure 4.3. A Tokina Macro lens was fitted to the camera with a manually adjustable aperture. A handheld ThermoView Pi20 fixed thermal imager was operated by Scott Kelly of Instrumentation Systems (ISS) Ltd. The induction melting equipment comprised of a generator, induction coil and crucible for hand tilt pouring. A probe type thermocouple was used to measure the temperature of the molten alloy. This experiment was also supported by casting operators at Polycast.



Figure 4.2: Crucible test section, clamped and suspended above alloy basin



Figure 4.3: High speed camera focused on crucible test section

4.2.3 Molten Alloy Imaging Experiment Method

Inconel 657 was melted in a crucible using an induction coil and heated to 1500 °C. The temperature of the molten alloy was measured using the thermocouple. Refractory particles of 3.5 mm diameter were added to the alloy melt. The handheld thermal imaging camera was pointed at the alloy in the crucible during electromagnetic stirring. The alloy was then poured into the crucible test section, to emulate molten alloy pouring out of a crucible during standard induction melting. Images of alloy pouring out of the crucible test section were captured with the high speed camera. The pouring of alloy through the crucible section was repeated multiple times and recorded with different camera settings.

Molten metal appears very bright when captured by a camera under operational settings for standard daylight. For this reason, different settings and operating conditions were trialled to find the optimum configuration, to ensure that trackable features within the fluid stream were visible. Images obtained from the high speed camera were viewed in Photron FastView software after each pour to determine if further setting adjustments were required. The images produced for each setting configuration are shown in Table 4.2. Use of DC lighting, trials with and without filters, changing shutter speed and adjusting aperture were tested with multiple metal pouring attempts, until the optimal camera settings were found. Ivan Zadrazil of Dantec Dynamics, a company which develops measurement systems for fluid mechanics research and spray analysis, supported this experiment by advising on high speed camera parameters. Dr. Zadrazil was also a coauthor of the aforementioned work by Charogiannis *et al.*

Parameter	Value
Camera resolution (pix)	1042
Imaging window (mm)	300
Pixel resolution (mm/pix)	0.288
Interrogation window	32
Max. feature displacement length (mm)	2.30
Max. velocity (m/s)	4.00
TR requirement (Hz)	1737
Frequency used (Hz)	1896
Pixels travelled	7.33
Number of images	142.2

Table 4.1: Frame rate calculations

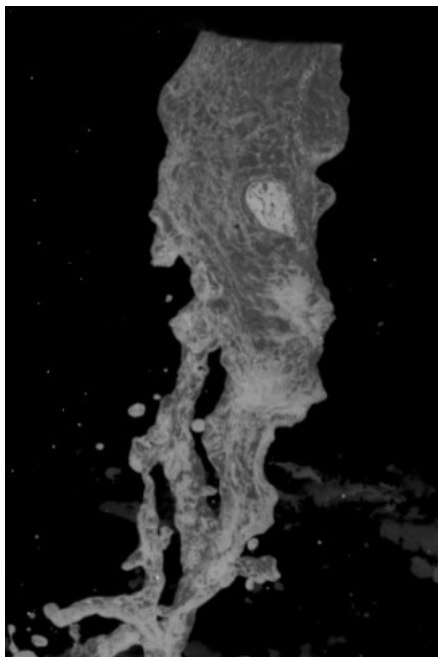
To successfully determine velocity profiles using image processing methods, the movement

4.2. MOLTEN ALLOY IMAGING EXPERIMENT

of trackable nonhomogenous features on the air-fluid surface interface of the molten metal must not be too great between frames. It was advised by Dr. Zadrazil that for fidelity of velocity measurement results using PIV, the distinguishable features should move no more than 8 pixels between any two consecutive frames of the images captured by the high speed camera. To ensure that 8 pixels per frame was not exceeded, the parameters in Table 4.1 were calculated. It was determined that a frame rate of 3000 frames per second (FPS) was required to achieve this. The camera was set to a resolution of 512 x 1024 pixels in order to capture the long, thin imaging window required for molten metal flow between the crucible outlet and alloy basin below.

4.2.4 Molten Alloy Imaging Experiment Results

It was evident upon reviewing the thermal imaging data of the alloy during electromagnetic stirring, that these refractory particles could not be seen. Refractory particles of 1 mm diameter and a different emissivity were also trialled and could not be seen. Additionally, from reviewing the high speed camera images of the molten alloy in pouring, both 3.5 mm and 1 mm diameter particles could also not be seen or identified. In their work on high speed imaging of flow during close-coupled gas atomisation, Mullis *et al.* used the PIV technique to gain valuable information regarding particle flow field [83]. They achieved this without the introduction of seed particles, relying on the capability of INSIGHT 3G software to detect individual particles created by the break-up of the melt stream during atomisation.



In this work, PIV software will be implemented to track non-homogenous features on the alloy surface, which are identifiable with the use of optimal camera settings. Optimal high speed camera settings for the lighting conditions at Polycast were as follows:

- Shutter speed: 1/40,000
- Frame rate: 3000 fps
- Resolution: 512 x 1024
- Aperture: f1/32, setting 'A'

No filters were used in the optimal images recorded. Ultimately, it was evident that adjusting shutter speed and aperture prevented the images from

Figure 4.4: Optimal image

4.2. *MOLTEN ALLOY IMAGING EXPERIMENT*

‘whiting out’, and images were captured with the required definition and quality. The addition of DC lighting was also trialled with the intention of improving image quality. However, it was not required to produce the optimal camera images. The iterative process of finding the optimal camera settings can be seen in Table 4.2. In gravity pouring, turbulent flow and velocity fields are produced as part of the surface-turbulence condition [84]. Figure 4.4 shows the turbulent flow produced during manual pouring of molten nickel alloy through the crucible test section. The rapidly changing shapes of the darker features during pouring of the alloy rendered the images captured in this experiment unsuitable for use with image tracking software to determine velocity profiles. Further experiments were conducted using an induction coil and a billet-loaded crucible to determine if features could be more reliably tracked in less turbulent alloy pouring.

4.2. MOLTEN ALLOY IMAGING EXPERIMENT

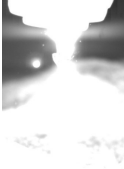
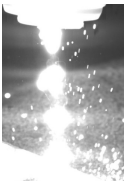


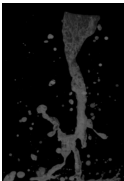
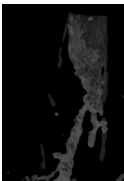
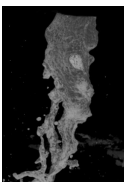
Captured Image	Settings
	<ul style="list-style-type: none"> • DC lighting used • Shutter speed: 1 frame/sec <p>Molten metal was very bright.</p>
	<ul style="list-style-type: none"> • No DC lighting used • Dark filter used • Shutter speed: 1 frame/sec <p>Molten metal was still very bright, saturating the camera images.</p>
	<ul style="list-style-type: none"> • 2 dark filters used • Shutter speed: 1 frame/sec <p>Molten metal flow more defined, however still very bright.</p>
	<ul style="list-style-type: none"> • Weld filter used • Shutter speed: 1 frame/sec <p>Weld filter did not allow any light through.</p>
	<ul style="list-style-type: none"> • f1/32 aperture • Shutter speed: 1/56000 sec <p>No filter used. Aperture and shutter speed adjusted.</p>
	<ul style="list-style-type: none"> • f1/32 aperture • Shutter speed: 1/50000 sec <p>No filter used. Shutter speed adjusted to brighten image.</p>
	<ul style="list-style-type: none"> • f1/32 aperture • Shutter speed: 1/40000 sec • Sand particles introduced <p>No filter used. Shutter speed was adjusted as images from Trial 6 were still dark, but fluid flow features were clearer.</p>

Table 4.2: Determining Optimal Camera Settings

4.3 Initial Induction Melting Experiments

4.3.1 Induction Melting Experiment Overview and Aims

Induction melting is a widely implemented casting method in the casting industry. The process involves placing a metal billet inside an induction coil, and inducing an alternating current (AC) which causes the billet to melt. Although in many cases alloy is manually tilt poured into an investment casting mould, the induction melting process with direct pouring by gravity into a mould attached below the crucible is also a common practice in the investment casting industry. The temperature and behaviour of fluid flow within a casting mould can be responsible for a large range of defects, including misruns and mould erosion. Therefore, to eliminate flow related defects in casting, it is beneficial to understand how the mould fills in terms of alloy temperature, velocity and flow direction.

There are many variables that can be adjusted in an industrial induction melting setup. Generator settings such as power, frequency and voltage can be adjusted. Billet location within the coil can also be altered by adjusting chamber tray height. However, this initial set of induction melting experiments sought to understand how variations in the alloy condition could affect the melting pattern of the alloy, both in heating and the resultant mould filling flow behaviour in alloy pouring. The tested alloy condition variations include the number of alloy pieces in the crucible, the presence of welds between billet pieces as shown in Figure 4.5, and the existence or lack of internal and external piping in billets. Figure 4.6 shows a defect free billet face compared to one with visible external piping.



Figure 4.5: Close up photograph of a welded joint between two billet halves



Figure 4.6: Billet faces without external piping (left) and with visible piping (right)

The experiments were held at EFD Induction in Wolverhampton, UK. These experiments were further supported by Thomas Sellers from alloy supplier Ross and Catherall, who

4.3. INITIAL INDUCTION MELTING EXPERIMENTS

provided both the billets and the X-ray in Figure 4.1. It was also supported by Scott Kelly of ISS Ltd who operated the thermal imaging camera, and staff at EFD Induction.

The aims of these initial induction melting experiments were as follows:

- Capture images of molten metal with distinguishable features leaving the crucible once melted fully by induction, which are suitable for tracking velocity analysis.
- Analyse velocity profiles using image processing software.
- Obtain top billet face temperature readings using thermal imaging analysis software.
- Determine the impact of melting one-piece billets vs. two-piece billets, welds, internal and external billet piping on flow patterns and measured temperatures.

4.3.2 Induction Melting Experiment Setup

An induction coil was connected to a standard industrial EFD power generator for induction melting. A ceramic crucible was positioned inside the induction coil, held in place by a clamp stand. A 50 mm diameter billet of nickel alloy IN713C was inserted into the crucible. A ThermoView Pi20 Fixed Thermal Imager camera fixed to a tripod was positioned to ensure viewing of the top billet face during induction heating and melting. A Photron FASTCAM SA4 high speed camera was focused on the crucible outlet, as shown in Figure 4.7. A basin for catching molten alloy pouring out of the bottom of the crucible was positioned below the coil-crucible setup. The clamp stand, alloy basin and tripod affixed to the thermal imaging camera were all contained within a raised metal tray filled with refractory material to prevent any potential damages by alloy spillage.

The total height of the induction coil was 200 mm, with an outer diameter width of 120 mm and inner diameter width of 110 mm. The coil consisted of 13 turns, with a coil diameter of 10 mm. The coil was cooled by inner water channels. There was a vertical distance of 20 mm between the bottom of the induction coil and the crucible outlet. From this coil positioning, the top section of the billet melts by the electromagnetic field generated by the induction coil, leaving the bottom portion of the billet length which sits outside of the coil, to melt at the end by conduction from the molten metal above. Figure 4.8 shows the IN713C billet, induction coil, clamp stand and alloy basin setup. Both the high speed camera and thermal imaging camera were fitted to tripods with attached spirit levels, to ensure that the equipment was level. A spirit level was also used to determine flatness of the billet and crucible on the clamp stand.

4.3. INITIAL INDUCTION MELTING EXPERIMENTS

Three types of test billets were used in this experiment: 2.9 kg billets, 2.9 kg welded two-piece billets, and 3.295 kg billets. The term ‘two-piece’ refers to two pieces stacked on top of each other in the crucible, compared to one billet piece. In this experiment, the two-piece billets comprised of two equal length pieces welded together.

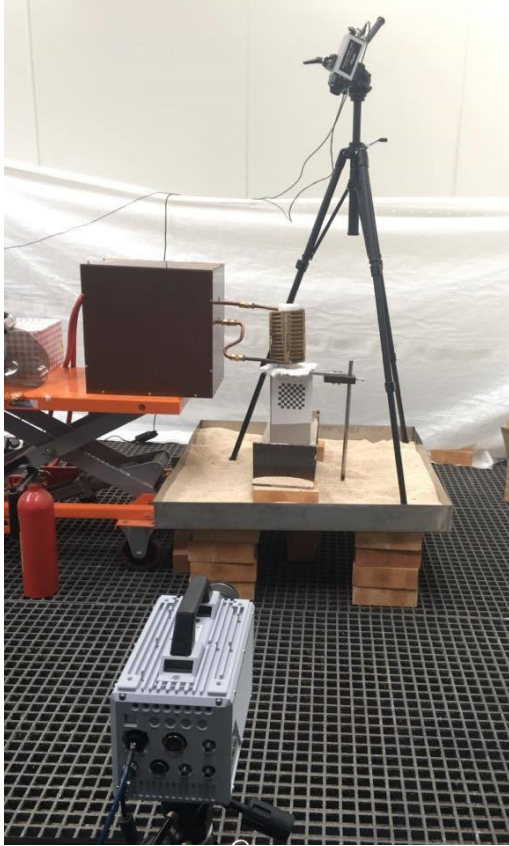


Figure 4.7: Experimental setup with IR and high speed camera on tripods



Figure 4.8: IN713C billet loaded into ceramic crucible in the induction coil

A total number of 15 melts were conducted, comprising of six 2.9 kg ‘concast’ (continuous casted) billets with no piping (Trials 1 - 6), three welded two-piece 2.9 kg billets with no piping (Trials 7 - 9), four 2.9 kg billets with varying levels of piping (Trials 10 - 13), and two billets of 3.295 kg with internal piping (Trials 14 and 15). The crucible was suspended above the vessel for catching molten metal, with a known reference length of 32.5 mm for the exit diameter of the crucible. Images showing varying levels of external visible piping on the billet faces of Trials 10 - 13 billet are shown in Figures 4.9 - 4.12. An X-ray showing the internal piping for Trials 14 and 15 is shown in Figure 4.1.

4.3. INITIAL INDUCTION MELTING EXPERIMENTS



Figure 4.9: Trial 10 piping on billet face



Figure 4.10: Trial 11 piping on billet face



Figure 4.11: Trial 12 piping on billet face



Figure 4.12: Trial 13 piping on billet face

4.3.3 Induction Melting Experiment Method

The equipment was set up as described and pictured in Section 4.3.2. The sample IN713C nickel alloy billet was inserted into the ceramic fibre crucible. A spirit level was used to ensure correct, flat positioning of the billet. Generator values for power and frequency were kept within a small range throughout the 15 trials. Power was kept within a range of 78-80 kW, frequency of 7.69-7.93 kHz, voltage at 599-602 V and a current between 219-230 A. Once set, the generator power was held at this level until the billet had melted, undergone electromagnetic stirring and poured into the basin below. Captured images from the high speed camera and videos from the fixed thermal imager were saved onto the computer, ready for image processing and analysis. Clean up was carried out after each trial, with new sheets of fibre insulation applied to the base of the thermal imager clamp stand and a new crucible for each trial. The process was repeated for each of the samples listed in Table 4.3, in Section 4.3.4.

4.3.4 Induction Melting Experiment Results

Table 4.3 provides an overview of the alloy conditions tested and total time taken to melt, maximum recorded temperature on the billet top face and pouring flow behaviour. In the ‘Billet Type’ column, ‘SC’ stands for solid concast, which means a continuous casted billet without internal or external piping. ‘TW’ stands for two-piece welded. Flow behaviour observations are listed in the ‘Flow’ column, where ‘CE’ is Camera Error, ‘L’ is laminar flow, ‘A’ is angled flow, ‘SA’ is split angled flow, and ‘T’ is turbulent flow. Unfortunately, high speed camera errors were frequent due to overheating of the high speed camera, which was causing it to switch off or capture only partial footage of the alloy pouring.

Trial	Billet Type	Mass (kg)	Melt Time (s)	Max. Temp (°C)	Flow
1	SC	2.9	96.00	2099.9	CE
2	SC	2.9	82.91	2099.9	L
3	SC	2.9	78.48	1672.7	L
4	SC	2.9	77.81	1753.4	L
5	SC	2.9	78.60	1608.0	CE
6	SC	2.9	77.41	1678.7	L
7	TW	2.9	67.60	1444.4	A
8	TW	2.9	75.98	1615.9	L
9	TW	2.9	77.37	1622.3	L
10	TW, small pipe	2.9	74.00	1511.6	CE
11	TW, normal pipe	2.9	72.98	1482.9	L
12	TW, medium-large pipe	2.9	75.05	1546.5	L
13	TW, largest pipe	2.9	74.78	1481.3	SA
14	Internal Piping	3.295	74.7	1419.9	T
15	Internal Piping	3.295	81.64	1567.3	L

Table 4.3: Induction melting trials overview

Total time taken to melt is the time elapsed from switching on the power generator to end of pour. This recorded time in seconds was taken manually using a stopwatch. Taking an average of the total time to pour for each billet type resulted in a time of 79.04 seconds for solid concast billets, 73.70 seconds for two-piece welded billets, 74.20 seconds for two-piece welded billets with varying levels of pipe, and 78.155 seconds for 3.295 kg billets with internal piping. The average maximum recorded top billet face temperature for solid concast billets was 1763 °C, with an average of 1561 °C for two-piece welded billets and

4.3. INITIAL INDUCTION MELTING EXPERIMENTS

1506 °C for two-piece welded billets with varying levels of pipe. Finally, the average maximum recorded temperature for 3.295 kg billets with internal piping was 1493.6 °C. Average values for total time to melt and maximum recorded top billet face temperature for solid concast billets did not take into account Trial 1, as the total melt time for this sample was significantly longer than the others, which made it an outlier.

4.3.5 Fixed Thermal Imager Results

Footage of the billet top face during heating and melting was captured on the IR camera, ready for analysis using Raytek DTPi software. The software relies on a fixed emissivity value to determine temperature measurements of the metal billet using thermal imaging. For IN713C, the emissivity value entered in the software was 0.85, as obtained in Section 2.3.2. The IR camera was positioned above the crucible, providing a top plane view of the induction heating, melting and electromagnetic stirring process. IR recordings were captured for all trials. Frames have been selected from Trials 1, 7 and 13, in Figures 4.13 - 4.15, to visually demonstrate the heating, melting and stirring process.

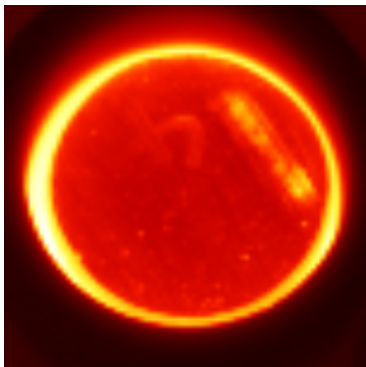


Figure 4.13: IR image of nickel billet heated to temperature

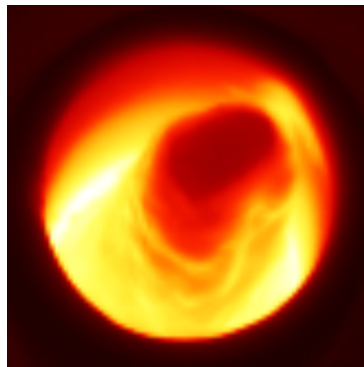


Figure 4.14: IR image of molten metal during electromagnetic stirring

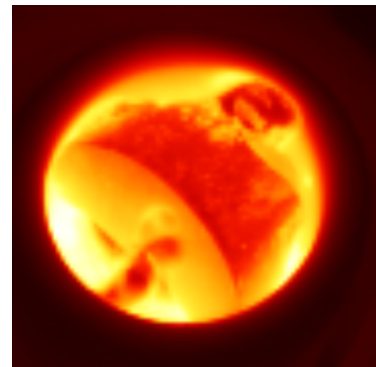


Figure 4.15: IR image of welded alloy melt behaviour, billet top piece turning

Figure 4.13 from Trial 7 shows the billet being heated, with the outer edges of the billet melted to a temperature of 1580 °C within the skin depth. Figure 4.14 shows the top part of the billet undergoing electromagnetic stirring caused by the induced electromagnetic field, driven by an AC. The stirring generates turbulent flow, which can be observed in this image. Figure 4.15 shows the behaviour of the welded alloy billets. The remaining solid piece of the top billet face becomes detached from the top portion of the billet due to the internal melting pattern, and in this image it can be seen turning over. Further effects on the flow patterns of welded billets on the flow leaving the crucible are visible

4.3. INITIAL INDUCTION MELTING EXPERIMENTS

from the high speed camera images.

The AOI tool in Figure 4.16 shows that the maximum temperature on the top billet face for that specified frame is 1537.9 °C. Minimum and average temperatures are subject to other influences that are likely to impact the results. This is due to the AOI capturing parts of the crucible material which will not only be a lower temperature, but also possess a different surface emissivity. Maximum temperature was recorded for the melt on the top plane, from above the crucible. Results were recorded for the temperature of the melt 10 s, 5 s, 1 s before melt drop, and 0 s at the point of melt release. The recorded temperatures can be found in Figure 4.17. The melt was released into the basin below once the last part of the billet was melted by conduction, as it was below the coil.

Maximum recorded top billet face temperatures were obtained by using the ‘Area of Interest’ (AOI) tool in the Raytek DTPi software. Readings were taken from the defined AOI, which was set as a circle defined on the inside of the crucible from the top plane view. Table 4.3 shows the table of maximum alloy temperatures within the AOI for solid billets, and those with internal piping. Figure 4.16 shows the software analysis window with footage of alloy undergoing electromagnetic stirring for Trial 5.

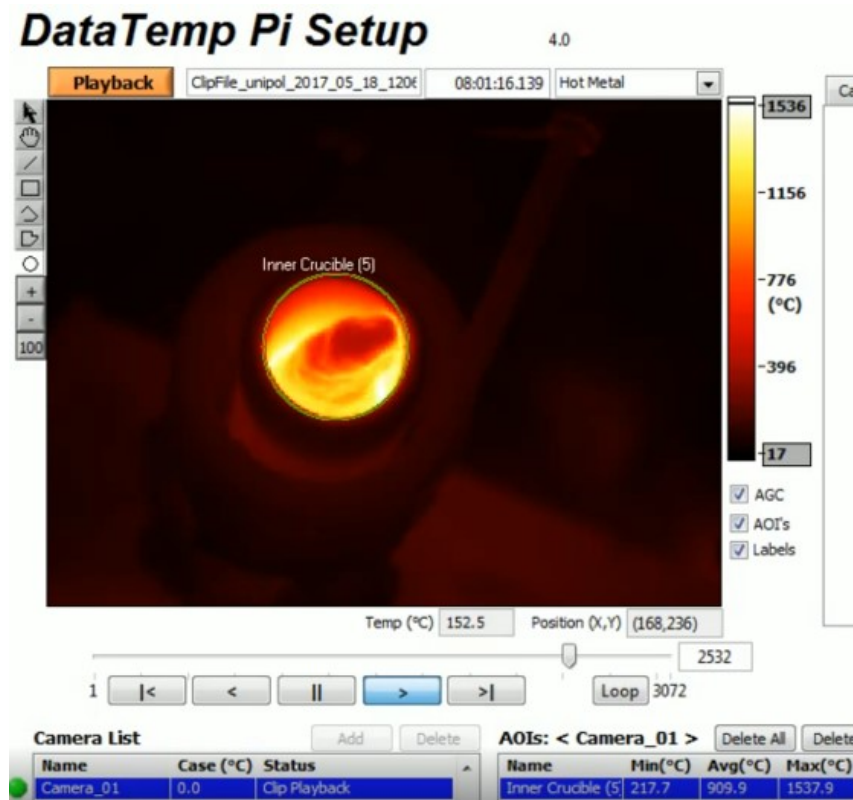


Figure 4.16: Example window of DTPi software for top plane temperature analysis of Trial 5

4.3. INITIAL INDUCTION MELTING EXPERIMENTS

Trial	Description	Frame no.	t before pour (s)	Temperature (degC)		
				Min	Avg	Max
1	Solid billet - 2.9 kg	2243	10	392.2	1378.4	2099.9
		2409	5	401	1474.2	2099.9
		2543	1	393.4	1473	2099.9
		2575	0	408.5	1727	2099.9
2	Solid billet - 2.9 kg	2055	10	379.7	1264	2073.1
		2221	5	406	1341.4	2059.4
		2354	1	460.4	1407.2	2080.7
		2387	0	316	1737.1	2099.9
3	Solid billet	2282	10	212.4	999.4	1607.4
		2447	5	226.6	1030.4	1658.4
		2581	1	258.6	1070.2	1681.1
		2614	0	271.1	1408.3	1842
4	Solid billet	2226	10	240.2	999.7	1692.9
		2393	5	247.2	1039.5	1744.2
		2526	1	252.8	1094.1	1771.2
		2559	0	299.5	1352.3	1881.3
5	Solid billet	2299	10	281.8	918.2	1443.2
		2464	5	305.5	965.9	1480.2
		2598	1	299.9	986.1	1567.3
		2631	0	402.2	1270.2	1676.6
6	Solid billet	2230	10	238.3	940.4	1525
		2397	5	281.8	1004	1560.4
		2530	1	322.8	1036.3	1557.2
		2563	0	411.5	1308.4	1686.1
7	Two-piece welded - 2.9 kg	1882	10	219.8	609.8	1203.8
		2084	5	288.7	868.6	1393.2
		2182	1	295.2	912.7	1393.7
		2215	0	300.8	939.9	1419.9
8	Two-piece welded - 2.9 kg	2189	10	354.7	982.6	1580.9
		2350	5	395.3	1026.7	1618.6
		2485	1	436.6	1076.6	1647.8
		2518	0	408.4	1322.1	1714.2
9	Two-piece welded - 2.9 kg	2219	10	397.6	965.7	1511.6
		2385	5	405.3	984.4	1511.6
		2518	1	430.7	1057.2	1595.8
		2550	0	449.2	1065.4	1619.6
10	Two-piece welded, small pipe - 2.9 kg	2160	10	353.9	908.8	1416.7
		2391	5	395.3	956.7	1443.2
		2457	1	405.3	1022	1515.8
		2490	0	413.1	1015.3	1476.4
11	Two-piece welded, normal pipe - 2.9 kg	2057	10	231.1	889.6	1406.2
		2223	5	274	899.8	1384.9
		2357	1	356.4	936.7	1453.5
		2390	0	385	957.3	1457.4
12	Two-piece welded, slightly larger pipe - 2.9 kg	2186	10	393.7	934.9	1453
		2351	5	404.6	946.2	1515.3
		2484	1	416	1016.9	1513.6
		2517	0	387.3	1255	1706.3
13	Two-piece welded, largest pipe - 2.9 kg	2154	10	385.8	943.8	1420.4
		2320	5	401.5	969.3	1442.7
		2454	1	407.6	1011.9	1492.1
		2487	0	455.4	1155.7	1588.3
14	Internal piping	2139	10	288.7	533.4	1137.3
		2303	5	341.1	818.5	1341.5
		2436	1	416.8	898.5	1448.1
		2469	0	389.7	1069.8	1458.4
15	Internal piping	2384	10	322.8	895.5	1465
		2549	5	353	962.2	1518
		2681	1	392.2	1029.3	1543.3
		2714	0	368.8	1300.7	1689.8

Figure 4.17: Table in Excel showing maximum alloy temperature from crucible top plane during electromagnetic stirring for solid billets

4.3. INITIAL INDUCTION MELTING EXPERIMENTS

Reviewing the thermal imaging data, it was evident that apart from two-piece welded billets and those of a higher mass reaching lower maximum recorded temperatures on the top billet face, the top face temperature measurement data at 10 s, 5 s, 1 s before melt drop did not show reliable trends for the different billet types. The results indicated that temperature readings were highly varied during the melting and pouring process.

There were multiple factors in this experiment which could cause this variability. Firstly, although the solid concast billets with no internal piping should be relatively consistent sample wise, this would not have been the case for the welded samples or those with piping. Welded billets had varying gap sizes, despite attempts to make this consistent between samples. Furthermore, defining the levels of piping occurring within the two-piece welded billets and those with internal piping was subjective. When testing naturally occurring variation from the manufacturing process, it was difficult to find identical samples with the same level of piping and positioning of piping to repeat the tests. Secondly, the use of the fixed thermal imager was an effective way to determine the melting behaviour of the billet from the top face plane. However, as this thermal imager works based on a fixed surface emissivity, this would not yield as accurate results as those which could be obtained from a 2-Colour IR thermometer which works on a slope value basis. IR thermometers with 2-Colour capability are able to account for the changing surface emissivity of a metal sample over a large temperature range as it changes from a solid state at room temperature to liquidus temperature and beyond.

From these initial induction melting experiments, it was evident that a more accurate thermal measurement was needed across the entire heating and melting range. In addition, a more controlled method of introducing defects into the billets which were the equivalent of piping defects was needed. Consequently, it was decided that further trials were required, and this is the subject of Section 4.4.

4.3.6 High Speed Camera Results

Due to the high levels of natural variation between the different alloy sample types, high speed camera images from these initial induction melting trials were evaluated for qualitative differences in pouring flow patterns, instead of conducting quantitative velocity analysis. It was clear that a more repeatable, controlled way of testing the effect of piping size and location was required in further trials to determine its true effect on pouring velocities and flow behaviour. Images from these initial induction melting experiments were also used to determine if distinguishable features could be tracked on the surface of

4.3. INITIAL INDUCTION MELTING EXPERIMENTS

the alloy flow pouring out of the crucible during induction melting, to produce measurable velocity profiles.

Use of the camera settings obtained from the primitive camera settings trials in Section 4.2 allowed for the last 3.638 seconds of each recording to be saved due to the limitations of the internal camera memory. As the pour time duration for the given induction melting equipment setup was found to be less than three seconds, this allowed for the total pour to be captured. The high speed camera was configured to produce monochrome images at 1024 x 512 resolution, with captured frames exported as TIFF files for image processing analysis. Figure 4.18 from Trial 6 shows the melt flow for a standard concast solid billet with a mass of 2.9 kg.

For one piece solid concast billets, pouring tended to be straight down with a laminar flow. In contrast, the effect on pouring behaviour of a two-piece welded billet with a large gap between billet pieces is shown in Figure 4.19, as the flow direction diverts off from the centre line, resulting in highly angled flow in Trial 7.



Figure 4.18: Trial 6 - Solid concast billet pour

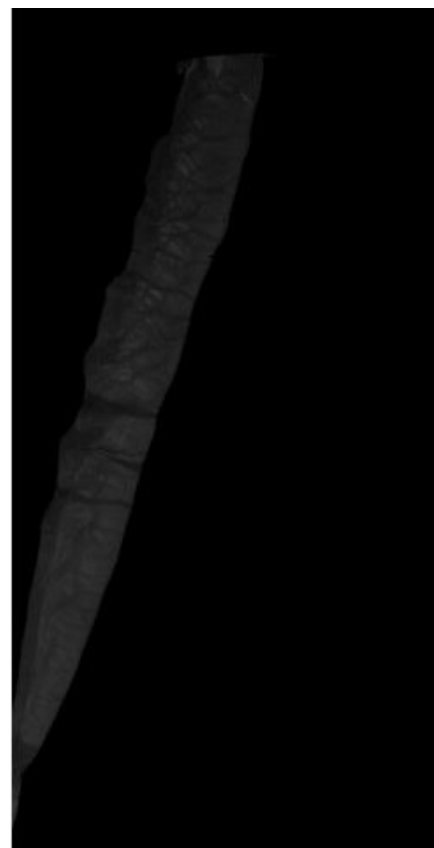


Figure 4.19: Trial 7 - Two-piece billet pour, poorly welded



Figure 4.20: Trial 13 - Two-piece welded billet, hole on pour face



Figure 4.21: Trial 14 - 3.295 kg billet with internal piping

Figure 4.20 shows the effect of a hole at the pouring face on the melt pattern of a two-piece welded billet. The flow splits into two separate streams, both of which are angled in opposing directions. Trials 14 and 15 involved billets with a larger mass of 3.295 kg, each with internal piping. Figure 4.21 shows Trial 14 during pour. The flow is much more turbulent compared to the laminar streams seen in the 2.9 kg solid concast one piece billets. It is not possible to determine from the parameters tested in this experiment if this more turbulent flow was due to the increased mass, presence of internal piping within a one piece billet, or a combination of both factors.

4.3.7 Velocity Measurements

Images showing qualitative characteristics of flow behaviour, maximum recorded top face temperature and total melt times were obtained from this initial induction melting experiment. Although it was understood that the direct effects of piping, welds, billet mass and number of pieces could not reliably be assessed from these experiments, a selection of the obtained high speed camera images were analysed to determine if flow velocities could

4.3. INITIAL INDUCTION MELTING EXPERIMENTS

be obtained. There are three methods that are commonly used to determine the velocity profile of fluids: Particle Image Velocimetry (PIV), Laser Doppler Velocimetry (LDV) and Hot Wire Anemometry. Commercial software for determining velocity profiles within fluids for industrial applications exists and is used for a wide range of applications across many different industries. Initially, plug-ins for open source software Fiji (previously known as Image-J), were trialled in an attempt to track and analyse the movement of the nonhomogenous features in the flow.

Different plug-ins were tested for their suitability and accuracy of measuring velocities of the molten metal leaving the crucible, including Manual Tracking and ‘WrmTrck’, designed to track the movement of worms. WrmTrck was tested due to the similarity of the dark bands present on the surface of the molten metal, to the worms that it was designed to track. The dark bands on the surface of the pouring metal can be seen in Figure 4.18. However, this plug-in was not successful in tracking the band movement.

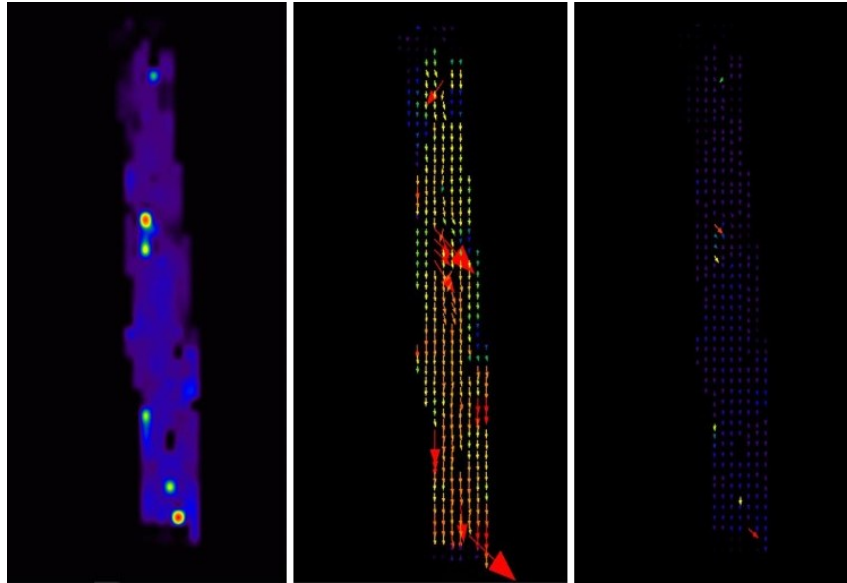


Figure 4.22: Magnitude, PIV and Vector Plots generated using PIV Fiji plug-in

Finally, a PIV plug-in was trialled, which was able to detect the movement of the dark bands. This plug-in performed PIV using an iterative scheme. Each iteration calculated the displacement using a normalised correlation coefficient algorithm, which compared an individual interrogation window with a larger searching window [85]. For the tested images, the maximum recorded rate was 3 pixels/frame. Flow velocity magnitude, PIV and vector plots generated using the PIV Fiji plug-in are shown in Figure 4.22. After reviewing the PIV plots, it was evident that the maximum shifts were exaggerated. The

4.3. INITIAL INDUCTION MELTING EXPERIMENTS

algorithm was not optimised for the specific setup, and a more suitable method for the application was required.

The PIV program was further developed to include coloured velocity vectors to give a visual representation of the shift per frame in the generated PIV plots, where the red end of the colour spectrum represents higher velocities and the dark blue end represents lower velocities. These coloured velocity vectors can be observed in Figure 4.26. The variation of the velocity vector colours over the length of the pouring alloy shows that the alloy accelerates due to gravity further down the image.

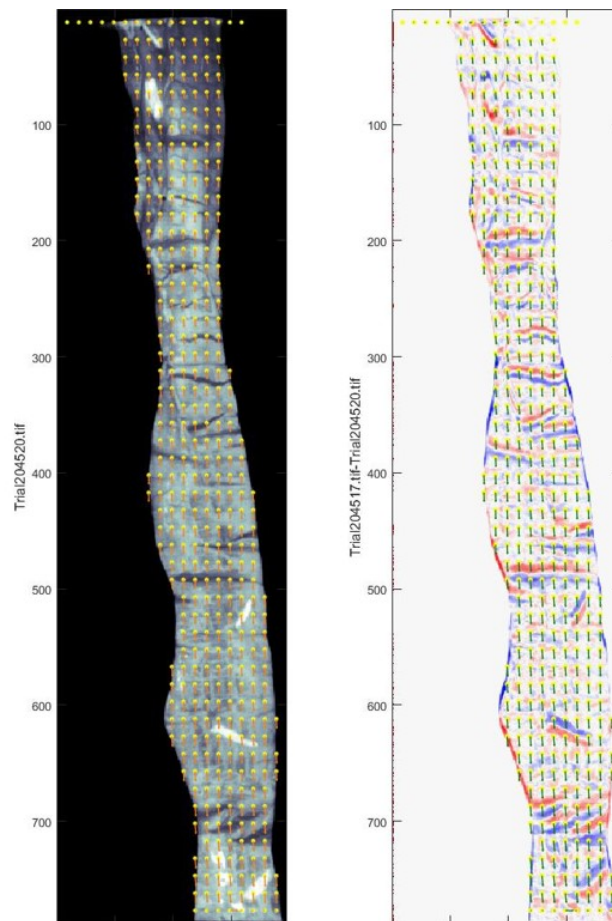


Figure 4.23: MATLAB PIV Plots

By collaborating with Dr. Igor Sazonov at Swansea University who had written an existing PIV program using MATLAB, it was possible to optimise the pre-existing code for this specific application. Initial plots were as shown in Figure 4.23. On the left is the first figure generated by the code, which shows the image of the final analysed frame of the molten metal, upon which a grid of yellow dots is assigned to the flow region of the image.

4.3. INITIAL INDUCTION MELTING EXPERIMENTS

The dark background is assigned as a masked region, upon which the yellow dots are not generated. On the right is the second figure generated when running the program. It comprises of two images are plotted on top of one another, separated by the number of frames which is dictated to the program via inputs upon running the code. In this case, the number of frames between the two images is $n = 3$. The dark bands functioned as non homogeneous features used for tracking.

These dark non homogeneous features are shown in red for their locations in the first frame, and then plotted as blue for their location in the last frame. The plotting of the initial and final locations of these features on the one image allows for examination of the shift between the two frames. Light non homogeneous features are initially plotted as blue, then red after the shift. For each yellow dot generated, velocity values in pixels per frame from the movement of the non homogeneous features were recorded and plotted on a graph. Figure 4.24 is an example of a graph plotted for shift between frames, in pixels per frame, across the grid at each dot location. The graph shows the x and y shift in pixels per frame. The graph indicates that the magnitude of the shift in the x direction were significantly smaller than in the direction of gravity, y direction. This is to be expected, as the flow is not at a large angle relative to the vertical centreline.

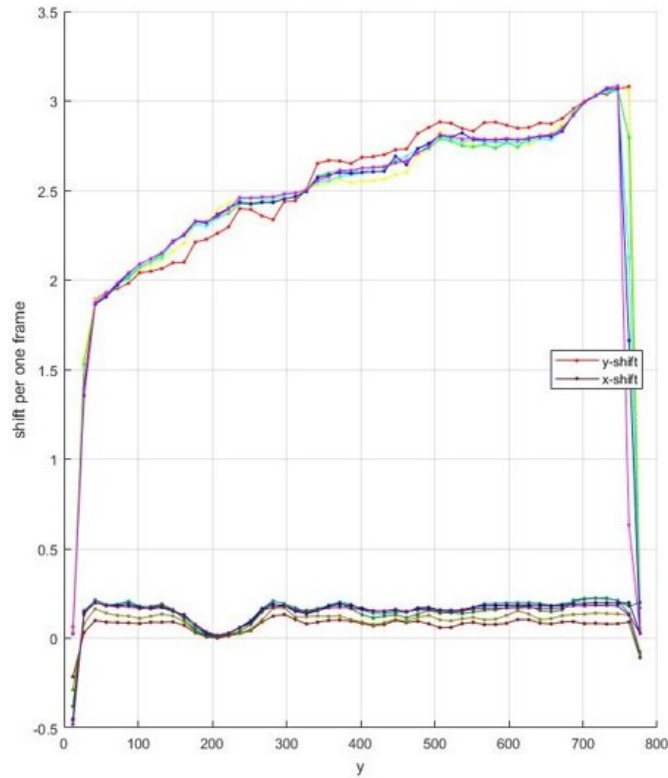


Figure 4.24: MATLAB PIV Graph Plots, x and y shift in pixels per frame

4.3. INITIAL INDUCTION MELTING EXPERIMENTS

Calculated values of the shift in pixels per frame depends on many parameters, including the number of steps between frames. Conducting a study on the accuracy of this shift calculation, the optimal n value for the most accurate calculation of shift between frames for this initial version of the code was $n = 3$. For a visual representation of velocities at the crucible outlet, which would also serve as the mould inlet in a standard VIM investment casting setup, a code was written using results files containing the y frame shift across the exit of the crucible.

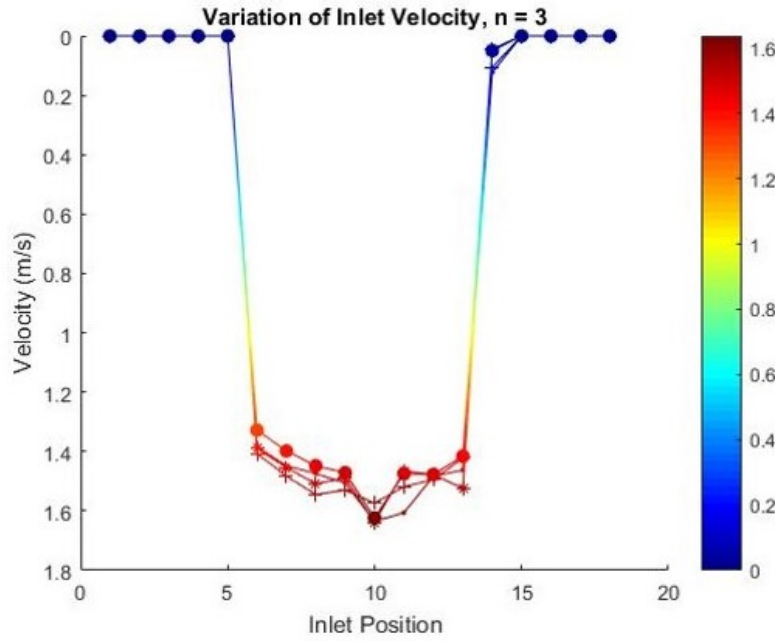


Figure 4.25: Inlet velocities, y direction for Trial 2

The y shift in pixels per frame was converted into velocities in m/s , and this graphical representation of y velocities at the mould inlet is shown in Figure 4.25. The second row of dots was taken as the equivalent of the mould inlet, due to the issues with programming an edge condition to account for the defined geometry of the crucible outlet.

File No.	Frame Step	Scale (pixels/m)	Row 2 v_y (m/s)	Row 2 Average v_y (m/s)
1	3	3418.8479	0 0 0 0 0 1.41 1.48 1.54 1.53 1.57 1.52 1.49 1.42 0.11 0 0 0 0 0	1.3419
2	3	3418.8479	0 0 0 0 0 1.33 1.40 1.45 1.47 1.62 1.47 1.48 1.42 0.05 0 0 0 0 0	1.2984
3	3	3418.8479	0 0 0 0 0 1.39 1.45 1.51 1.49 1.64 1.47 1.48 1.52 0.04 0 0 0 0 0	1.3322
4	3	3418.8479	0 0 0 0 0 1.38 1.45 1.47 1.51 1.64 1.61 1.48 1.46 0.12 0 0 0 0 0	1.3468

Table 4.4: Table showing conversion of pixels per frame to metres per second

Table 4.4 demonstrates how velocities in m/s were calculated for Trial 2 from the conducted experiments. Zero values present in Table 4.4, and subsequently the graph shown in

4.3. INITIAL INDUCTION MELTING EXPERIMENTS

Figure 4.25, are representative of the masked black background with no moving features. Table 4.5 is a summarised version of the full table in Appendix A, which demonstrates the dependency of frame step size (n) on the calculated velocity in the y direction, $v_y(\text{m/s})$. For this data set from Trial 2, the frames were recorded at 3000 fps, which results in a time step of 0.000333 seconds per frame. The scale of the images was 3272.7 pixels/m, which was used in conjunction with the time step value to convert the shift in pixels per frame to metres per second.

File No.s in Sequence	n	Average Row 2 $v_y(\text{m/s})$
1-2	1	1.248
2-3	1	1.234
3-4	1	1.186
4-5	1	1.190
5-6	1	1.225
6-7	1	1.209
1-3	2	1.374
2-4	2	1.339
3-5	2	1.228
4-6	2	1.309
5-7	2	1.253
1-4	3	1.342
2-5	3	1.298
3-6	3	1.332
4-7	3	1.347
1-5	4	1.224
2-6	4	1.181
3-7	4	1.189
1-6	5	1.189
2-7	5	1.187
1-7	6	1.225

Table 4.5: Testing the effect of frame step number on computed velocities

The PIV program was further developed to include coloured velocity vectors to give a visual representation of the shift per frame in the generated PIV plots, where the red end of the colour spectrum represents higher velocities and the dark blue end represents lower velocities. These coloured velocity vectors can be observed in Figure 4.26. The variation of the velocity vector colours over the length of the pouring alloy shows that the alloy

accelerates due to gravity further down the image.

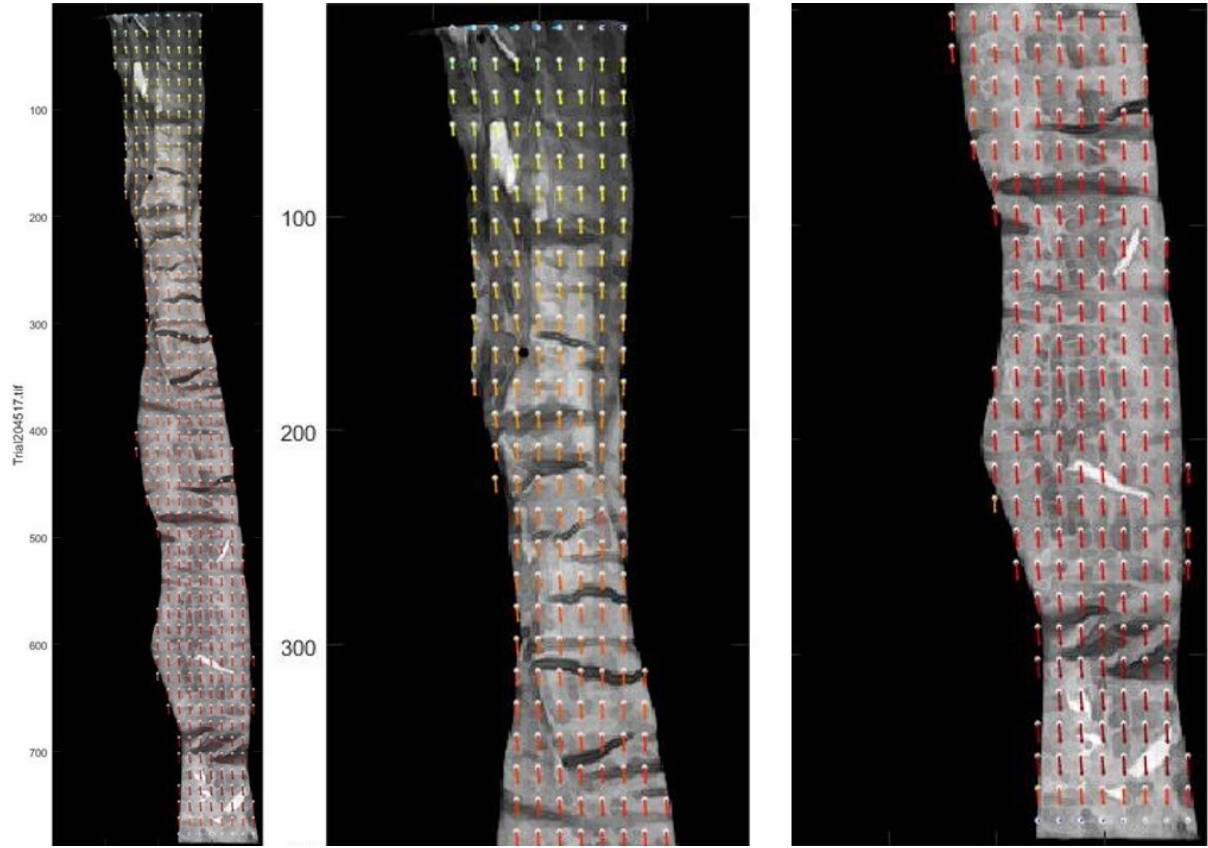


Figure 4.26: Left to right: full image of PIV plot with velocity vectors, top half of pouring alloy image, bottom half of pouring alloy image

4.4 VIM-IC Design of Experiments: L9 Array

4.4.1 Design Of Experiments: L9 Array Overview and Aims

As outlined in Section 1.1, the VIM process at Uni-Pol Group involves melting a nickel alloy billet with direct pouring of the molten alloy into an investment casting mould. The bottom section of the billet melts by conduction due to its position within the coil. As previously identified from reviewing the results of previous experiments, a more precise and repeatable way of testing parameters related to alloy condition was required. It was also important to isolate the effects of different alloy parameters. The need for a Design of Experiments (DOE) created based on an L9 array was recognised. This allowed the results to be analysed using the ANOVA method. This set of experiments using an L9 array to determine the effect of alloy condition parameters on melt pattern was conducted

at Uni-Pol Mexico in Mexicali, Mexico. The samples were cut to length by Ross and Catherall in the UK, and holes were created at the workshop in Swansea University. The alloy was transported to the Uni-Pol Mexico site. A bespoke vacuum melting chamber with top and side viewing ports to facilitate melt pattern observation and temperature measurements under vacuum conditions was designed in the UK, and installed at the Uni-Pol Mexico site.

4.4.2 Partial Factorial Design: L9 Array

Partial factorial design can be achieved using orthogonal arrays as a map for a series of experiments. The technique utilises an array as a subset of the full factorial experiment, where no two experiments are identical. The purpose of using an orthogonal array is to identify parameter interactions, with the capability to isolate certain interactions and determine their effects as negligible if they are present across all results [86]. Table 4.6 provides a route map for the experimental parameters, as a guide for the DOE.

Run	Disc Height (mm)		Hole Diameter (mm)		Position	
	Level	Value	Level	Value	Level	Value
1	1	15	1	0	1	B
2	1	15	2	2	2	M
3	1	15	3	10	3	T
4	2	35	1	0	2	M
5	2	35	2	2	3	T
6	2	35	3	10	1	B
7	3	50	1	0	3	T
8	3	50	2	2	1	B
9	3	50	3	10	2	M

Table 4.6: DOE table for experiments based on L9 array; three parameters at three levels

All billets consisted of 50 mm diameter IN713C nickel alloy, in two pieces, and a total of 3 kg in mass. A mass of 3 kg was the equivalent of a total stacked billet length of 185 mm. The three parameters varied in this L9 array are disc height, hole diameter and hole position. Alongside the L9 array, 50 mm diameter one-piece billets of 3 kg mass were also melted for comparison. Both the L9 array and one-piece billets were repeated a total of three times, to increase reliability of results. During the production process, offcuts of metal are sometimes used to reach the total 3 kg required for casting. For this reason,

4.4. VIM-IC DESIGN OF EXPERIMENTS: L9 ARRAY

one parameter to be varied was height of the lower disc of the two pieces. ‘Disc height’ refers to the height of the bottom piece of billet, measured in mm. For Parameter Level (PL) 1 in disc height, the bottom piece of the two billet pieces stacked in the crucible was 15 mm long and the top piece was 170 mm in length. PL2 of disc height comprised of a bottom disc of 35 mm length, and a top billet piece of 150 mm length. Finally, disc height PL3 represented a bottom billet piece length of 50 mm and a top billet piece length of 135 mm. The three different PLs for disc height are shown in Figure 4.27. The purpose of varying the disc height was to determine the distance required for piping from the pour face, to ensure that the flow behaviour of the pouring alloy was unaffected.

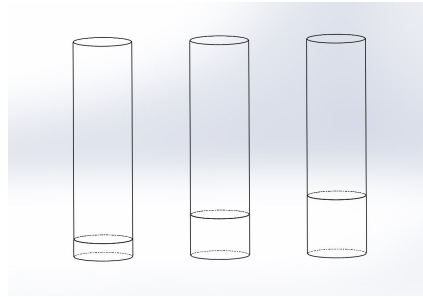


Figure 4.27: Disc Height PLs (left to right): PL1: 15 mm, PL2: 35 mm, PL3: 50 mm

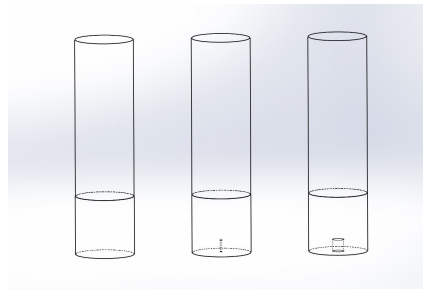


Figure 4.28: Hole Diameter (left to right): PL1: 0 mm, PL2: 2 mm, PL3: 10 mm

Previous initial experiments suggested that defect size on the pour face could cause a diversion in flow direction in the direct pouring induction melting process. Holes were created at a depth of 10 mm in billet end faces using drills with a carbide tip. ‘Hole diameter’ is the diameter of these drilled holes in mm, where 0 mm is representative of a billet with no hole. The purpose of this was to test the effect of no piping compared to the presence of piping with 2 mm and 10 mm diameter. Figure 4.28 shows PLs 1-3 for hole diameter, represented in an image with disc height of 50 mm and hole position of ‘Bottom’ solely for demonstration purposes. As shown in Table 4.6, the hole position

varies between samples, and is not always at PL1.

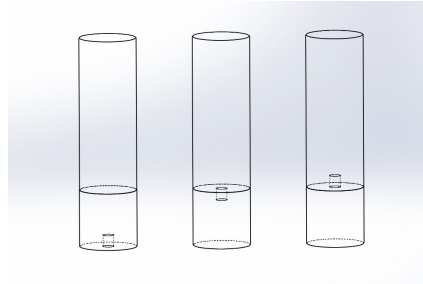


Figure 4.29: Hole Position (left to right): PL1: Bottom (B), PL2: Middle (M), PL3: Top (T)

Finally, ‘Hole Position’ refers to the position of the hole relative to the two-piece billet faces. ‘Bottom’ (B) is the bottom face of the bottom billet piece. ‘Middle’ (M) is the top face of the bottom billet piece, and ‘Top’ (T) is the bottom face of the top billet piece. This range of PLs for hole position can be seen in Figure 4.29. A hole of 10 mm diameter and disc height of 50 mm has been used for demonstration purposes in this image.

4.4.3 Bespoke VIM Chamber

A bespoke VIM chamber was designed with the help of Richard Wilton, Uni-Pol Group, to aid noncontact temperature measurement during induction heating and pouring via the top plane and crucible exit, with an additional viewing window for a high speed camera to record alloy pouring. Figure 4.30 is a photograph of the front view of the chamber, with the large front viewing port fitted with glass. The side viewing port and the locations of the top and front viewing ports can be seen in Figure 4.31, which is a photograph of the left side view of the chamber. All viewing ports contain glass to ensure that the chamber is sealed during the VIM process. Finally, Figure 4.32 shows a rear view of the chamber, with a port to install and access the induction coil. Once installed, a base plate was fitted to the bottom of the chamber to obtain the required vacuum level.

Top and side viewing ports were created with the intention of allowing temperature measurement during induction melting and at the crucible exit during pouring. The front viewing port was designed to provide a field of view equivalent to the length and width of a standard casting tree mould.

The bespoke vacuum melting chamber was manufactured in stainless steel, with a piece of glass fitted in the front viewing port. Standard borosilicate glass with 10 mm thickness is used on the top viewing port. The intention of fitting a side viewing port was to allow for

4.4. VIM-IC DESIGN OF EXPERIMENTS: L9 ARRAY

temperature measurement of the alloy during pouring, using the ThermoView Pi20 Fixed Thermal Imager to record both pouring temperature and flow images. However, as stated in Section 2.48 and shown in Figure 2.15, ThermoView Pi20 thermal imaging camera can not measure the temperature of target objects obscured by glass. This is due to the range of wavelengths which the thermal imaging camera was able to detect. Therefore, the side viewing port was rendered obsolete for temperature measurement this set of experiments.

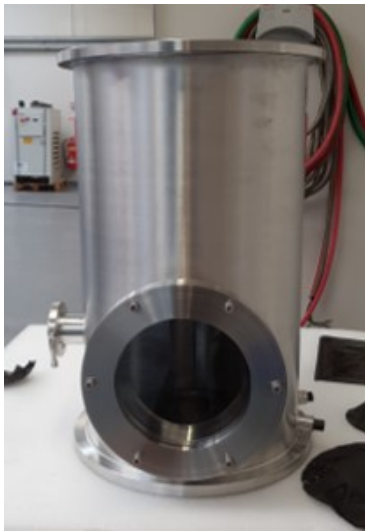


Figure 4.30: Bespoke VIM chamber front view



Figure 4.31: Bespoke VIM chamber left side view



Figure 4.32: Bespoke VIM chamber rear view

4.4.4 DOE: Alloy Preparation

The required alloy lengths for the L9 array were cut by Ross and Catherall UK, as requested. Photographs of PLs 1-3 for disc height are shown in Figures 4.33 - 4.35, with disc heights of 15 mm, 35mm and 50 mm respectively. The alloy pieces were paired up accordingly and labelled using a permanent marker.

There were certain alloy pieces which required either a 2 mm or 10 mm diameter hole to be drilled into the centre of a billet face. These were identified and given to the Swansea University workshop for drilling. A photograph showing billet pieces with a 2 mm diameter hole and 10 mm diameter hole can be seen in Figure 4.36.

The finished cut, drilled and labelled pieces were then packaged and shipped to the Uni-Pol Mexico site, ready for use in the DOE trials.



Figure 4.33: PL1: 15 mm disc, 170 mm top billet piece



Figure 4.34: PL2: 35 mm disc, 150 mm top billet piece



Figure 4.35: PL3: 50 mm disc, 135 mm top billet piece



Figure 4.36: Billet pieces with 2 mm hole (left) and 10 mm diameter hole (right)

4.4.5 DOE: L9 Array Experiment Setup

The bespoke VIM chamber was installed at the Uni-Pol Mexico site. Figure 4.37 shows the experimental setup for the DOE L9 array experiments. A crucible loaded with alloy is suspended above an alloy basin covered in Kaowool fibre blanket on the chamber base plate. The crucible is held in place with a clamp stand. The chamber base plate is raised to the base of the chamber and sealed using a clamp when VIM is in progress.

Raising the base plate positions the crucible and alloy within the length of the induction coil. The induction coil is connected to a generator and the chamber is connected to a vacuum pump to allow casting in vacuum conditions.

A Raytek Endurance 1R 2-Colour ratio infrared thermometer was mounted to a plate above the top viewing port of the bespoke VIM chamber. The Photron FASTCAM SA4 high speed camera was mounted on a tripod and set at a height and angle which was level with the chamber front viewing port. The IR thermometer and high speed camera were

4.4. VIM-IC DESIGN OF EXPERIMENTS: L9 ARRAY

connected to computers to allow the temperature data and images to be saved. These experiments were supported by staff at Uni-Pol Mexico.



Figure 4.37: Bespoke VIM chamber installed on site with IR thermometer above top viewing port and high speed camera focused on front viewing port

4.4.6 DOE: L9 Array Experiment Method

An aluminosilicate ceramic fibre crucible is loaded with two pieces of alloy, according to the chosen configuration listed in the L9 array. The loaded crucible is placed on the clamp stand, which is set according to the stand height which is representative of the billet location within the coil in standard casting production. This stand height corresponds to the bottom billet face at a vertical distance of 35 mm from the bottom of the coil in the VIM process. The base plate is raised to the base of the chamber and held in place by a clamp to create a seal. The focus and positioning of the IR thermometer is checked to ensure that the target measurement spot is correctly focused on the centre of the top billet face. The vacuum pump is switched on, with the chamber pressure set to 0.5 mbar.

Once this vacuum level has been achieved, the IR camera and high speed camera are set to recording mode. The slope setting on the IR thermometer is set to 1.00, with a transmittance setting of 0.91 to account for the borosilicate glass on the top viewing port. These values are based upon the calibration work conducted in Section 2.4. The high speed camera records monochrome TIFF images which are set to a resolution of 512 x 1024 pixels to provide the long, thin imaging window required to capture the length of the

molten metal. Runs which lasted a standard length of time allowed the camera to be set to 3000 fps, whereas longer runs required a lower number of frames per second, specifically 1500 fps, to capture the total pour footage. To prevent the camera from ‘whiting out’ causing an overexposed image, the shutter speed was set to 1/40,000 and aperture to f/132, setting ‘A’. Details of how these optimal camera settings were determined can be found in Section 4.2.

The generator is switched on and conducts a standard VIM industrial melting cycle. In this case, the voltage is set to 555 V and frequency is set at 7.93 kHz. The generator will continue to hold this set voltage until a sensor detects a change in the magnetic field which is produced when the alloy becomes fully molten. At this point, the generator switches off and the alloy pours freely by gravity into the alloy basin below. Once the pouring is complete, the high speed camera is instructed to finish recording, as it is set to record only the last few seconds of footage due to internal memory limitations. The chamber base plate is lowered, allowing for removal of the alloy basin and crucible. This process is then repeated three times for each of the configurations on the L9 array. The process was also repeated for three one-piece billets of 185 mm length for comparison.

4.4.7 DOE: L9 Array IR Thermometer Results

The IR thermometer is capable of recording temperatures of 600 - 1800 °C in 2-Colour mode, with 95 % attenuation for temperatures of 800 °C and above. The measured solidus of IN713C obtained from performing the DSC technique is 1331.9 °C, with a liquidus value of 1389.3 °C. This places the mushy zone temperature range of this alloy comfortably within the measurement range of the IR thermometer. However, the initial recorded temperature of the top billet face for each of the samples varies between runs. Due to the size of the target measurement spot, it exclusively measures the temperature within an approximately 5 mm diameter circular area, in the centre of the billet face. The variation in initial recorded temperatures would therefore be affected by the fashion in which the billet melts, and at which point the temperature would exceed 600 °C within the target measurement spot.

The measured top billet face temperature for the duration of induction heating and melting, in the three repeated trials for ‘Run 1’ in the L9 array, are plotted on the graph in Figure 4.38. ‘Trial 1a’ refers to the first trial of Run 1, with Trials ‘1b’ and ‘1c’ the second and third repeats of Run 1 respectively. The region in which the measured heating pattern starts to visibly change behaviour is circled and highlighted on the graph, and is known

in industry as the ‘superheat’ region. Both in Figure 4.38 and in the graphs for Runs 2-9, this region is located before the onset of the known mushy zone range of temperatures, for this marked onset of a difference in the heating curve behaviour. A dip in temperature on the curve prior to the ‘superheat’ region can be observed at a temperature value which is below the experimentally obtained solidus and liquidus values for IN713C. It is important to note that from the literature, solidus and liquidus values for IN713C varied greatly. This could be due to variations in elemental compositions. Furthermore, the measurement region or ‘spot size’ of the IR thermometer examines a spot size which is ten times smaller than the total diameter of the billet top face. Therefore, as it is only measuring a very small region of the total billet top face, it is likely that the measured temperatures are of rapidly moving alloy and prone to large temperature differences. The flipping of the top piece of detached billet is also a potential cause for such large variations in temperature prior to the superheat region. Temperature data has been removed beyond the pouring point, so that the final temperature marked on the graph with respect to time is the measured temperature at the alloy pouring point.

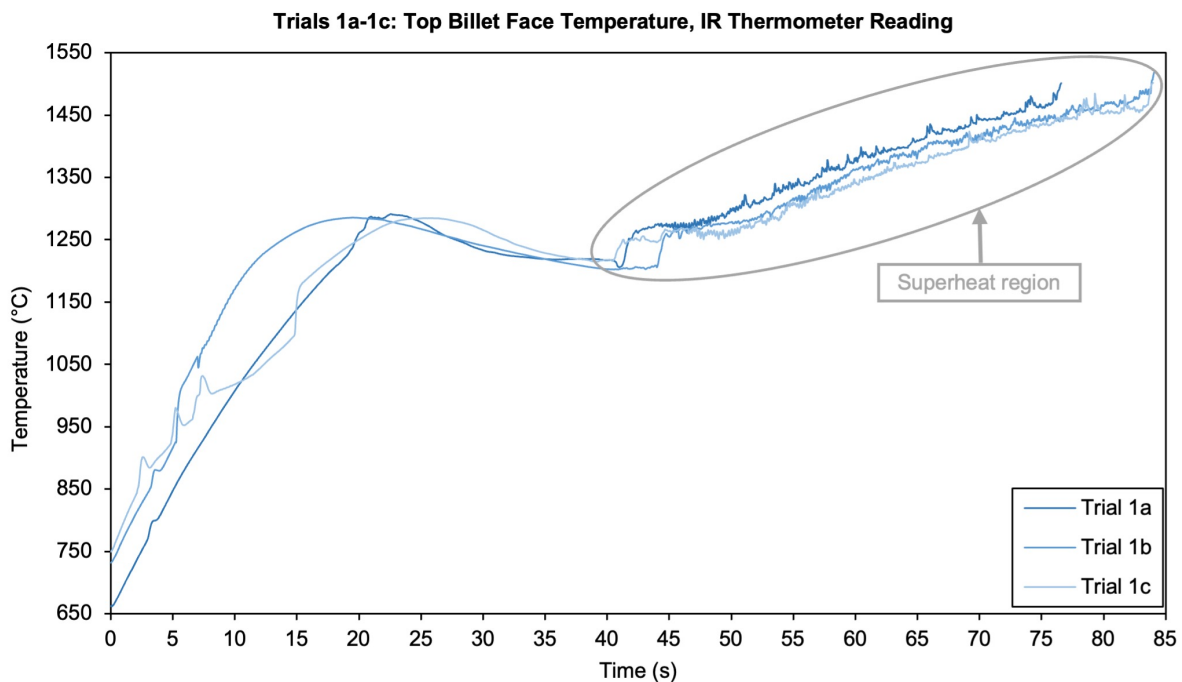


Figure 4.38: Trials 1a-1c: Top Billet Face Temperatures in Induction Heating and Melting

4.4.8 ANOVA Analysis of IR Thermometer Results

For Figures 4.39 and 4.40, 880 °C was chosen as an arbitrary start temperature. This was due to the variation in initial detected temperatures between trials, and this value

4.4. VIM-IC DESIGN OF EXPERIMENTS: L9 ARRAY

was above the lowest recorded temperatures for all runs. For the graphs below involving differences in parameters measured in seconds, the variations in time differences relative to the total times were so small that they could be considered insignificant. The average values for the three one-piece billets of 185 mm length are also included on each graph.

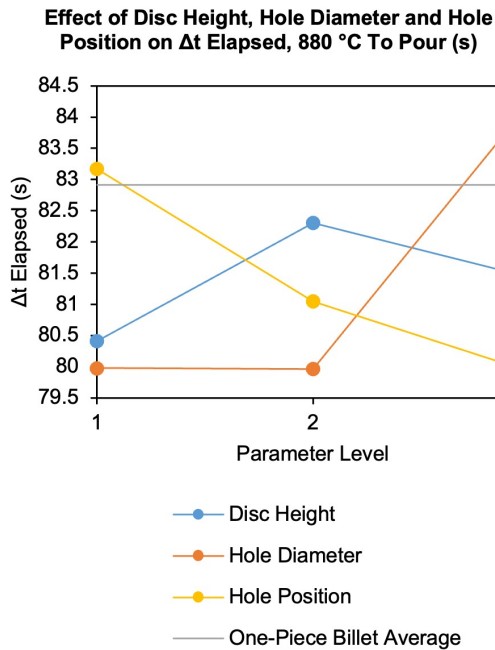


Figure 4.39: Time Between 880 °C to Pour

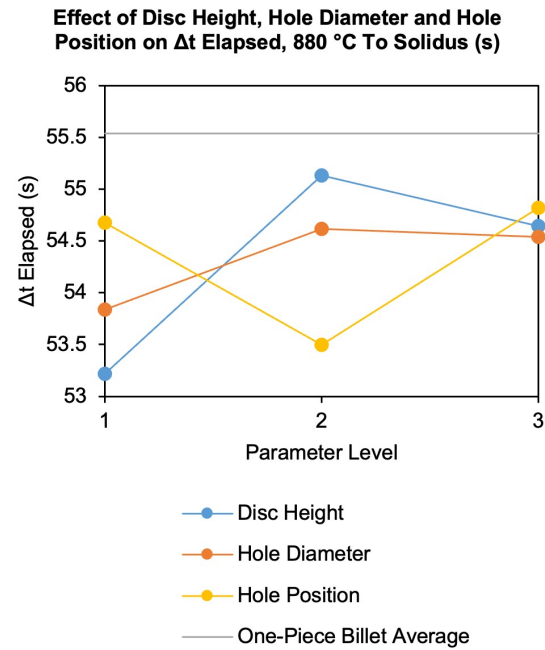


Figure 4.40: Time Between 880 °C to Solidus

Similarly, the measured temperature differences for changing disc height, hole diameter and hole position for Figures 4.41-4.44 were statistically insignificant compared to the overall magnitude of the recorded temperatures. It was an unfortunate outcome of this DOE, that the top billet face temperature is unaffected in heating and melting with changes in disc height, hole diameter and hole position.

However, further temperature measurement trials proved that changes to the generator power and frequency result in differences in billet top face temperatures during heating and melting. In these further temperature measurement trials, the corresponding crucible outlet temperatures were also recorded during alloy pouring. Differences in pouring temperatures at the crucible outlet were observed when factors such as billet mass were varied. Details of these trials can be found in Section 4.5.4.

Effect of Disc Height, Hole Diameter and Hole Position on Superheat Duration (s)

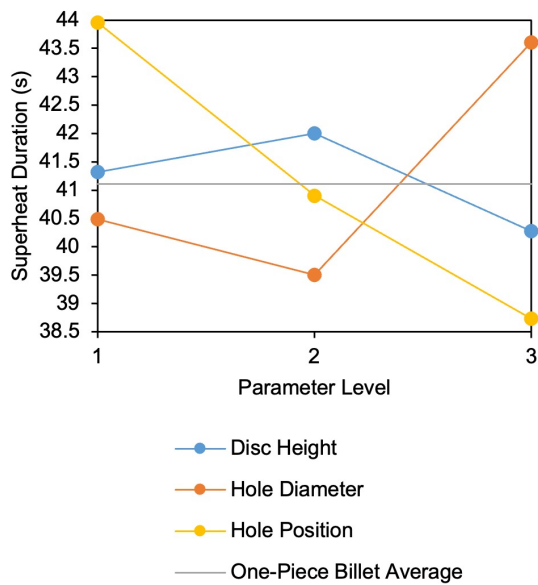


Figure 4.41: Superheat Duration

Effect of Disc Height, Hole Diameter and Hole Position on Superheat Start Temp. (°C)

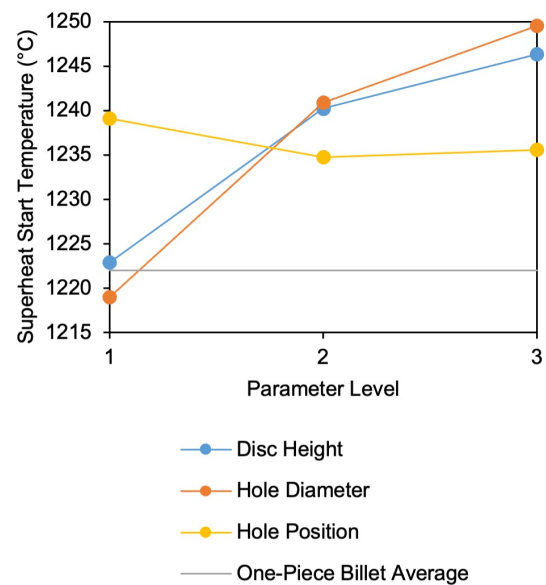


Figure 4.42: Superheat Start Temp.

Effect of Disc Height, Hole Diameter and Hole Position on Pour Temp. (°C)

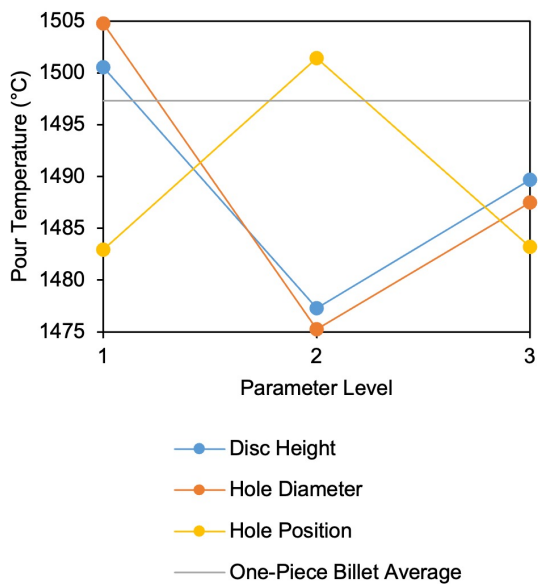


Figure 4.43: Pour Temp.

Effect of Disc Height, Hole Diameter and Hole Position on Maximum Recorded Temp. (°C)

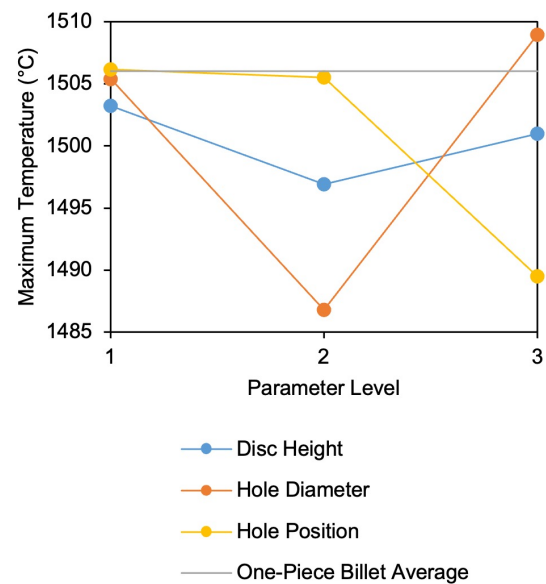


Figure 4.44: Maximum Recorded Temp.

4.4.9 DOE: L9 Array High Speed Camera Results

The high speed camera images captured of the full pouring duration for each trial were examined to obtain pour time duration. The pour time was measured by counting the

4.4. VIM-IC DESIGN OF EXPERIMENTS: L9 ARRAY

number of frames between the first image with a complete, unbroken stream of fluid from the crucible outlet down to the alloy basin within the image window, to the last recorded image with a complete, unbroken stream of fluid. The reason for choosing to count pour duration between frames of complete, unbroken flow is due to the dripping which can occur with the final remnants of the alloy at the end of the pour. The emptying of the final remnants within the crucible with broken, dripping flow can distort the total pour time of the bulk mass flow.

The images were also measured and analysed at the start, middle and end of the pour time for flow width, flow angle and flow velocity. The start of the flow was taken as the first frame with complete, unbroken flow. The end flow frame was taken as the last frame with complete, unbroken flow, with the middle flow frame taken as the frame in the middle of the start and end frames.

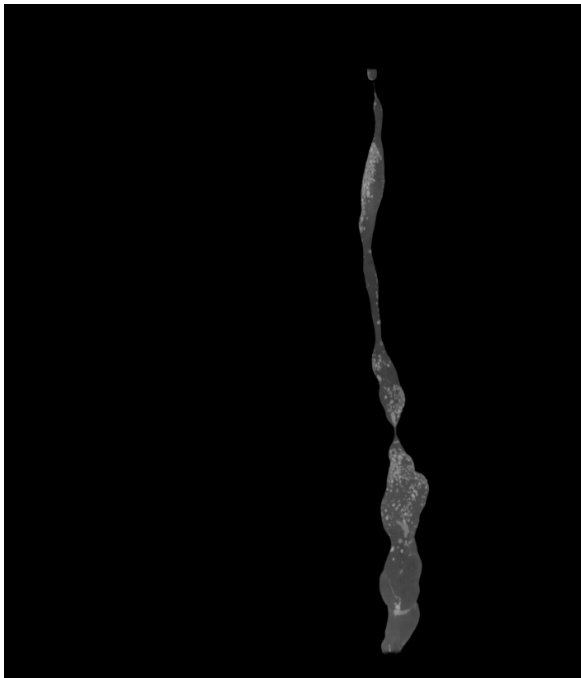


Figure 4.45: Trial 4b end of pour small width

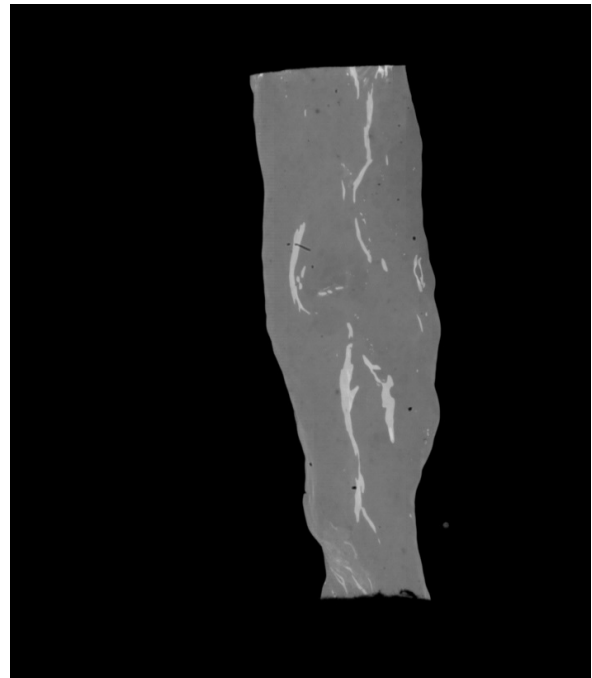


Figure 4.46: Trial 1c mid pour, large width

Figures 4.45-4.48 have been included as example start, middle and end frames with fluid flow at the smallest and largest flow widths and angles. Standard flow did not occur at a large angle to the centre line, and the alloy flowed steadily with a medium flow width. Flow width was measured using Fiji open source software to measure flow widths by entering a measurement scale in pixels per mm, which was achieved by defining a known reference length of the crucible exit in mm, and measuring this known length in pixels.

4.4. VIM-IC DESIGN OF EXPERIMENTS: L9 ARRAY

Flow angle was also achieved by measuring the angle of the flow using Fiji. A line was drawn from the middle of the flow width at the top of the frame, to the middle of the flow width at the bottom of the frame, to determine the angle of the stream of fluid relative to the vertical axis of the image. Although this was not a perfect method for capturing diversions in flow angle throughout the frame, this method was adhered to in order to provide consistency in the angle measurement method, as standardisation was required. For the purposes of ANOVA analysis, the absolute flow angle value was taken.

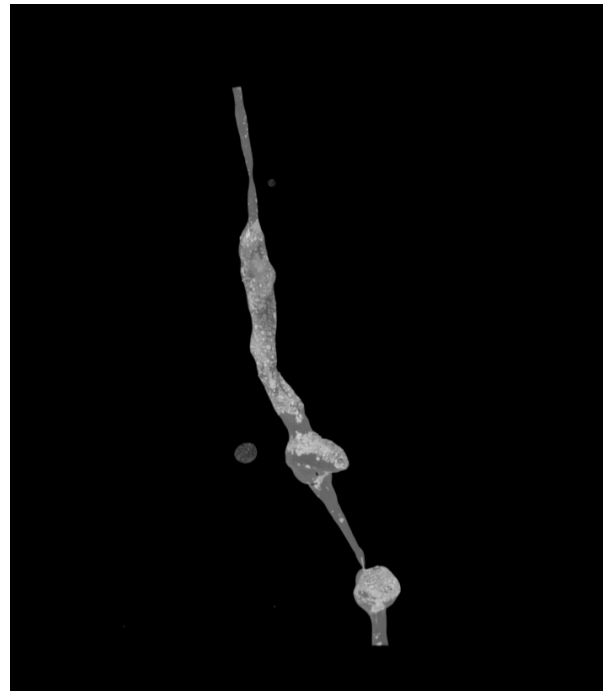
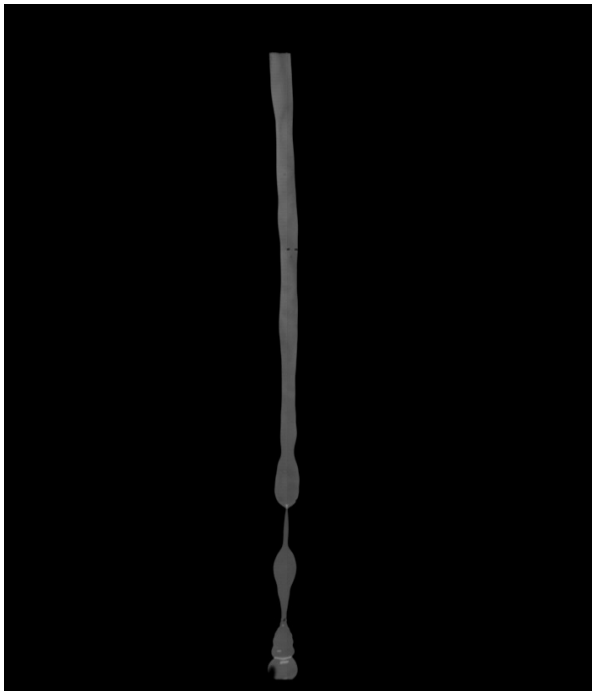


Figure 4.47: Trial 7a start of pour, small angle Figure 4.48: Trial 3c end of pour, large angle

Flow velocities in the x (horizontal) and y (vertical) directions at the beginning, middle and end of the flow were obtained by processing the velocities using a version of the MATLAB PIV program previously mentioned in Section 4.3.7, which had been further built upon and optimised. In this optimised version of the program, a step number between frames of $n = 5$ produced the most accurate velocity measurements. As previously discussed regarding an earlier version of the code, the program generates a grid over the surface area of the flow, masking the dark background.

Figure 4.49 shows the first image analysed by the program, $n = 0$, for Trial 1a at the start of the pour. The grid has been generated across the flow region, with coloured velocity vectors. Figure 4.50 shows the final image analysed by the program, $n = 5$, with the generated grid and velocity vectors for Trial 1a at the end of the pour.

4.4. VIM-IC DESIGN OF EXPERIMENTS: L9 ARRAY

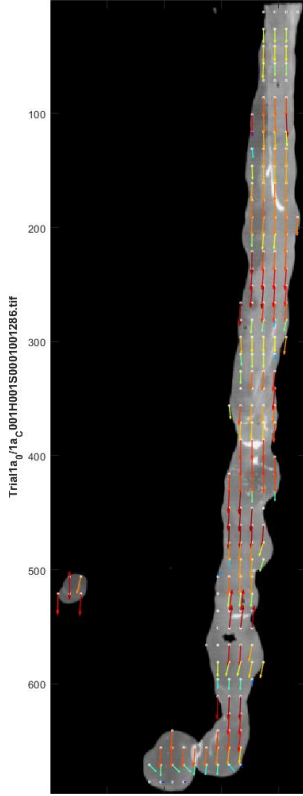


Figure 4.49: Trial 1a - First analysed image, $n=0$ with generated grid and velocity vectors

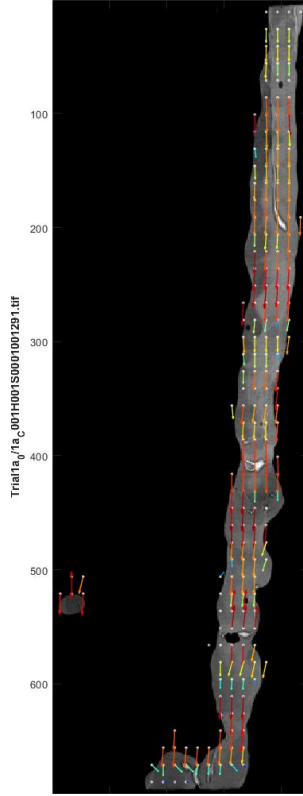


Figure 4.50: Trial 1a - Final analysed image, $n=5$ with generated grid and velocity vectors

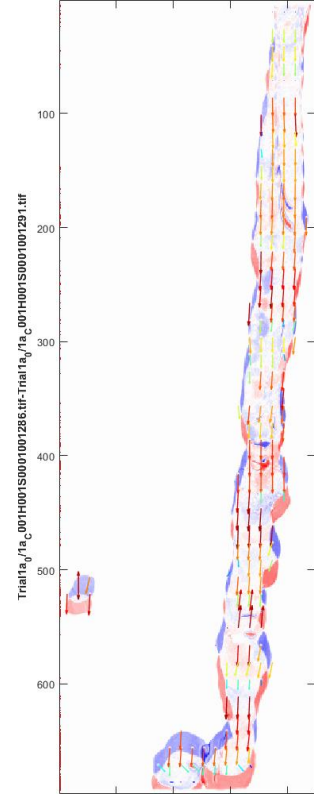


Figure 4.51: Trial 1a - Image $n=0$ imposed upon $n=5$ showing shift between frames

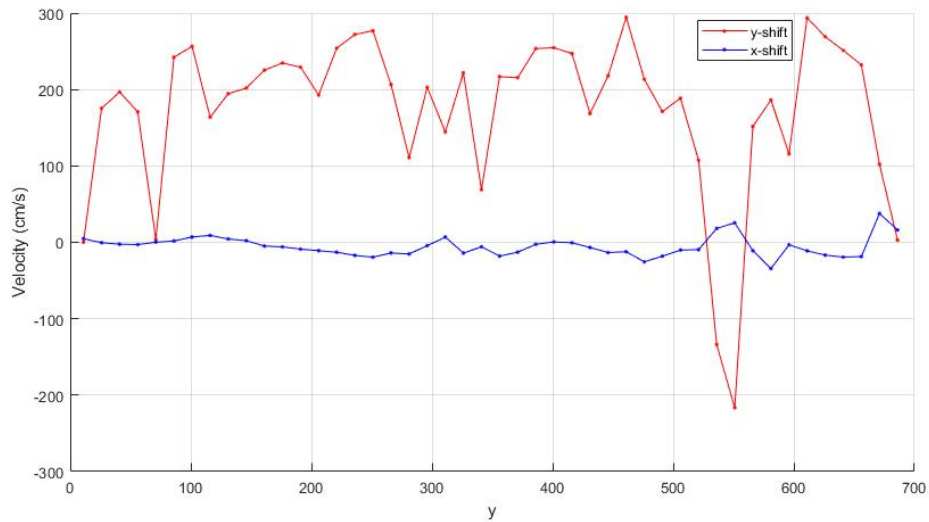


Figure 4.52: Trial 1a, start of pour: Average x and y velocities in cm/s for each row of dots in the grid generated on the flow surface

Finally, Figure 4.51 shows $n = 0$ imposed upon $n = 5$. Figure 4.52 is a graph showing the average x and y velocities per row of the generated grid, with the ‘ y ’ distance in pixels on the horizontal graph axis relating to the vertical distance from the crucible outlet ($y=0$ pixels) down to the alloy basin ($y = 700$ pixels).

The average flow velocity in the x and y directions are taken for the beginning, middle and end of the pour are recorded. A positive velocity value in the x direction refers to moving towards the right side of the image, whereas a negative x velocity value refers to a feature moving to the left side of the image. The grid row from which the average velocities are taken is selected after assessment of the point from which the velocity vectors are producing reasonable values in the gravity direction, and displays reliable levels of feature tracking. From the chosen grid row, the flow velocity magnitude is obtained by taking the square root of the sum of $x^2 + y^2$ average velocity values. This not only simplifies the interpretation of velocity values for start, middle and end of the pour, but also eliminates the effect of negative velocity values in the x direction caused by directional differences. It is important to note that the upward, counter direction to gravity velocities seen between $y=500-600$ in Figure 4.52 have been generated by the tracking of the separate alloy droplet on the left side of the frame in Figures 4.49-4.51, and the refractory particle on the main stream of alloy which appears as black in Figures 4.49 and 4.50. This highlights the importance of manual processing and interpretation of the data, with averaged values from the fourth and fifth rows of the grid taken to account for difficulties in calculating velocity at the crucible outlet boundary.

4.4.10 ANOVA Analysis of High Speed Camera Results

Average values for the three one-piece billets, 185 mm length, are included on each graph. **Pour Time, Figure 4.53:** The presence of a hole at PL1, on the pour face closest to the crucible outlet, significantly increases the total pour time. This could be due to the alloy pouring out of the hole on the pour face, before the rest of the bottom of the billet is molten, which restricts the flow rate due to a smaller opening.

A 15 mm disc height results in a shorter pour time than 35 mm and 50 mm discs. This may be due to where the contact point of the two billet pieces is positioned relative to the bottom of the coil, or billet. The contact point of the 50 mm disc is situated within the region of the magnetic field and within the coil length, while the 35 mm disc split is located at the height at which the magnetic field region acting upon the billet ends. A 15 mm disc is below the region of the magnetic field and coil length, within the length of the

billet that is melted by conduction. This could cause the greatest difference in pour time, as it acts as what the industry has coined a ‘penny’. The purpose of the penny in industry is to ensure that the top billet piece is fully molten before the penny is melted. This could result in an overall lower pour time due to the whole charge being fully molten and ready to pour once the final piece melts. There may be a positive trend with the presence of a hole and its increasing diameter. However, the effect on pour time with increasing hole diameter is reduced compared to the effect of varying disc height and hole position. The impact of hole diameter on pour time is less conclusive, as the differences in pour time are small.

Flow Width - Start, Figure 4.54: Flow width is significantly narrower at the start of the pour for 50 mm discs. Start of pour flow width also seems to be affected by hole diameter. The presence of a hole (PL2 and PL3) results in a thinner flow width, with the smallest initial flow widths occurring for 2 mm diameter holes, followed by 10 mm diameter holes and then significantly wider initial flow width when no holes are present (PL1). Finally, flow width is much smaller when the holes are present on the pour face. This reflects the expected physics, with reduced mass flow when pouring through a hole.

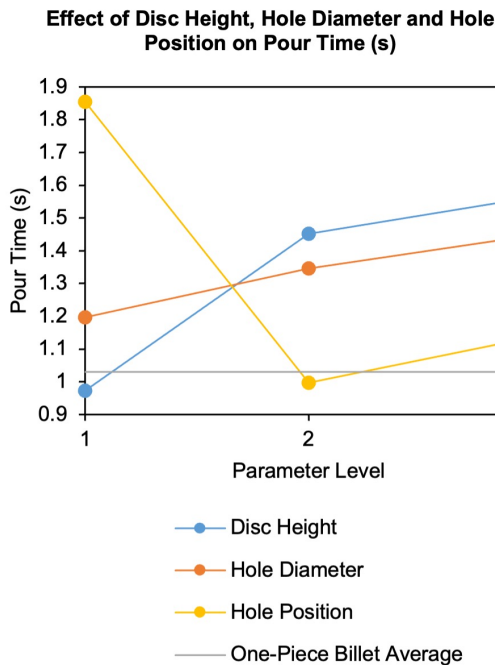


Figure 4.53: Pour Time

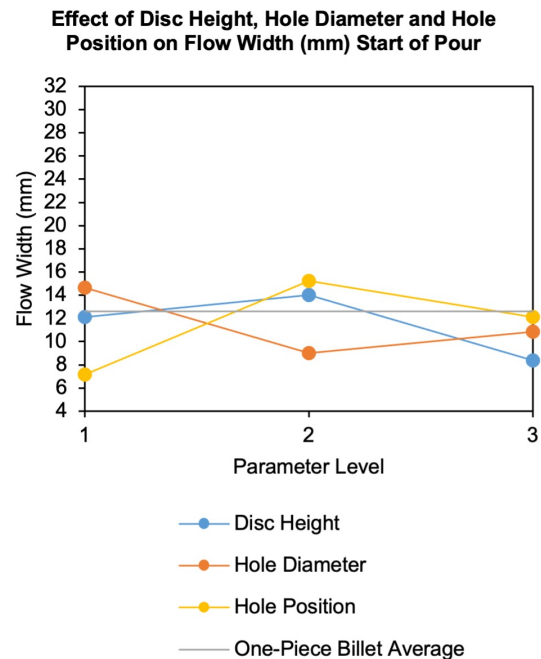


Figure 4.54: Flow Width: Start of Pour

Flow Width - Middle, Figure 4.55: Flow width at the middle of the pour remains significantly thinner for holes present on the pour face, at PL1. Disc height at PL1 is conversely the opposite, with the widest flow widths observed for the 15 mm discs. Flow

widths remain lowest for 2 mm diameter holes, and widest for those with no holes present.

Flow Width - End, Figure 4.56: Although PL2 indicates the lowest average flow width for both disc height and hole diameter at the end of the pour, and flow width appears to decrease with an increasing hole position distance relative to the pour face, the differences may not be significant. The variations are significantly lower in magnitude than the differences observed at the start and middle of the pour, with the end of pour flow width averages varying within a maximum range of 2.6 mm.

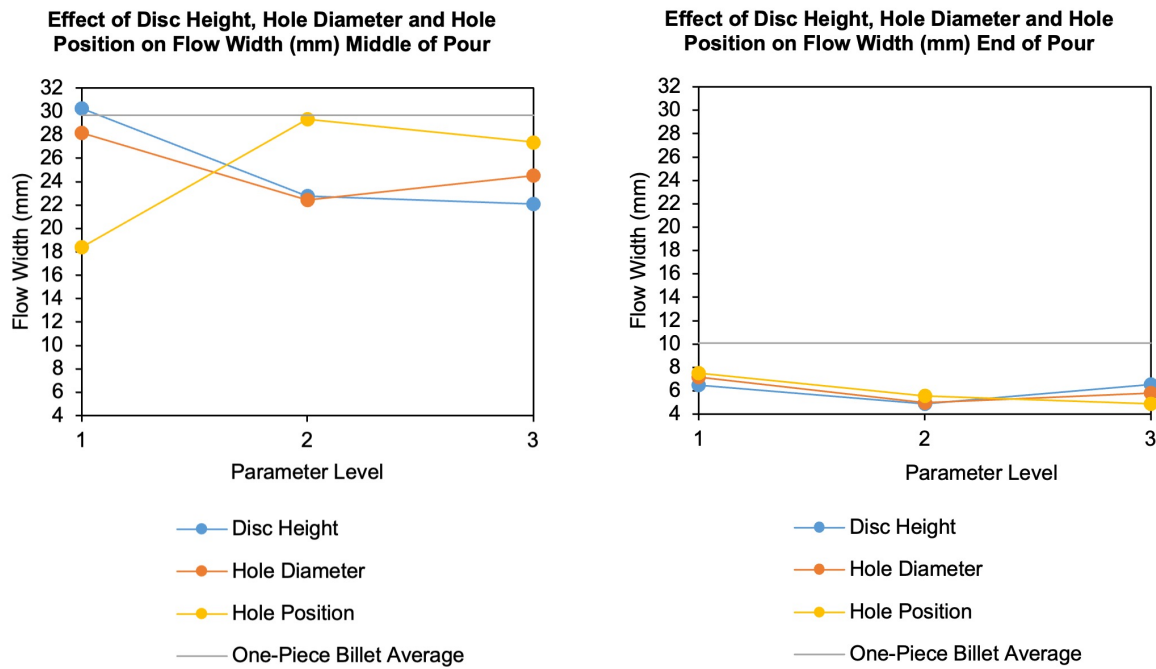


Figure 4.55: Flow Width: Middle of Pour

Figure 4.56: Flow Width: End of Pour

Flow Angle - Start, Figure 4.57: The greatest angles are observed in 35 mm discs, compared to 15 mm and 50 mm discs. In the experiments, many crucible cracks and failures were observed during the induction heating process when using a 35 mm disc. It is possible that the 35 mm disc height is situated such that it is causing vibrations within the crucible from its interaction with the magnetic field produced by the coil. A significantly larger flow angle was observed with no holes present, compared to the presence of holes. A strong positive trend can be deduced between flow angle and hole position, with smaller angles resulting from a shorter distance between the crucible outlet and hole position.

Flow Angle - Middle, Figure 4.58: Although the magnitude of flow angles is decreased for the middle of the pour compared to the start, the influence of 35 mm discs on larger

4.4. VIM-IC DESIGN OF EXPERIMENTS: L9 ARRAY

flow angles is still present. It is possible that the presence of a hole on the pour face increases flow angle in the middle of the pour, but as the total range of angle values is lower than at the start of pour, the impact of hole position on flow angle is less conclusive.

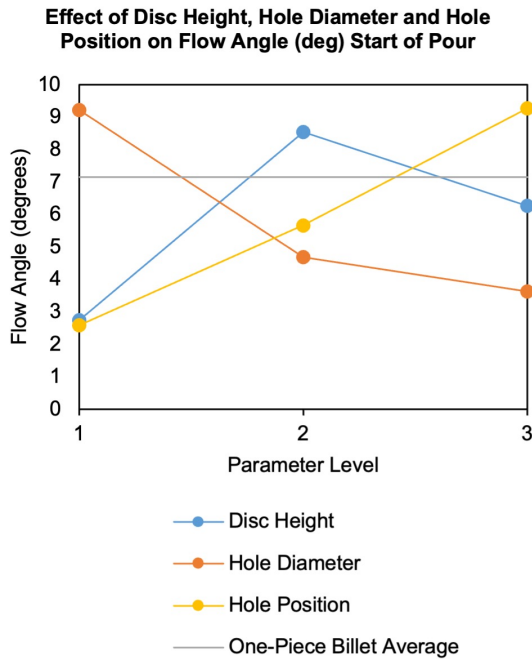


Figure 4.57: Flow Angle: Start of Pour

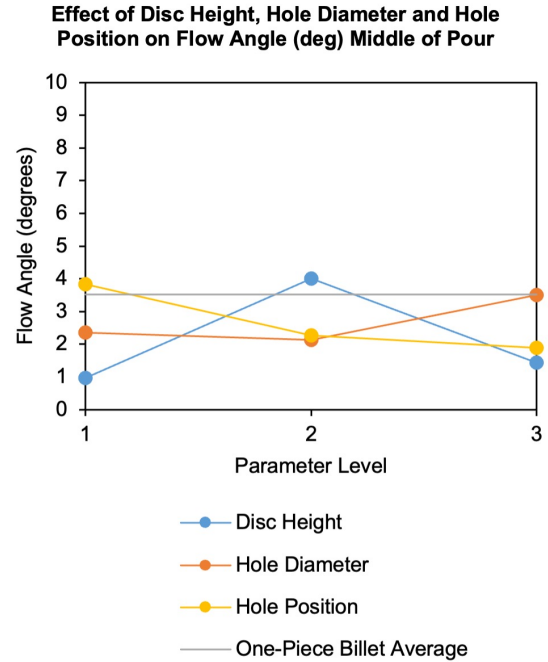


Figure 4.58: Flow Angle: Middle of Pour

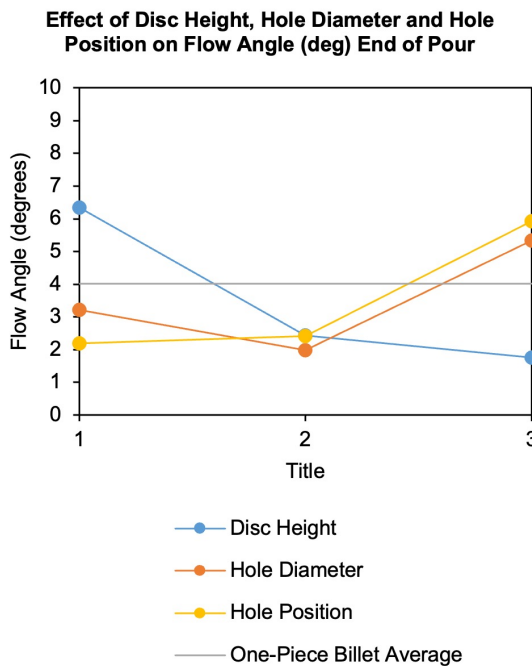


Figure 4.59: Flow Angle: End of Pour

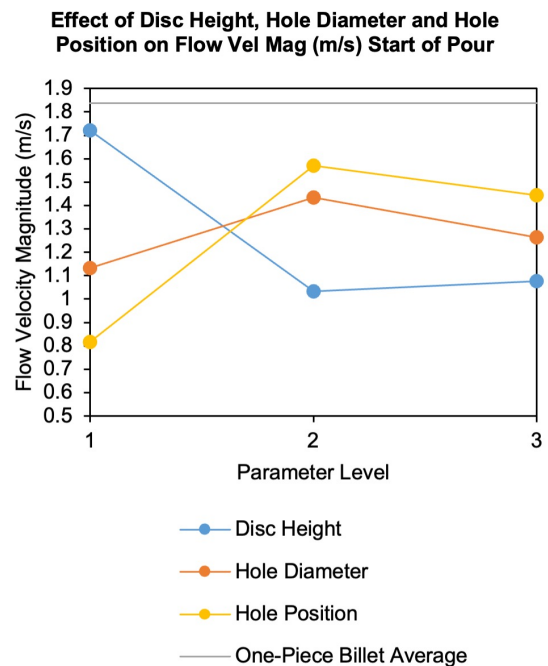


Figure 4.60: Flow Vel Mag: Start of Pour

Flow Angle - End, Figure 4.59: The end of the pour demonstrates a larger range of pour angles compared to the middle of the pour. A 15 mm disc height results in the largest end of pour angles. 10 mm diameter holes also produce an increased angle, alongside a larger distance between the hole and the pour face.

Flow Velocity Magnitude - Start, Figure 4.60: At the start of the pour, a 15 mm disc height results in a higher velocity magnitude of flow leaving the crucible. Conversely, a hole positioned on the pour face at PL1 results in lower flow velocities.

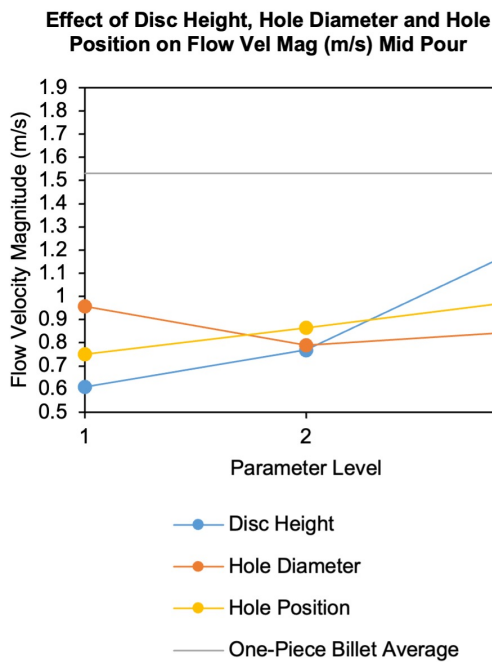


Figure 4.61: FlowVel Mag: Middle of Pour

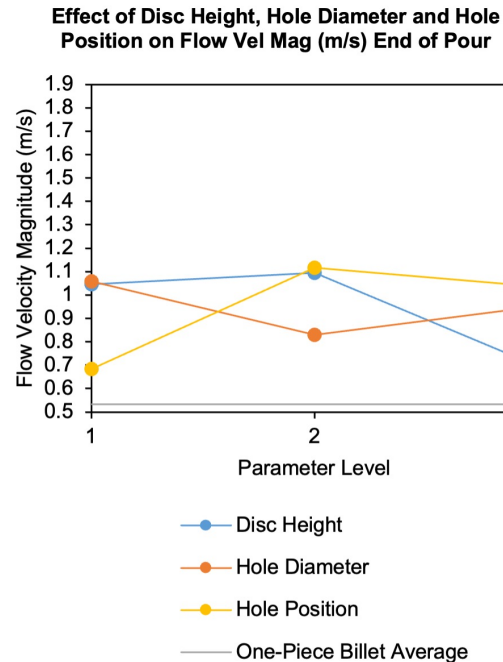


Figure 4.62: Flow Vel Mag: End of Pour

Flow Velocity Magnitude - Middle, Figure 4.61: A positive trend can be seen for both disc height and hole position, where increasing disc height and the distance between pour face and the hole results in a larger velocity magnitude mid pour. A 50 mm disc height appears to significantly increase velocity magnitude for the middle of the pour.

Flow Velocity Magnitude - End, Figure 4.62: A disc height of 50 mm results in a lower velocity magnitude at the end of the pour, compared to the other disc heights. The influence of hole diameter or presence of a hole on the end of pour velocity is unclear. However, a hole on the pour face results in a lower velocity magnitude at the end of pour.

The results of these ANOVA analyses will be further examined in the ‘Modelling Industrial Experiments’ chapter, with the aim to develop a greater understanding of the mechanisms causing the phenomena observed in experimental results with changing flow width, angle

and velocity magnitude.

4.5 Induction Melting: Testing Process Parameters

4.5.1 Induction Melting: Testing Process Parameters

Overview and Aims

Following the DOE L9 Array experiments, the need to understand the effect of other process parameters on the temperatures attained in induction heating, melting and pouring was identified. Further experiments were conducted to test these other process parameters. The aims of these trials were as follows:

- Determine the effect on alloy temperatures in heating, melting and pouring of varying number of billet pieces, billet mass, billet position within the coil, generator power, crucible outlet diameter and alloy type.
- Define the pouring temperature range at the crucible exit.
- Measure the time to melt from generator ‘switch on’ to alloy pouring with varying process parameters

Table 4.7 lists the permutations of trials with varying process parameters, where ‘NP’ is Number of Pieces, ‘SH’ is ‘Stand Height’ in mm, and ‘COD’ is ‘Crucible Outlet Diameter’ in mm. For every trial, billet pieces of 50 mm diameter were melted. Melt time in seconds is measured from the point at which the generator is switched on, until alloy pouring.

Changing the stand height affects the position of the billet within the coil, where the stand height is the distance between the bottom of the crucible and the bottom of the coil. Power is listed in kW, with ‘75, 30’ referring to setting the power to 75 kW for the first minute, and 30 kW for the remainder of the time.

In order to understand the effect of varying process parameters on pouring temperatures, a second IR thermometer was acquired to facilitate temperature measurement at the crucible outlet. This second IR thermometer was an Endurance E1RH-F2-L-0-0 model 2-Colour IR thermometer, with a temperature measurement range of 1000-3200°C.

An induction coil with the same cross section and a different diameter was used for this set of further experiments, compared to the DOE L9 Array experiments. The power level was also varied. Details of these differences are listed in the experimental setup.

4.5. INDUCTION MELTING: TESTING PROCESS PARAMETERS

Trial	Mass (kg)	Alloy	NP	Power (kW)	SH (mm)	COD (mm)	Melt Time (s)
1	3	IN713C	1	75	40	32.5	91
2	3	IN713C	1	75	40	32.5	91
3	3	IN713C	1	75	40	32.5	91
4	3	IN713C	2	75	40	32.5	95
5	3	IN713C	2	75	40	32.5	91
6	2.5	IN713C	1	75	40	32.5	85
7	2.5	IN713C	1	75	40	32.5	85
8	2.5	IN713C	1	75	40	32.5	85
9	3.5	IN713C	1	75	40	32.5	83
10	3.5	IN713C	1	75	40	32.5	95
11	3	IN713C	2	75, 30	40	32.5	116
12	3	IN713C	2	75, 30	40	32.5	117
13	3	IN713C	2	85	40	32.5	85
14	3	IN713C	2	85	40	32.5	85
15	3.5	IN713C	2	75	40	32.5	100
16	3.5	IN713C	2	75	40	32.5	101
17	3	IN713C	1	75	26	32.5	71
18	3	IN713C	1	75	26	32.5	88
19	3	IN713C	1	75	26	32.5	88
20	3	IN713C	1	75	50	32.5	91
21	3	IN713C	1	75	50	32.5	92
22	3	IN713C	1	75	50	32.5	94
23	3	IN713C	1	75	40	25	91
24	3	IN713C	1	75	40	25	91

Table 4.7: Testing process parameters trials overview

It should be noted that this was not a planned, efficient orthogonal array of experiments to determine the effect of varying parameters on flow characteristics and alloy temperatures. The author was aware that the foundry had devised a list of trials to be conducted, which are listed in Table 4.7. It was considered a good opportunity to test the effect of varying additional parameters, such as power and mass, despite the lack of efficient sampling.

4.5.2 Induction Melting: Testing Process Parameters Experiment Setup

The same bespoke VIM chamber was used as the one in the DOE L9 array experiments, at the Uni-Pol Mexico site. These experiments were supported by staff at Uni-Pol Mexico. A crucible loaded with alloy was suspended above an alloy basin covered in Kaowool fibre blanket on the chamber base plate. The crucible was held in place with a clamp stand. The chamber base plate was raised to the base of the chamber and sealed using a clamp when induction melting is in progress. For this set of experiments, the induction melting was done in air conditions. This was due to safety issues experienced previously with the front viewing window shattering upon contact with the molten alloy.

Raising the base plate positions the crucible and alloy within the length of the induction coil. The induction coil is connected to a generator, set at 646 V and 7.93 kHz. The inner diameter of the coil was 110 mm, with an outer diameter of 130 mm. Otherwise the coil had the same total height and number of turns as the previously described industrial induction coil.

An Raytek Endurance 1RL 2-Colour ratio IR thermometer was mounted to a plate above the top viewing port of the bespoke VIM chamber, with a Raytek Endurance 1RH mounted on a tripod focused just below the crucible exit. A test crucible loaded with alloy was placed on the clamp stand, with the chamber base plate raised into place. The IR thermometer above the chamber was focused to ensure that the centre of the top billet face was in focus. Additionally, the 1RH IR thermometer was positioned at a distance from the crucible, and focused such that the total width of the crucible exit was captured within the measurement spot. The IR thermometers were connected to computers to allow for temperature measurements to be recorded.

4.5.3 Induction Melting: Testing Process Parameters Experiment Method

An aluminosilicate ceramic fibre crucible was loaded with either one or two pieces alloy, according to the chosen configuration listed in Table 4.7. The loaded crucible was placed on the clamp stand, which was set according to the stand height listed in the table. The base plate was raised to the base of the chamber and held in place by a clamp to secure it. The focus and positioning of the IR thermometers was checked to ensure that the target measurement spots were correctly focused on the centre of the top billet face and

just below the crucible outlet.

The IR thermometers were set to recording mode. The slope setting on the IR camera was set to 1.00, with a transmissivity setting of 0.91 to account for the borosilicate glass on the top viewing port. The transmissivity value for the IR thermometer recording alloy leaving the crucible outlet was set to 1.00, as there was no glass fitted in the viewing port. These values are based upon the calibration work conducted in Section 2.2.1.

The generator was switched on and a standard industrial melting cycle was conducted. In this case, the power is set to 75 kW, with voltage of 646 V and a frequency of 7.96 kHz. The generator continued to hold this set voltage until a sensor detected a change in the magnetic field which was produced when the alloy became fully molten. At this point, the generator switched off and the alloy poured freely by gravity into the alloy basin below. Once the pouring was complete, the temperature recording is stopped. The chamber base plate was lowered, allowing for removal of the alloy basin and crucible. This process was then repeated for each of the configurations as listed in Table 4.7.

4.5.4 Induction Melting: Testing Process Parameters Experiment Results

The measured temperature of the billet top face was recorded over the duration of the induction melting process. Once the billet reached its fully molten state and began to pour, the temperature of liquid alloy leaving the crucible was recorded over the duration of pouring. A direct comparison of the measured temperatures in alloy heating and subsequent pouring allows an understanding to be developed of which parameters cause a significant impact upon the induction melting phenomena. In turn, the effect of varying different parameters on the flow behaviour and temperature distribution of molten alloy in mould filling can be understood. The following graphs allow the direct comparison of temperature recordings, compared to baseline trials for the specified parameters.

Figures 4.63 and 4.64 allow the effect of melting a singular piece of 3 kg IN713C alloy to be compared to melting two IN713C pieces of equal length and a total mass of 3 kg, stacked upon each other. Comparing the effect of melting one piece of IN713C, to two pieces, for a mass of 3 kg it was not possible to discern a direct effect on the pouring temperatures. However, lower initial top face temperatures were detected. This could be due to the contact layer effect occurring from two pieces instead of one single billet.

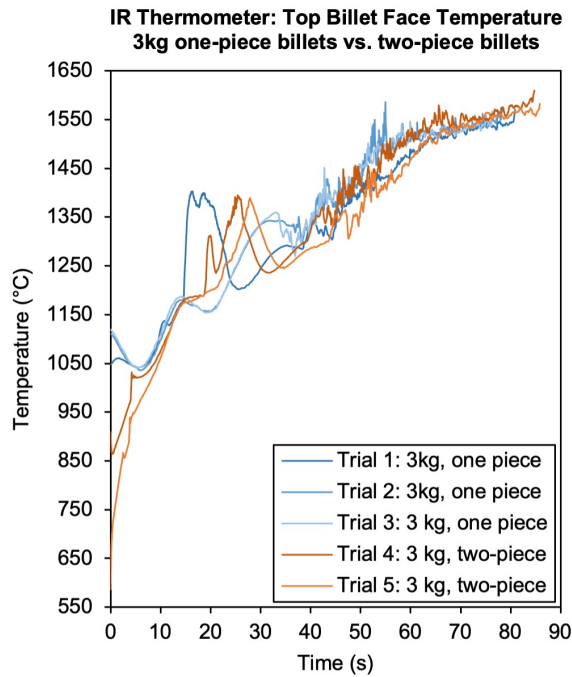


Figure 4.63: Trials 1-5, top face temps

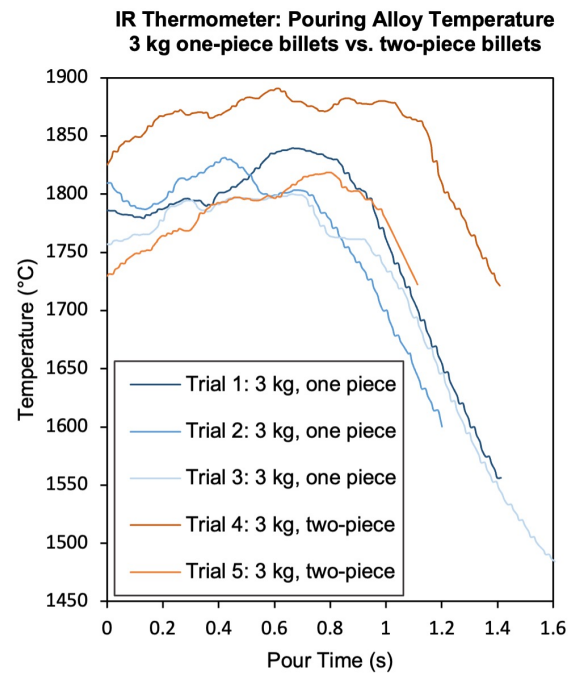


Figure 4.64: Trials 1-5, pouring temps

Figure 4.65 compares the effect of varying billet mass for IN713C, with one-piece billets melted of 2.5 kg, 3 kg, and 3.5 kg mass. There did not appear to be a significant difference in top billet face temperatures for 2.5 kg and 3 kg billets. As shown in Table 4.7, a longer time to melt was observed for 3 kg billets compared to 2.5 kg. In addition, it is clear that lower top face temperatures were produced in 3.5 kg billets compared to 2.5 kg and 3 kg billets. As the generator settings, stand height and crucible outlet diameter were kept constant across the trials, it was likely that the lower temperatures and longer time to pour for single piece billets of increased mass was due to the system requiring a longer time to melt larger masses, as more energy was required to melt them.

A significant difference was observed in the pouring temperatures with varying mass, as shown in Figure 4.66. 2.5 kg billets poured in less time than 3 kg billets, due to the lower total mass. However, the greatest difference was observed when comparing the pouring behaviour of 3.5 kg billets to those of 2.5 kg and 3 kg mass. The 3.5 kg billets took multiple times longer to finish pouring, with broken flow observed for the initial segment of the pour. This suggested a potential instability produced in the system when the mass of the billet approaches 3.5 kg. This could potentially be avoided by adjusting other process parameters, such as generator power, stand height or crucible outlet diameter.

4.5. INDUCTION MELTING: TESTING PROCESS PARAMETERS

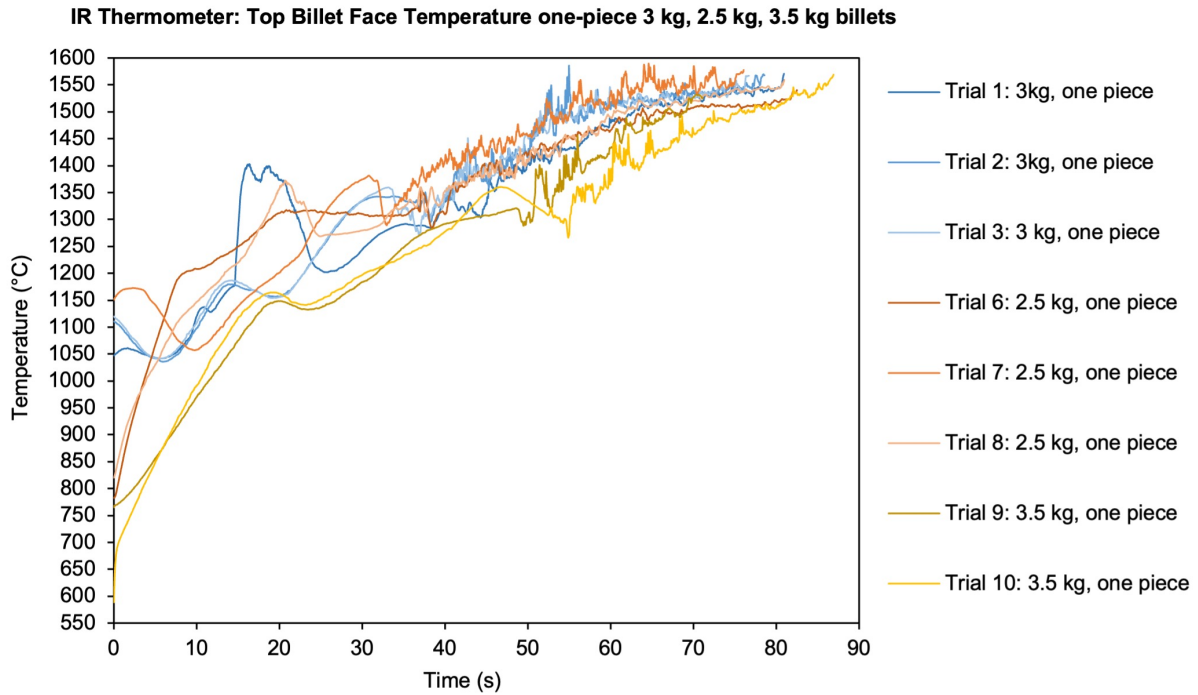


Figure 4.65: Trials 1-3, 6-10, top face temperatures

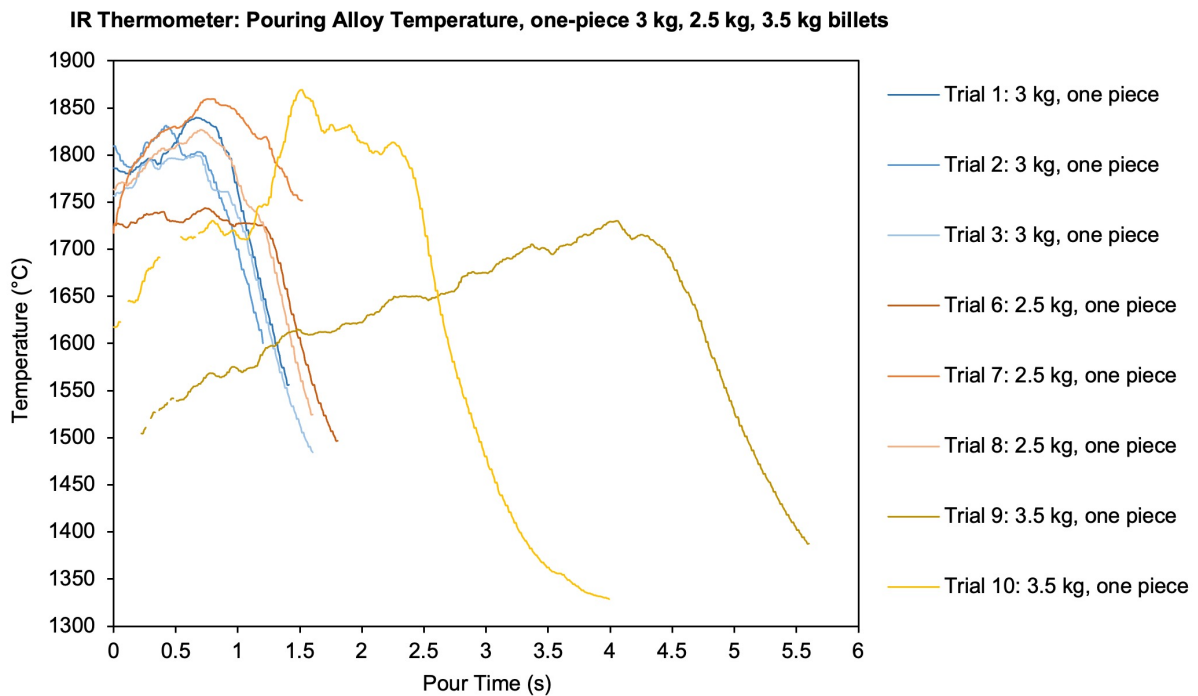


Figure 4.66: Trials 1-3, 6-10, pouring temperatures

The effect of varying generator power on the heating and pouring behaviour of 3 kg two-piece IN713C billets was tested, as shown in Figure 4.67. Table 4.7 shows a clear

4.5. INDUCTION MELTING: TESTING PROCESS PARAMETERS

relationship between power setting and melt time, with significantly longer times recorded for the lower power cycle, and shorter melt times for the 85 kW power.

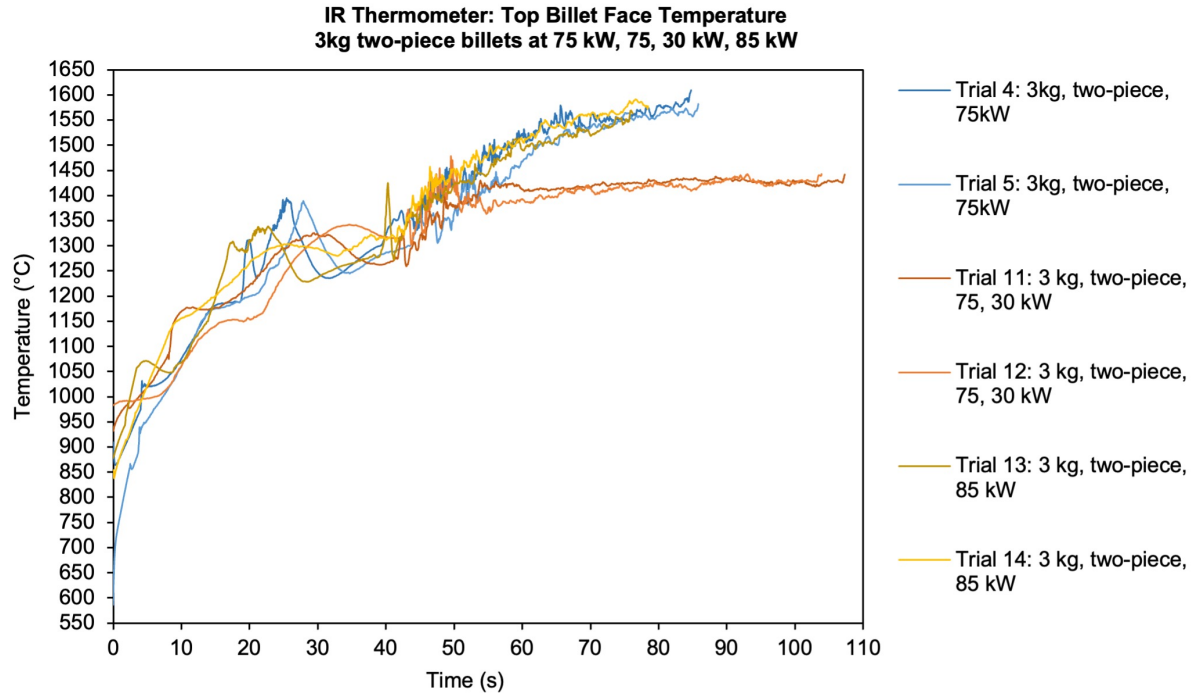


Figure 4.67: Trials 4, 5, 11-14, top face temperatures

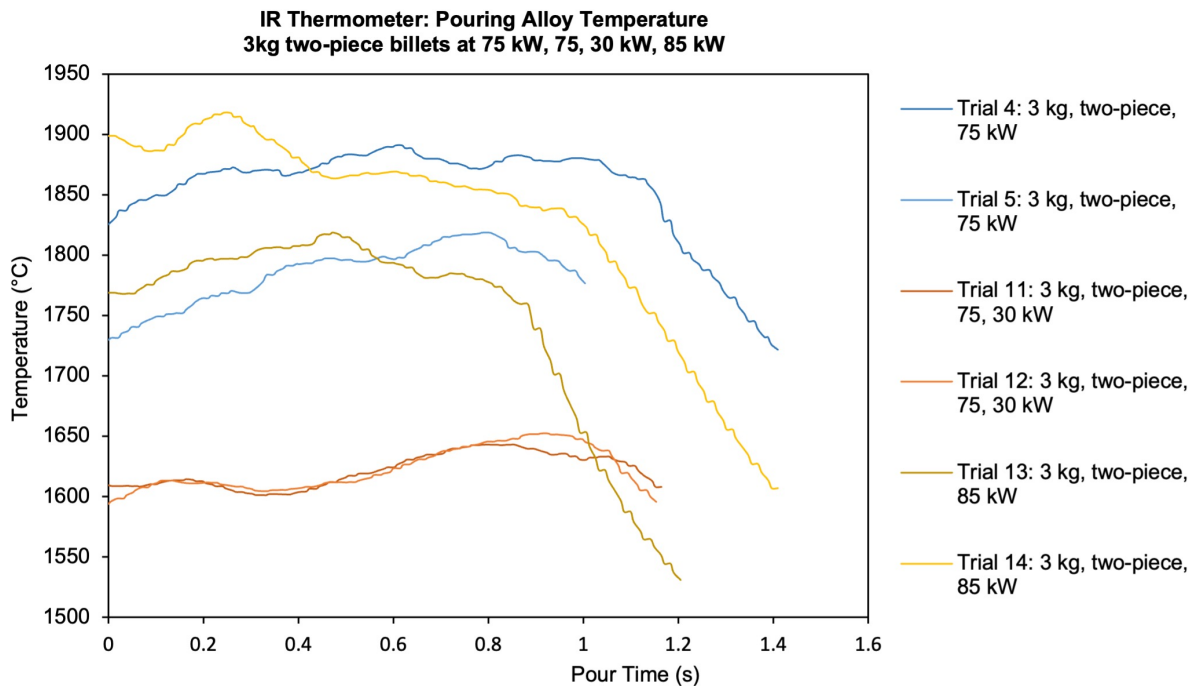


Figure 4.68: Trials 4, 5, 11-14, pouring temperatures

4.5. INDUCTION MELTING: TESTING PROCESS PARAMETERS

The standard melt cycle involved setting the power to 75 kW for the duration of the melt. The lower power cycle involved setting the power to 75 kW for one minute, followed by holding the power at 30 kW for the remainder of the melt. Finally, the higher power cycle consisted of holding the power at 85 kW for the duration of the melt.

The decrease in maximum recorded temperatures for the top billet face of Trials 11 and 12, involving the lower power cycle, was evident in the Figure 4.67. Equally, the pouring temperatures observed for these trials were also notably lower. The effect of setting the generator power to 85 kW on billet heating and pouring temperatures was less certain from examining the graphs. Figure 4.68 shows a larger temperature range observed in the pouring of billets melted using 85 kW, compared to those of 75 kW for the entire duration or 75 kW for one minute followed by holding the power at 30 kW for the remainder.

Examining Figure 4.69, it was not possible to determine the effect on top billet face temperatures of varying the number of pieces for 3.5 kg billets. However, examining Figure 4.70 it appeared that melting a 3.5 kg billet in two pieces instead of one greatly reduces the instability of the pouring behaviour. The pour time was also considerably reduced when melting this higher alloy mass in two pieces. In mould filling, broken flow, lower temperatures and longer pouring times are all risk factors which can contribute towards increased incidences of defect occurrence such as misrun, porosity and cold shuts.

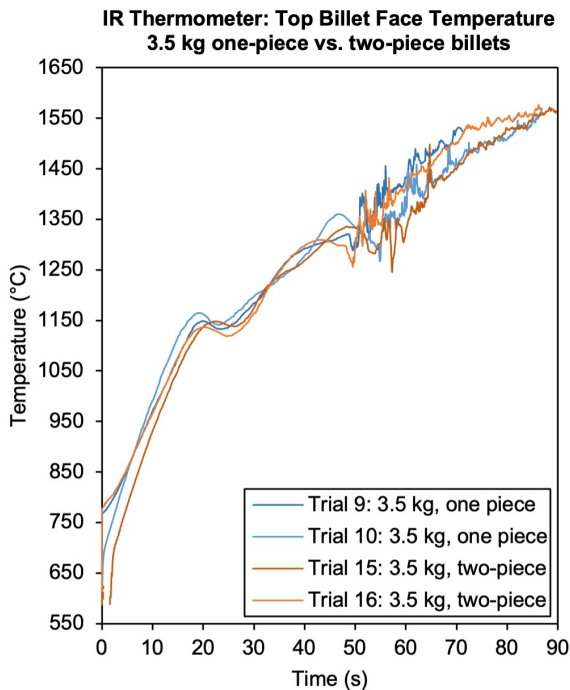


Figure 4.69: Trials 9, 10, 15, 16, top temps

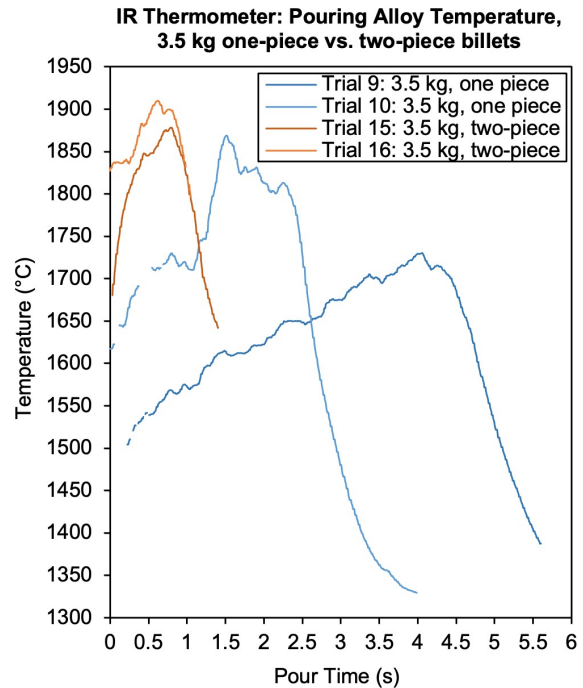


Figure 4.70: Trials 9, 10, 15, 16, pour temps

4.5. INDUCTION MELTING: TESTING PROCESS PARAMETERS

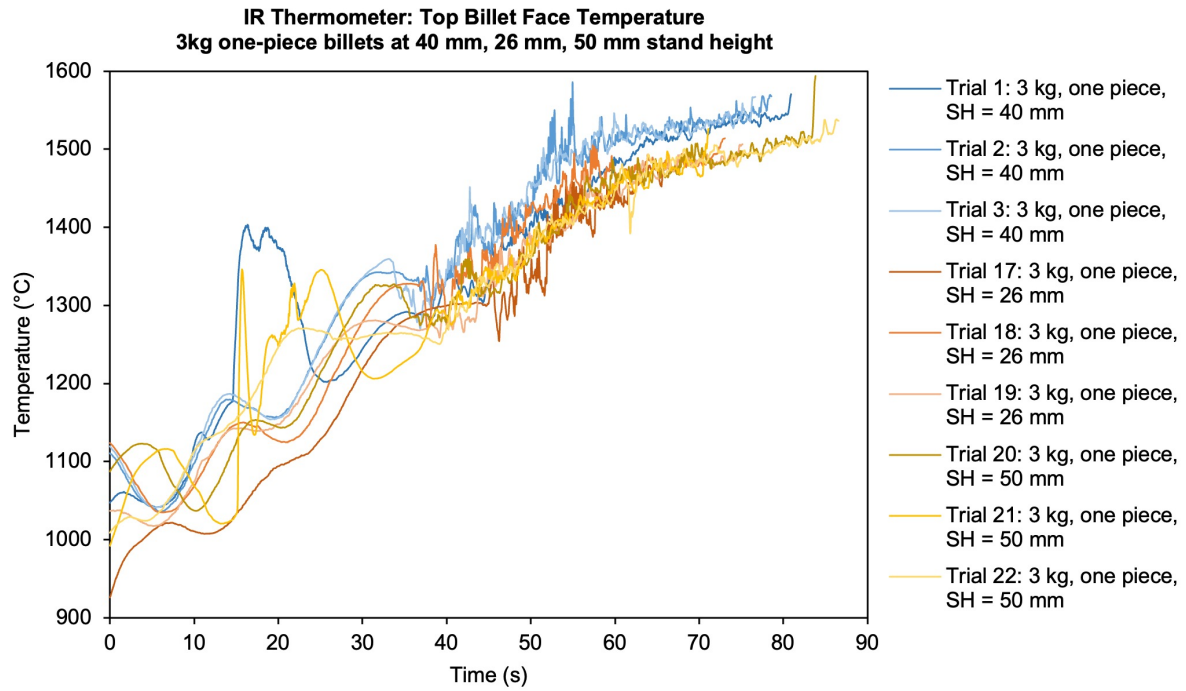


Figure 4.71: Trials 1-3, 17-22, top face temperatures

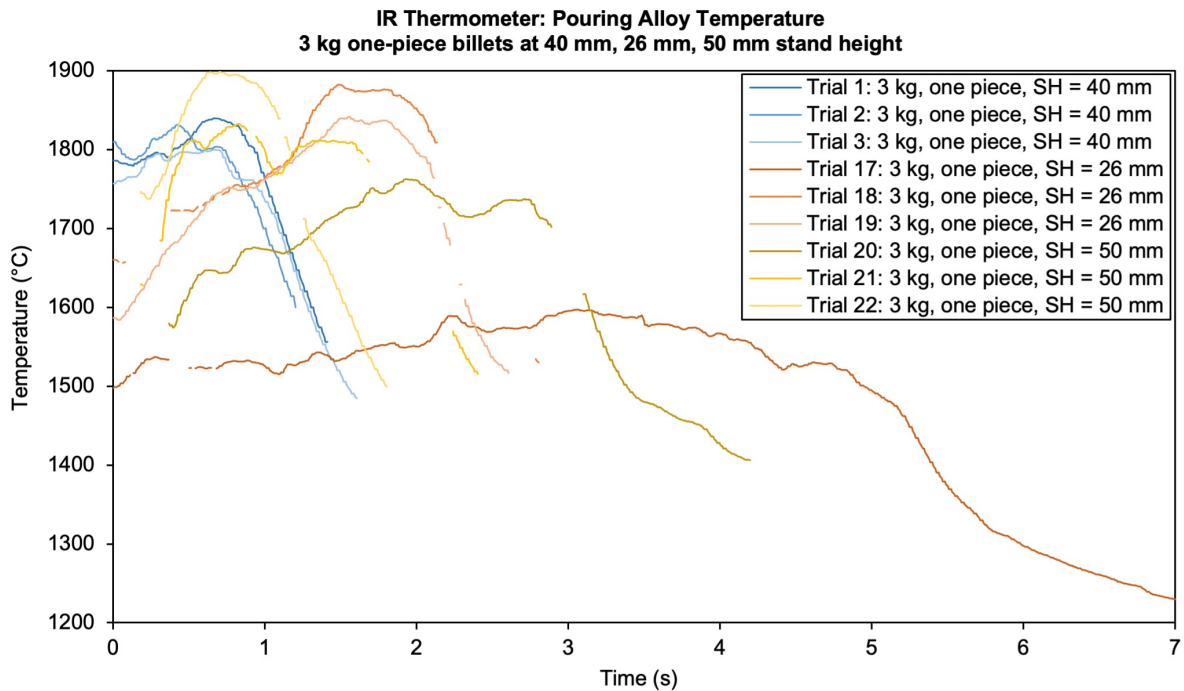


Figure 4.72: Trials 1-3, 17-22, pouring temperatures

Figure 4.71 indicated that the heating behaviour of the billet could be sensitive to billet position within the coil height, especially for a stand height of 26 mm compared to 40 mm and 50 mm. As a lower stand height value means that the bottom of the billet is

4.5. INDUCTION MELTING: TESTING PROCESS PARAMETERS

closer to the bottom of the coil, it is logical that a stand height of 26 mm would result in a faster heating rate of the top billet face. Figure 4.72 showed that the effect of varying stand height produced drastic differences in pouring. This highlights the importance of finding the narrow range of stand heights in which pour behaviour is favourable for the given billet mass. An incorrectly positioned billet, too low or high within the coil could cause broken flow and excessive pour times of up to seven seconds.

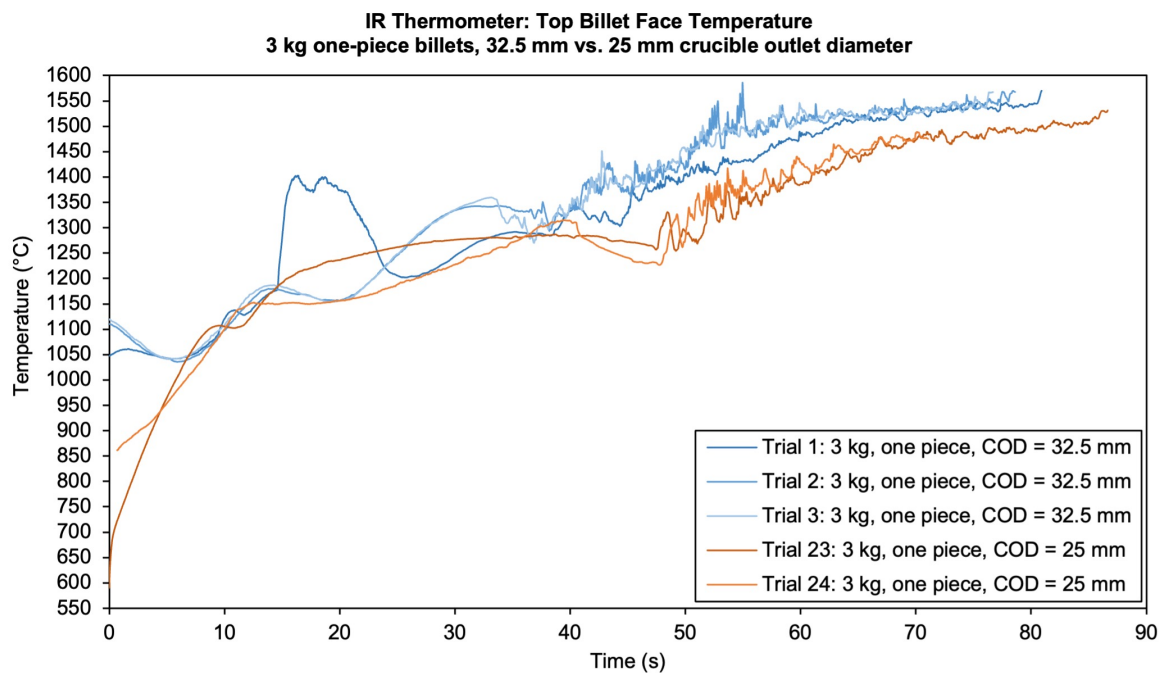


Figure 4.73: Trials 1-3, 23, 24, top face temperatures

Finally, Figure 4.73, suggests that the use of a crucible with an outlet diameter of 25 mm instead of 32.5 mm affects billet heating behaviour. All other crucible dimensions and process parameters were constant, thus this effect could not be explained.

Pouring temperatures also showed marked differences in Figure 4.74, with a reduced temperature range and a higher bottom temperature limit in the pours using crucibles with smaller outlet diameter. If proven, use of crucibles with 25 mm outlet diameter could be useful in preventing defects produced by lower pouring temperatures. Further tests are required to prove this effect.

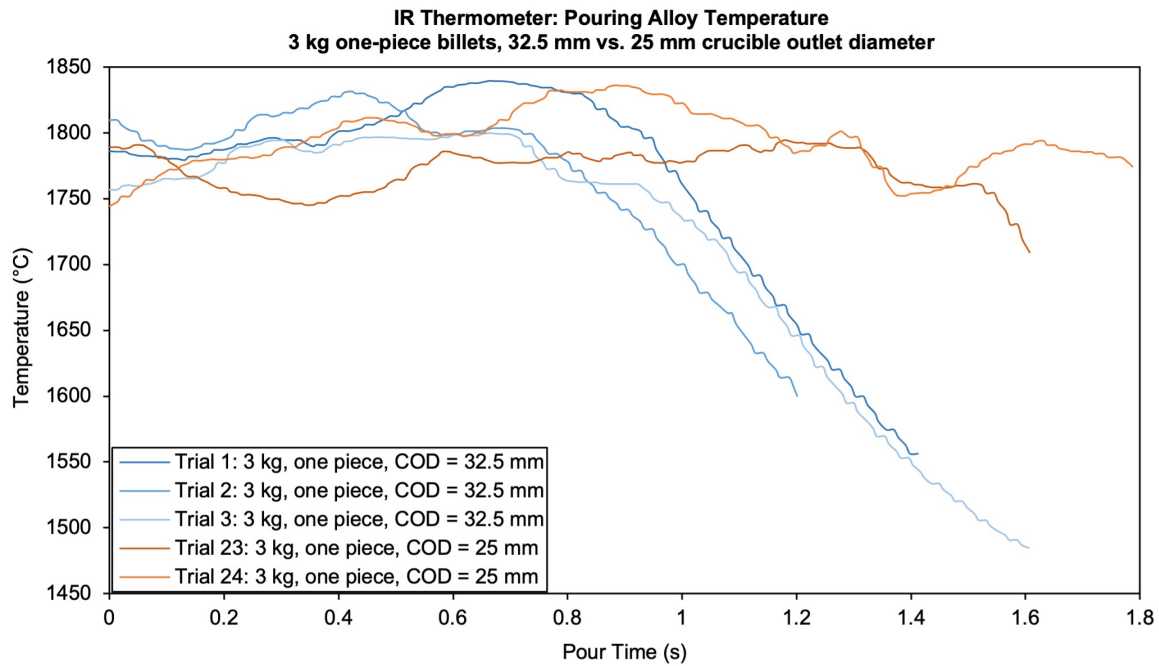


Figure 4.74: Trials 1-3, 23, 24, pouring temperatures

4.6 VIM-IC and Pouring Experiments Discussion

From the experiments performed in this chapter, it is evident that the presence of piping has an effect on total pour time. It also influences flow characteristics such as width, angle and fluid velocity. The presence of piping does not appear to have a large impact on top billet face temperature during induction melting. Although changes in temperature were observed between different runs of the DOE L9 array, these changes relative to the magnitude of the measured temperatures were not significant.

From examining the high speed camera images of different flow types, it is evident that Rayleigh-plateau instability is present when examining breakup behaviour in Figures 4.45-4.48. Rayleigh-plateau instability occurs due to the progressive narrowing of fluid jet radius, and is a known problem for fluids accelerating due to gravity according to Rapp [87]. In their work, Rapp describes the development of jet instability. After a given distance, the jet will present small ripples which are generated due to oscillations. If the oscillations occur at the correct frequency, they increase in amplitude and visible perturbations build up, resulting in a destabilised jet. Eventually, once a critical jet length is exceeded, the fluid breaks into droplets. It is stated that the curved surfaces on the jet cause an increase in Young-Laplace pressure gradients, which ultimately results in destabilisation and formation of the droplets. Figures 4.45, 4.47 and 4.48 demonstrate

the ‘main droplet and ligament’ structures observed by Oh *et al.* [88] in their studies of molten metal jet breakup behaviour. Meanwhile, Figure 4.46 has a wider overall flow width throughout the length of the jet, with curvatures caused by perturbations instead of flow breakdown into ligament sections.

Further to the flow instabilities and perturbations seen in Figures 4.45-4.48, a type of ‘corkscrewlike’ pattern of flow instability can be seen in Figure 4.75. This twisting and ‘corkscrewlike’ structure is similar to the sinuous mode flow breakup observed by Speirs *et al.* [89]. Although the circumstances for pouring are very different between molten metal and liquid helium, the purpose of their work was to define different breakup modes or regimes for jet flow instability. This type of instability pattern is further discussed in Section 5.25, as similar patterns are observed in the pouring simulations.

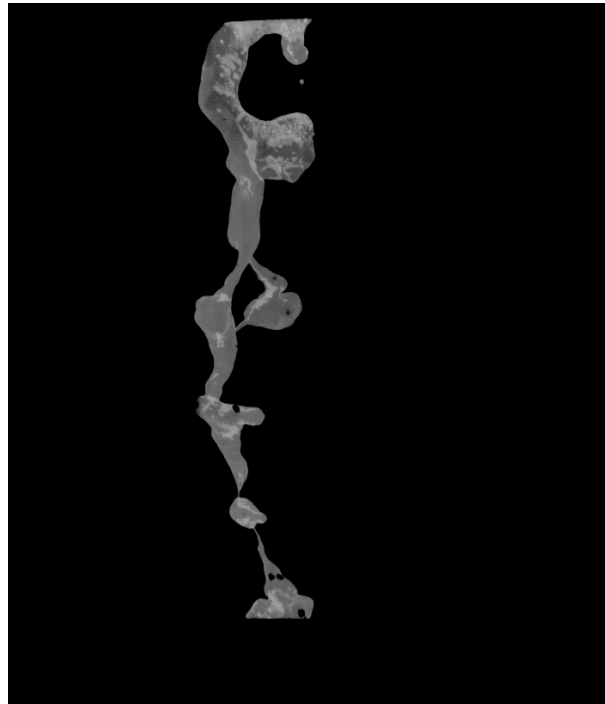


Figure 4.75: One-piece billet, end of pour high speed camera image

Examining the crucibles following their emptying of alloy, there were differences between the level of leftover alloy in the crucible between runs which poured completely, and those which did not. For example, Figure 4.76 shows the difference between the leftover alloy in the bottom of a crucible for a run which has poured completely, compared to the leftover alloy from Run 6. As Run 6 comprised of a two-piece billet with a bottom piece disc height of 35 mm, the crucible cracked slightly during pouring as the disc could be heard rattling during induction heating. When the crucible cracked mid melting, alloy would

4.6. VIM-IC AND POURING EXPERIMENTS DISCUSSION

pour out of the side of the crucible where it had cracked. This leaked alloy can be seen circled in orange in the image. Run 6 also has a 10 mm diameter hole located on the billet pouring face, and it is clear that the alloy has poured through this hole without fully melting through the bottom face of the billet. Figure 4.77 shows the remnants of alloy solidified within the crucible outlet, hanging from the crucible. This can occur where the alloy has mostly poured through, but the last part of the flow has solidified within the outlet at the end of the pour.



Figure 4.76: Alloy leftover from a complete pour (left) vs. Run 6



Figure 4.77: Leftover alloy solidified in crucible outlet after pouring

It is not possible to know if the range of pour times, flow widths, angles or velocities measured in the DOE L9 array experiments could potentially result in casting defects based on this data alone. To answer this, further casting trials involving mould filling are required, or mould filling simulations to predict defect occurrence. However, it is possible to examine trends from the ANOVA analysis data, and comment on the potential effect of particularly high or low values for each parameter.

An optimal pour time should allow the mould to fill in a short enough time to prevent defects such as misrun, but last long enough to ensure that flow instabilities are minimised. Very short pour times could result in significant mould erosion due to excessively high alloy velocities. From Figure 4.53, a hole positioned on the bottom billet face of the disc almost doubles the pour time compared to a one-piece billet. This could potentially be problematic, as both the alloy and mould experience cooling during pouring. The longer that the alloy spends cooling before mould filling has completed, the closer its temperature drops towards the mushy zone range. It is within this temperature range that misruns are likely to occur due to partial or full solidification mid filling. Lower alloy temperatures can also result in a higher incidence of porosity.

Equally, a flow width which is too thin has the potential to cool too quickly during pouring. A flow width which is too wide is likely to cause flow instabilities during pouring, which can contribute towards mould erosion. For holes on the bottom billet face, it is clear from Figures 4.54 and 4.55 that flow widths are significantly decreased. This is another factor which could further contribute towards misrun and porosity, for samples with a hole on the billet pouring face.

Highly angled flow could result in a mould filling asymmetrically. For a multi-tier investment casting tree mould design, a mould in which one side fills before the other could potentially allow the casting tree to cool asymmetrically, causing thermal stresses and bending throughout the casting tree. Initial flow angle appears to be largest for two-piece billets with a hole in the ‘top’ billet position, or with no hole at all in Figure 4.57. Flow angle also appears to be reduced for runs in which the hole is in the ‘bottom’ position. However, from examining the effect of holes in the ‘bottom’ position on pour time and flow width, it is clear that these factors are compromised for a hole in ‘bottom’ position. For a two-piece billet sample, a disc height of 15 mm also appears to greatly decrease the initial pour angle. This is beneficial, as ideally for a symmetrical mould, flow angle should be minimised relative to the centre line. Flow angles in the middle and end of the pour are smaller compared to the differences observed at the start of the pour. Arguably, flow angles and other flow parameters at the end of the pour are less important than the middle and start of the pour. The end of the pour consists of filling the top part of the central sprue in the mould, and is unlikely to affect the filling of the castings themselves.

Lowest flow velocities are seen at the start of the pour in Figure 4.60 for billets with a hole in the ‘bottom’ position. This is likely due to the reduced mass flow rate of alloy passing through a billet with a hole on the pouring face. Highest initial velocities are seen

4.6. VIM-IC AND POURING EXPERIMENTS DISCUSSION

in one-piece billets, and for two-piece billet samples with a disc of 15 mm height. It is not possible to determine the effect of these velocities on velocity related defects such as mould erosion without performing mould filling simulations. However, it is understood that higher filling velocities could contribute to greater levels of mould erosion and therefore inclusions in the finished castings. Gravity filled investment casting tree moulds are at an increased risk of mould erosion regardless, due to the nature of the high filling velocities and instabilities in flow from acceleration due to gravity.

It must be noted that flow width, angle and fluid velocity data is measured using two dimensional high speed camera images, when in reality these parameters are also subject to change in the third dimension. This was due to the limitation of the bespoke VIM chamber only having one viewing port large enough to record this data. A side viewing port was situated at 90° to the front viewing port, but it was too small and low relative to the chamber height to capture this data from a perpendicular viewing point.

Upon testing the effect of other process parameters in further induction melting experiments, it appears that both longer pour times and broken flow can be caused by one-piece billets of 3.5 kg mass and deviations in billet position within the coil, i.e. ‘stand height’. This can be seen in Figures 4.66 and 4.68. Broken flow could cause issues with mould filling, as these pieces of alloy could solidify within the mould, essentially causing misruns. The temperature of the alloy during pouring can also be controlled by adjusting the generator power. This was tested for two-piece billets of 3 kg mass in Figures 4.67 and 4.68. For applications requiring a small grain size, use of the ‘75, 30 kW’ power setting appears to reduce the range of pouring temperatures, while avoiding the high temperatures which could cause larger grain sizes or even columnar grains to form. Increasing the power to 85 kW for the duration of the melt causes a greater alloy pouring temperature range to be produced. This is undesirable as the higher temperatures may increase fluid velocity related defects such as inclusions, and the lower temperatures produced are more likely to result in porosity and misrun. This emphasises the importance of the delicate balance involved in determining the correct stand height for the given billet mass and generator power. However, the effect of varying generator power must also be tested for one-piece billets to understand the effect on pouring temperatures.

For all induction melting industrial experiments in this chapter, the crucibles were not preheated prior to loading the billet with alloy and performing the casting trials. This was due to the safety concerns regarding handling a crucible preheated to temperatures in excess of 1000°C. It was difficult to balance the loaded crucible on the clamp stand

fixture for these trials, and to do so with a hot crucible would raise major safety concerns. Therefore, safety was prioritised and crucibles were not preheated prior to the pouring trials. This is, however, a limitation of the temperature data from these induction melting experiments. Any data for alloy temperature during heating or pouring could differ compared to the alloy temperatures that would be produced if the crucible had been preheated in a typical casting scenario with mould filling. This is due to the potential differences in heat loss from the alloy that could take place if the crucible had been preheated.

4.7 VIM-IC Experiments Conclusion

In this chapter, a number of industrial induction melting experiments were conducted. Molten metal imaging experiments determined the best settings to use for the Photron FASTCAM SA4 high speed camera, to capture molten metal flow characteristics in high definition, from which fluid velocities can be calculated. The presence of piping on flow characteristics was investigated, including within one and two piece billets [OB2, OB3, OB4]. Due to unreproducible nature natural piping, holes were manufactured in piping-free concast billets to mimic the behaviour of piping in a more controlled way. A DOE L9 array of experiments was conducted using a bespoke VIM chamber, investigating the impact of disc height, hole diameter, and hole position on flow behaviour. During these measurements top-face temperatures were measured and high speed camera images were recorded. Parameters to characterise flow are extracted from these images, including velocities using a PIV MATLAB program. Using ANOVA analysis, trends in the flow are observed and will be compared with corresponding simulations in the next chapter. Interestingly, the variation in top face billet temperatures is found to be very small across the DOE L9 array of experiments, indicating it unlikely to be beneficial for predicting pouring behaviour.

To investigate whether top face billet temperatures were affected by process parameters including billet mass, number of billet pieces, power, billet position, and crucible outlet diameter, further trials were conducted. These trials had an additional purpose of alloy pouring temperature measurement, which were not measured in the set of DOE L9 array experiments due to lack of availability of a second IR thermometer [OB2]. Ultimately, changing process parameters such as billet mass and generator power resulted in marked differences in the top billet face temperature. From these experiments involving the temperature measurement of alloy during pouring, it was found that large temperature

4.7. VIM-IC EXPERIMENTS CONCLUSION

ranges up of to 400 °C could exist. It was also clear from these experiments measuring alloy pouring temperature that the temperature of the top billet face at pouring point was not representative of the actual temperature range of the alloy leaving the crucible, and that the pouring temperature was not constant due to the temperature gradient throughout the billet. Identifying the presence of a temperature gradient within the billet is crucial for building more accurate thermal models and specifying initial model conditions in the next chapter.

The data obtained from the DOE L9 array experiments is used to validate the VIM-IC heating and pouring models in the next chapter. Despite some differences within the experimental setup, measured alloy pouring temperatures from the experiments testing process parameters also serve as a good guide for model validation of pouring temperatures in the next chapter.

Chapter 5

Modelling VIM-IC: Induction Melting and Pouring

5.1 Modelling VIM-IC Overview

VIM computational models can be used as an effective tool to determine the temperature distribution throughout the alloy in the crucible, allowing for mould filling and subsequent solidification of an investment casting mould to be modelled effectively. Modelling the industrial VIM-IC process has been split into three separate models. The separation of these different modelling steps allows for the entire manufacturing process to be modelled efficiently. In both this chapter and Chapter 6, ESI ProCAST software is used to model the VIM-IC process in a series of models built to simulate the process, from induction melting to mould filling and solidification. Technical support was provided by Ole Koeser and Ronan Cronin of ESI Group.

ESI ProCAST is a software which uses FEM, and is typically used to model thermal heat transfer and radiation, and fluid flow in mould filling. Firstly, the induction melting process is simulated using the in-development ‘EMAG’ module with a thermal only induction heating model, not including computational modelling of the fluid flow in the melting process. It is important to note that although coupling fluid flow would allow for the physics of electromagnetic stirring to be captured, the purpose of this work was to create a model which is useful for generating alloy temperature profiles for casting defect prediction in industrial settings. Not only was modelling fluid flow in induction heating not possible due to fluid flow frequency limitations for the EMAG solver, but modelling

fluid would not be practical in terms of computational expense. To model induction heating with electromagnetic stirring, the time and cost associated with performing these simulations would outweigh the costs of running experimental trials instead. Furthermore, it is not common for foundries to possess the computing hardware with the capabilities required for running these coupled models.

The second part of modelling the VIM-IC process involves simulating the mould furnace preheat step. Preheating the assembled crucible and mould is crucial to prevent crucible failures due to thermal shock, and casting defects such as misruns and porosity, as part of the standard manufacturing process. Finally, the mould filling process can be simulated by applying the thermal conditions of the billet generated from the induction heating model, as an initial condition for the billet in an assembled crucible and mould geometry. The initial thermal conditions of the crucible and mould are imported from the mould furnace preheat model. The alloy drops into the mould cavity below the crucible, with both mould filling and solidification simulated in this final model. The ultimate goal of this work is to develop a modelling process which accurately captures defects in the finished castings, with the aim to determine if the existence of piping, its size and location relative to the pour face, and disc height affects casting defect prevalence and severity.

In addition to the standard models developed for modelling the industrial process, pouring simulations which replicated the DOE L9 array experiments in Chapter 4 were developed. This was to provide validation for the VIM models, with direct comparison to experimental results to determine if it was possible to predict characteristics of the resultant alloy pouring using a thermal only induction heating model. ANOVA analysis was conducted for simulation results, comparing the trends with those observed from experimental data. Additional data, including temperature data of the alloy during pouring was captured by analysing pouring simulation outputs. This chapter covers VIM and pouring simulations replicating the DOE L9 experimental array. Mould preheat, filling and solidification models are described in Chapter 6.

5.2 Modelling VIM-IC: ESI ProCAST EMAG Module Overview

The ESI ProCAST ‘EMAG’ module, which forms part of the ESI ProCAST Visual-Cast software package, is electromagnetics modelling package in the beta stage of software development. The module works by solving Maxwell’s equations, with defined voltage

5.3. MODELLING VIM-IC: ESI PROCAST EMAG MODULE GOVERNING EQUATIONS AND PHYSICS

boundary conditions applied to the nodes of induction coil terminals for the application of induction heating in the context of VIM-IC.

The EMAG solver is described as a ‘low frequency electromagnetic edge element solver’ [90]. It is important to note that a limitation of using this solver to model the industrial VIM-IC process is that fluid flow can not be reliably modelled as part of the induction heating process for frequencies above 1 kHz. As the desired frequencies for this application were in excess of 1 kHz, fluid flow could not be accounted for during the induction heating stage. The benefit of modelling induction heating using the EMAG solver is that it is built into ESI ProCAST Visual-Cast, which is optimised for modelling the industrial investment casting process in both filling and solidification.

Using EMAG, a harmonic solution in the frequency domain is produced for the generated magnetic field distribution. This computed initial solution is repeated for the duration of the heating simulation, which only requires one time step to be computed when modelling electromagnetics. This neglects the effect of displacement currents as these are time-varying electric fields, which is the $\partial D/\partial t$ term within Maxwell’s equations defined in the terms of rate of change of electric displacement field, D . Although this is by definition not a fully coupled solution, the phase shift in the frequency domain is addressed using a complex formalism. This allows the EMAG solver to serve as a close approximation for modelling electromagnetic applications in a time and computationally efficient manner.

5.3 Modelling VIM-IC: ESI ProCAST EMAG Module Governing Equations and Physics

This section defines the formalisms under which EMAG solves Maxwell’s equations [90]. Firstly, as written in (3.4), Gauss’ law for magnetism states that the total magnetic field, or magnetic flux density, B through any closed surface is zero, so that $\nabla \cdot B = 0$. i.e. there can be no magnetic monopoles. The conservation of magnetic flux is implemented by the solver as follows, where S is the vector area of the surface that the magnetic flux is passing through:

$$\oint B \cdot dS = 0 \tag{5.1}$$

Secondly, the contour integral of current density J is governed by $\nabla \cdot J = 0$, where the

5.3. MODELLING VIM-IC: ESI PROCAST EMAG MODULE GOVERNING EQUATIONS AND PHYSICS

electric continuity equation is implemented as follows for the vector area S of the closed surface which the electric current is passing through:

$$\oint J \cdot dS = 0 \quad (5.2)$$

Ampere's excitation law allows the magnetomotive force to be defined by $\nabla \times H = J$. The contour integral of magnetic field strength H is defined by:

$$\oint H \cdot dl = I \quad (5.3)$$

This applies for a differential of the closed curve which encloses a two dimensional surface integral, for which dl is an infinitesimal element. Faraday's induction law can be applied to calculate the electromotive force, which is the contour integral of electric field E , given a sinusoidal magnetic flux density of the form $e^{j\omega t}$:

$$\oint E \cdot dl = -\frac{d\Phi_B}{dt} = -j\omega\Phi_B \quad (5.4)$$

In (5.4), complex imaginary unit $j = \sqrt{-1}$, ω refers to the angular frequency and Φ_B is the total magnetic flux through the surface enclosed by the closed curve. This total magnetic flux, Φ_B , is described in (5.5):

$$\Phi_B = \oint A \cdot dl \quad (5.5)$$

where solenoidal magnetic vector potential A is formalised by (5.6):

$$B = \nabla \times A \quad (5.6)$$

The total electric current flowing through a surface, I and total magnetic flux through a surface, Φ_B are defined as (5.7) and (5.8) respectively:

$$I = \int J \cdot dS \quad (5.7)$$

$$\Phi_B = \int B \cdot dS \quad (5.8)$$

According to Helmholtz's theorem, the Helmholtz decomposition of the electric field can be written as follows:

$$E = -j\omega A - \nabla U \quad (5.9)$$

The magnetic field, B , is related to the magnetic field strength, H according to the following equation:

$$B = \mu H \quad (5.10)$$

where μ is the magnetic permeability. Ohm's law relates the current density J and the electric field E , according to the following equation:

$$J = \sigma E \quad (5.11)$$

where σ is the electrical conductivity. From these equations, the governing equation can be derived:

$$\nabla \times \left(\frac{1}{\mu} \nabla \times A \right) = J = \sigma(-j\omega A - \nabla U) \quad (5.12)$$

The ESI ProCAST EMAG module solver solves these equations in the frequency domain as an initial step for the simulation. From the fields calculated in this initial step, a static heat source is determined, which depends on the electromagnetic properties of the materials being modelled. This is then coupled with a time-domain heating model, to calculate the temperature over time as a result of the induction heating process.

5.4 Modelling VIM-IC: Material Properties

In addition to the thermophysical properties of materials, when modelling electromagnetics it is important to consider the electromagnetic properties of materials. The magnetic permeability and electrical conductivity for each studied material are shown in Table 5.1.

According to Fisk, Inconels can be considered to be paramagnetic, which means that it has a relative permeability of 1 [4]. However, it should be noted that this is only true when the alloy is at or above the Curie temperature. The Curie temperature of IN713C

5.4. MODELLING VIM-IC: MATERIAL PROPERTIES

cannot be found in the literature, and values range widely for different types of Inconel. Therefore, it is difficult to estimate the value of the Curie temperature for IN713C. However, it is important to note that IN713C contains a significant alloy weight percentage of Chromium, at 12-13 % [60]. According to Barton *et al.*, the presence of Chromium within the composition of an alloy results in a significantly lower Curie temperature [91]. Although the Curie temperature of IN713C is not known, the lowering of the Curie temperature caused by significant levels of Chromium has informed the decision to treat the alloy as paramagnetic throughout the heating simulation. This assumption has its limitations, and the model could be improved by conducting experiments to determine the Curie temperature. The relative permeability of IN713C below the Curie temperature could then be adjusted accordingly, by inputting magnetic permeability as a temperature dependent value. Relative permeability is the ratio of the permeability of a given material to the permeability of a vacuum μ_0 , where $\mu_0 = 1.26 \times 10^{-6}$ henry per metre. The relative permeability of copper is also 1, according to Paul [92]. The relative permeability of both aluminosilicate ceramic fibre and air are also assumed to be unity.

Material	Magnetic Permeability (henry/m)	Electrical Conductivity (S/m)
IN713C	1.26×10^{-6} [4]	660 000 [93]
Copper	1.26×10^{-6} [92]	6×10^7
Aluminosilicate Ceramic Fibre	1.26×10^{-6}	1×10^{-12}
Air	1.26×10^{-6}	1×10^{-12}

Table 5.1: Electromagnetic properties for the studied materials

Electrical conductivity of IN713C was set as a constant value of 660 000 Siemens per metre (S/m), which was the average value taken across a temperature range from the COMSOL materials database [93]. The electrical conductivity of copper was taken to be 6×10^7 S/m, and zero for both aluminosilicate ceramic fibre and air. As ProCAST software does not allow a zero value to be applied as a material property value, a very small value of 1×10^{-12} S/m was assigned.

As previously mentioned in Section 2.2, the thermal conductivity values for IN713C in excess of the solidus temperature were artificially increased, steadily up to 1800 W/m·K at liquidus temperature. This was to account for the lack of fluid flow in the induction heating model, which would otherwise cause faster heat transportation to occur throughout the

billet due to the effect of electromagnetic stirring.

5.5 Modelling VIM-IC: Geometry and Mesh

5.5.1 Coil Test Section: Mesh Refinement Study

To create a satisfactory mesh for the VIM-IC geometry in the context of conducting induction heating simulations, it is important to consider the distribution of elements within the conductor volumes. In the case of the VIM-IC setup, it is important to create a mesh which is appropriately refined in both the coil and billet skin depth regions. Using (3.7), for a frequency of 7.93 kHz, the skin depth of copper and IN713C were calculated to be 0.73 mm and 6.93 mm respectively.

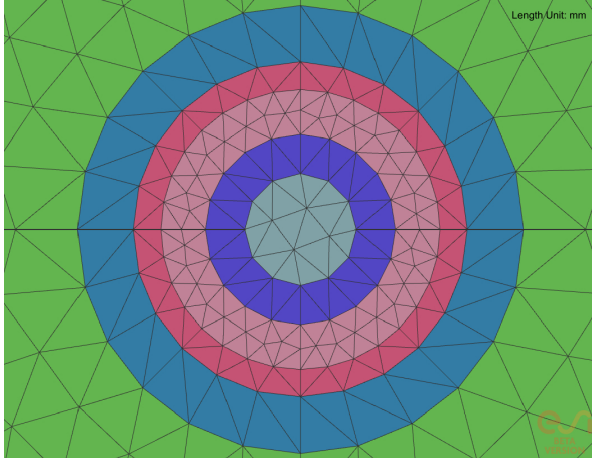


Figure 5.1: Coarse coil mesh

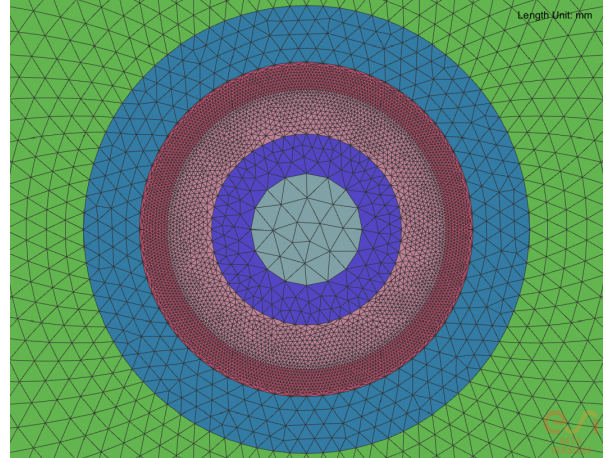


Figure 5.2: Fine coil mesh

As the convention dictates that four elements must be distributed across the skin depth of each conductor volume, this would require a very small element size, with an edge length of 0.18 mm within the skin depth for the coil. As the meshes of the VIM models of the VIM-IC setup without a skin depth refined coil mesh were already in excess of 20 million elements, it would not be practical to mesh the coil skin depth with the dictated skin depth element size values. Therefore, a study was conducted to test the effect of a coil section meshed with the prescribed element lengths within the skin depth region, compared to a coil meshed with a practical, coarser mesh size. The generated magnetic field for both coil test sections were compared, to ascertain if a coarser coil mesh produced satisfactory results. Figures 5.1 and 5.2 show the meshed coil test sections, with a coarse and fine mesh respectively. The 10 mm diameter coil test sections were 2.4 mm thick, with the surrounding air volumes also meshed to this thickness. The total outer radius

of the air volume was 80 mm. The fine mesh was developed according to the prescribed element edge length values required within the skin depth, with the light pink region representing the coil region. The regions within the coil geometry represent the water cooling channels, with the outer blue and green regions representing the surrounding air volumes. The finite element meshes for these coil test models were created using ProCAST Visual-Mesh software. 3D tetra elements were generated based upon the defined 2D tria element surface mesh. Both the 2D and 3D meshes passed the relevant mesh quality checks. This built in software function allows for any topological mesh problems to be detected, which searches for any issues with surface mesh boundaries such as cracks and holes, overlapping elements, and element intersections. It also allows for minimum edge lengths and internal angles to be checked. Equally, the volume mesh quality check was performed, to ensure that the minimum Jacobian value of 0.7 was met.

The material properties for air and copper were assigned according to the values listed in Table 2.1 and 5.1. In this model, water cooling channels were modelled as air volumes. The boundary conditions assigned to this model related to both heat transfer coefficients, and applying the physics of electromagnetics. Although the water cooling channels and surrounding air were each made from two separate volumes, an ‘equivalence’ interface condition was assigned between the two regions. This was to ensure that a heat transfer continuum was maintained between the two domains. The main purpose of this model was to compute a representative electromagnetic field which would have been produced by the coil geometry in experiments. It should be noted that the temperature throughout the coil volumes was not part of this study and was overlooked in the initial model development. This could impact the temperature of the coil volumes, but this has not been accounted for. Additionally, this model could be improved if the water cooling channels were modelled as water instead of air. Between the coil and cooling channel, and the coil and surrounding air volume, a heat transfer coefficient value of 50 000 W/m²K was applied. This ensured rapid cooling of the coil, to ensure that it did not heat excessively. As the electromagnetic properties of copper were set as constant values and not temperature dependent, it was not important for this model to accurately capture the heating within the coil itself and cooling via internal channels or to the ambient air volume. In ProCAST Visual-Cast software, when there is a temperature discontinuity at the interface between two volumes, a ‘coincident’ interface is assigned to enable a heat transfer coefficient to be applied. ‘Coincident’ refers to ‘coincident nodes’, as the nodes created in mesh generation must be duplicated at a volume interface in order for distinct temperatures to exist on each side of the interface. The temperature of all volumes was set to an ambient temperature of

5.5. MODELLING VIM-IC: GEOMETRY AND MESH

25 °C. A Dirichlet voltage boundary condition of 555 V was applied to the nodes on the top face of the coil section, with a Dirichlet voltage boundary condition of 0 V applied to nodes on the surface of the bottom face of the coil geometry. By applying Dirichlet voltage boundary conditions to the nodes at the coil terminals, the tangential electric field across these nodes was fixed at zero as a result. To ensure that the studied domain included air, an artificial air enclosure volume was created to ensure that the air domain does not extend indefinitely. A magnetic vector potential was set to zero throughout the exterior surfaces of all volumes.

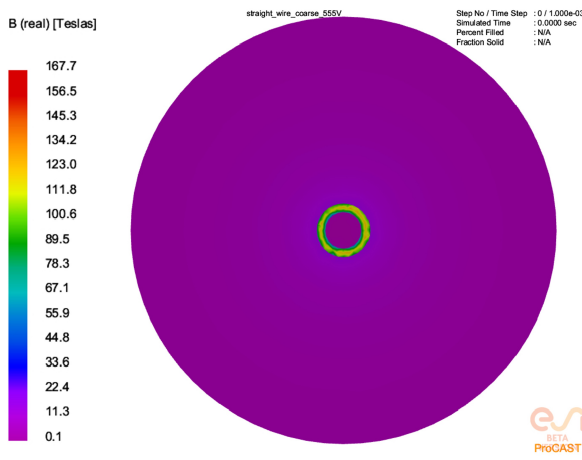


Figure 5.3: Coarsely meshed coil: B (real)

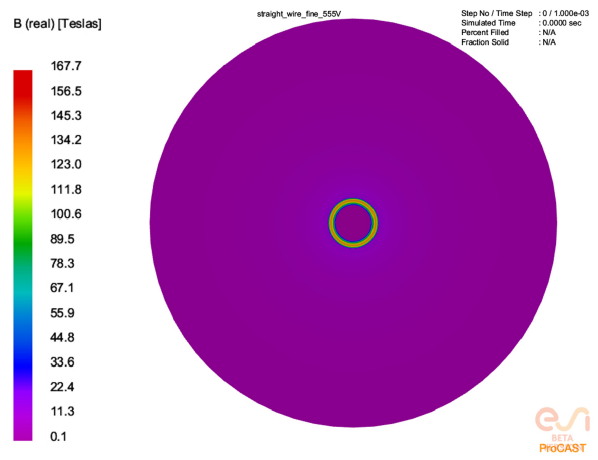


Figure 5.4: Finely meshed coil: B (real)

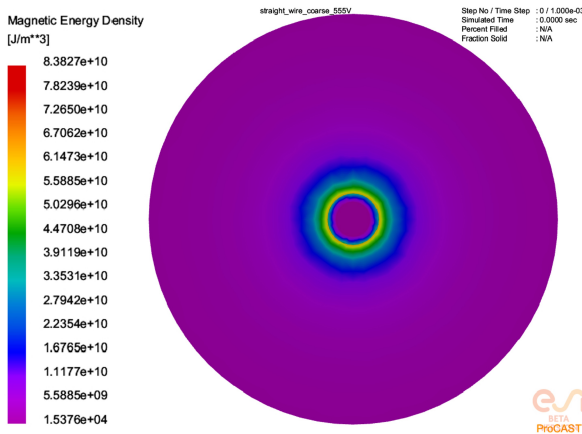


Figure 5.5: Coarsely meshed coil: Magnetic Energy Density

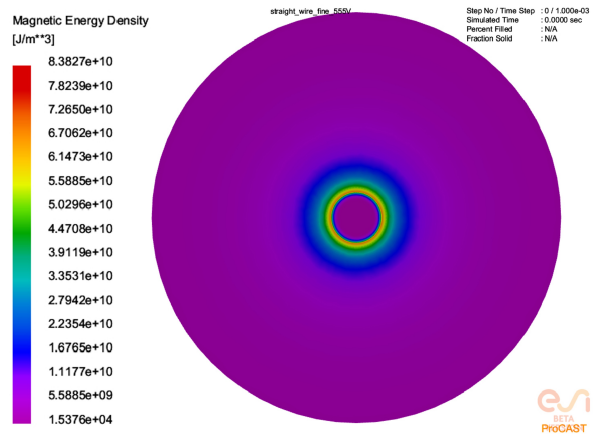


Figure 5.6: Finely meshed coil: Magnetic Energy Density

The induction simulation was performed using the electromagnetics solver from the ‘EMAG’ module in ESI ProCAST Visual-Cast software, which is currently in its beta development stage. Within the simulation parameters, the applied frequency of the electric field source

was set to 8 kHz and the model was run for a total of ten time steps, as this was sufficient to determine the electromagnetic field produced by the coil under the given conditions. The magnetic flux density ‘B (real)’ in Teslas within the volumes for a coarsely meshed coil compared to a finely meshed coil can be seen in Figure 5.3 and 5.4. It is evident that a similar distribution of magnetic flux density within the coil regions exists, with a higher definition of the distribution observed for the finely meshed coil test section. More importantly, the magnetic energy density in J/m^3 in the surrounding air volumes can be compared for Figures 5.5 and 5.6, which are the coarsely and finely meshed coils respectively.

In the VIM-IC model geometry including the crucible and billet in induction heating, the total distance between the outer surface of the coil and the furthest node within the skin depth region of the billet is 21.6 mm. This lies within the region of the air volumes tested in this coil section test model. It is evident that the magnetic energy density produced is comparable in the surrounding air regions. Although a more refined mesh within the coil and its surrounding air volume allows for higher definition results in the immediate elements surrounding the coil volume, the magnetic energy density produced by the magnetic field in the region of the billet heating zone is satisfactory. It should be noted that a graph could be plotted from a radial section, to provide further quantitative detail on the maximum difference between B(real) and Magnetic Energy Density for the coarse and fine mesh models, as part of assessing the effect of mesh independence.

5.5.2 Modelling VIM-IC: Geometry and Mesh

A cross section of the meshed geometry of the IN713C billet, crucible, coil and surrounding air volume in the VIM-IC industrial process can be seen in Figure 5.7.

This mesh is made from 3D tetra elements, which were generated based upon the defined 2D surface mesh. This mesh was created using ESI ProCAST Visual-Mesh software. The 3D tetra elements were created using a default volume mesh algorithm, with refinements applied to elements within the skin depth of both the billet and the induction coil. The calculated billet skin depth was created as a separate billet outer layer volume, which allowed for mesh refinement within this region. A tetra mesh with a gradual, linear size transition was assigned to this skin depth layer volume with four layers within this defined thickness. This allowed for the convention to be followed regarding modelling electromagnetics and recommended element distributions across skin depth regions. The coil was meshed as per the coarsely meshed coil in Subsection 5.4.1. The mesh of

5.5. MODELLING VIM-IC: GEOMETRY AND MESH

the VIM-IC geometry passed the relevant surface and volume mesh quality checks, as described in Subsection 5.4.1.

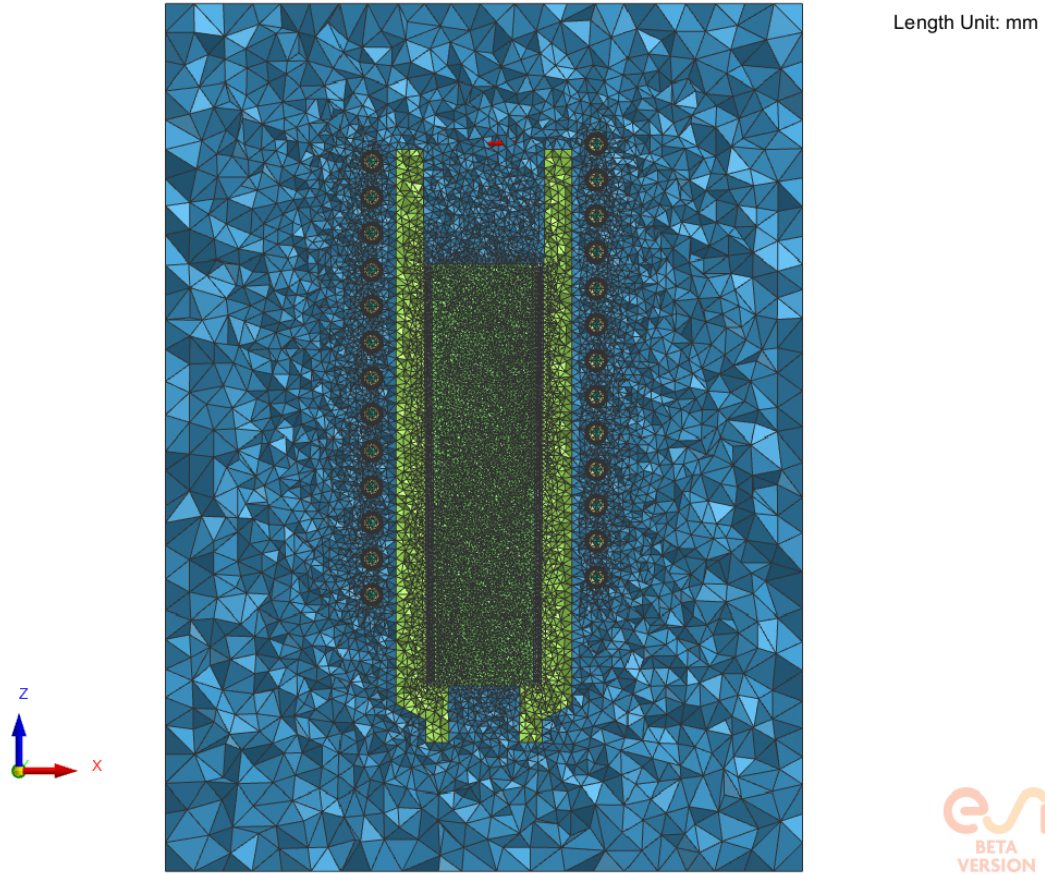


Figure 5.7: VIM geometry: tetra element 3D mesh cross section

The coil consisted of 13 turns, with a total height of 200 mm. The total coil outer diameter was 110 mm, with a wire diameter of 10 mm. The billet was 50 mm in diameter, with a total height of 185 mm. This billet height for the given diameter was the equivalent of 3 kg of IN713C. The tested crucible geometry had an outlet diameter of 32.5 mm. It is important to note that in the real world VIM-IC setup, a small gap exists between the billet and crucible walls to allow clearance for the billet to be inserted. However, in this model geometry, the billet was considered to fit perfectly within the crucible, and this gap was not meshed. This was a necessary simplification of the model geometry, alongside the lack of an applied radius for the inner surfaces of the crucible.

5.6 Modelling VIM-IC: Materials and Boundary Conditions

All volumes were assigned an initial ambient temperature of 25 °C, with all material properties applied as defined in Tables 2.1 and 5.1. The surrounding air volume and internal volumes within the coil cooling channels were assigned with the thermophysical and electrical properties of air. The billet and its outer skin depth layer volume were assigned with the properties of IN713C. Finally, the crucible was defined as aluminosilicate ceramic fibre, with the induction coil set as copper material.

All separate meshed volumes which were assigned as the same material were given an ‘equivalent’ interface setting, to ensure that the separately meshed volumes were treated as part of the same volume. Between the coil and cooling channel, and the coil and surrounding air volume, a heat transfer coefficient of 0 W/m²K was applied. These conditions were implemented using a ‘coincident’ interface. A heat transfer coefficient value was estimated for the interface between the billet and crucible to be 500 W/m²K for an induction heating model. For the heat exchange between the billet and surrounding air volume, an emissivity of 0.85 was applied to the interface between the billet itself and the air. This value was applied as it served as a reasonable estimate for a fixed emissivity value, based upon the experiments in Section 2.4.

A Dirichlet voltage boundary condition of 555 V was applied to the nodes at one coil terminal, with a Dirichlet voltage boundary condition of 0 V applied to nodes on the surface of the other coil terminal. By applying Dirichlet voltage boundary conditions to the nodes at the coil terminals, the tangential electric field across the nodes at the terminals was fixed at zero as a result. The surrounding air was accounted for by using an artificial air enclosure volume, created to ensure that the air domain does not extend indefinitely. A magnetic vector potential was set to zero throughout the exterior surfaces of all volumes.

5.7 Modelling VIM-IC: Simulation Parameters

The model was run using ESI ProCAST Visual-Cast software, with the EMAG module applied for modelling electromagnetics in combination with thermal effects. The applied frequency of the electrical field source was set to 7.93 kHz. Time steps were significantly reduced around the estimated pouring time to 0.01 seconds, as it was important to capture

the progression of the melting front close to the bottom billet face.

5.8 Modelling VIM-IC: Results

The generated magnetic flux density and magnetic energy density can be seen in images of a cross section of the VIM-IC geometry, Figures 5.8 and 5.9.

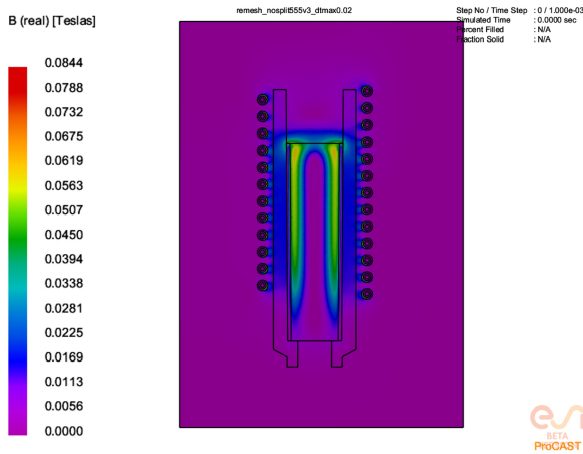


Figure 5.8: VIM-IC Model: Magnetic Flux Density

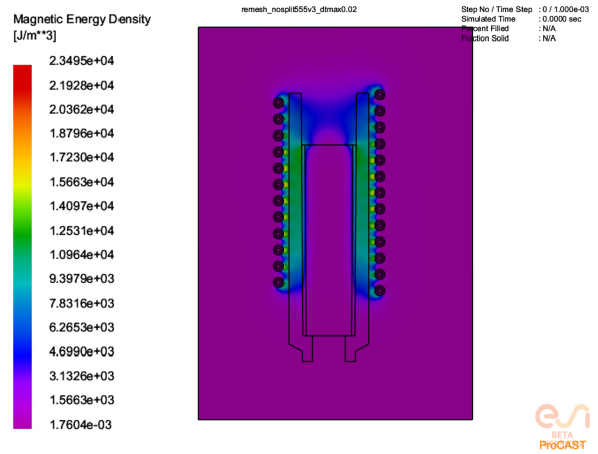


Figure 5.9: VIM-IC Model: Magnetic Energy Density

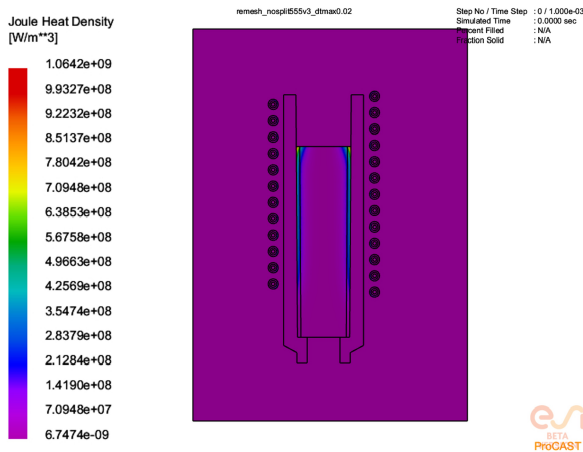


Figure 5.10: VIM-IC Model: Joule Heat Density

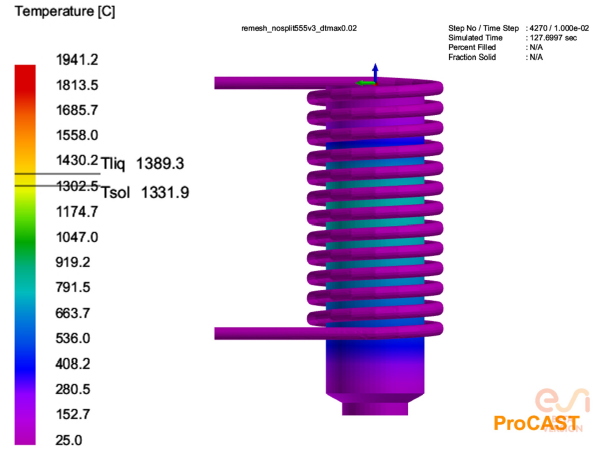


Figure 5.11: VIM-IC Model: temperature in coil and crucible at pour point

It is evident from Figure 5.10 that the most concentrated region of joule heating lies within the skin depth volume of the billet, as calculated using the skin depth equation. Figure 5.11 shows the temperature distribution across the crucible and coil at the predicted

5.8. MODELLING VIM-IC: RESULTS

pouring time step. Accurate prediction of the time step at which the alloy would start pouring is arbitrary, and it can be difficult to predict the criteria for pouring initiation from the bottom billet face. A fraction solid value of 0.3, $fs_{0.3}$, was chosen as the point along the fraction solid curve at which the alloy would pour from the bottom billet face. This is due to the ‘mobility limit’ of 0.3 as a default value in models with flow activated.

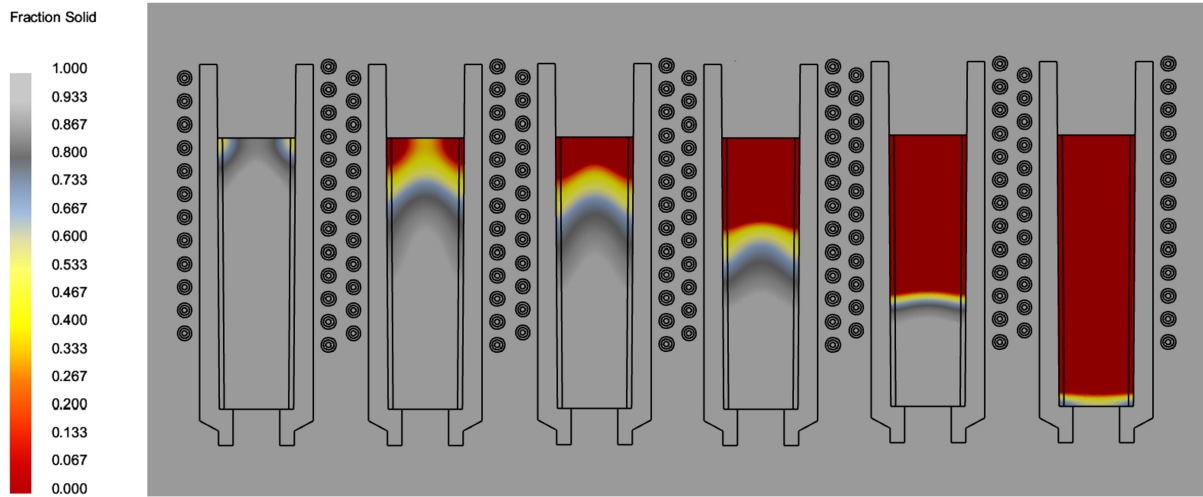


Figure 5.12: Fraction solid: melt front progression in induction heating (left to right)



Figure 5.13: Billet heated by induction for 50 seconds before generator switch off [94]

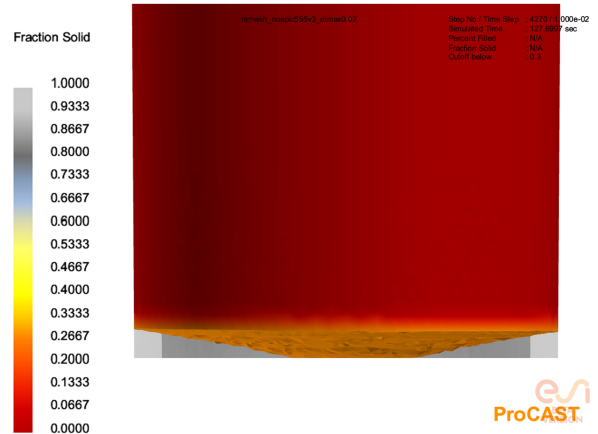


Figure 5.14: VIM-IC Model: Fraction solid distribution at pour point, cut off at $fs_{0.3}$ plot

5.8. MODELLING VIM-IC: RESULTS

The time step at which the alloy along the bottom billet face surface first reaches $fs_{0.3}$ was 127.7 seconds, which was considered to be the pour point. Progression of the melting front throughout the induction heating simulation can be seen in Figure 5.12. Although the melting pattern is different to the pattern displayed in the small induction melting experiments, this is due to the difference in induction coil position relative to the overall length of the billet. In the small scale induction melting experiments, the coil was positioned centrally relative to the overall billet length, whereas the billet is positioned significantly lower relative to the coil for the industrial application. This allows the last section of the billet length to melt by conduction.

Figure 5.13 is a photograph of a billet from an industrial trial in which the generator was switched off at 50 seconds. This can be compared to the early melt front progression in Figure 5.12, to determine if the melting pattern obtained by modelling induction melting without fluid flow activated produces a reasonable representation of the phenomena. Equally, Figure 5.14 shows a cut off result for $fs_{0.3}$ and below at the predicted pouring time step of 127.7 seconds. This shows the potential initial width through which the alloy would flow during pouring.

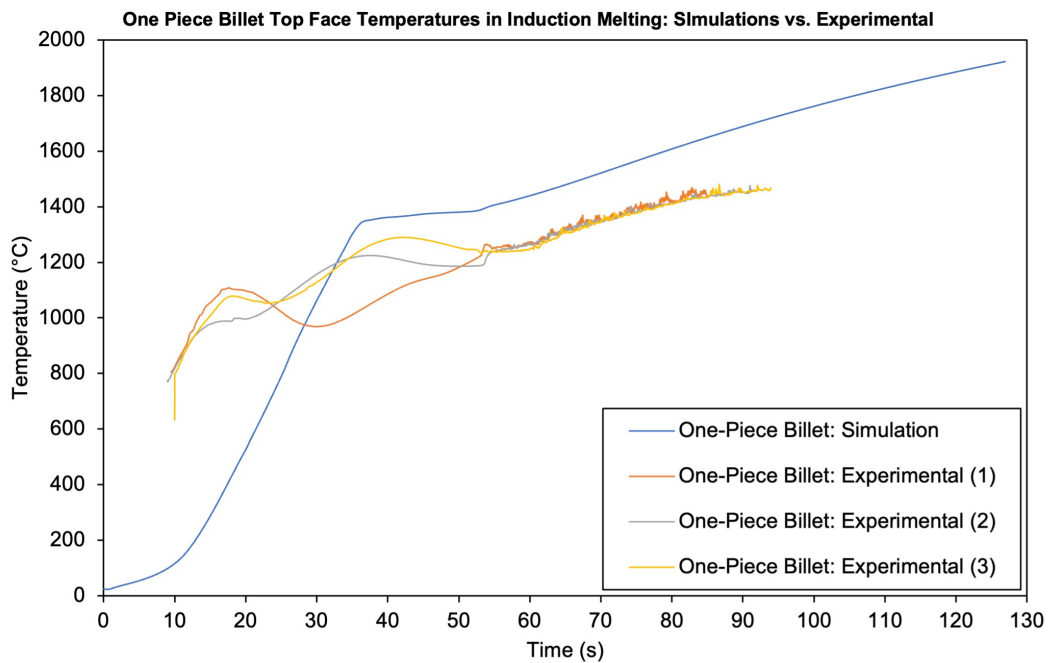


Figure 5.15: VIM-IC induction heating model vs. experiment, top face temperatures during VIM

The temperature of a node in the centre of the billet top face during induction heating until the pour time step is plotted in Figure 5.15, plotted alongside three experimentally measured billet top face temperatures in induction heating until pouring. In Figure 5.16,

5.8. MODELLING VIM-IC: RESULTS

the temperature gradient for the length of the billet is shown at the predicted pouring time step. This is plotted graphically, as a profile of the temperatures along the length of the billet centre line at the pouring time step can be seen in Figure 5.17. Although the initial modelled heating rate was different compared to the experimental data, the accuracy of the temperature distribution throughout the billet at melting point was considered a more important simulation output than the top billet face temperature throughout heating and melting. The top billet face temperature was not representative of the temperature distribution throughout the billet, and was therefore not a useful parameter to measure, as it is not indicative of the internal temperature distribution, alloy pouring temperatures or casting outcomes. It should be noted that the difference in temperature gradient above the liquidus temperature is likely due to the artificially increased thermal conductivity within this region. The thermal conductivity was artificially increased above liquidus, which caused this gradient change and is representative of what we see in experiments with regards to temperature.

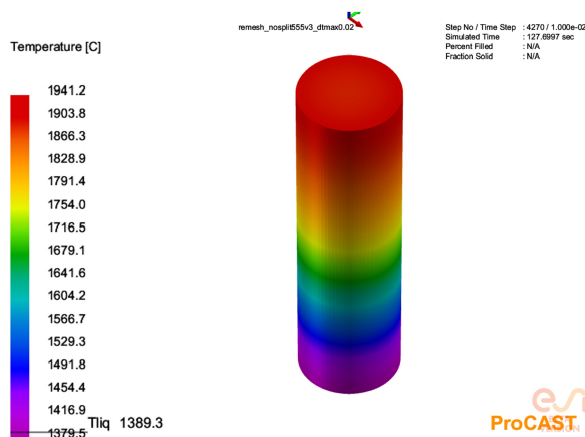


Figure 5.16: VIM-IC Model:
Billet temperature distribution at pour point

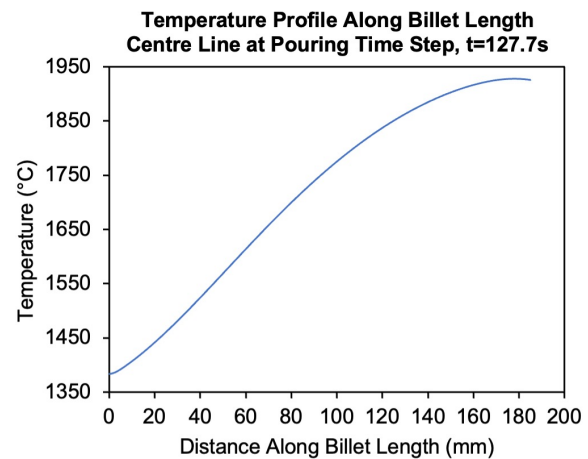


Figure 5.17: No Split Billet
Length Temperature Profile, Pour Point

An image showing the temperature of alloy across the bottom of the billet, with a cut-off display showing only temperatures above $f_{0.3}=1383.8$ °C, is shown in Figure 5.18. The temperature profile across the billet bottom face at pouring point is plotted in Figure 5.19. In both Figures 5.18 and 5.19, the alloy would be expected to pour via the purple coloured region, or above the dotted line representing $f_{0.3}$.

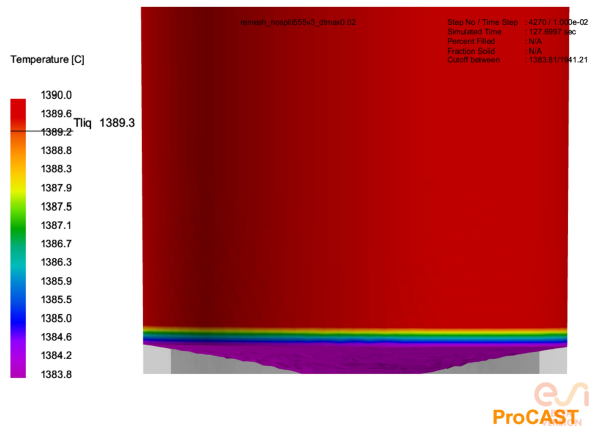


Figure 5.18: VIM-IC Model:
Billet temperature distribution at pour point

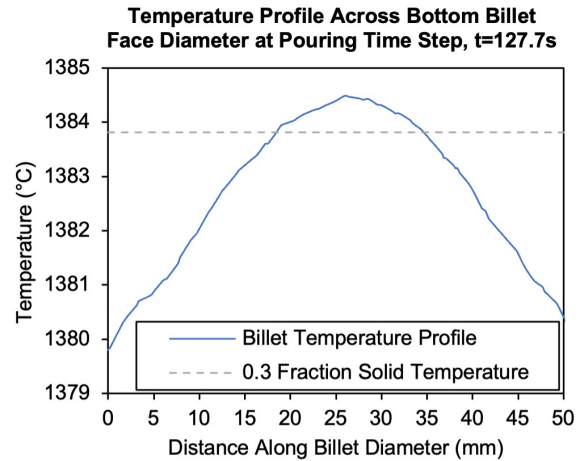


Figure 5.19: No Split Billet Bottom Face
Temperature Profile, Pour Point

5.9 Modelling VIM-IC: Discussion

From Figures 5.8 and 5.9, by examining the concentrated regions of magnetic energy density, the centre of the top billet face does not experience a high magnetic energy density. This explains why the top centre piece of the billet remains solid initially in induction heating. Secondly, it is clear that the magnetic energy density of the magnetic field is concentrated within the length of the coil, causing the bottom part of the billet to melt by conduction from the progressing melt front.

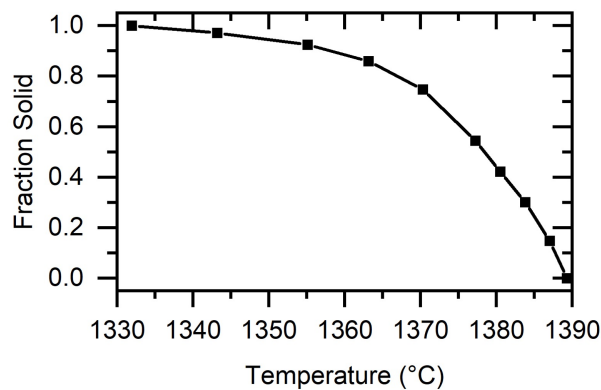


Figure 5.20: Fraction solid curve: solid to liquid state transition between solidus (1) and liquidus (0) temperatures [94]

Although fluid flow was not activated in this induction heating model, the ‘mushy zone’ of the alloy between the solidus and liquidus temperatures was defined using a fraction solid curve. This curve dictates the relationship between the alloy temperature and its

progression through the mushy zone, controlling the mobility of the alloy throughout this temperature range. The fraction solid curve can be seen in Figure 5.20, taken from the work of Thomas *et al.* [94]. The temperature at which the alloy starts to become mobile within the mushy zone is different for each alloy, and the definition of a fraction solid curve predominantly serves as a tool for modelling alloy movement. The mobility temperature, or fraction solid value, varies between different alloys dependent upon their composition and there is no simple rule. The fraction solid value of 0.3, $f_{0.3}$, was selected as the predicted value at which the alloy would begin to move, due to this default setting value for the mobility limit of alloys in ProCAST software. At $f_{0.3}$, the alloy temperature is 1383.8 °C.

Comparing the first two melt front progression images in Figure 5.12 to Figure 5.13, which is a photo featuring a billet taken from an industrial trial in which the generator was switched off at 50 seconds, the predicted melting front pattern of a thermal induction melting model without flow appears to generate a reasonable initial melting pattern. The fraction solid distribution at the billet bottom face at $t=127.7$ s, the predicted pouring time step, is shown in Figure 5.14. This image was created using the ‘cut off’ function in ESI ProCAST Visual-Viewer software, and displays the fraction solid distribution at the bottom of the billet for values of $f_{0.3}$ and below. This was the first time step at which the fraction solid reached a value of $f_{0.3}$ or below for the elements on the bottom billet face.

Figure 5.15 shows the evolution of the temperature of the central node on the top billet face in VIM-IC, until estimated pour point. Experimentally measured billet top face temperatures in heating until pouring are also plotted on the same graph for comparison. The offset between the recorded top face temperatures and the start time for the simulation data set has been estimated, as for the DOE L9 Array experiments, the time from generator switch on until alloy pouring was not recorded. This time offset was applied based upon the point at which the gradient of the heating curve changes for a final time in the simulations, and is necessary as the infrared thermometer lowest accurate detectable temperature reading for the IR thermometer unit was 800 °C. Therefore, experimental heating data for the top billet face does not exist below this value. Comparing the IR thermometer experimental readings with the simulated heating temperatures, the computational model heats the billet to pouring point over a longer time period than in the real VIM-IC setup. However, the gradient of the temperature curve in the final portion of heating where the simulated temperatures exceed the liquidus is comparable to the gradient of the experimentally obtained heating curve in what is coined as the ‘superheat’ region in industry.

The temperature distribution throughout the billet at $t=127.7$ s, the predicted pouring time step, is shown in Figure 5.16. The temperature distribution throughout the billet volumes will be mapped onto a billet volume for pouring and mould filling simulations, and used as the initial condition for these subsequent models. Although the magnitude of the temperature gradient throughout the billet length may be surprising, the pouring temperatures recorded in induction heating trials in Section 4.5 were within a similar range. It is important to note that the outer diameter of the coil used in Section 4.5 trials, compared to the DOE L9 Array experiments varied by 10 mm. The applied voltage difference of 555 V in the DOE L9 Array experimental trials, compared to 646 V in Section 4.5, should also be considered when making comparisons between the pouring temperatures observed in these VIM-IC simulations and the experimental data of pouring temperatures. However, it serves to demonstrate that such a large temperature gradient throughout a 185 mm long billet is not unreasonable. It should also be noted that the temperature gradient throughout a billet volume at the pouring time step will differ from the pouring temperatures recorded experimentally, as the billet will be subject to cooling as it pours and the generator switches off automatically at pour initiation. The pouring temperatures, accounting for the effect of cooling, can be measured in subsequent pouring simulations. A profile of the temperatures along the length of the billet centre line at the pouring time step can be seen in Figure 5.17. Pouring simulations results for the VIM-IC one-piece billet are listed in Section 5.23, alongside the DOE L9 Array pouring simulations results.

Figure 5.19 shows a billet temperature profile at the pouring face that is not symmetrical, with the peak of the profile offset slightly to the right of the billet centre line. Upon examination of the model geometry relative to the billet bottom face temperature profile, it is likely that the asymmetry of the temperature profile is due to the orientation of the coil. The temperature at the diameter of the billet is also slightly higher on the right hand side of the billet. This could potentially result in a flow angle during pouring, as one side of the billet bottom face melts before the other. In the two-piece billet models used in the L9 array, the resultant flow angle would likely also be influenced by the disc height, as a contact interface close to the pouring face could reduce the impact of uneven melting. In figures which feature the geometry and results plots, the side of the coil with more turns is on the right hand side of the billet. The presence of fewer turns on one side of the coil is due to fewer turns on the side of the coil from which the terminals which connect to the generator. This can also be seen in Figure 5.21 in a three dimensional view.



Figure 5.21: 3D render of copper induction coil

5.10 Modelling VIM-IC: Conclusion

By performing thermal only electromagnetics simulations, it is possible to develop an understanding of how the billet melting front progresses in VIM-IC. Examining the fraction solid results throughout the heating simulations provides an insight into induction melting behaviour, in the form of qualitative data regarding melt pattern. In addition to this qualitative data, the initial flow width at pouring and the temperature of the alloy at the crucible outlet for the duration of the pour can be estimated by investigating the temperature profile at both the billet pouring face across its diameter, and throughout the length of the billet.

The temperature range displayed throughout the billet length is within a similar range as the measured pouring temperatures in Section 4.5 for a 3 kg billet of the same dimensions. However, the limitation in comparing the billet temperature gradient for a one-piece billet in VIM-IC at 555 V and 7.93 kHz to those of Section 4.5, is the difference in generator settings. The melting data in Section 4.5 involved a coil set to 646 V with a frequency of 8 kHz, and a coil with a larger total outer diameter by 10 mm. The pouring temperatures were not recorded for the melts conducted under the conditions described in this chapter, i.e. 555 V and 7.93 kHz, both for the one-piece billet and the DOE L9 array experiments. This was due to the second IR thermometer being obtained at a later date. Therefore, it was not possible to measure the top billet face temperature in heating, and the pouring temperatures for the same trials. Despite the differences in generator parameters, the comparable temperature range of 1379.5-1941.2 °C obtained in the simulations for the

billet at the predicted pouring time step are in agreement with the range observed in the experimental data.

Results such as predicted initial flow width for the one-piece billet in VIM-IC modelling are listed in Section 5.15. Although initial flow width data was found to match more closely when measuring the length of alloy across the billet bottom face at $fs_{0.3}$ and below in the EMAG thermal only model, compared to initial flow width data from VIM-IC pouring simulations, this is best explained in the context of the other results obtained in modelling VIM-IC for the DOE L9 array experiments.

The next stage of this work will investigate if using a thermal only model for induction heating has good predictive value for determining the effect of disc height for two-piece billets, piping size and location on variables such as pour time, flow width, flow angle and fluid velocity.

5.11 Modelling VIM-IC: DOE L9 Array Overview

The effect of varying disc height for two-piece billets, and the introduction of holes of varying size and position was tested experimentally in Section 4.4. In this chapter, the aim was not only to develop a model with good predictive value for the initial condition of a mould filling model for a one-piece billet, but to develop a representative way of modelling the thermal contact resistance between two billet pieces. It was also key to decipher a way of modelling holes, to test if the effect of piping in the alloy could also be predicted effectively. As previously mentioned in Section 4.4, the objective of varying hole size and location was to determine if a particular size of a ‘solid’ disc without holes could prevent potential defects from occurring in model filling by altering flow characteristics and pouring temperatures. Modelling heat transfer between two-piece billets and the existence of holes without the activation of fluid flow was a challenge which required the employment of different heat transfer coefficients as a modelling technique to achieve this.

5.12 Modelling VIM-IC: DOE L9 Array Geometry and Mesh

The geometry of the coil, crucible and surrounding air volume remained the same for the VIM-IC models of the DOE L9 array. The tetra meshes generated for this set of models were created with the same method and quality criteria as described in Sections 5.41 and

5.42. However, modelling a billet in two pieces involved creating two separate volumes for the billet pieces. In addition to the two volumes representing billet pieces, a hole volume was created for runs from the DOE L9 array which featured a hole. For interface assignment regions, a dummy ‘slice’ volume was created for runs involving holes in the top or middle positions. Figure 5.22 shows the mesh for run 3 of the L9 array. The mesh for Run 3 includes a two-piece billet with a 15 mm bottom disc height, a meshed hole volume and corresponding ‘slice’ volume on top of the hole volume, which has a height of 2 mm and 10 mm diameter, matching that of the hole volume. The details of slice volumes, assigned interface types and heat transfer coefficients are explained in Section 5.13.

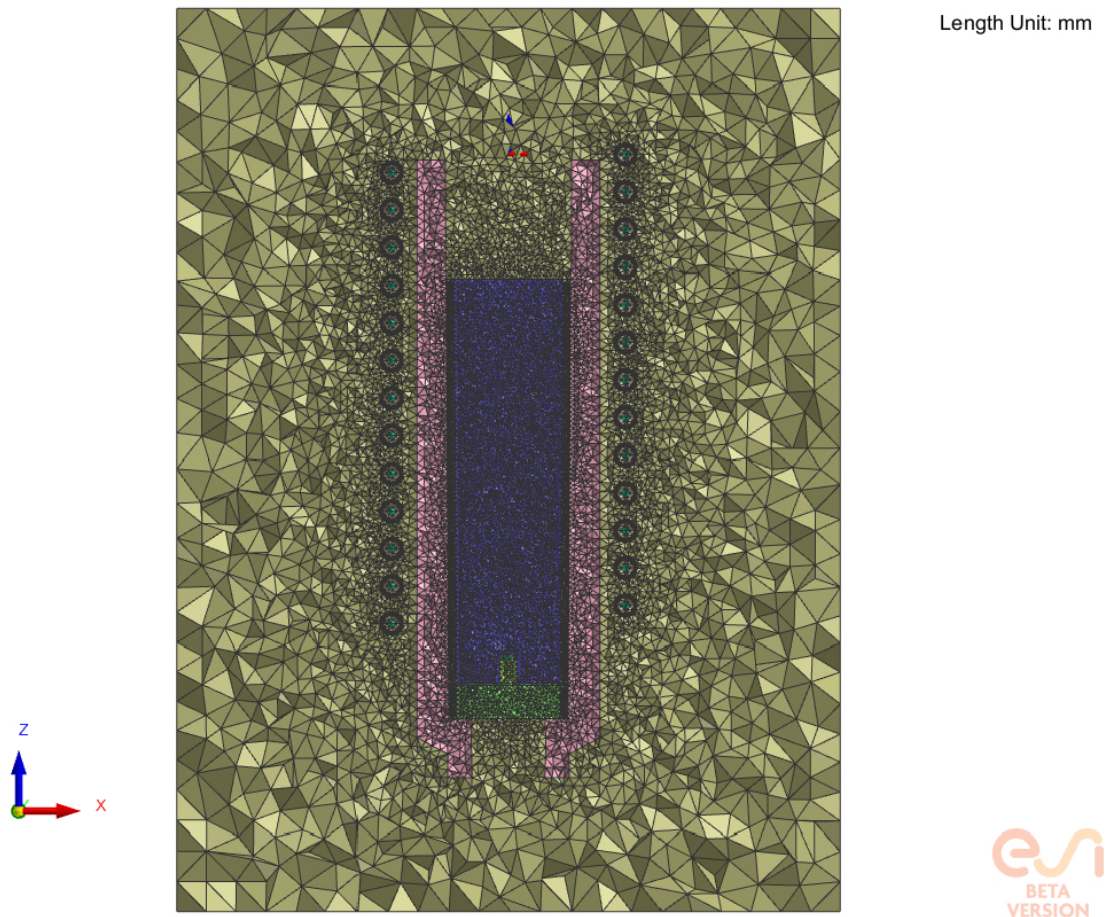


Figure 5.22: Run 3 tetra mesh featuring hole and slice volumes

5.13 Modelling VIM-IC: DOE L9 Array Materials and Boundary Conditions

Modelling the heat transfer between two billet pieces in contact with a thermal only model involved conducting sensitivity studies to ascertain heat transfer coefficient values which could realistically represent the presence of a thermal contact resistance between the two billet pieces. Initially, constant values of heat transfer coefficient were trialled for ‘Run 1’ of the DOE L9 array, with no holes and a 15 mm disc height bottom billet piece. Values between 50-10 000 W/m²K were applied to the interface between the two stacked billet volumes, with the direction of heat transfer assigned as from top to bottom. In ESI ProCAST software, it is only necessary to define the direction of heat transfer for heat transfer coefficient values which are temperature dependent and not constant. However, by taking the temperature profile along the billet length for the time step at which the melting front has made contact with the interface across the full diameter of the billet, it was clear that these values were not high enough. Values of 50-1 000 W/m²K were representative of a thermal contact resistance much higher than those experienced by two pieces of metal in contact. As metals are highly thermally conductive, although the heat transfer coefficient values were numerically high, this was not unreasonable to represent such a high heat transfer rate. Finally, the values of 100 000 W/m²K and 3 000 000 W/m²K were tested at the interface between the pieces. Tested values of constant heat transfer coefficients are shown in Figure 5.23.

It was evident that even with a heat coefficient value as high as 100 000 W/m²K, a large temperature discontinuity existed at the distance along the length of the billet which corresponded to disc height, which is 15 mm for the Run 1 model. This can be seen in Figure 5.24. However, by increasing this value to 3 000 000 W/m²K, it was evident that this was representative of a temperature profile at the pouring time step which very closely matched the temperature profile throughout the length of a one-piece billet. As a significant temperature discontinuity still existed at a constant heat transfer coefficient value of 100 000 W/m²K, yet value of 3 000 000 W/m²K resulted in the equivalent of no thermal contact resistance at the billet interface, a temperature dependent heat transfer coefficient was implemented. The purpose of applying a temperature dependent heat transfer coefficient was to simulate the existence of a thermal contact resistance which would disappear in principle when the melt front progresses through the interface. A value of 100 000 W/m²K was applied to the interface for alloy temperatures up to liquidus. At 1390 °C and above, a value of 3 000 000 W/m²K was applied as a heat

5.13. MODELLING VIM-IC: DOE L9 ARRAY MATERIALS AND BOUNDARY CONDITIONS

transfer coefficient. This was devised by comparing known differences in total melting times for two-piece billets compared to one piece-billets in Section 4.5.

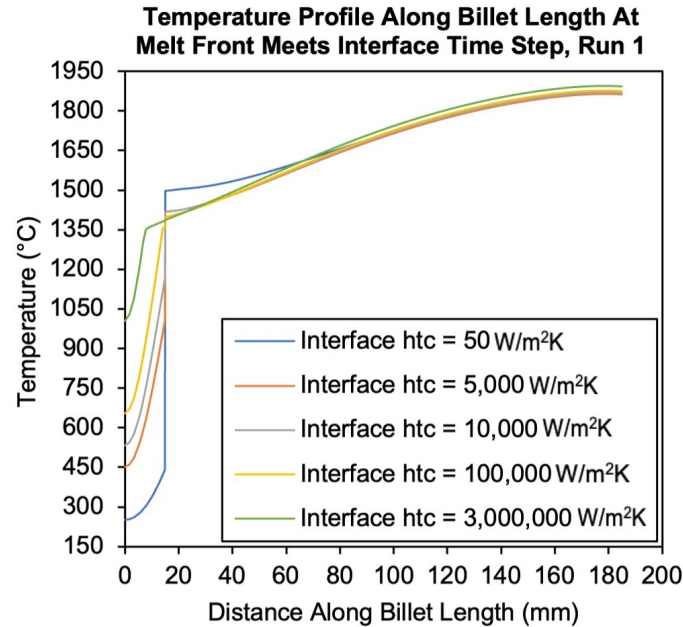


Figure 5.23: Testing constant heat transfer coefficient values applied at split billet interface, at the time step at which the melting front meets the billet interface for Run 1

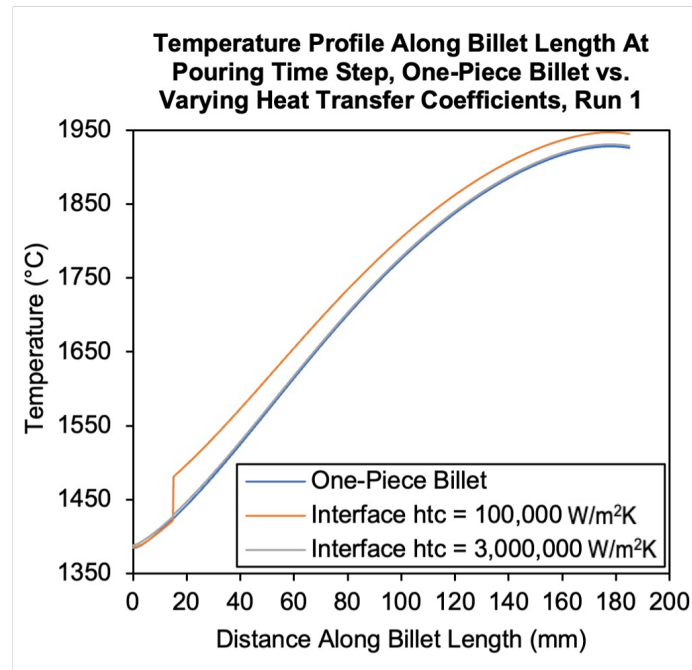


Figure 5.24: Pouring time step billet length temperature profile, one-piece billet vs. fixed heat transfer coefficient values applied at billet interface for Run 1

5.13. MODELLING VIM-IC: DOE L9 ARRAY MATERIALS AND BOUNDARY CONDITIONS

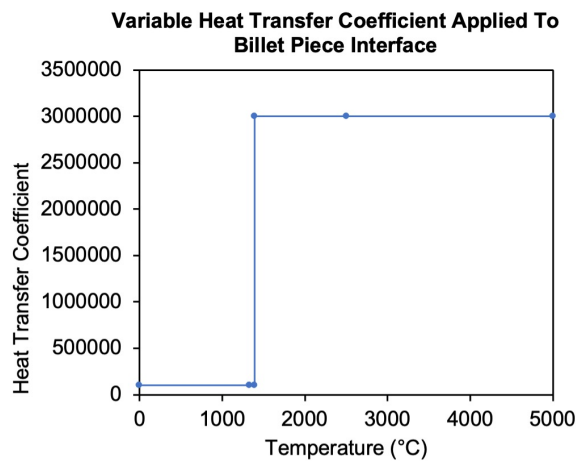


Figure 5.25: Temperature dependent

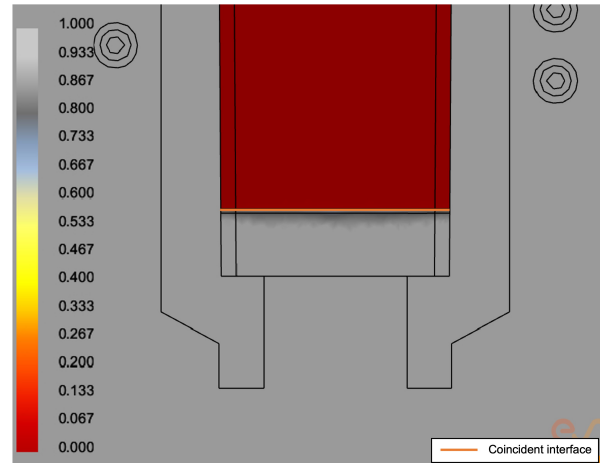


Figure 5.26: Coincident interface condition for heat transfer coefficient for split billet interface Run 1, 15 mm disc with no holes

The variable heat transfer coefficient value shown in Figure 5.25 was applied at the interface between two billet pieces, which was assigned as a ‘coincident’ interface type across the billet faces in contact. This interface is highlighted in orange in Figure 5.26. From this image showing the fraction solid progression of the melt front, it is evident that a temperature discontinuity exists between the two surfaces.

The variable heat transfer coefficient value was applied to the billet faces in contact for all runs in the DOE L9 array. The temperature profiles along the billet length for Runs 1, 4 and 7 which did not feature any holes, at the time step at which the melt front is in full contact with the interface, are shown in Figure 5.27. In this graph, the temperature discontinuities are seen at the interface for the given disc heights in Runs 1, 4 and 7. Further details of the simulation parameters used for these models and additional results are described in Sections 5.14 and 5.15 respectively.

Modelling the effect of piping, which was tested by manufacturing billet holes for the DOE L9 array runs, is a challenge when implementing a thermal only model of induction heating. Without fluid flow, it is not possible to assign a hole volume as a void alloy volume with 0 % fill. Therefore, the existence of holes was simulated using different interface types assigned to different volume faces. The rationale behind this was to account for the alloy pouring through the void holes internally, by encouraging greater heat transfer to take place at hole volume interfaces, compared to the hole volumes compared to the interface contact regions between two billet faces. Although this is not the physical reality, this method was chosen to mimic the effect of internal hole volumes without fluid flow, allowing heat transfer to progress with less inhibition through the defined hole faces.

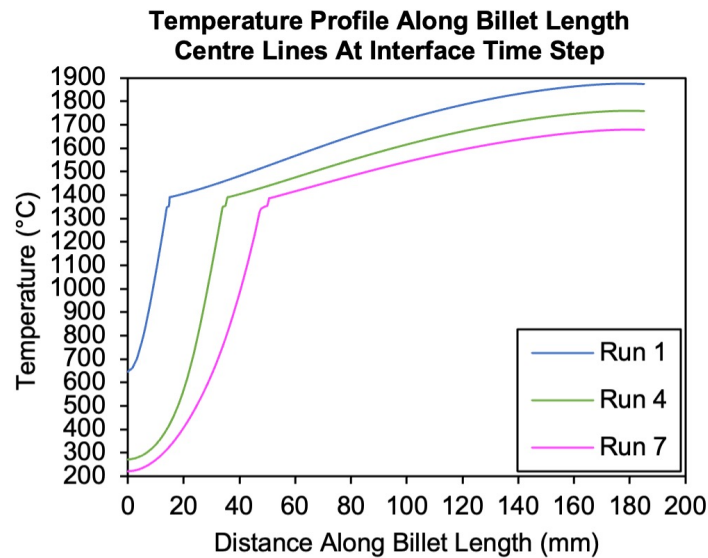


Figure 5.27: Temperature along billet length for Runs 1, 4 and 7 (no holes) at the time step for which the melting front is located at the billet split interface

When assigning a volume as an alloy type material in ProCAST, it is possible to define the percentage fill of the volume. This is typically used to allow any vacancies in internal mould volumes to be filled with alloy and to be treated with properties of that alloy during filling and solidification, even if the mould starts as empty and void at the start of the simulation. As fluid flow was not enabled for these induction heating simulations, all hole volumes were assigned as 100 % filled, with only the equivalent and coincident interface types dictating the rate of heat flow through the volumes. Details of the differences between the DOE L9 array runs and the definition of ‘top’, ‘middle’ and ‘bottom’ hole positions can be found in Subsection 4.4.2.

The approach taken to modelling holes was dependent upon the position of the holes. Firstly, holes in the ‘top position’ as shown in Figure 5.28, which represents Run 3 in the DOE L9 array were simulated by applying two types of interface between the relevant volumes. A hole ‘slice’ volume was created, for holes in top and middle positions, with a height of 2 mm and a diameter matching that of the hole. The hole slice volume was positioned on top of the hole volume. This was necessary in order to define different interface types to different faces of the hole volume. As a casting software optimised to be user friendly for casting engineers in industry, certain features are simplified to cater for the common use scenario. In industry, the ability to define the heat exchange relationships between volumes in contact is beneficial, without needing to define potential heat transfer coefficients for every volume face in contact separately. The hole ‘slice’ volume allowed for

5.13. MODELLING VIM-IC: DOE L9 ARRAY MATERIALS AND BOUNDARY CONDITIONS

an equivalent interface to be assigned to the top and bottom surfaces of the hole. For the curved surface of the volume of alloy representing the hole itself, and the interface between the top and bottom billet pieces, the variable heat transfer coefficient in Figure 5.25 was applied. This configuration of heat transfer coefficients would allow the heat to flow freely throughout the length of the hole, with a resistance between the curved side face of the hole volume and the top billet piece. It also modelled the effect of resistance between billet pieces at the interface between the two pieces. The effect of these interfaces in action for a hole in ‘top’ position can be seen in Figure 5.29. For the given time step, the fraction solid of the interface between the hole volume and bottom billet piece is lower than the regions in contact with the top billet piece face. This is the intended effect of using differences in heat transfer coefficient values between hole volume interfaces and the contact interface between two billets; in reality, alloy would pour through the void hole volume and make contact with the lower billet piece, before the outer volumes of the billet around the hole melt down to the lower billet piece. It should be noted that in Figure 5.29, there is a graphical error within the hole volume when looking at the section view causing the hole volume itself to appear as if it is not fully molten at this time step. In the 3D view it is fully molten.

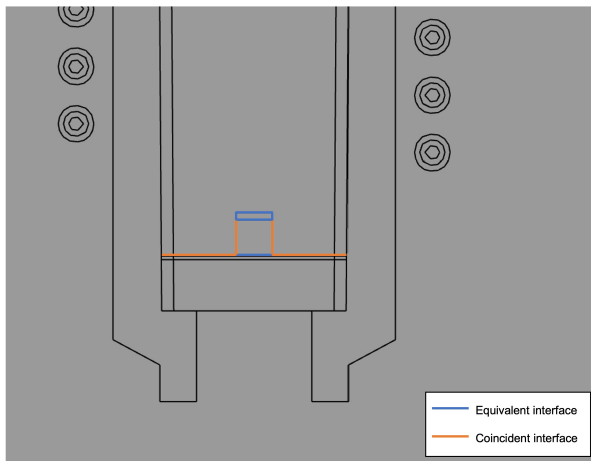


Figure 5.28: Coincident interface condition for top hole position configuration

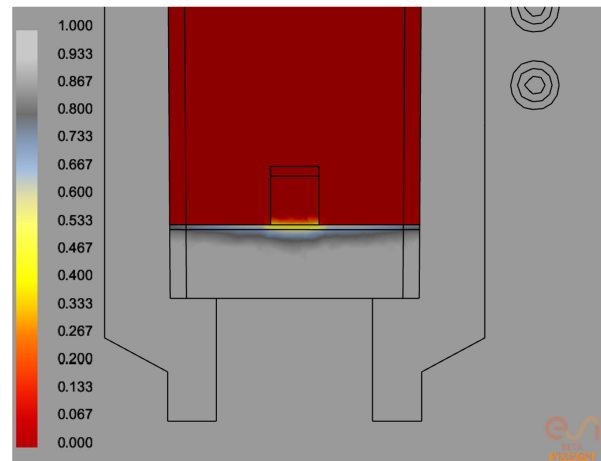


Figure 5.29: Top hole position fraction solid distribution of melt front at interface point

For runs with holes in the ‘middle’ position, an equivalent interface was applied between the top hole face and the top billet piece. A coincident interface was implemented between the top and bottom billet pieces, and between the curved face of the hole and the bottom billet piece. Finally, a hole slice volume was added in contact with the bottom face of the hole. This allowed for an equivalent interface to be applied to the bottom face of the hole.

5.13. MODELLING VIM-IC: DOE L9 ARRAY MATERIALS AND BOUNDARY CONDITIONS

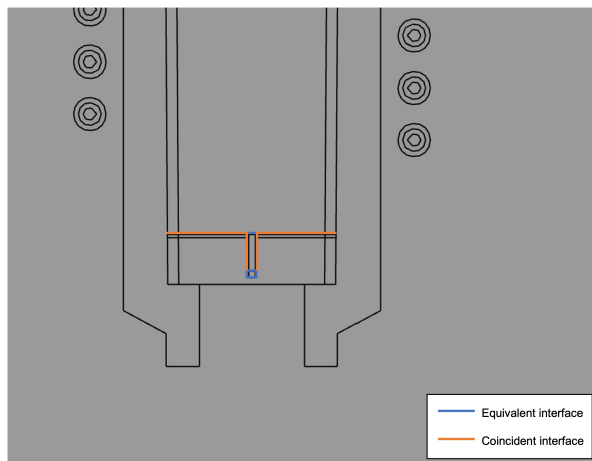


Figure 5.30: Coincident interface condition for middle hole position configuration

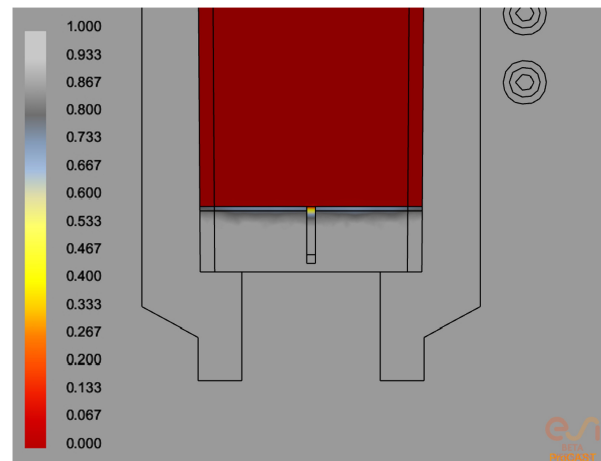


Figure 5.31: Middle hole position fraction solid distribution of melt front at interface point

This interface setup served to emulate the effect of alloy flowing freely through the billet length, with the effect of thermal resistance in place between the billet faces. The effect of the heat transfer interfaces in this configuration can be seen in Figure 5.31, where the hole volume in the top face of the bottom billet piece demonstrates a further progression of the melt front than the surrounding bottom billet piece volume.

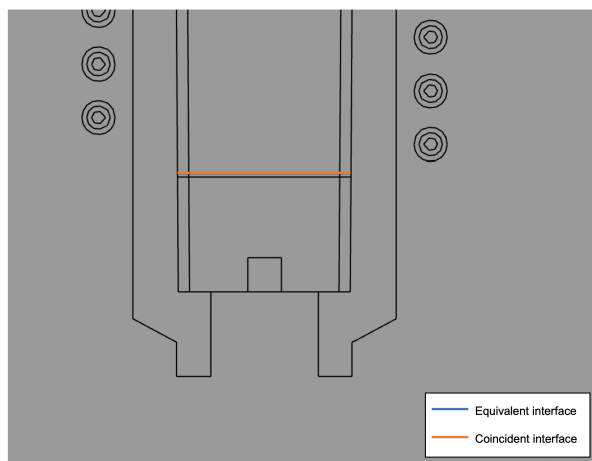


Figure 5.32: Coincident interface condition for bottom hole position configuration

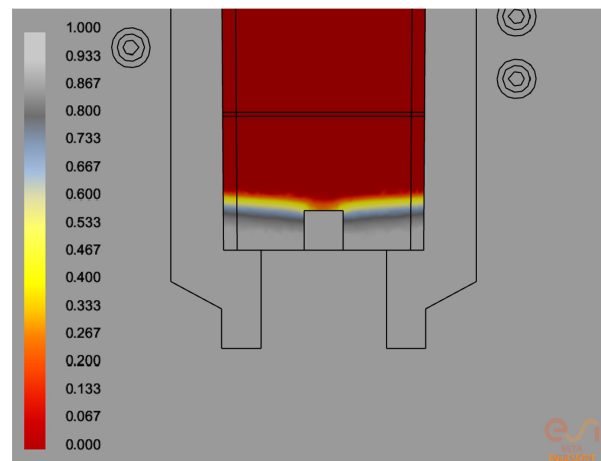


Figure 5.33: Bottom hole position fraction solid distribution close to pour point

Finally, for runs with a hole in the ‘bottom’ position at the crucible outlet, these hole regions were defined as an air volume. This approach was taken as it was closer to the real circumstances in the DOE L9 array experiment. Other approaches involving the use of heat transfer coefficients and selective application of interface configurations were used in the absence of the ability to model with flow for holes in the top and middle positions.

A coincident interface was modelled between the top and bottom billet pieces, with the same variable heat transfer coefficient applied. This is shown in Figure 5.33, which was taken at the predicted pouring time step for Run 8.

It is evident from Figure 5.33 that the simulated holes, compared to the true holes, create less distortion of the isotherms around the hole. Examining the distortion pattern of the fraction solid around the true hole in Figure 5.33, it appears that the alloy would likely pour through a central portion of the total hole diameter initially, before pouring through the full diameter of the hole and beyond. It is important to note that the simulation of holes in the top and middle positions using differences in heat transfer coefficient is employed only as an approximation, as the activation of fluid flow in the VIM model is not an option in this case.

5.14 Modelling VIM-IC: DOE L9 Array Simulation Parameters

Simulation parameters for the VIM-IC DOE L9 array models were the same as those used for the standard one-piece VIM-IC model. This includes the requirement for a reduced time step of 0.01 seconds for the time steps leading up to the alloy pouring time step, to ensure that the melt front progression and predicted pour point is independent of the time step size.

5.15 Modelling VIM-IC: DOE L9 Array Results

Interrogation of simulation data and results was performed using the ESI ProCAST Visual-Viewer post processing software. Figure 5.34 is a graph comparing the top face temperatures for Runs 1-9 of the L9 array, alongside the one-piece billet, in the VIM-IC induction heating models until the predicted alloy pouring timestep. This data was obtained by using the ‘evolution’ function within the Visual-Viewer software, and selecting a node in the centre of the top billet face. This allowed the temperature of the top billet face over time to be extracted for each VIM-IC thermal model. It is important to note that the pouring time steps for Runs 6 and 8 are estimated and may not be exact, due to issues with modelling pouring when a hole is present on the pouring face of the billet. This is further explained in Section 5.23. Simulation data has still been included for runs 6 and 8, as the top billet face heating data is relevant. The discrepancy regarding obtaining the pouring time step is only relevant for runs with a hole on the bottom face.

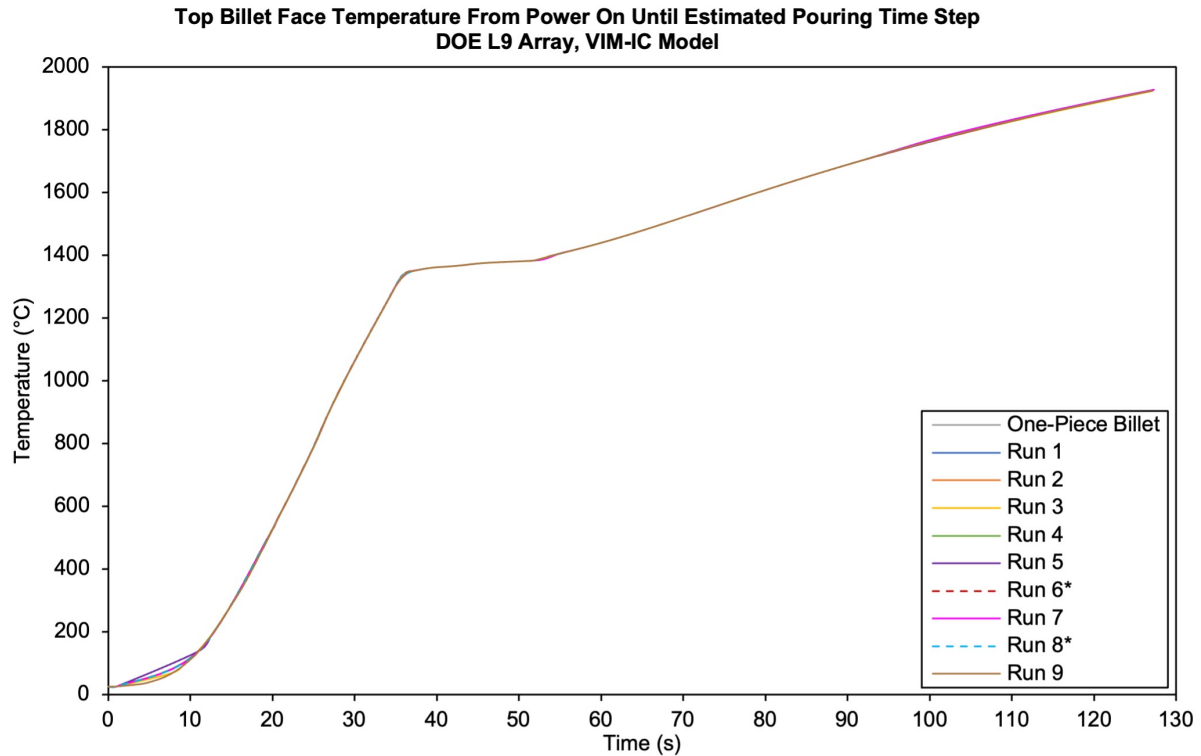


Figure 5.34: Top billet face temperatures in VIM-IC induction heating simulations

*Temperature curves for models for runs 6 and 8 were stopped at predicted pouring time steps and were not suitable for use as an initial condition for the ANOVA analysis of simulation results. This is further explained in Section 5.21.

In the subsequent pouring simulations, the differences in initial flow widths for the DOE L9 array runs were less clear. Better flow width predictions in comparison to the pouring simulations were seen with the measurement of the width of $fs_{0.3}$ and below, across the bottom of the billet at the pouring time step. Therefore, the flow width was estimated from the VIM-IC thermal only model, according to the distribution of fraction solid at the billet bottom face. Run 2 shows the thinnest initial flow width at the bottom billet face in Figure 5.35, with the widest flow width for Run 4 in Figure 5.36.

The fraction solid plots for the billets with holes on the pouring face, Runs 6 and 8, at the predicted pouring time step are shown in Figures 5.37 and 5.38. In both cases, the melt front tapers towards the centre line and progresses towards the middle of the top face of the pouring hole.

5.15. MODELLING VIM-IC: DOE L9 ARRAY RESULTS

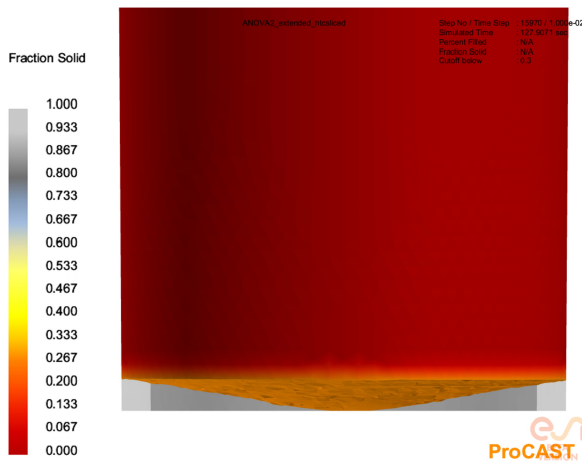


Figure 5.35: Run 2 billet pour face fraction solid at pour, $fs_{0.3}$ and below cut off image

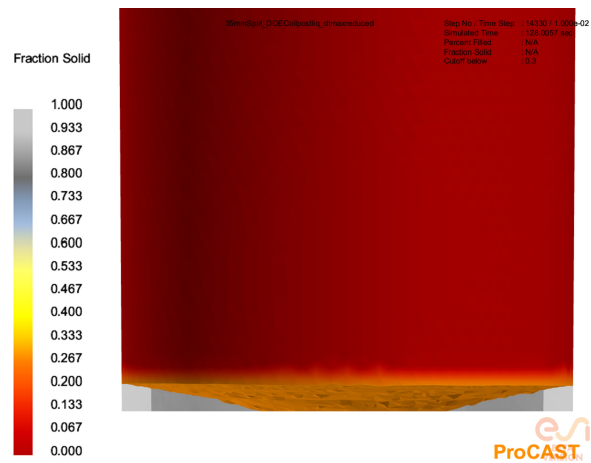


Figure 5.36: Run 4 billet pour face fraction solid at pour, $fs_{0.3}$ and below cut off image

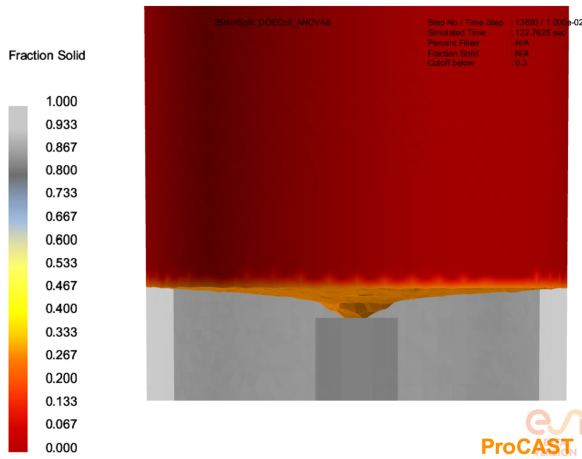


Figure 5.37: Run 6 billet pour face fraction solid at pour, $fs_{0.3}$ and below cut off image

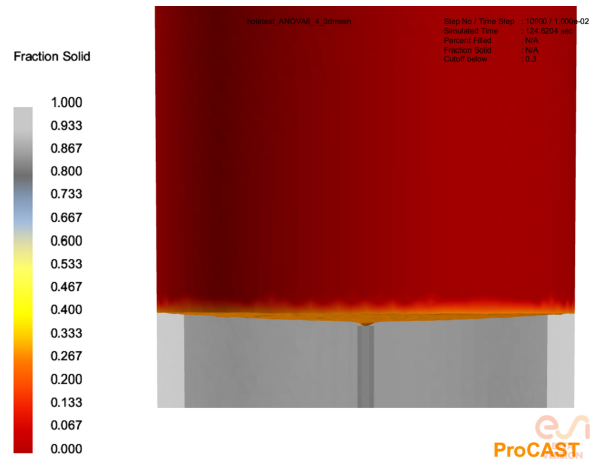


Figure 5.38: Run 8 billet pour face fraction solid at pour, $fs_{0.3}$ and below cut off image

Figure 5.39 is a graphical representation of the temperatures across the pouring face at pouring point for Runs 1-9 and the one-piece billet. These data sets were obtained by using the 'profile' function in Visual-Viewer software, which allows the distribution of a given parameter to be plotted across the distance between two nodes, at the given time step. In this case, a node on each side of the billet diameter was selected to create the profile. $fs_{0.3}$ is also shown, to represent the point at which the alloy could theoretically pour. The pouring time step was defined as the point at which the curve representing $fs_{0.3}$ first makes contact with the top face of the hole volume on the bottom billet face, or the bottom billet face itself. As the flow widths of Runs 6 and 8 from thermal modelling were not used in Figure 5.40 due to the limitations involved, the predicted fraction solid distributions at the predicted pouring point for these runs have therefore been marked by

a dashed line.

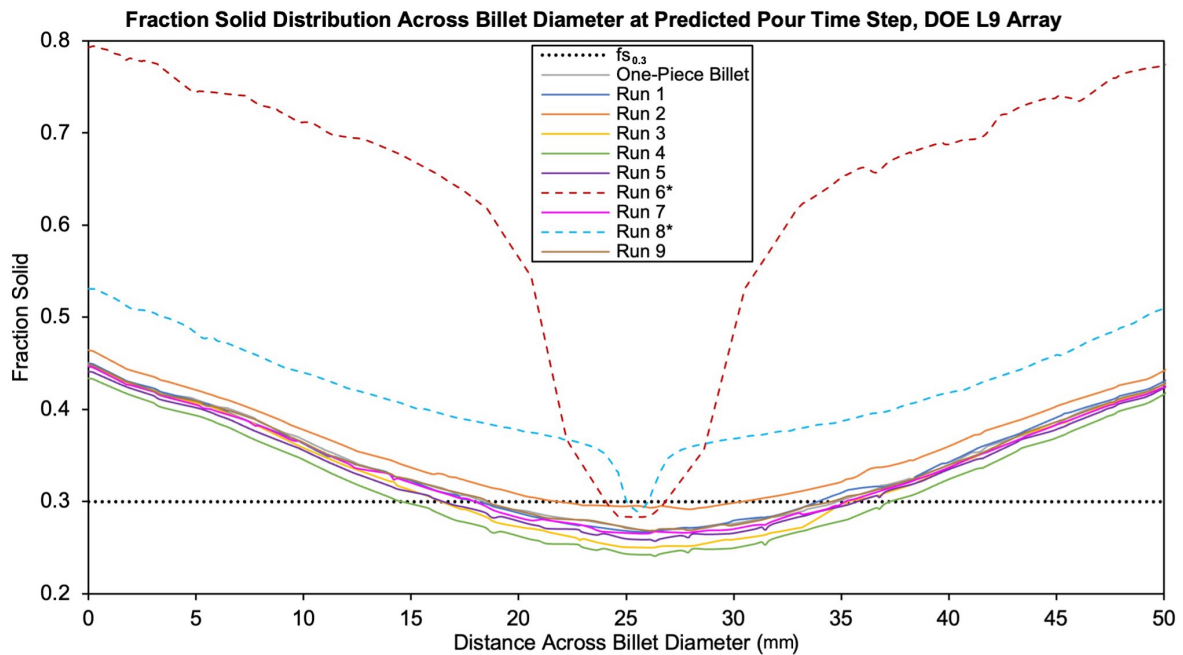


Figure 5.39: Fraction solid distribution at pouring across billet diameter for Runs 1-9

*Simulations for models for runs 6 and 8 were stopped at predicted pouring time steps and were not suitable for use as an initial condition for the ANOVA analysis of simulation results. This is further explained in Section 5.21.

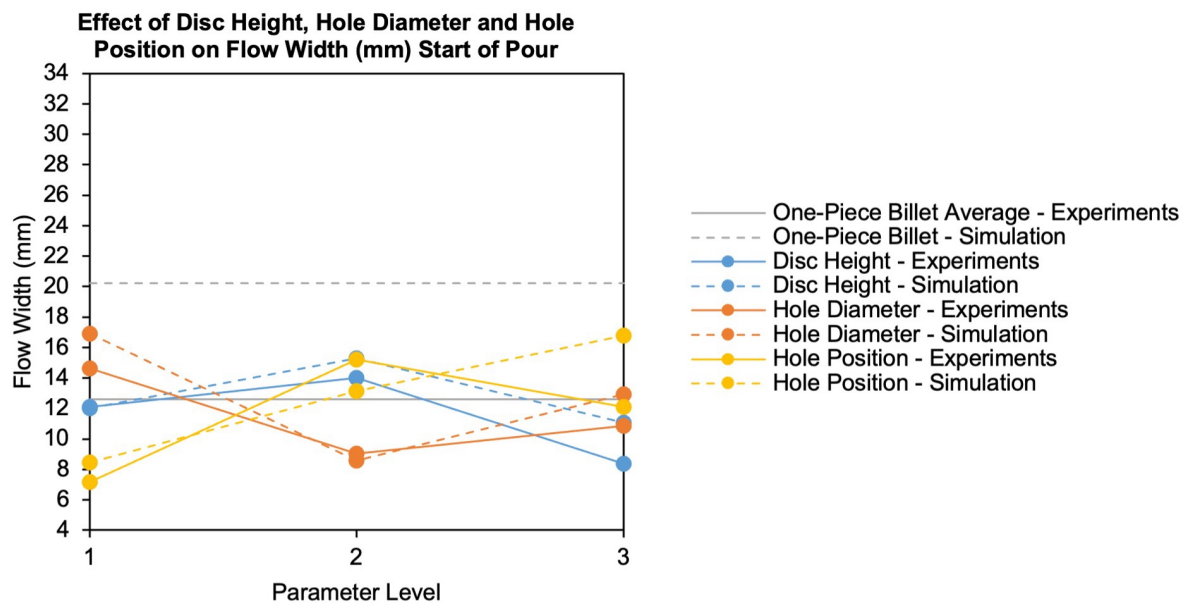


Figure 5.40: ANOVA Flow Width, Start of Pour, Simulations vs. Experiments

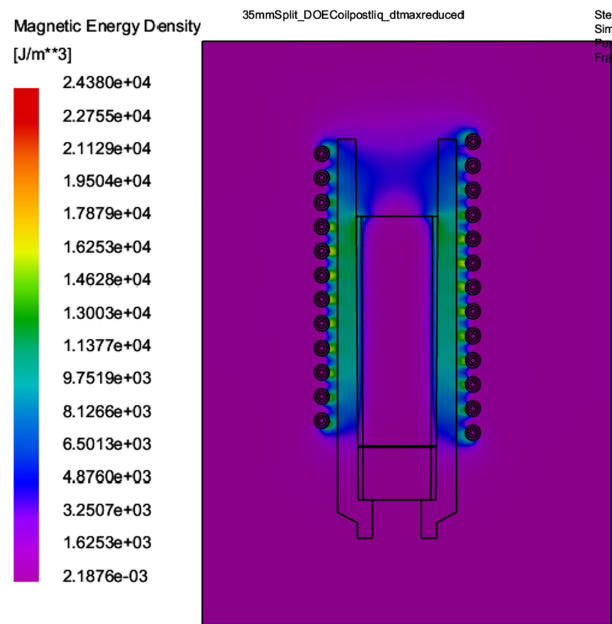


Figure 5.41: Magnetic Energy Density for Run 4, 35 mm disc with no holes

Figure 5.40 shows the trends for simulated flow widths of Runs 1-9 and one-piece billet, compared to the experimentally obtained data. Despite reasonable predicted flow widths, for consistency in comparison to ANOVA analysis graphs for other parameters in which Runs 6 and 8 were replaced with the experimentally obtained values, the flow widths for these two runs were also replaced with experimentally obtained values. Figure 5.41 is a section view plot of the magnetic energy density for Run 4.

5.16 Modelling VIM-IC: DOE L9 Array Discussion

From Figure 5.34, it is evident when examining the data sets that the top billet faces for Runs 3, 5 and 9 are heating at a slightly different rate until 12 seconds, with Runs 3 and 9 heating at a lower rate initially, and Run 5 heats at a slightly faster rate. However, the heating curves align after this initial time period.

Ultimately, the experimentally obtained heating curves and top billet face temperature at pouring point fluctuated minimally in the ANOVA analysis of IR thermometer results in Section 4.4.8. Also, it is evident that as a large temperature gradient exists throughout the billet, the final ‘pouring’ temperature of the alloy recorded from the top billet face does not represent the range of temperatures observed throughout the billet and during pouring. From experimental data in Section 4.5.4, it is apparent that the main process

5.17. MODELLING VIM-IC: DOE L9 ARRAY SIMULATION RESULTS CONCLUSION

parameters which produce marked differences in the top billet face temperature curves are significant changes in operating parameters such as generator power, instead of alloy based parameters such as number of billet pieces, for billets of the same total mass.

It is evident when comparing Figures 5.37 and 5.38 to Figure 5.35 and 5.36 that the predicted alloy initial pouring width from examining the fraction solid distribution at the bottom billet face was significantly thinner for those with holes on the bottom face, compared to those without holes.

When examining Figure 5.40, with the values for Runs 6 and 8 replaced by experimental data, the trends for varying disc height, hole diameter and hole position appear to be a good match in simulations compared to the experimental data. The main discrepancy between experimentally obtained initial flow width and those measured in the EMAG thermal only model is in the effect of hole position at PL 3, which is the ‘top’ hole position. There is also a clear difference between the predicted initial flow width for the one piece billet VIM-IC thermal model, compared to the experimentally obtained average for one-piece billets.

Finally, in the DOE L9 array experiments, runs for which the disc height was 35 mm were prone to crucible failure, with cracking and alloy prematurely dripping out of the side of the cracked crucible before the generator switched off at pouring point. The billet pieces could also be heard rattling around for these experimental runs involving 35 mm discs. It was hypothesised that the interface between a 35 mm bottom billet piece and the top billet piece could potentially have been located at the boundary of the heating region, and therefore magnetic field, produced by the coil. Figure 5.41 shows the magnetic energy density, with a sectioned image of the VIM-IC setup for Run 4 which involved a 35 mm disc. The top of the 35 mm disc piece appears to be close to the boundary of the magnetic field on the right hand side of the image.

5.17 Modelling VIM-IC: DOE L9 Array Simulation Results Conclusion

The thermal only VIM-IC simulations can provide useful data such as billet temperature gradient throughout the billet length at the pouring time step, and a correct predicted heating rate within the ‘superheat’ region. However, the model has its limitations. Firstly, due to the lack of fluid flow modelling during induction heating, the model cannot be used as an initial condition to accurately predict pouring behaviour for cases with holes on the

bottom billet face. Secondly, the final heating temperature and time to pouring differs from reality, despite producing a reasonable temperature gradient as an initial condition for pouring. Ultimately, the accuracy of the time taken to heat and predicted top billet face temperature at pouring point is not crucial for predicting defect prevalence in mould filling. This is because neither of these factors appear to have a meaningful impact on mould filling temperature and flow prediction.

To understand the impact of disc height, hole diameter and position on factors affecting mould filling and the casting process, pouring simulations using the pouring time step from thermal VIM-IC induction models will be used as the initial condition for pouring simulations, replicating the DOE L9 array experiments. This will provide information including flow width at middle and end of pour, flow angle, fluid velocity and pour time. ANOVA analysis for trends investigating the impact of disc height, hole diameter and position can then be compared to those obtained from simulations. Pouring temperatures will also be plotted and compared in the pouring simulations, as this data is more reflective of useful data for mould filling inlet conditions over the course of the pour, compared to billet temperature gradient at pour point. This is due to thermal cooling that occurs during pouring.

5.18 Modelling VIM-IC Pouring: DOE L9 Array Overview

Pouring simulations were conducted, replicating the experiments in the DOE L9 array. The temperature gradient across the billet from the predicted pouring timestep in the VIM-IC thermal models was imported as an initial condition for the pouring models. A volume of air was meshed below the crucible, matching the distance from the experiments between the crucible outlet and side of the alloy basin which was visible as a boundary in the high speed camera images. This corresponded to a length of 183 mm. By defining this length as per the experimental distance between the crucible outlet and top of the alloy basin, this allowed for direct comparison of flow parameters for the given pouring distance. The alloy was allowed to fall by gravity into the air volume below, with measured parameters for start, middle and end of pour recorded, alongside pouring time.

5.19 Modelling VIM-IC Pouring: DOE L9 Array Governing Equations and Physics

By solving the Navier-Stokes equation, the fluid flow module in ESI ProCAST Visual-Cast software performs mould filling including free surface modelling and fluid flow computation. The Navier-Stokes equations are a nonlinear system of partial differential equations which describe the flow of incompressible fluids. For an incompressible, viscous fluid with constant density, the Navier Stokes equations are as follows [95]:

$$\frac{\partial q}{\partial t} + (q \cdot \nabla)q = -\frac{1}{\rho}\nabla P + \nu \nabla^2 q \quad (5.13)$$

$$\nabla \cdot q = 0 \quad (5.14)$$

where $q(x, t)$ is the velocity vector and $P(x, t)$ is the pressure. The constant ρ is density, and ν is the kinematic viscosity. In three dimensions, the system is considered with the initial velocity field:

$$q(x, 0) = q_0(x) \quad (5.15)$$

In addition, boundary conditions are applied according to the given scenario. The non-dimensional form of the Navier-Stokes equations can be obtained by scaling velocity and length by an intrinsic scale for the given scenario. These nondimensional equations can be expressed as follows:

$$\frac{\partial q}{\partial t} + (q \cdot \nabla)q = -\nabla P + \frac{1}{Re}\nabla^2 q \quad (5.16)$$

$$\nabla \cdot q = 0 \quad (5.17)$$

where Re denotes Reynolds number, which in many scenarios has a significant influence on flow stability. Reynolds number is defined as (5.18):

$$Re = \frac{Ud}{\nu} \quad (5.18)$$

where in the case of the Reynolds' experiment, U is the mean speed and d is the diameter of a pipe.

Not only are the free surface movement and filling behaviour simulated, but the effect of both natural and forced convection currents, dynamic pressure of the liquid, entrapped gas and the behaviour of fluid flow with the use of a ceramic filter. In this work, the 2021.5 version of the ProCAST solver was used to model fluid flow with the default fluid solver. This default solver utilises a lumped mass approximation for the gas phase in mould filling, in which individual gas pockets are assumed to be at the same pressure and temperature. The benefit of using this approximation is that it substantially simplifies the system of equations needing to be solved. With the lumped mass approximation, the Navier-Stokes equations are solved only at the fully and partially wet nodes, where 'wet nodes' are those in contact with the liquid alloy. It should be noted that in modelling the gas phase, the velocity field is not explicitly calculated. To model the velocity field beyond the free surface of the liquid, extrapolation is required [96].

5.20 Modelling VIM-IC Pouring: DOE L9 Array Geometry and Mesh

This model consisted of an IN713C billet volume, crucible and air volume below the crucible for observing pouring behaviour. As before, the 3D tetra elements were generated based upon the 2D mesh. The 3D mesh for all volumes was created using a uniform mesh type.

The meshing criteria was selected based upon the recommended values for simulations involving fluid flow. For the billet volume and meshed volume below the crucible in which the alloy flowed into, the elements were defined with a transition factor value of '0.8' and shape factor of 1.5. For the crucible volume, the 3D elements were created with a transition factor of 1.5, and shape factor of 2. This was according to the recommended mesh definitions by ESI Group for 3D mesh generation in alloy and mould volumes. As before, the mesh was generated using ESI ProCAST Visual-Mesh software and can be seen in Figure 5.42. In this image, the dark pink volume within the crucible outlet is also defined as an alloy cavity.

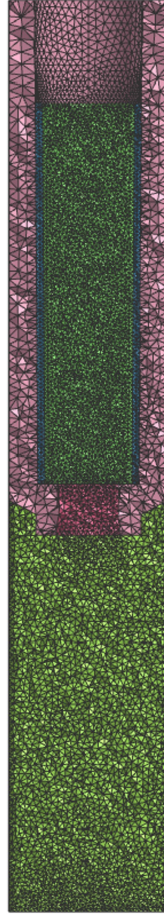


Figure 5.42: Section view of 3D tetra mesh for pouring simulation setup

5.21 Modelling VIM-IC Pouring: DOE L9 Array Materials and Boundary Conditions

For the pouring simulations, the alloy was assigned as IN713C, with an aluminosilicate ceramic fibre crucible and air volume below the crucible for pouring into the cavity. In these simulations, as fluid flow was activated in this model and was not a thermal only model, the original material properties were used without artificially increasing the thermal conductivity above liquidus temperature. The air volume below the crucible, and the volume of air within the crucible outlet was defined as an alloy type volume, with 0 % fill. This allowed molten alloy to pass through these volumes under gravity during alloy pouring, modelling the free surface of the IN713C alloy passing through this volume. If the air volume had been defined as air, the alloy would not be able to flow through it, and it would have been modelled as a domain of air through which heat transfer

5.21. MODELLING VIM-IC POURING: DOE L9 ARRAY MATERIALS AND BOUNDARY CONDITIONS

properties would be calculated. The billet volume was defined as 100 % filled with alloy. For these models, the temperature of the billet at the predicted pouring time step from the associated VIM-IC model was imported as the initial temperature condition of the billet for pouring. The temperature of the crucible volume was also imported from the induction model, for the pouring model. The vacant alloy volumes within the crucible outlet and below the crucible were set at 1390 °C, which is just above liquidus temperature to prevent any errors in allowing the simulation to run.

All alloy volumes, whether filled or not, were defined as having an ‘equivalent’ interface where these volumes were in contact. For all remaining interfaces in which an alloy defined volume, filled or not, was in contact with the crucible volume, a temperature dependent heat transfer coefficient was applied with a ‘coincident’ interface. This temperature dependent heat transfer coefficient was defined as an ‘S’ shaped curve, with points of change around the solidus and liquidus temperatures. This graph for heat transfer coefficient is shown in Figure 5.43. The heat transfer was defined in the direction of alloy to crucible.

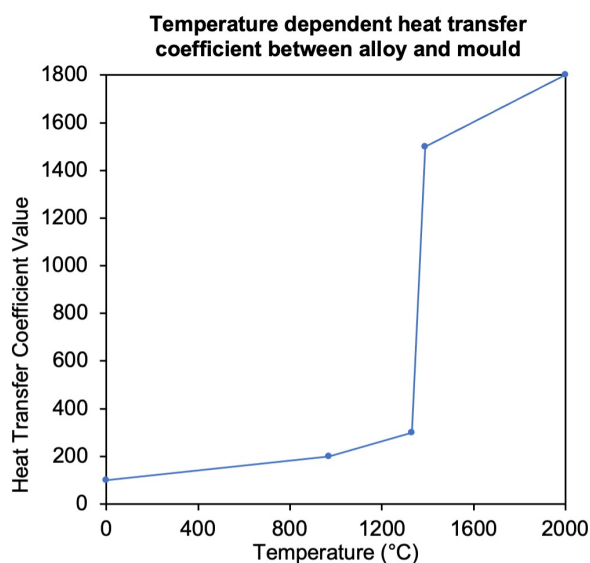


Figure 5.43: Temperature dependent heat transfer coefficient between alloy and mould

The billet top face and free surface of IN713C alloy during pouring was assigned an emissivity value of 0.85, as this was the value obtained for the emissivity of IN713C in Section 2.4. The crucible, and interfaces between the crucible and the vacant alloy volumes were assigned with an emissivity of 0.7, which was estimated for the overall system based upon best practice recommendations by ESI Group. The volumes were allowed to cool to ambient temperatures, with the same condition assigned to the billet, crucible, and

alloy vacant volumes for free surface cooling to be enabled. An outlet pressure of 1 bar was assigned to the bottom of the vacant channel volume. Finally, a wall condition was assigned to the curved surface of the vacant channel volume below the crucible.

5.22 Modelling VIM-IC Pouring: DOE L9 Array Simulation Parameters

The VIM-IC pouring models were set to run for a simulated time of 5 seconds, to allow for the complete emptying of alloy from the crucible. A mobility limit of ‘0.3’ was set, which allowed for the alloy to start or stop movement at the $fs_{0.3}$ limit. Finally, the convergence tolerance parameters for thermal results ‘TCONVTOL’, velocities results ‘VCONVTOL’ and ‘PCONVTOL’ were all set to 0.001. Reducing these convergence criteria ensured the fidelity of the computed thermal and flow results.

Modelling of the effect of turbulence on flow behaviour is very demanding in terms of numerical modelling. It requires a high mesh density and is computationally expensive, which leads to long calculation times that are not consistent with the requirements of industrial process modelling. For this reason, ESI ProCAST has developed specific methodologies to deliver robust results with a coarser mesh than would be required for a solver using a k-epsilon turbulence model for flow. The methodology is activated by the ‘WSHEAR’ solver run parameter. Both ‘WSHEAR’ and ‘WALLF’ are applied to describe fluid flow near to the crucible walls. ‘WSHEAR’ allows for velocities to be non-zero at the crucible wall [97]. By setting ‘WSHEAR’ to a value of 2, a velocity profile is created at the wall that is corresponding to turbulent boundary layers. The parameter ‘WSHEAR’ is used together with ‘WALLF’, which defines the level of roughness of the mould, or in this case, crucible surface. ‘WALLF’ is used to calculate the velocity at the free surface of a mould wall, and is not used away from the free surface. To calculate this free surface velocity at the mould wall, the core velocity of the closest node in the volume is identified. The free surface velocity is calculated by multiplying the core velocity of this closest node by the ‘WALLF’ parameter. In this model, ‘WALLF’ has been set to 0.9, where 0.99 corresponds to more slip along the wall or mould surface, and 0.8 will act as if the mould surface has a higher roughness level. Setting ‘WALLF’ to 0.9 is recommended for sand gravity casting and investment casting cases. Using both parameters together enables realistic flow behaviour to be modelled, without implementing a computationally expensive turbulence model. The ability to implement a k-epsilon turbulence model is possible within the ProCAST solver capabilities, but has not been investigated in the

current studies. Although the comparison between a standard RANS k-epsilon turbulence model and the use of these parameters to define fluid behaviour at the walls has been conducted internally by ESI Group, these validation studies remained internal due to commercial sensitivity.

5.23 Modelling VIM-IC Pouring: DOE L9 Array Results

Images of flow at the beginning, middle and end of the pour were taken for each of the VIM-IC pouring models for the runs from the DOE L9 array, in addition to those for a one-piece billet. These flow images at the beginning, middle and end of the flow were taken to assess flow angle and flow width for comparison to the experimental data. Flow widths were measured at the crucible outlet, for the beginning, middle and end of pour frames. Total pour times were measured from the time step at which the alloy first reaches the bottom of the empty channel volume below the crucible, to the last frame with unbroken flow reaching the bottom of the channel volume. It is important to note that the VIM models and pouring models are not coupled, as in reality, the generator switches off as soon as the alloy begins to pour. Therefore, temperature distribution of the billet and crucible at the alloy pouring time step in the melting model is used as the initial condition for the pouring model.

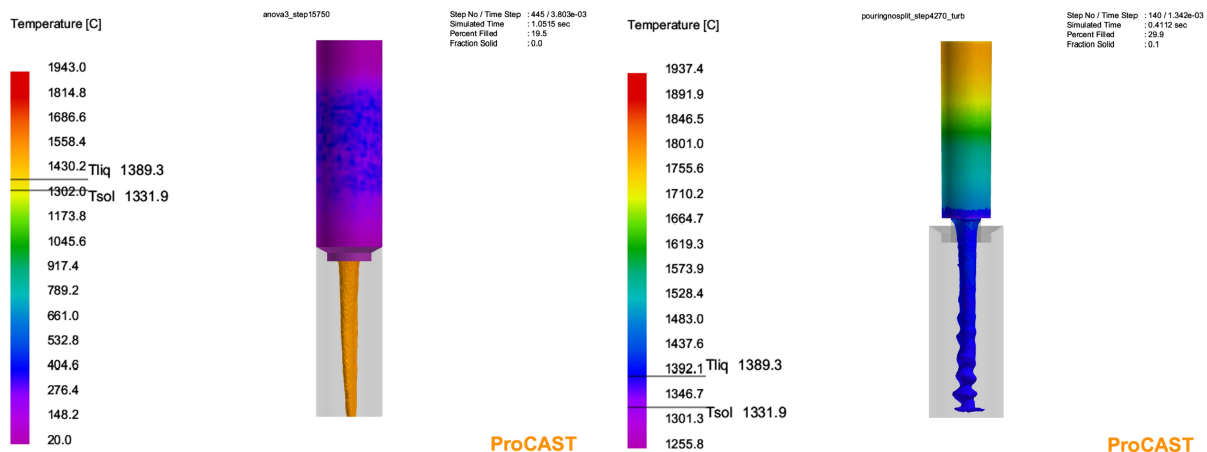


Figure 5.44: Run 3, alloy pouring out of the crucible into an empty channel volume

Figure 5.45: One-piece billet during pouring, billet and alloy volumes

Figure 5.44 shows the temperature distribution throughout the crucible and alloy volumes for the pouring model of Run 3. Figure 5.45 is a temperature plot of the one-piece billet

5.23. MODELLING VIM-IC POURING: DOE L9 ARRAY RESULTS

during pouring, just before the start of pour frame as the initial flow has not yet reached the bottom of the channel volume. In Figures 5.45 and 5.46, the crucible volume is hidden to provide visibility of the temperature distribution throughout the alloy within the crucible. Figures 5.46-5.49 show various examples of unstable flow patterns during pouring for the DOE L9 array runs. Figures 5.47-5.52 feature only the vacancy within the crucible outlet and the channel volume.

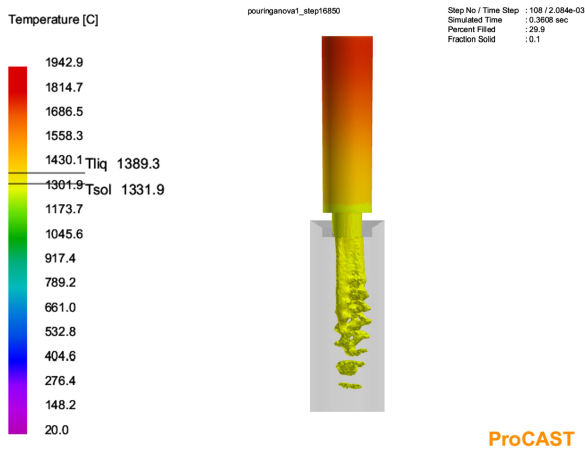


Figure 5.46: Run 1, alloy pouring temperature with rayleigh plateau instability

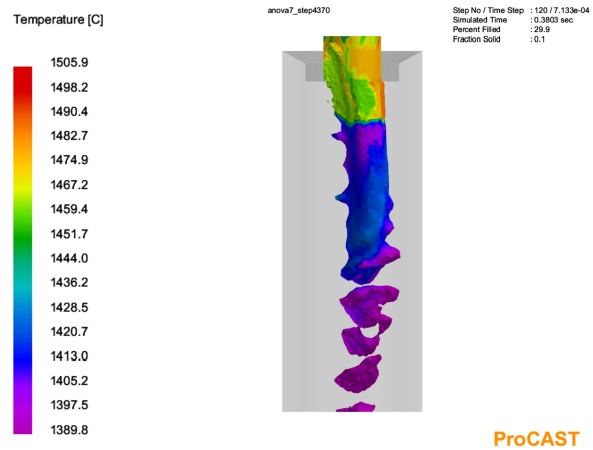


Figure 5.47: Run 7, alloy temperature plot with further rayleigh plateau instability

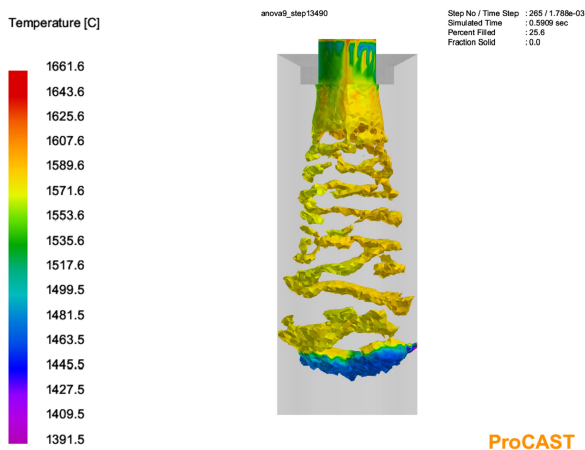


Figure 5.48: Run 9, flow showing 'corkscrew' style flow perturbations

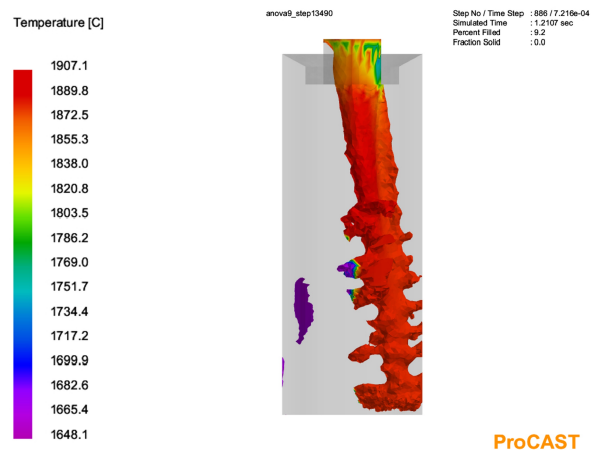


Figure 5.49: Run 9, flow showing 'tree-like wire' style flow pattern

Figure 5.50 shows the velocity of alloy during pouring for the one-piece billet. Figures 5.51 and 5.52 are examples of angled flow during alloy pouring, for Runs 4 and 5 respectively. Both Runs 4 and 7 involve the use of a 35 mm disc height for the lower billet piece, which is speculated to have caused high angle flow as the contact interface between the two billet

5.23. MODELLING VIM-IC POURING: DOE L9 ARRAY RESULTS

pieces is approximately the same height as the large changes in magnetic field generated by the coil; see Figures 5.8 and 5.9. Finally, Figure 5.53 shows leftover alloy after pouring for Run 1, which is hanging from the crucible outlet.

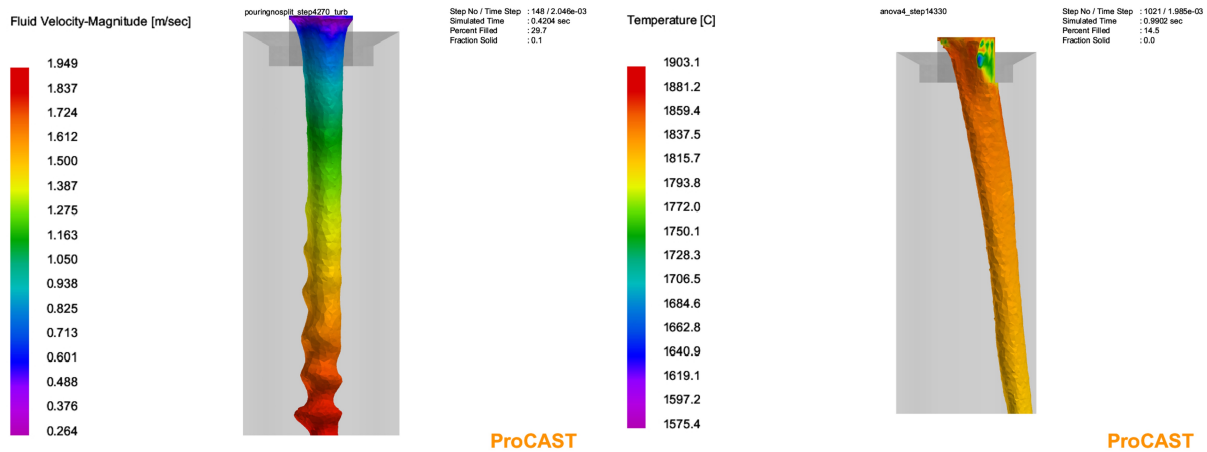


Figure 5.50: One-piece billet fluid velocity, vena contracta and perturbations

Figure 5.51: Run 4 temperature plot with highly angled flow

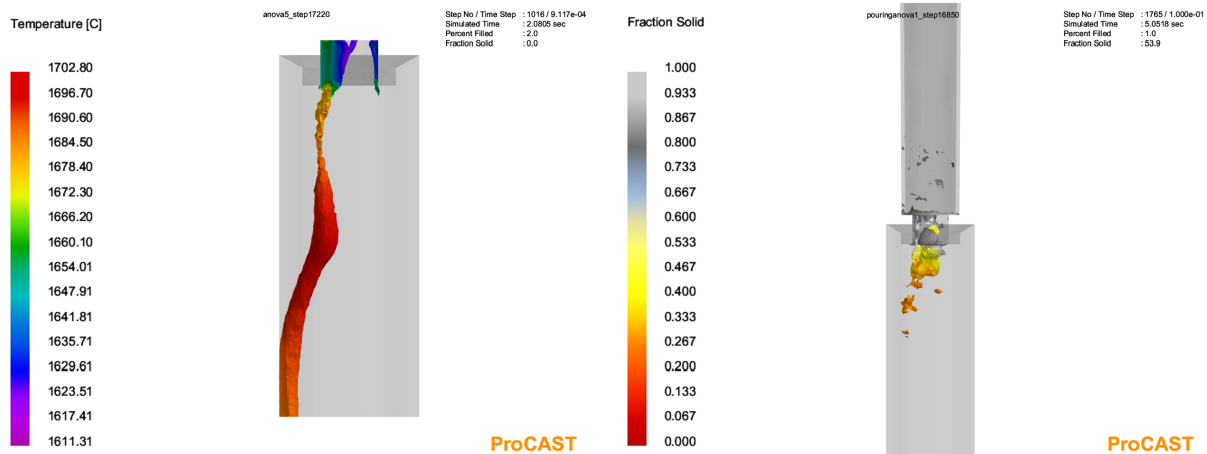


Figure 5.52: End of pour flow temperature for Run 5

Figure 5.53: Run 1, leftover alloy solidifying at crucible outlet after crucible emptying

A cross-section ingate measuring 50 mm \times 50 mm was positioned just below the crucible outlet for the VIM-IC pouring models in post-processing. This allowed the average temperatures and average magnitude of fluid velocities at the crucible outlet during alloy pouring to be measured. Figure 5.54 shows the temperatures at the crucible outlet during pouring for the one-piece billet, and Runs 1, 4 and 7. Figure 5.55 also shows the one-piece billet temperature during pouring, which allows for comparison to Runs 2, 3, 5 and 9.

5.23. MODELLING VIM-IC POURING: DOE L9 ARRAY RESULTS

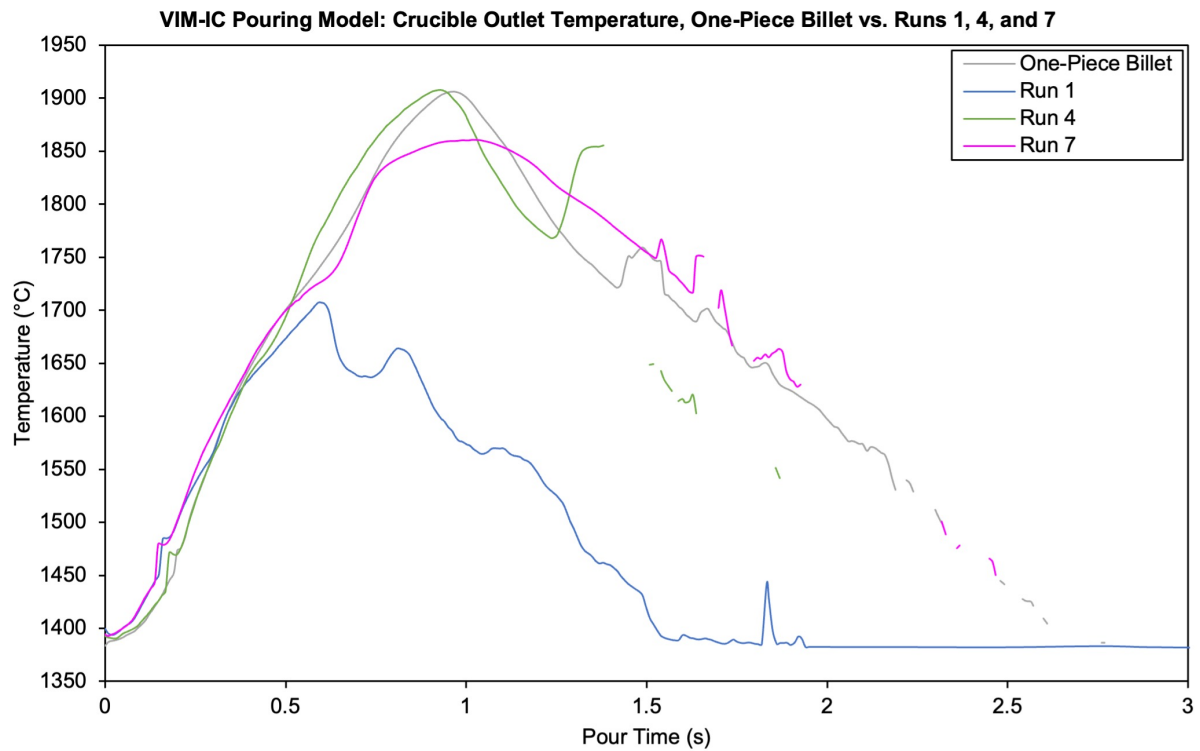


Figure 5.54: VIM-IC pouring models, temperature ingate plots at crucible outlet

*Runs 6 and 8 not included as pouring could not be accurately modelled for these configurations.

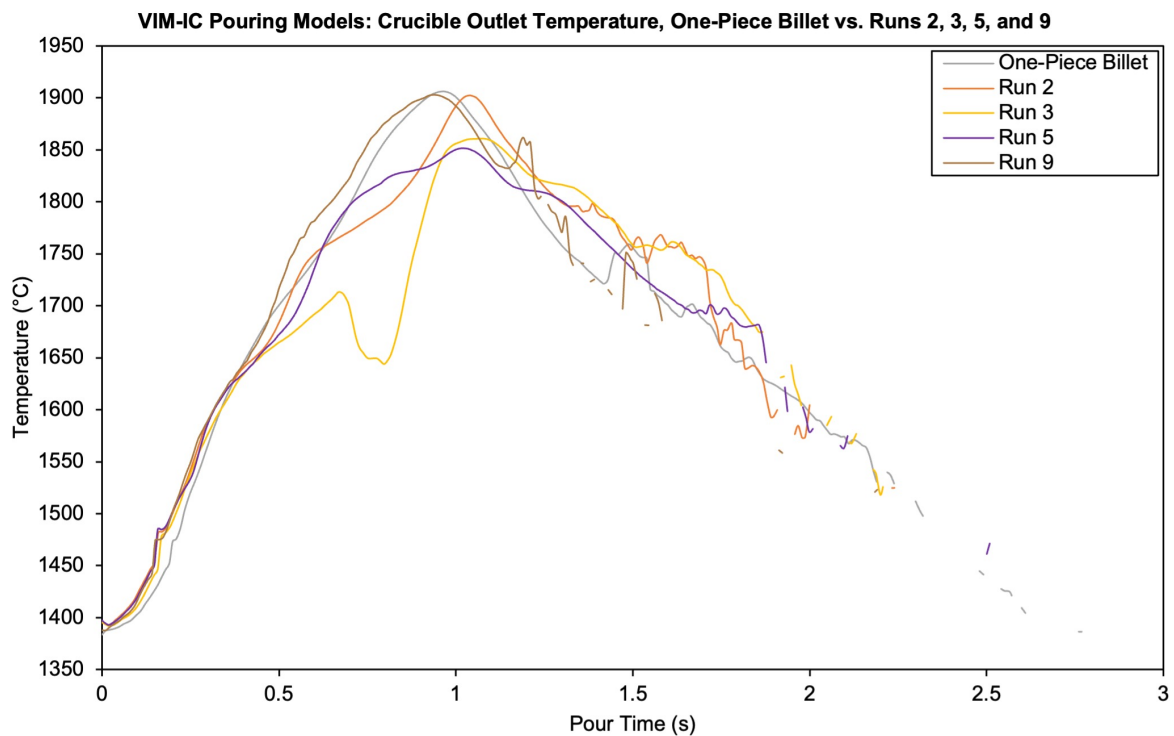


Figure 5.55: VIM-IC pouring models, temperature ingate plots at crucible outlet

*Runs 6 and 8 not included as pouring could not be accurately modelled for these configurations.

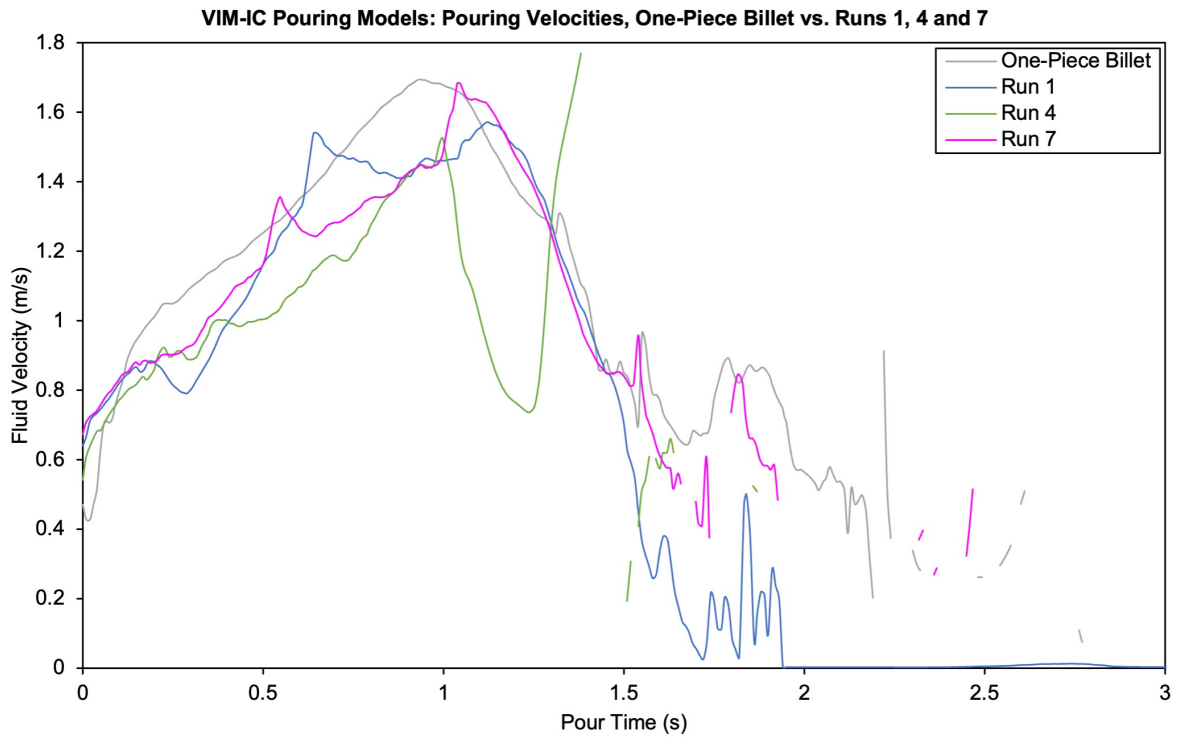


Figure 5.56: VIM-IC pouring models, velocity magnitude ingate plots at crucible outlet
 *Runs 6 and 8 not included as pouring could not be accurately modelled for these configurations.

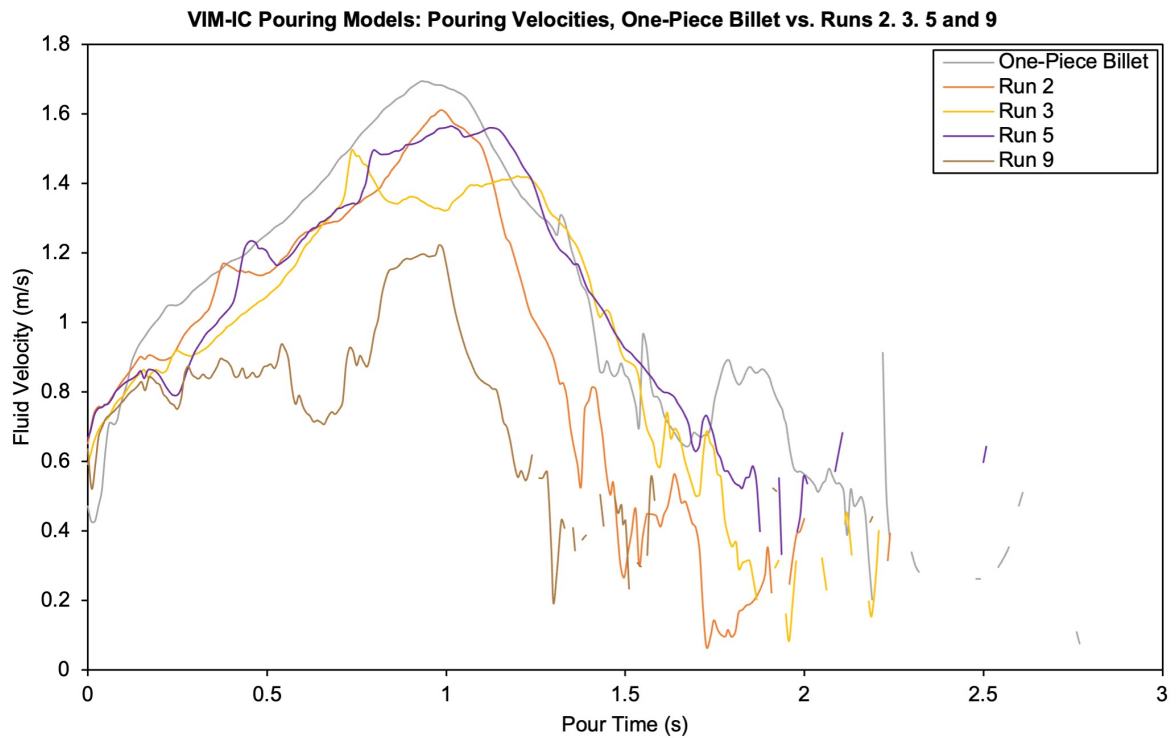


Figure 5.57: VIM-IC pouring models, velocity magnitude ingate plots at crucible outlet
 *Runs 6 and 8 not included as pouring could not be accurately modelled for these configurations.

5.24. MODELLING VIM-IC POURING: DOE L9 ARRAY ANOVA ANALYSIS OF SIMULATION RESULTS

Figure 5.56 shows the average fluid velocity magnitude at the crucible outlet to be compared for the one-piece billet, and Runs 1, 4 and 7. Figure 5.57 compares the one-piece billet average fluid velocity magnitude at the crucible outlet to those of Runs 2, 3, 5 and 9.

5.24 Modelling VIM-IC Pouring: DOE L9 Array ANOVA Analysis of Simulation Results

ANOVA trend graphs were created for the simulation data on pour time, flow width, flow angle and fluid velocity magnitude. The trends from the DOE L9 array experiments were also plotted on the same graph for comparison, with dashed lines show the simulation trends and solid lines showing experimental trends. Parameter levels 1-3 denote different values for the given parameters. For disc height, these are 15 mm, 35 mm and 50 mm respectively. Hole diameters at levels 1-3 are 0 mm, 2 mm and 10 mm, with all holes possessing a depth of 10 mm. Finally, hole positions refer to bottom, middle and top. Bottom position is on the bottom face of the lower billet disc piece. Middle refers to the top face of the disc piece, and the top position refers to the bottom face of the longer billet piece on top of the disc. The full list of configurations for Runs 1-9 can be reviewed in Table 4.6.

As previously mentioned, pouring simulations for Runs 6 and 8 were not included in the ANOVA analysis graphs for the VIM-IC pouring models. This was due to issues with the obtaining the correct fraction solid profile for the pouring initiation time step. By applying the fraction solid distributions in Figures 5.37 and 5.38 for the pouring models of Runs 6 and 8 respectively, the pouring behaviour cannot be modelled effectively. In reality, the alloy initially would start to pour from the billet hole aperture before resolidifying. The resolidified front would then remelt as the melting front moved further downwards, and the alloy would begin to pour again via the hole aperture. Once the alloy starts to move beyond the bottom billet face, the sensor would detect the pouring initiation and would the power would be switched off. To model this effectively in a VIM-IC induction melting model, the movement of the free surface at the hole aperture during induction melting would need to be modelled. This could only be implemented with an electromagnetics model with fluid flow activated, which is not possible due to software limitations for fluid flow modelling at frequencies above 1 kHz, and also the computational expense that would be involved. Therefore, the data for Runs 6 and 8 used to create these ANOVA trend graphs was taken from the experimental runs.

5.24. MODELLING VIM-IC POURING: DOE L9 ARRAY ANOVA ANALYSIS OF SIMULATION RESULTS

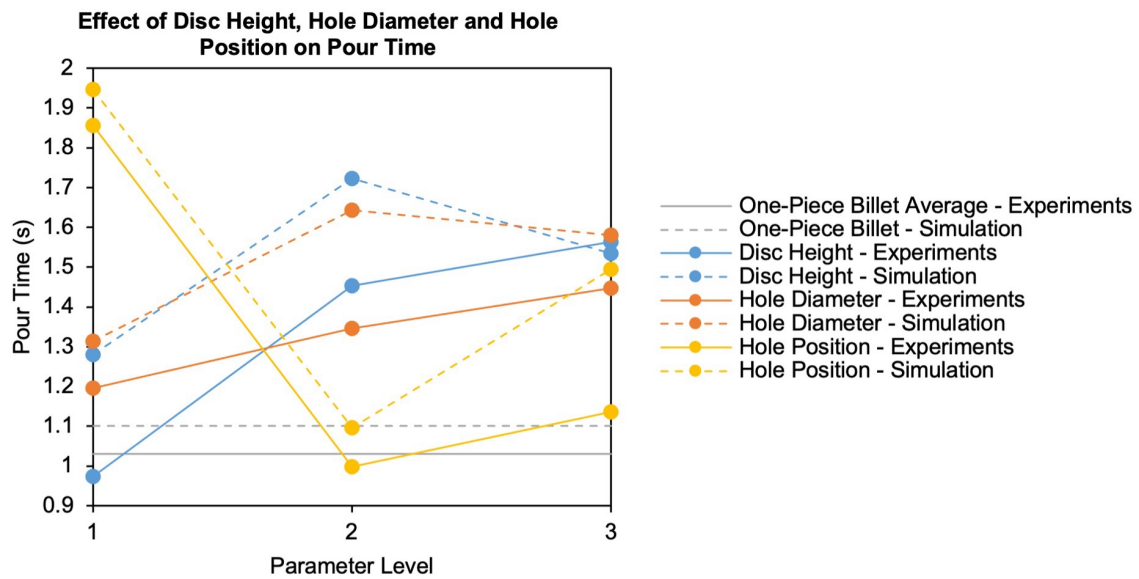


Figure 5.58: ANOVA Pour Time, Simulations vs. Experiments

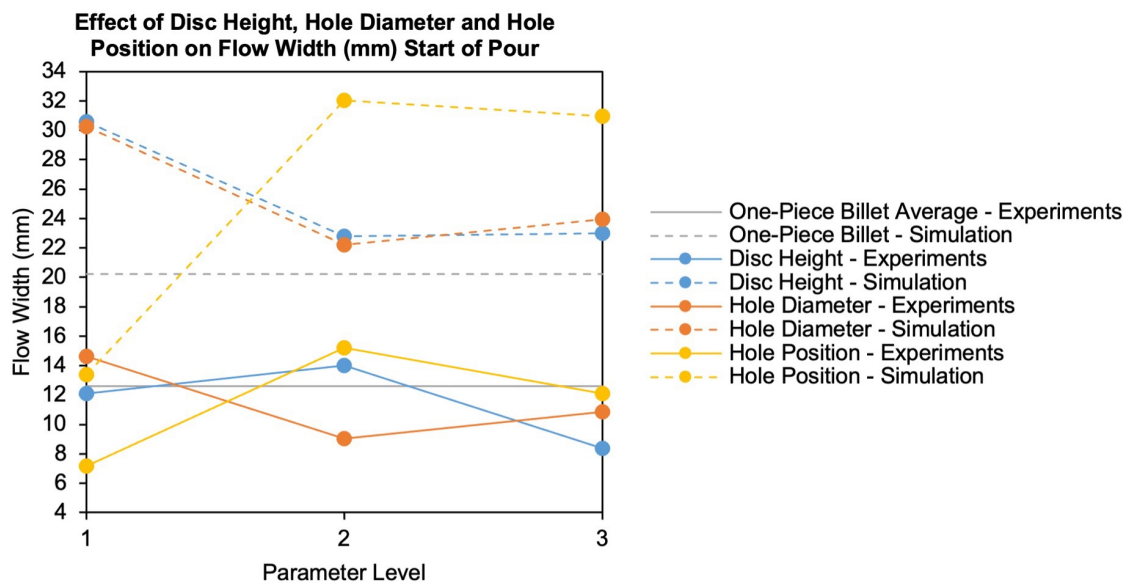


Figure 5.59: ANOVA Flow Width Start of Pour, Simulations vs. Experiment

Figure 5.58 shows the trends for increasing disc height, hole diameter and changing hole position on the total alloy pour time. The average measured pour time for one-piece billets from experiments is in close agreement with the predicted pour time for a one-piece billet from the pouring simulation. The pour time trends show reasonable alignment for changing disc height, hole diameter and position for PLs 1 and 2. However, there appears to be some variation in trends between simulations and experiments at PL3 for hole

5.24. MODELLING VIM-IC POURING: DOE L9 ARRAY ANOVA ANALYSIS OF SIMULATION RESULTS

position. The experimentally obtained difference for pour times between PLs 2 and 3 for disc height and hole diameter show very little difference in the measured times. Therefore, the differences in simulated pour time values at PL3 for disc height and hole diameter may be insignificant.

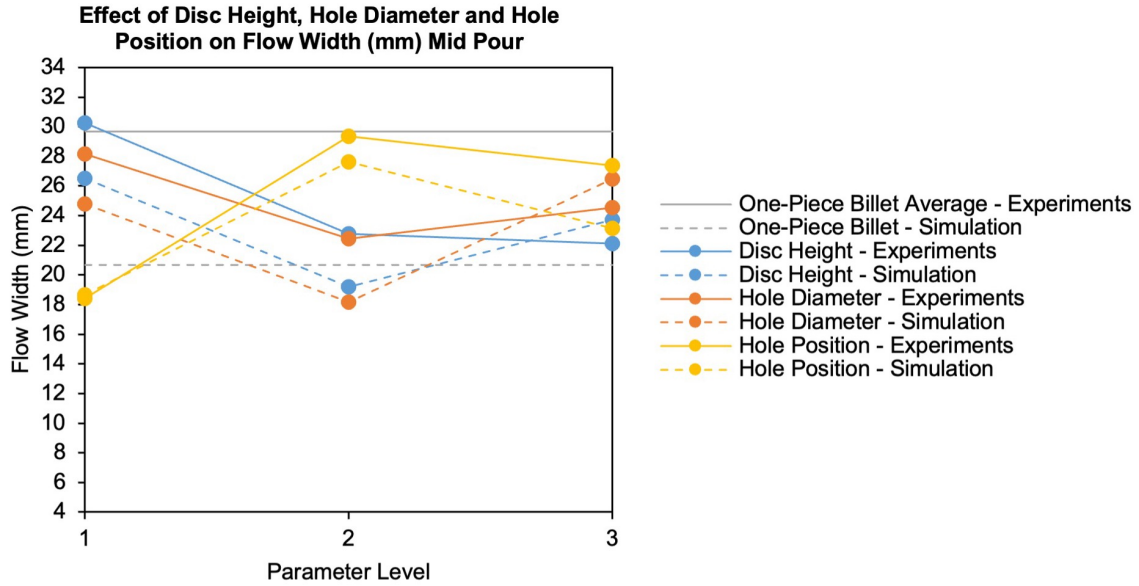


Figure 5.60: ANOVA Flow Width Mid Pour, Simulations vs. Experiments

Although flow width at the start of the pour was predicted using the fraction solid distribution at the bottom billet face for the pouring time step in Figure 5.40, the flow width at the crucible outlet was measured for the first frame at which the flow reached the bottom of the channel volume for each of the pouring models. The trends for the initial flow widths obtained from this method can be seen in Figure 5.59. Similarly, in Figure 5.60, the trends for mid pour flow width in the DOE L9 array follow comparable patterns compared to the trends seen from experimental data, although there are some differences. However, the flow width mid pour for the one-piece billet simulation varies significantly compared to the averaged value from the experimental data. For flow width at the end of the pour, Figure 5.61, the widths measured in simulations are larger than those captured from high speed camera data in the experiments.

Flow angle at the start of the pour can be seen in Figure 5.62. In this case, the trends are not comparable. It appears that the start of pour flow angle deviation from the centreline is lost in the simulations, compared to the larger initial flow angles in experiments.

5.24. MODELLING VIM-IC POURING: DOE L9 ARRAY ANOVA ANALYSIS OF SIMULATION RESULTS

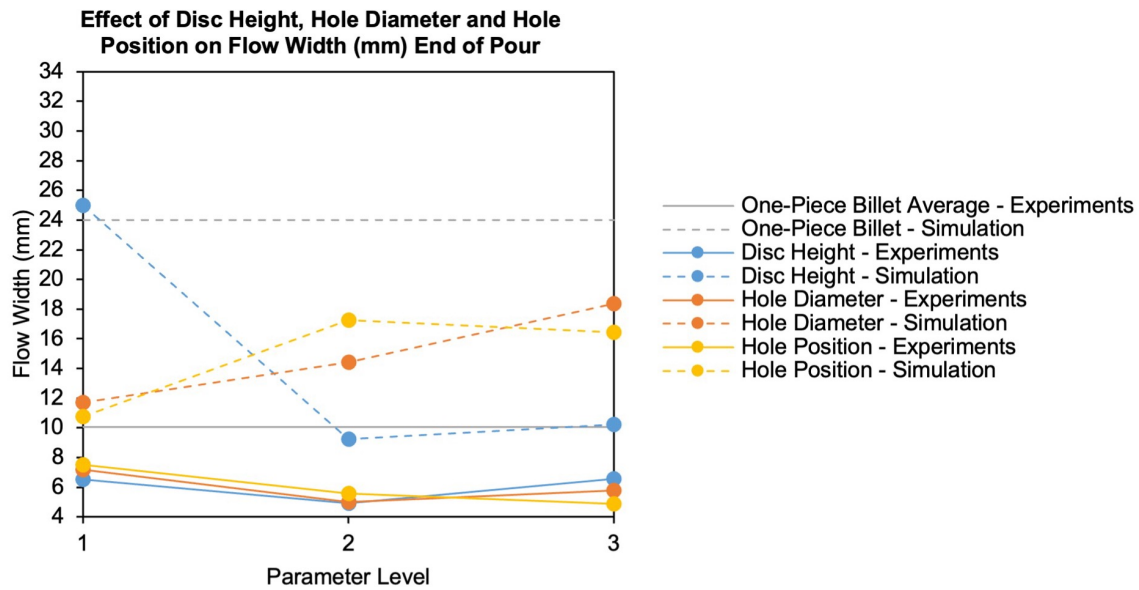


Figure 5.61: ANOVA Flow Width End of Pour, Simulations vs. Experiments

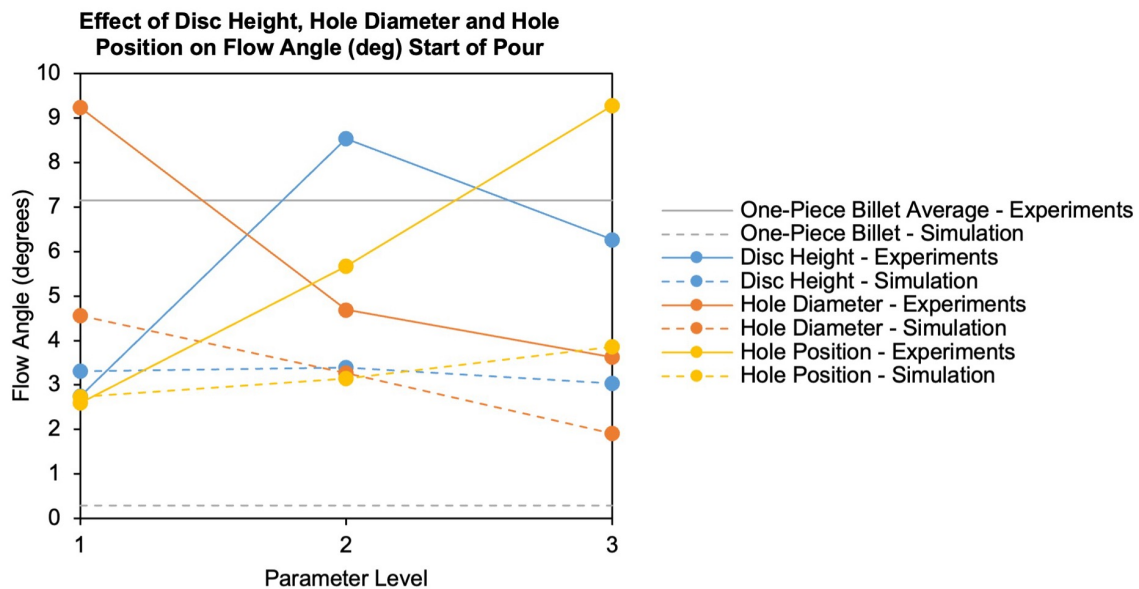


Figure 5.62: ANOVA Flow Angle Start of Pour, Simulations vs. Experiments

Simulated flow angles mid pour match very closely for the DOE L9 arrays, compared to the experimental data. In Figure 5.63, the disc height trends in simulations and experiments are so similar that they are plotted on top of one another. Equally, the simulation trends for hole diameter and position can only be seen by PL3, as the data for PLs 1 and 2 are plotted on top of each other. However, there is a notable difference between the simulated one-piece billet flow angles and those obtained from experiments, for the start of pour

5.24. MODELLING VIM-IC POURING: DOE L9 ARRAY ANOVA ANALYSIS OF SIMULATION RESULTS

and mid pour. Finally, end of pour flow angle displays similar trends in simulations for disc height and hole position, compared to experimental data in Figure 5.64. The end of pour flow angle for a one-piece billet in the simulation is comparable to the angle of average one-piece billet end flow angle from experiments.

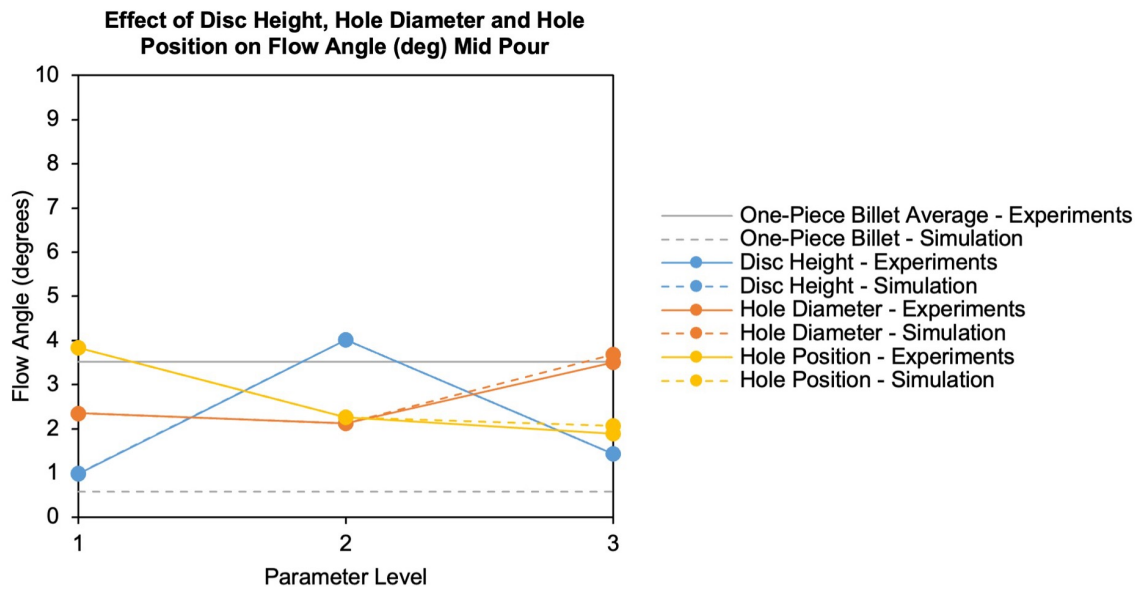


Figure 5.63: ANOVA Flow Angle Mid Pour, Simulations vs. Experiments

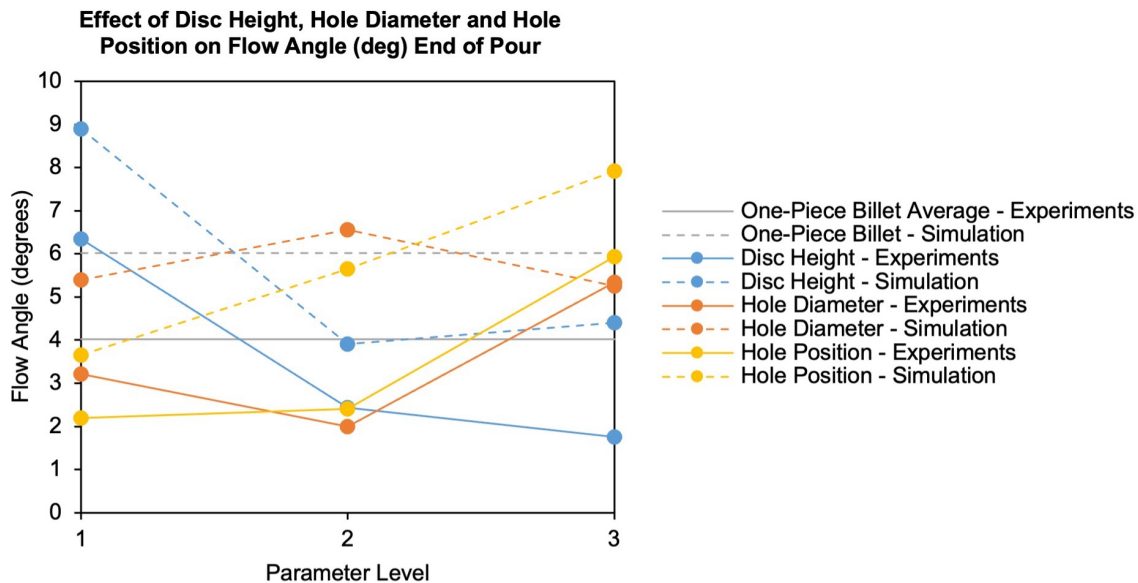


Figure 5.64: ANOVA Flow Angle End of Pour, Simulations vs. Experiments

Average fluid velocity magnitude of the pouring alloy was measured by using the ‘ingate’ function, in ESI ProCAST Visual-Viewer post processing software, where ‘fluid velocity’ is

5.24. MODELLING VIM-IC POURING: DOE L9 ARRAY ANOVA ANALYSIS OF SIMULATION RESULTS

the magnitude of the individual velocities in the x, y and z directions. For these models, the negative z direction is downwards and in the direction of gravity. This involved defining a 50 mm \times 50 mm section to capture all alloy pouring from the crucible outlet. The section was set as parallel to the crucible outlet, at the equivalent location below the crucible outlet that the high speed camera velocities were obtained from, which was most commonly at 'row 2' of the grid generated by the MATLAB velocity program.

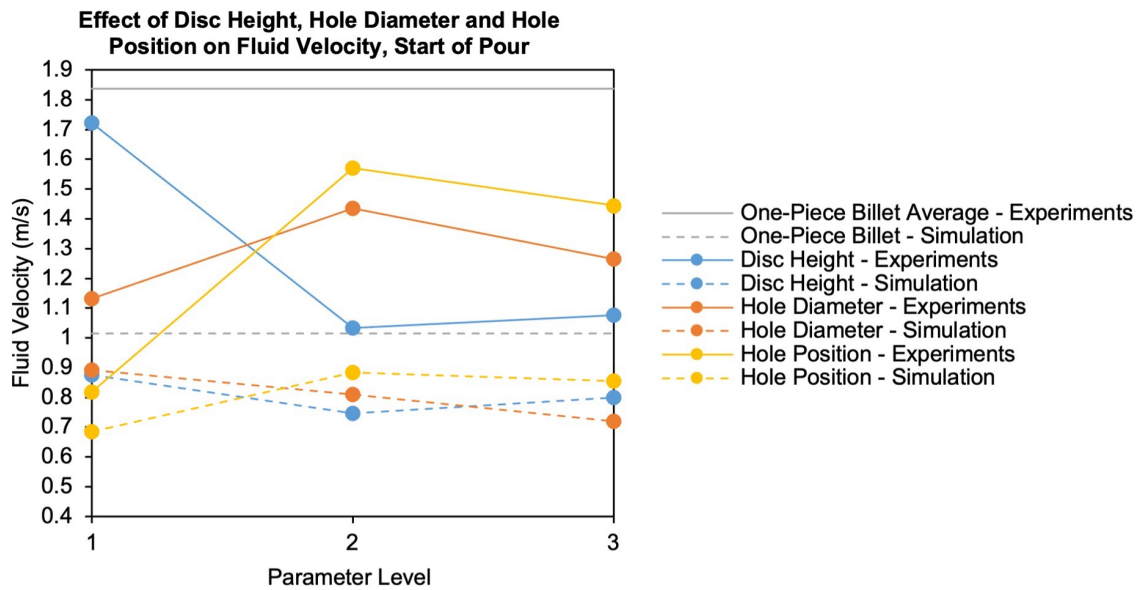


Figure 5.65: ANOVA Fluid Vel. Start of Pour, Simulations vs. Experiments

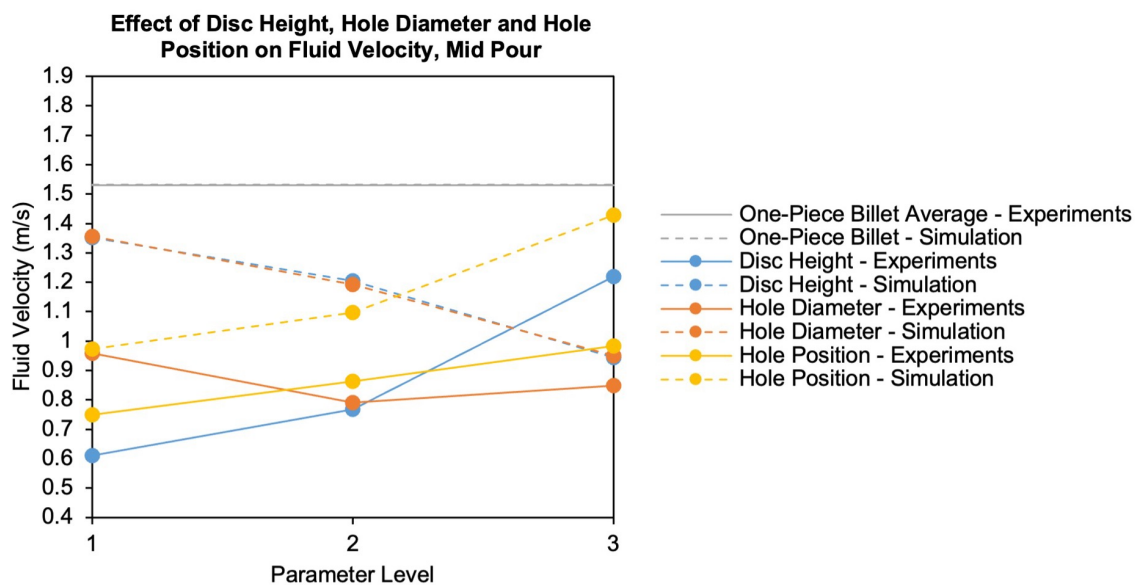


Figure 5.66: ANOVA Fluid Vel. Mid Pour, Simulations vs. Experiments

The average fluid velocity magnitude at the crucible exit for the start of pour and mid pour were not comparable between simulations and experiments in terms of trends, as shown in Figures 5.65 and 5.66. There is a big difference between the simulated and experimentally measured fluid velocity of the one-piece billet at the end of a pour. However, similar trends were noted for the DOE L9 arrays between simulations and experiments for average fluid velocity magnitude at the end of the pour, which is shown in Figure 5.67.

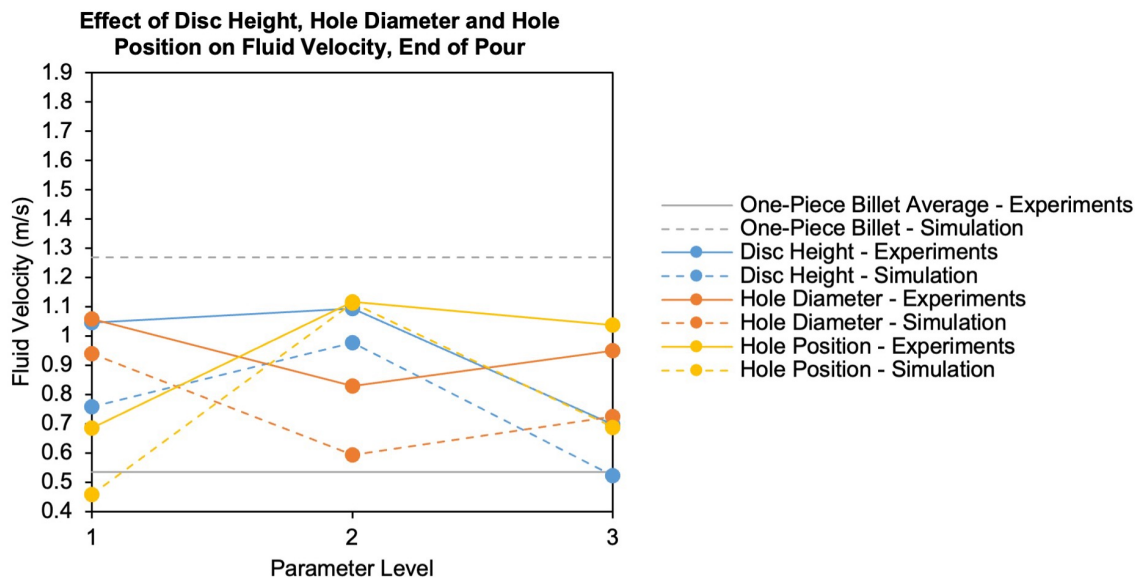


Figure 5.67: ANOVA Fluid Vel. End of Pour, Simulations vs. Experiments

5.25 Modelling VIM-IC Pouring: Discussion

In Figure 5.44, alloy is pouring from the crucible. The temperature distribution throughout the crucible length shows a hotter external surface temperature in the region of the upper half of the billet length. The flow leaving the crucible is laminar by the time step shown, as the flow has stabilised at at this point of the pour. Figure 5.46 shows both the physics of ‘vena contracta’ and rayleigh-plateau instability in action. According to Daugherty *et al.* [98], the vena contracta is defined as the section of minimum area upstream of an orifice. An orifice is defined as usually a circular opening in the wall of a tank, or in a plate normal to the axis of a pipe. It is stated that the plate can be at the end of a pipe. For the crucible, this is a similar setup in which a circular orifice is situated at the end of the ‘pipe’ or crucible. However, it is also noted by Daugherty *et al.* [98] that if a free jet is discharged downwards vertically, gravity will cause the fluid to accelerate. This causes an increase in velocity, and the area will continue to decrease. It is stated that in some cases

there appears to be no section of minimum area, and that the vena contracta should be taken as where the marked contraction ceases. It should also be before the point at which gravity has significantly impacted upon the velocity of the flow, pushing it in excess of the true velocity of the fluid jet. In this image, the flow contracts in width before the effect of acceleration due to gravity causes visible perturbations. This frame captures the flow just before the initial ‘start of pour’ frame, as the alloy has not yet reached the bottom of the channel volume.

Divergence of the flow from contracting and laminar behaviour, which is visible in these figures, is due to rayleigh-plateau instability as described in Section 4.6. Figure 5.46 shows the instability of fluid pouring from the crucible in the initial pouring stage for Run 1, as the critical pouring length is exceeded and the metal destabilises into droplets along the length of the flow. In addition, Figure 5.47 shows another example of rayleigh plateau instability for Run 7. The flow instability patterns in Figures 5.48 and 5.49 can be categorised separately from the standard rayleigh-plateau instability and perturbations seen in the previous figures. The winding pattern and instability seen in Figure 5.48 is similar to the corkscrewlike sinous type breakup mode in Figure 4.75, for the end of pour frame for the first one-piece billet experimental run.

Figure 5.49 shows a ‘tree-like wire’ style of instability flow pattern, which was the term coined by Song *et al.* in their paper investigating the morphology of liquid metal for different velocities and values of applied electric potential [99]. Figure 5.50 shows the velocity of a one-piece billet during pouring. Vena contracta is observed until acceleration due to gravity causes perturbations in the flow. With the growing flow instability after the initial narrowed flow section, under gravity the instabilities increase which results in a divergent flow direction beyond the flow narrowing. The acceleration due to gravity of the fluid velocity magnitude along the length of the fluid flow can be observed in the velocity plot, with flow perturbations growing in the yellow to red region.

Figure 5.51 shows an example of a large flow angle mid pouring for Run 4. Although the flow direction diverges from the centre line at a large angle, the flow itself appears to be laminar. Figure 5.52 shows the end of pour frame for Run 5. In this case, the flow is also at a large angle to the centre line but the width is much narrower as the flow is about to break at the thinnest section along the flow length.

Upon emptying the crucible, the simulation for Run 1 resulted in leftover alloy solidifying at the crucible outlet. This was also observed in certain instances for the DOE L9 array VIM-IC pouring experiments, as shown in Figure 4.77. The presence of leftover alloy

hanging from the crucible outlet as shown in Figure 5.53 is visible in both the temperature measurement ingate in Figure 5.54 and the fluid velocity magnitude measurement in gate in Figure 5.56. As the leftover alloy hanging from the crucible outlet extends past the ingate measurement location, the measured temperature and velocity continues to be recorded for Run 1 in both of these graphs. Examining Figure 5.54, the lowest maximum temperature is recorded in Run 1, followed by Run 7. It is also evident that alloy dripping out of the crucible occurs for all other runs, apart from Run 1. The ability to avoid alloy dripping for an extended period of time after the main bulk of the pour has completed is beneficial. However, as the dripping appears to occur at the end of the pour once the mould is mostly filled, the broken flow seen in the simulations for the latter part of the one-piece billet pour and Runs 2-9 would likely end up solidifying within the sprue section of the mould. Therefore, broken flow in these cases would be unlikely to affect quality of the finished castings.

Furthermore, the ability to reduce the range of the temperature gradient throughout the billet in induction melting is also favourable. High temperatures which greatly exceed the liquidus temperature can result in much higher velocities during mould filling, due to the change in viscosity at higher temperatures. This can, in turn lead to problems such as mould erosion, where particles of zircon become delaminated from the inside of the shell mould. Another benefit of reducing the temperature range and eliminating the excessively high temperatures in mould filling is the effect that this has upon the grain structure of castings. In many cases, there is not a stringent criteria for the grain structure of castings in many automotive applications. However, for example, castings created for aerospace applications may require grain structure to be controlled, with smaller grain sizes favoured over larger columnar grains. It is known that higher temperature alloy takes longer to solidify, and results in larger grain sizes or even columnar grains. In cases where smaller grain sizes are required, it is often a balancing act between pouring alloy at temperatures high enough to prevent porosity, but low enough to retain the required grain structure size. ESI ProCAST software has a built-in CAFE solver which allows for grain structure prediction in casting solidification. The effect on casting defect prevalence of the crucible outlet temperatures in Figures 5.54 and 5.55 will be tested in VIM-IC mould filling and solidification simulations in Chapter 6. However, initial examination of the Run 1 temperature pouring profile in Figure 5.54 suggests that a 15 mm disc or ‘penny’ could be beneficial for casting outcomes, as the alloy pouring temperature range is reduced and broken flow is minimised.

Another interesting crucible outlet temperature profile is that of Run 3 in Figure 5.55.

5.25. MODELLING VIM-IC POURING: DISCUSSION

There appears to be a notably large step change in the temperature across the crucible outlet alloy pouring temperature profile. This is likely due to the presence of a 10 mm diameter hole in the ‘top position’, which is located in the bottom face of the top billet length. As the bottom billet piece has a disc height of only 15 mm, the effect of a hole with a 10 mm diameter is more likely to be visible in the pouring temperature profile than those located in the ‘top’ position with a taller disc height below, or smaller hole diameter. For all of the pours, including the one-piece billet, there appears to be a step change in the temperature at around 0.2 seconds.

Despite some differences in operating parameters, for a 3 kg billet the predicted temperature ranges in Figures 5.54 and 5.55 are comparable to those measured in experimental pouring temperature measurements in Section 4.5.4. The shape of the pouring temperature profile was also similar, with the curve reaching a peak temperature before decreasing across the latter portion of the pour. Most of the initial alloy pouring temperatures at the crucible outlet are lower in simulations compared to those recorded in experimental data.

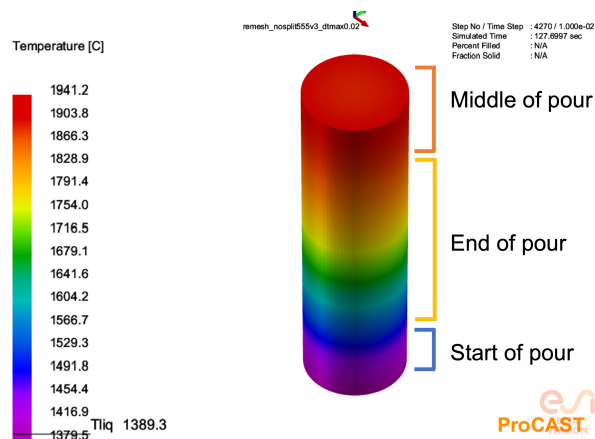


Figure 5.68: Hypothesised billet portion pour order

In the VIM-IC thermal induction heating models, the peak temperatures were observed at the top of the billet and not halfway up the billet length. If the alloy dropped into the cavity below the crucible from bottom to top, the peak temperatures would be expected closer to the end of the main pouring curves. Although some thermal cooling takes place for the duration of the pour, it would be unlikely to decrease the alloy temperature by 200 °C over the course of one second for the latter portion of the pour. The hypothesised billet portion pouring order is illustrated in Figure 5.68. Pouring initiates through an opening in the bottom face of the billet. As the alloy pours through this initial opening, the melting front widens the hole through which molten alloy is pouring. This results in

a wider pour width. Alloy from the top and middle of the billet length pours through the opening in the bottom billet face, moving past the alloy in the bottom corners of the crucible, close to the outlet. The alloy in the bottom corners remains somewhat stationary, until the alloy above has moved past it and left the crucible. Finally, the stationary alloy which is left over in the crucible leaves the crucible. This pour pattern is responsible for the temperature curve plotted for alloy below the crucible outlet during pouring, as pouring initiates with a low alloy temperature. This low alloy temperature increases to a peak maximum temperature, followed by a decrease in temperature at the end of the pour.

Figures 5.56 and 5.57 show the pouring velocities of the alloy leaving the crucible outlet. In both graphs, it is clear that initial pouring velocities are lowest for one-piece billets compared to two-piece billets with discs of any height. This could be due to the effect of thermal contact resistance between the bottom billet disc and top longer billet piece, in the form of a temperature dependent heat transfer coefficient, causing the alloy to homogenise to different extents by the pouring time step. This homogenisation could result in a flatter melting front than those which approach the bottom billet face in pouring of a one-piece billet. Flow initiates at a lower velocity compared to the peak filling velocities, which is likely due to the slower initial pouring as the mobility of the alloy initiates. The molten alloy is moving through the bottom billet face via the defined pouring width, which would likely occur slowly at first. Once the pouring width opens up as a wider aperture, the alloy would flow more freely from the crucible, allowing it to accelerate due to falling under gravity.

The lower velocities for alloy leaving the crucible correspond to the lower temperatures of alloy observed in the later part of the pours in both Figures 5.54 and 5.55. The initial pouring velocities for Runs 3, 5 and 9 were markedly higher than for other configurations. In both the simulated pouring alloy temperature and velocity graphs, the pieces of data separated from the initially connected pouring lines represent broken flow leaving the crucible. As previously mentioned, to ensure that the total pouring times and representative start and end frames were selected for ANOVA analysis, the end of the pour was considered to be the point at which the flow broke at any point along the length of the channel below the crucible.

Regarding pouring velocities at the crucible outlet, it would be difficult to predict the effect on defect prevalence solely from examining the velocity curves in Figures 5.56 and 5.57. However, the velocity profiles of Runs 3 and 9 appear to be of note. Firstly, Run 4 dips

greatly in velocity at the end of the main bulk of the pour, shortly followed by a very sharp rise in velocity before broken flow sets in. This could potentially be due to the disc height of 35 mm for the bottom billet piece in Run 4. From the DOE L9 array VIM-IC pouring experiments, this disc height appeared to be problematic regarding crucible breakages and causing highly angled flow at the start of the pour. Run 9 appears to have a notably lower fluid velocity magnitude throughout pouring. The pouring simulations showed significantly more unstable flow for Run 9, as shown in Figures 5.48 and 5.49.

From examining both graphs, it is clear that pour time for Run 4 is markedly shorter than those of the other runs. Run 4 shows great variability in alloy temperature and fluid velocity magnitude at the end of the main bulk of the pour, before broken flow is observed. Run 4 is configuration with a 35 mm disc height, which was a known factor in the volatility of pouring behaviour for the experiments.

One important factor in modelling mould filling in ESI ProCAST Visual-Cast software is total pour time. When modelling mould filling according to the typical use scenario, a mould inlet condition is applied for fluid flow entering the mould. Often, the main parameters which are defined are the pour time to allow the mass flow rate to be estimated, the mass of alloy, and the alloy pouring temperature. For this reason, it is a great strength of the VIM-IC pouring model that the pour time for the one-piece billet matches closely with the experimentally obtained pour time and also the trends seen in the DOE L9 array experimental models. As mass flow rate determines factors such as mould filling velocity, which in turn affects the prevalence of potential defects such as mould erosion, pour time is a key factor in predicting casting scrap rate outcomes. Furthermore, if the mass flow rate is exceptionally slow, defects such as misruns could occur due to alloy solidifying in the mould before the mould is completely filled. The trends in Figure 5.58 demonstrate a good agreement in trends between pour time from simulations compared to experiments. If the EMAG module was used by foundries using VIM-IC to model billet temperature profiles and subsequent pouring for industrial cases, the most common use scenario would be for one-piece billets. Therefore, the ability to predict pour time for a one-piece billet with high accuracy is a valuable outcome for this pouring model.

As previously discussed, initial flow width can be predicted to a good degree of accuracy for DOE L9 array models by measuring the fraction solid distribution below $fs_{0.3}$ at the bottom billet face from VIM-IC thermal only induction heating models as shown in Figure 5.59. However, the trends in initial flow width are not in as close agreement for the widths measured from the start of pouring frame in the initial flow model, which is

the first frame in which the alloy stream reaches the bottom of the channel volume.

It could be argued that reliable prediction of flow width mid pour is a more useful outcome of a VIM-IC pouring model. By mid pour, the flow appears to have stabilised and is more representative of the behaviour for the main bulk of the pour. Flow width has an impact upon the mass flow rate for a pour, for a given alloy configuration. Unfortunately, the values for flow width mid pour for a one-piece billet VIM-IC pouring model are not as close to the experimentally obtained average mid flow width for the one-piece billets. However, the trends show similarities for flow width in the middle of pouring for the DOE L9 array runs tested. At the end of the pour, the flow width in experiments did not vary by as large width differences between different runs as the start and middle of the pour. Flow width at the crucible outlet for the end of the pour in simulations was larger than those observed in experiments, in which the flow width variation was very small. However, this is likely to be less important than mid pour flow width, as the end of the pour fills the sprue part of the mould cavity and should not affect the filling of the castings. Therefore, the filling data at the end of the pour and solidification data for the top part of the sprue is less important than the information captured within the casted part volumes, for which defect prediction is particularly important.

Although a variation of up to 10° in initial flow angle may sound like a significant variation, Figure 4.48 shows how large the experimentally measured flow angles can be. At the start of pour, flow angles measured from high speed camera data of pouring experiments showed a much greater variation in angles across parameter levels than those seen in simulations. This could be a potential limitation of the pouring models, as simulating initial filling angles could provide interesting data for defect outcomes as a large deviation from the centre line in flow angle could cause a mould to fill asymmetrically. In the experiments, high initial angle flow was prevalent in configurations with the hole positioned in the ‘bottom’ position and a disc height of 35 mm. However, apart from the effect of parameters causing large initial initial flow angles, this angled flow could potentially be attributed to differences in one side of the billet melting before the other side. This appears to be linked to the side of the coil which had more turns, i.e. the side with the terminals. Finally, it is important to note that induction heating and melting is a volatile phenomena. It is not straightforward, as the generator system aims to hold steady the power as it adjusts other values in response as it aims to maintain a constant power value. The reality is that it is a challenge to ensure that the melting sequence is consistent between runs, but every effort is made to provide this consistency.

Simulated flow angle for the middle of the pour follows the same trends for all of the parameters tested in the experiments, as shown in Figure 5.63. Many of the values match so closely that the data sets are plotted on top of each other. However, there is a lesser flow angle observed in the simulated one-piece billet, compared to the experimental average of three one-piece billet runs. Again, flow data for the middle of the pour is particularly useful to be able to predict accurately. It reflects a point at which the flow has become stable and is representative of the main bulk of the pour.

Flow angle at the end of the pour is shown in Figure 5.64. There are similarities in the trends shown for disc height and hole position when comparing experiments to simulations. As previously mentioned, the end of the pour would correspond to the filling of the top part of the sprue and would therefore be unlikely to affect the filling of castings.

Finally, in the ANOVA analysis for VIM-IC pouring models, fluid velocities for one-piece billets vary greatly in the simulations compared to the experiments at the start and end of the pour; see Figures 5.65 and 5.67. However, the fluid velocities match closely for one-piece billets mid pour, in simulations vs. experiments. In Figure 5.67, it is evident that the impact of disc height and hole position upon fluid velocity at the end of the pour is captured well in simulations, as the trends are in agreement with the experimental data. For the start of the pour, the fluid velocity trend variations are much larger in experiments compared to those observed in simulations. Mid pour, the predicted fluid velocity for a one-piece billet matches exactly with the mid pour velocity in experiments. This can be seen in Figure 5.66, and as previously mentioned, the flow has stabilised by mid pour and is also representative of the bulk flow behaviour compared to characteristics observed at the beginning and end of the pour. Simulated end of pour fluid velocity for the DOE L9 array runs follows similar trends to those seen in experiments.

It is important to note that differences in flow widths, flow angles and fluid velocity magnitudes may not only be due to limitations in VIM-IC pouring simulations and the use of only an imported temperature distribution throughout the billet with no flow data. Firstly, the use of experimental data for Runs 6 and 8 for the ANOVA simulation data trends could potentially skew the responses to parameter variation. Secondly, differences observed could also be due to the limitations of using only one high speed camera to capture flow leaving the crucible in the bespoke VIM chamber. With only one viewing port large enough to capture the flow leaving the crucible on the front of the chamber, and access to only one high speed camera at the time, it was not possible to determine these flow characteristics in three dimensions. Values for flow width, flow angle and fluid

velocity were based only on two dimensional images due to the limitations of the chamber design and access to the required additional high speed camera equipment.

5.26 Modelling VIM-IC Pouring: Conclusion

Modelling alloy pouring for the VIM-IC process using the temperature profile of a billet from a thermal only induction heating model as an initial condition, provides reasonable and representative results for flow characteristics in many cases. Regarding particularly important parameters such as pour time and overall pouring temperature range, the model was able to provide great predictive value.

The compromises outlined in this modelling methodology are necessary to render it workable for many foundries in industry. For the application of simulating the effect of varying billet parameters in an industrial setting, modelling fluid flow in induction heating models would be time inefficient and require costly computing equipment which many foundries would not feasibly have access to. By importing the VIM-IC temperature data at pouring point as an initial condition, pouring models with reasonable flow characteristics can be generated while providing useful information when modelling two-piece billets with holes in varying positions.

Further work exploring the development of modelling techniques which could simulate pouring with a hole on the bottom billet face is required. However, to achieve the goal of obtaining data to better inform industrial processes to improve the yield of investment casting tree mould designs, it is possible to review the flow width, fluid angle and fluid velocity data for Runs 6 and 8 from the DOE L9 array experiments. The flow widths, angles and fluid velocities for Runs 6 and 8 could potentially be applied to a mould filling simulation using ESI ProCAST Visual-Cast software, by applying a user defined inlet condition for flow at the mould inlet. This would allow for a flow width and flow angle which varies across the pour duration, and individual x, y and z directional fluid velocity components to be dictated for the entire pour. To understand the temperature profile across the duration of the pours for Runs 6 and 8, which would also need to be defined, further trials with a second IR thermometer measuring temperatures at the crucible exit need to be conducted. It would also be beneficial to conduct further trials for the other runs in the DOE L9 array experiments to measure the crucible outlet temperatures. However, running a large number of additional trials would be costly, especially with the number of repetitions required for trials of each run configuration.

5.27 Modelling VIM-IC: Conclusion

Modelling induction heating with a thermal only model of the VIM-IC process allows for an accurate prediction of pouring times and alloy temperature profiles, which are arguably the two key parameters used in standard mould filling simulations [OB1, OB2, OB3]. This was achieved by devising methodologies for modelling piping and thermal contact resistance without activating fluid flow in the model [OB5].

Use of the ingate function in post-processing allowed for pouring temperatures to be obtained, as a second IR thermometer was not available for the DOE L9 array experiments [OB3]. Importing the thermal gradient of the billet as an initial condition for the VIM-IC pouring models results in flow characteristics which are in agreement with many of the important ANOVA trends obtained from experimental data [OB2, OB3]. This includes many of the flow characteristics at the mid pour time step, for both one-piece and DOE L9 array alloy configurations. Flow characteristics mid pour are particularly important to predict, as this likely represents the flow behaviour for the bulk of the pour once the flow has stabilised. Pouring data suggests that Run 1, with a 15 mm disc and no holes, could produce more favourable results in terms of lowering defect occurrence [OB4]. Conversely, Run 4, which consists of a 35 mm disc and no holes, could potentially result in unfavourable mould filling [OB3]. The next chapter will determine the effects of parameters in the L9 array on defect occurrence.

Chapter 6

Modelling VIM-IC: Mould Filling, Solidification and Defect Prediction

6.1 Modelling VIM-IC Mould Filling and Solidification Overview

In the casting industry, ESI ProCAST software is widely used to provide guidance on mould design and process parameters. The primary purpose of modelling mould filling is to minimise casting defects, within an industry which has not historically favoured computational modelling and requires solutions in a time efficient manner. Although in a standard use scenario, a filling inlet condition would be implemented at the inlet of a meshed mould within an air enclosure geometry, in this chapter the aim is to model mould filling with the temperature profile of alloy in the crucible set as an initial thermal condition. To improve upon the accuracy of the mould filling models, the initial thermal profile for the crucible and mould volumes is imported from a mould preheating model, in to the mould filling model.

6.2 Modelling VIM-IC: Mould Preheat and Cooling

6.2.1 Modelling VIM-IC Mould Preheat and Cooling Overview

In the VIM-IC process, prior to performing casting in a VIM chamber, the assembled refractory mould with attached crucible is preheated in a furnace. By preheating the

mould assembly, the risk of thermal shock to the crucible and mould during VIM casting is reduced. Increasing the mould temperature prior to casting is also important to prevent solidification related casting issues such as porosity and misrun. The assembled mould geometry was preheated, simulating the process of heating in a furnace at a temperature of 1100 °C and then cooling until the point of alloy pouring. This includes furnace time, transfer from the furnace to the VIM chamber, time taken for the vacuum level to be reached and the changes in film coefficient values with the vacuum pressure conditions. In this model, it is assumed that the crucible and mould assembly has reached a uniform temperature of 1100 °C throughout the mould and crucible volumes in the furnace and the model is allowed to cool until the point of alloy pouring. Wrapping is also applied as a boundary condition to the external surfaces of the vermicullite mould layer, to simulate the effect of insulation in the defined areas.

6.2.2 Modelling VIM-IC Mould Preheat and Cooling: Governing Equations and Physics

In addition to the governing equations and physics described for the VIM-IC pouring models in Section 5.19, an additional aspect of modelling radiative heat transfer was introduced in both the VIM-IC mould preheating models, and the combined mould filling and solidification models. To model radiative heat transfer, ‘view factor’ was considered.

The Stefan-Boltzmann law can be applied to a grey body (non-black body) in a black enclosure, to calculate the net rate of heat loss q of the grey body as follows [100]:

$$q = A_1 \epsilon \sigma (T_1^4 - T_2^4) \quad (6.1)$$

where A_1 is the area of the grey body, ϵ is the emissivity of the grey body, σ is the Stefan-Boltzmann constant, T_1 is the temperature of the grey body and T_2 is the black enclosure temperature.

When modelling radiation heat transfer for castings, in the context of simulations in an industrial environment, it is necessary to model radiation exchange in a representative manner while maintaining time efficiency. View factors allow the radiation between surfaces to be considered by applying a surface-to surface approach, based upon the geometry of the problem. For a simple geometry, the view factor F_{ij} between two areas, A_i and A_j , can be calculated as follows [101]:

$$F_{ij} = F_{A_i \rightarrow A_j} = \int_{A_i} \int_{A_j} \frac{\cos(\theta_i)\cos(\theta_j)}{\pi S^2} \cdot A_j dA_i \quad (6.2)$$

where F_{ij} is the ratio of the radiation received by A_j from A_i , to the absolute value of radiation emitted by area A_i . Connecting vector S , with angles θ_i and θ_j describe the relative position and orientation between the areas. The angles are spanned between normal vectors n_i and n_j respectively. However, although (6.1) describes how view factor can be calculated for basic geometries, in the case of view factor calculation in ESI ProCAST Visual-Cast software, this is performed by a complex radiation algorithm. Using an algorithm to calculate view factors for an FEM model with discretised elements, view factors can be calculated using ray tracing techniques and the Monte Carlo method, or a modified form of this method to calculate radiation with respect to neighbouring bodies [102].

6.2.3 Modelling VIM-IC Mould Preheat and Cooling: Geometry and Mesh

To create the mesh for this mould preheat model, the crucible surface mesh from the induction melting model was imported into this model in ESI ProCAST Visual-Mesh software. The CAD for the investment casting tree was appended, ensuring that the sprue was aligned with the crucible outlet cavity. This casting tree geometry comprised of a generic turbocharger turbine wheel design and a multi-tier casting tree with 16 wheels. The tree sprue design was comprised of four tiers, each with four castings per tier.

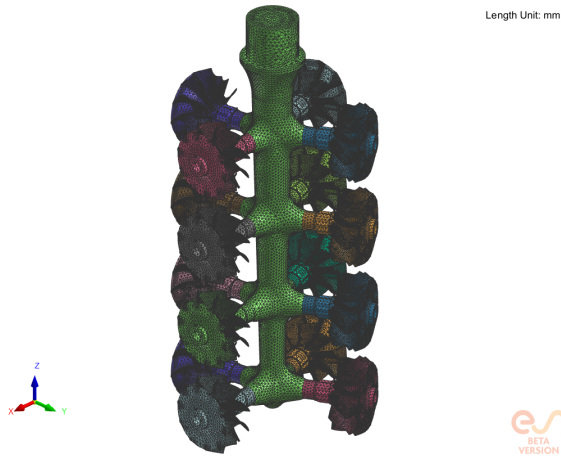


Figure 6.1: Meshed investment casting tree geometry, sprue and wheel castings

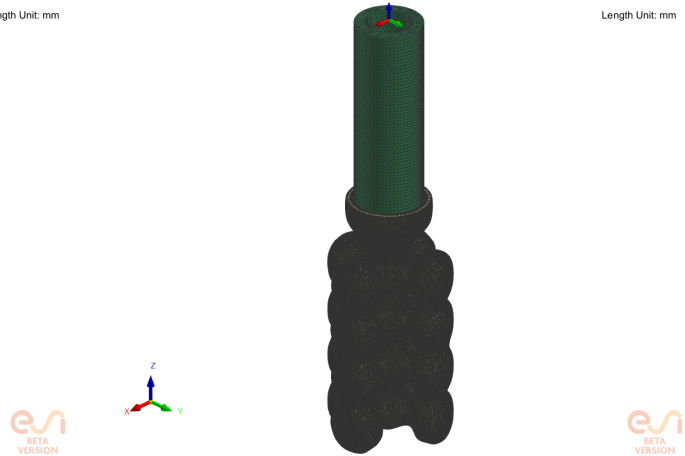


Figure 6.2: Meshed investment casting shell mould created around crucible assembly

Once this geometry setup was established, the casting tree geometry which would make up the internal mould cavity volumes were meshed first. It was crucial to ensure that a minimum of two elements were applied to every component surface edge in the two dimensional tria element mesh, including the thin turbocharger turbine wheel blade sections. Once the mesh was created for one wheel casting on the investment casting tree mould design, it was transformed and copied for all castings on the tree. This ensured a consistent mesh across all castings. Apart from the smaller elements in the thin geometry sections such as blades, an element size of 1 mm for the surface mesh was applied to the wheel castings. Finally, the central sprue was meshed with an overall element edge length size of 2 mm for elements within the sprue. The surface mesh of the sprue and attached castings can be seen in Figure 6.1.

Following the creation of the investment casting tree surface mesh, which was attached to the crucible mesh, the ‘shelling’ mesh function was used to grow meshes comprising of elements which were extended in the ‘normal’ direction to the elements of the casting tree surface mesh and surface of the crucible, up to a defined height. The first shell layer was 2 mm of zircon, which required the mesh surface to be remeshed using the ‘wrap’ mesh function. This ensured that the distribution of surface elements across the wrap mesh were between 0.8-1 mm edge length, which allowed the required mesh quality levels to be maintained. Instances of topological issues identified in mesh quality checks were repaired manually, as minor topological issues can occur in using the shelling mesh generation algorithm. These steps were repeated for the generation of two more shell layers of mullite and vermicullite, 6 mm and 2 mm thickness respectively. The final surface mesh of the shelled mould and crucible assembly can be seen in Figure 6.2.

As before in the VIM-IC pouring models, the 3D mesh for all volumes was created using a uniform mesh type. The meshing criteria was selected based upon the recommended values for simulations involving fluid flow, for which the elements within the ‘alloy’ defined volumes were given a transition factor value of ‘0.8’ and shape factor of 1.5. For the crucible and mould shell volumes, the 3D elements were created with a transition factor of 1.5, and shape factor of 2. As before, these settings were chosen according to the recommended mesh definitions by ESI Group for 3D mesh generation in alloy and mould volumes. Finally, once an appropriate 3D tetra mesh was created which passed the recommended mesh quality checks, an air domain ‘enclosure’ volume was created as a 2D surface mesh. This allows for the air domain to be modelled, without extending indefinitely. The implementation of this air enclosure allows for the effect of radiation between nearby castings within the tree to be modelled. The air enclosure was a basic

cylindrical shape, with a diameter of 390 mm and height of 680 mm. The element edge length size for this enclosure 2D mesh was selected as 50 mm, according to the recommended values by ESI Group for modelling radiation with an air enclosure volume. The 3D volume mesh of the crucible and mould assembly with the 2D meshed air enclosure can be seen in Figure 6.3.

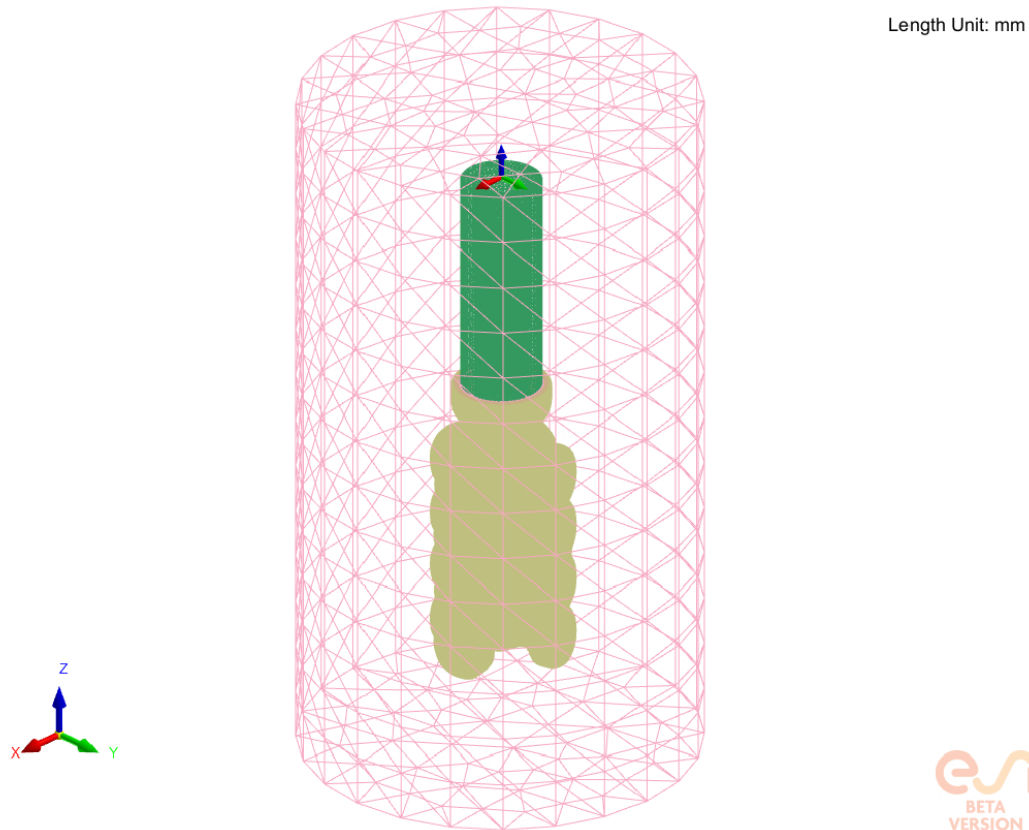


Figure 6.3: Crucible and mould assembly meshed with 3D tetra mesh and 2D tria based air enclosure mesh

6.2.4 Modelling VIM-IC Mould Preheat and Cooling: Materials and Boundary Conditions

For this mould preheat simulation, the internal mould cavity volumes were assigned as 0 % filled. The crucible was assigned as aluminosilicate ceramic fibre, with the shell volume layers assigned as refractory zircon, mullite and vermiculite. The air enclosure volume was converted to an ‘enclosure’ type volume, ensuring that the element normal orientations were correct. All volumes were assigned a temperature of 1100 °C.

The contact interfaces between empty alloy volumes within the casting tree cavity were all defined as an ‘equivalent’ interface. For the interfaces between shell layer volumes,

6.2. MODELLING VIM-IC: MOULD PREHEAT AND COOLING

the heat transfer coefficient was given a value of $300 \text{ W/m}^2\text{K}$. This value was informed by ESI Group, who have conducted extensive industrial validation in comparison with simulations to determine this as a reasonable value for heat transfer coefficient between shell volumes. This could be further improved by conducting temperature validation tests to compare the difference between shell temperatures during cooling measured with a thermocouple, to computed shell temperatures in a cooling model. However, due to challenges experienced with attachment of the thermocouple to the shell mould, it was concluded that the compromises which would have to be made would result in the experimental setup deviating far from the standard shell setup in cooling.

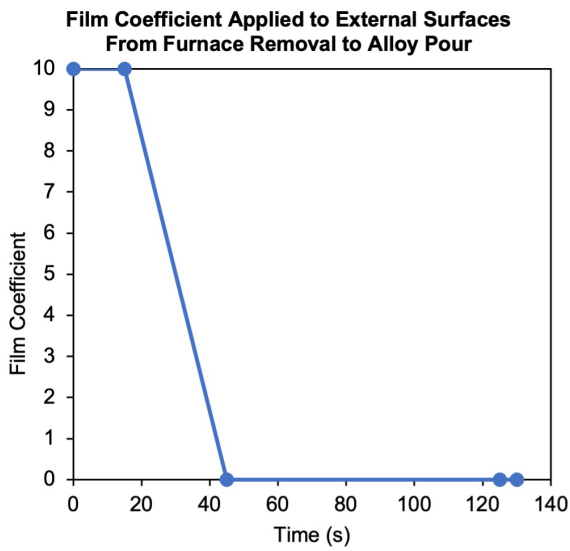


Figure 6.4: Film coefficient transition from atmosphere conditions to vacuum, from furnace removal to alloy pouring point

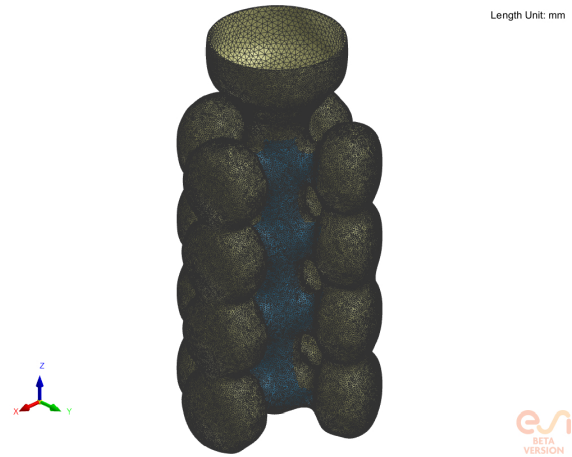


Figure 6.5: Meshed investment casting shell mould and crucible, with region in which wrap boundary condition is applied in the blue region

The interfaces between shell volumes were defined in an outwards direction, away from the centre of the mould. This allowed heat transfer to be modelled as moving towards the direction of the surrounding enclosure. An emissivity value of 0.7 was assigned to the external surfaces of the crucible, zircon, mullite, and exposed vermicullite region of the shell. The defined wrap regions on the surface of the vermicullite mould layer were assigned an emissivity value of 0.2. For all external surfaces apart from the region specified with wrap boundary conditions, the film coefficient effect was applied for the time in which the mould was in standard atmosphere conditions, at an ambient temperature of 25°C . The effect of film coefficient was reduced gradually for the time period in which the vacuum pump would be switched on, reaching zero by the time that the vacuum pressure would be achieved according to the standard VIM-IC industrial process. The

time dependent definition of film coefficient for the mould preheating model can be seen in Figure 6.4. The value of film coefficient defined as $10 \text{ W/m}^2\text{K}$ was assumed due to convective heat losses taking place in air with no forced convection [103]. The rate at which film coefficient would drop to zero when approaching vacuum was assumed to be linear. Although the linearity of the decrease in film coefficient is not known, for high temperatures, radiative losses would dominate as the primary avenue for heat loss. The accurate measurement of film coefficient for complex scenarios is non-trivial, and due to the dominance of radiative losses, a linear drop to zero was considered sufficient for this work. A linear decrease of convective heat transfer coefficients with decreasing vacuum pressure has also been demonstrated for other applications [104]. View factor modelling was enabled for the heat exchange thermal boundary conditions on the external surfaces of all volumes, apart from the wrapping region.

The defined wrap region for which the lower emissivity was assigned can be seen in blue, in Figure 6.5. As the emissivity for the wrapped regions was set at a value of 0.2 instead of 0.7 for the exposed vermiculite external shell region, the wrapped areas would experience less heat loss. This blue region was within the cut-off region of the tree mould, in which Kaowool wrap can be used in industry to retain heat in this area. To apply a boundary condition of a lower emissivity value compared to the rest of the shell mould for modelling wrap is a simplification which removes the need for wrap layer mesh generation in the required regions. This can be an effective method for modelling wrapping in cases where the wrap makes direct contact with the external shell layer of the mould. However, for more complex wrapping configurations such as bag wrapping, the creation of wrap geometry meshes may be required to effectively model internal radiation between the wrap and shell.

The enclosure volume was assigned as the ambient temperature of 25°C , with an emissivity of 0.7. These values were recommended by ESI Group for this type of modelling problem, where heat loss is mostly due to radiative losses.

6.2.5 Modelling VIM-IC Mould Preheat and Cooling: Simulation Parameters

A thermal only simulation was performed, as no alloy fluid flow was present in this mould preheat and cooling model. The model was run for a total of 135 seconds in simulated time, which accounted for the removal of the mould from the furnace, transfer to vacuum chamber, time taken for the vacuum pump to achieve the required vacuum level, followed

by the time taken for the generator to melt the alloy until pouring point.

6.2.6 Modelling VIM-IC Mould Preheat and Cooling: Results

The simulated temperature distribution across the external surfaces of the crucible and mould assembly after furnace removal, at the predicted time for alloy pouring is displayed in Figure 6.6. It should be noted that the wrapped region temperatures are representative of the mould surface temperature under the wrapping, and do not represent the external surface temperatures of wrapping.

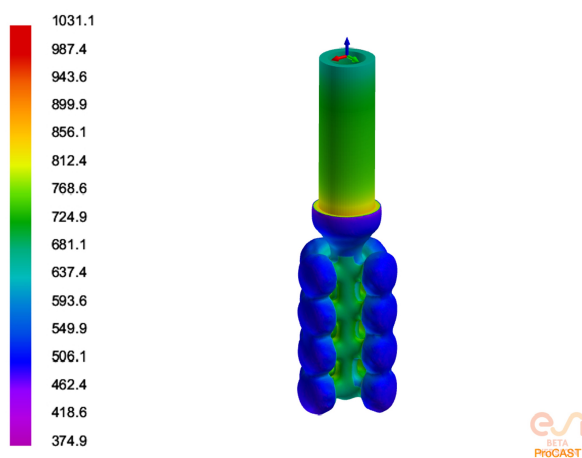


Figure 6.6: Mould assembly temperature distribution at alloy pouring point, after preheating and cooling

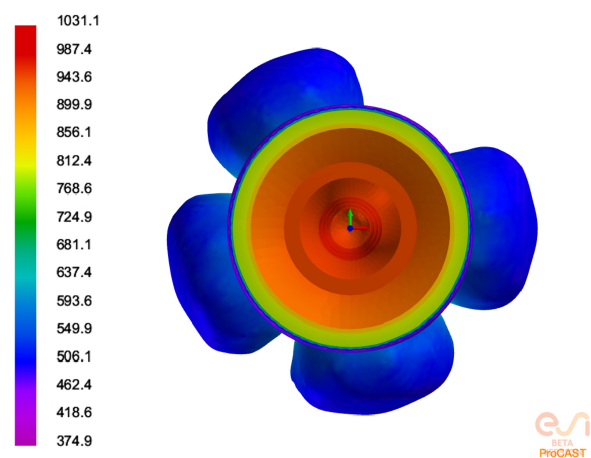


Figure 6.7: Top view of shell mould after preheating and cooling, showing internal mould temperatures with crucible geometry hidden

Figure 6.7 is a top view of the shell mould volumes only, with a view of the internal cavity and temperatures within the mould at alloy pouring point.

6.2.7 Modelling VIM-IC Mould Preheat and Cooling: Discussion

Examining Figures 6.6 and 6.7, the temperatures across the external mould and crucible surfaces are visible alongside the internal mould temperatures. For external mould surface temperatures, the visible outermost volume is the vermiculite shell layer. The green region within the cut-off zone, where the wrapping boundary condition was applied, is hotter than the surrounding dark blue vermiculite shell surface. This is due to the lower emissivity value which was applied to this region, which allowed the mould surface to remain hotter within the wrap regions compared to exposed vermicullite. It should be noted that

these hotter regions denote the temperature of the shell, and are not representative of the wrapping external surface temperatures. The external surface temperatures of the Kaowool wrap material would be cooler than the exposed vermicullite, due to its properties as an insulator. To further strengthen the confidence in these temperature results, calibration experiments using thermocouples should be conducted. These experiments should record the temperature over time of both the exposed shell surface, and the surface under the wrapping material during cooling. A shell cooling temperature measurement experiment, using thermocouples to measure the temperature during cooling until alloy solidification was considered. However, the process of attaching wire thermocouples to the external surface of a mould at 1100 °C, both under wrapping and on an exposed mould surface, would potentially introduce complexities that would impede the accurate measurement of temperatures on those surfaces. To hold a thermocouple in place, in both instances, would require either making holes in the mould surface or attaching the thermocouples with cement, or potentially making holes and using cement. In both instances, the creation of a hole or addition of cement would likely affect the accurate measurement of surface temperatures in an experiment which would seek to obtain this information for the standard casting procedure. Therefore, the decision was made to not conduct a temperature validation experiment for mould preheating and cooling, as the measured temperatures may not be representative of the true temperatures experienced in standard operations, due to the introduction of cement or holes within the shell. For the internal shell surface temperatures, Figure 6.7 shows the hotter internal mould cavity with a view of the zircon, mullite and vermicullite shell layers. Vermicullite also functions as an insulating material, and is applied as the outermost layer of shell mould. It is evident from Figure 6.7 that the insulating vermicullite layer is significantly cooler than the zircon and mullite layers. From this top view of the mould, it is possible to see the temperature differences throughout the shell volumes, with radiative heat transfer from hot to cold moving away from the mould and into the surrounding air enclosure domain.

6.2.8 Modelling VIM-IC Mould Preheat and Cooling:

Conclusion

The purpose of modelling the preheating and cooling of a crucible and mould assembly was to create a model capable of predicting a reasonable temperature distribution throughout the crucible and mould volumes for use as the initial temperature conditions in a mould filling and solidification model. Simplifications were made, in terms of modelling wrapping as an emissivity boundary condition applied to the external surface of the mould. This

6.3. MODELLING VIM-IC: MOULD FILLING, SOLIDIFICATION AND DEFECT PREDICTION

allowed for wrapping mesh generation complexities to be avoided, providing a timely solution obtained in less than an hour when running the ProCAST solver on 16 cores. Crucible and mould temperatures resulting from preheating the assembly in a furnace at a temperature of 1100 °C, and the resultant cooling of the assembled mould until alloy pouring was predicted. The effect of using Kaowool wrap as insulation was modelled using emissivity boundary conditions on the surface of the mould, setting the wrap region emissivity at a lower value of 0.2, compared to 0.7 for the rest of the mould surface. The temperature distribution of the crucible and mould assembly after 135 seconds of cooling is mapped onto the crucible and shell layer volumes, and acts as an initial condition for the mould filling simulations in Section 6.3.

6.3 Modelling VIM-IC: Mould Filling, Solidification and Defect Prediction

6.3.1 Modelling VIM-IC: Mould Filling, Solidification and Defect Prediction Overview

In this section, a mould filling and solidification model which combines data from both the VIM-IC induction heating model, and the mould preheating and cooling model, is developed for the purpose of defect prediction in a multi-tier investment casting tree. The alloy fills the mould by gravity, dropping into the attached mould below the crucible. After solidification, the casting trees are assessed for the predicted prevalence of porosity, mould erosion and misruns. Differences in severity of the predicted defect rates for each of the tested configurations were compared. The tested configurations were a one-piece billet and the DOE L9 array configurations, excluding Runs 6 and 8. Ultimately, the value of creating VIM-IC induction heating models which predict accurate pouring temperatures and flow characteristics, is in the ability to use these alloy temperature profiles to predict the effect on casting defect occurrence.

6.3.2 Modelling VIM-IC: Mould Filling, Solidification and Defect Prediction Governing Equations and Physics

The Niyama criterion Ny was determined by a series of experiments in which steel castings of various diameters were examined. It states that microporosity will form if [105]:

$$Ny = \frac{G}{\sqrt{-\dot{T}}} < 1K^{1/2}min^{1/2}cm^{-1} \quad (6.3)$$

where G is the temperature gradient in K/cm, and \dot{T} is the cooling rate in K/min. However, as noted by Dantzig *et al.* [105], the Niyama criterion was developed for shrinkage porosity in steels specifically, and is often applied to other alloys despite the lack of experiments performed to determine if this criterion is true for any other type of alloy.

By developing a dimensionless form of the Niyama criterion, Ny^* , Carlson *et al.* proved the ability to predict the presence and quantity of shrinkage pore fraction volumes in the solidification of castings [106]. Not only does the dimensionless form consider the effect of casting conditions on the development of shrinkage porosity, but it also accounts for material properties of the alloy, solidification characteristics and critical pressure for the formation of porosity.

6.3.3 Modelling Mould Filling and Solidification: Geometry and Mesh

The geometry of the crucible and mould assembly comprised of the same surface mesh generated for the mould preheating and cooling model, with the addition of a meshed billet piece volume inside the crucible.

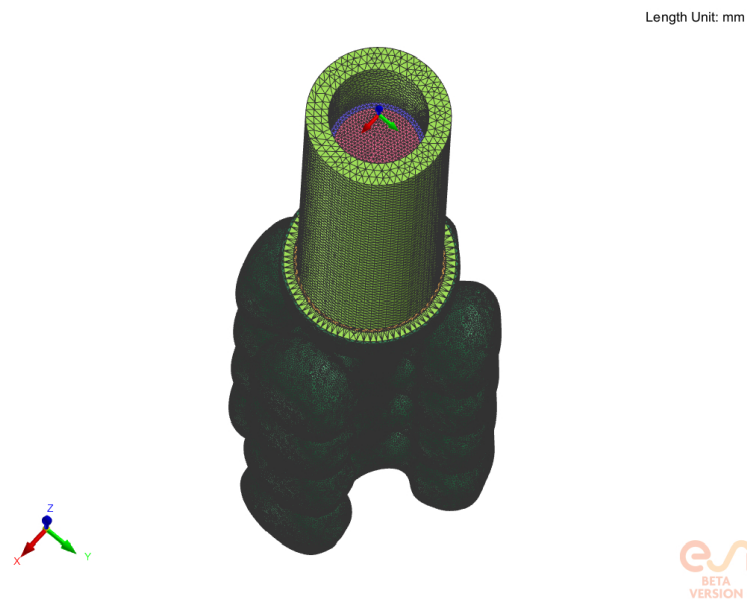


Figure 6.8: Crucible, billet and mould assembly, 3D tetra mesh

6.3. MODELLING VIM-IC: MOULD FILLING, SOLIDIFICATION AND DEFECT PREDICTION

Once the surface mesh was generated for the whole system, the volume meshes for alloy and mould volumes were generated according to the criteria described in Section 6.2.3. A 2D air enclosure, with the same dimensions as described in the same section was created to allow the view factors to be modelled. The meshed geometry is shown in Figure 6.8. The enclosure mesh is not visible in this image, as it obscured the visibility of the billet mesh.

6.3.4 Modelling Mould Filling and Solidification: Materials and Boundary Conditions

The mould cavity volumes, which comprised of the sprue and castings, were assigned as IN713C alloy with an initial fill of 0 %. The billet in the crucible was set to 100 % fill, and also assigned as IN713C. The temperature dependent thermal conductivity values for IN713C were assigned as per the standard values in Figure 2.1, without the artificial increase at liquidus temperature. The crucible was assigned as aluminosilicate ceramic fibre, and the shell mould volumes were assigned as zircon, mullite and vermicullite, with zircon on the surface in contact with the alloy and vermicullite on the outermost surface.

The temperature profile of the billet at the pouring time step for a one-piece billet, and each of the DOE L9 arrays apart from Runs 6 and 8 was imported as the initial mapped thermal condition for the alloy in this mould filling model. For the crucible and mould volumes, the temperature profiles were imported from the mould preheating and cooling model at $t = 135$ s, as a mapped initial condition. An additional run was conducted, testing the alloy at a constant temperature of 1466 °C. This was the average top billet face temperature at pouring point for the three experimental trials of one-piece billets.

The temperature dependent heat transfer coefficient between the alloy and crucible, and alloy and zircon volume, was defined according to the curve in Figure 5.43 with a ‘coincident’ type interface in each instance. The heat transfer coefficient between mould volumes was defined as 300 W/m²K, which were also assigned as ‘coincident’ type interfaces. Wrapping boundary conditions were applied as described in Section 6.2.4.

An emissivity value of 0.85 was applied to the external face of the billet volumes, as this was the value obtained for the emissivity of IN713C in Section 2.4. An emissivity of 0.7 was assigned to the external surfaces of the crucible, zircon, mullite, and exposed vermicullite region of the shell. The defined wrap regions on the surface of the vermicullite mould layer were assigned an emissivity value of 0.2. For all external surfaces apart from the region specified with wrap boundary conditions, the film coefficient effect was applied gradually

6.3. MODELLING VIM-IC: MOULD FILLING, SOLIDIFICATION AND DEFECT PREDICTION

over one second, after five seconds had passed. This was to account for the time taken from alloy pouring to opening the VIM chamber, causing the alloy to return to standard conditions without a vacuum. The application of film coefficient for the VIM-IC mould filling and solidification model can be seen in Figure 6.9. The ambient temperature was set to 25 °C, with an appended air enclosure to allow view factors to be modelled in all regions apart from the wrapped area.

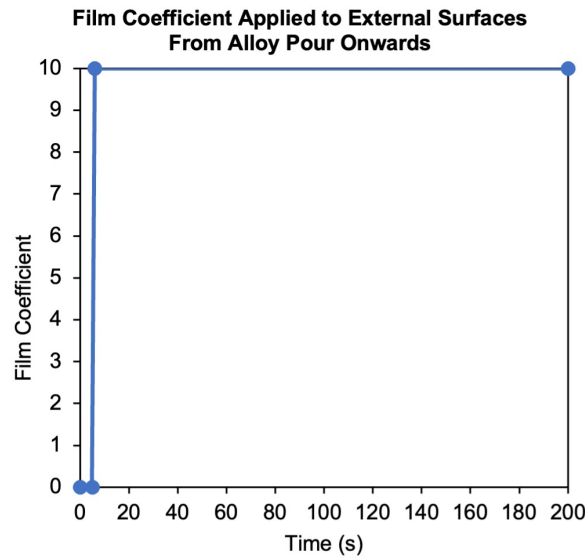


Figure 6.9: Film coefficient transition from vacuum conditions to atmosphere, from alloy pouring point onwards

6.3.5 Modelling Mould Filling and Solidification: Simulation Parameters

The mould filling models were simulated with fluid flow active until the mould filling was complete. After this, the model was set to switch to a thermal only simulation. This minimised the computational expense of accounting for fluid flow after the mould was full. As per the settings used in the VIM-IC pouring simulations, a mobility limit of ‘0.3’ was applied, which allowed for the alloy to start or stop moving at the $fs_{0.3}$ limit. For porosity size and location prediction, the dimensionless Ny^* criterion was set to 0.95, as recommended by ESI Group for this alloy type. The parameter ‘FEEDLEN’ is used to define the critical length above which feeding is insufficient and porosity may develop. In this case, ‘FEEDLEN’ was set to 5 mm.

The same methodology for delivering flow results which account for turbulence at the surface of both the crucible and mould. The ‘WSHEAR’ solver run parameter was

6.3. MODELLING VIM-IC: MOULD FILLING, SOLIDIFICATION AND DEFECT PREDICTION

implemented. By setting ‘WSHEAR’ to a value of 2, a velocity profile is created at the wall that is corresponding to turbulent boundary layers. The parameter ‘WSHEAR’ is used together with ‘WALLF’, to define surface roughness of the mould surface. ‘WALLF’ was set to 0.9.

6.3.6 Modelling Mould Filling and Solidification: Results and Discussion

ESI ProCAST software allows for prediction of casting defects including misrun, inclusions and porosity. Although the occurrence of inclusions cannot be predicted, the regions which are high risk for mould erosion due to fast moving metal during mould filling can be predicted. In order to understand the prevalence and location of defects, both the tiers and individual wheels on the investment casting mould tree design were numbered as shown in Figures 6.10 and 6.11.

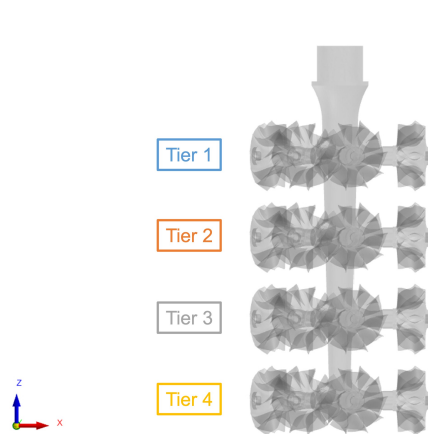


Figure 6.10: Mould design side view with numbered tiers

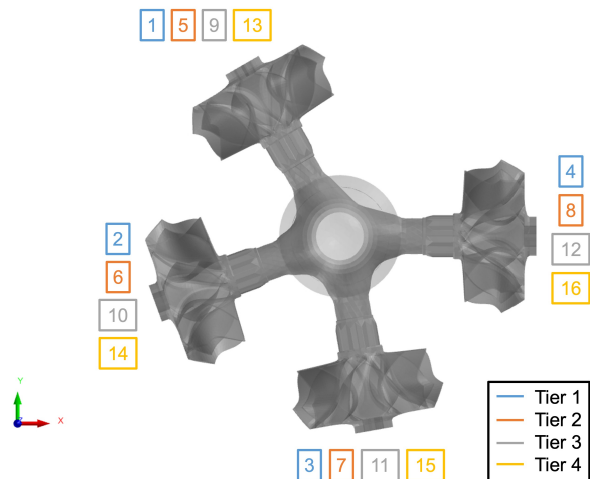


Figure 6.11: Mould design top view with numbered wheels

Tier 1 is the top tier which is closest to the top of the sprue, with Tier 4 labelled as the bottom tier. The numbered tiers are shown in Figure 6.10, which is a side view of the mould design. Wheels are numbered in an anti-clockwise direction from the ‘cut-off zone’ in the mould, as shown in Figure 6.11 which is a top view of the mould design. with the lowest numbered wheel on each tier referring to the wheel to the left of the cut-off zone. ‘Cut-off zone’ refers to region of the mould which has the largest gap between wheels. It is given this name, as it is a necessary gap between wheels which allows a tool to be inserted between wheels to cut them off from the tree. In this design, there are 16 wheels in total, with four tiers and four wheels per tier.

6.3. MODELLING VIM-IC: MOULD FILLING, SOLIDIFICATION AND DEFECT PREDICTION

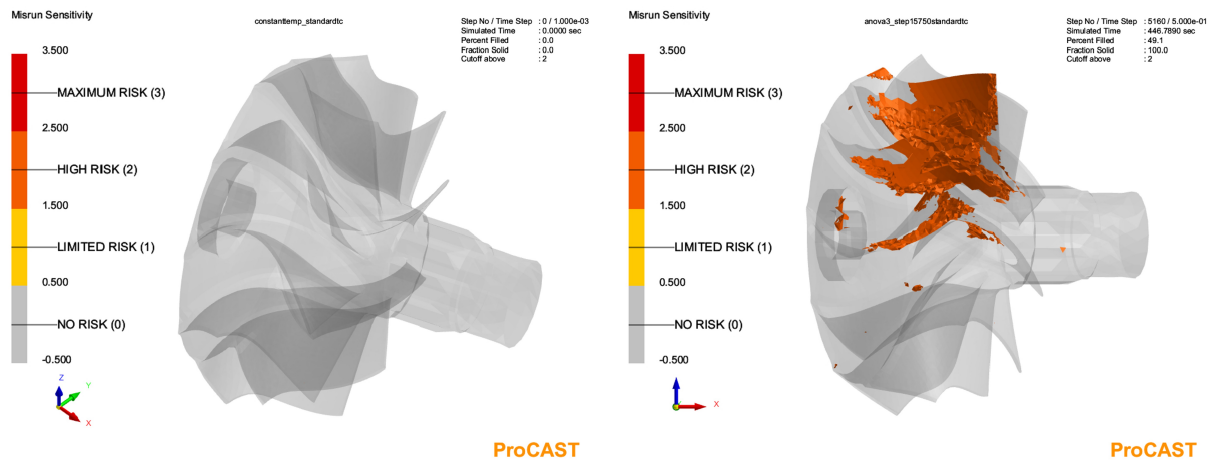


Figure 6.12: Casting with no misrun predicted Figure 6.13: Casting with misrun predicted

According to ASM International, ‘misrun’ is the name given to when casting is incomplete due to premature solidification of the alloy [107]. Papanikolaou *et al.* stated that a high risk of misrun, in which a metal solidifies before filling of the mould cavity is complete, can be caused by a number of factors. These factors are alloy temperatures which are too low, improper fluidity, pouring which is too slow and mould cavities with thin cross sections [108]. In the case of turbocharger turbine wheels, the blades are particularly thin sections of the mould cavity. This makes them potentially prone to misrun, if the alloy temperature is too low or mould filling takes place too slowly, allowing the metal to solidify before filling the cavity completely. To predict misruns in ESI ProCAST Visual-Viewer post-processing software, a ‘critical’ fraction solid value must be defined. This value dictates the fraction solid at which misruns are predicted, if the alloy reaches this fraction solid value before the filling of the cavity is complete. In this case, a fraction solid value of 0.25 was selected. This is due to the mobility limit having been set at a fraction solid value of 0.3. Setting the critical fraction solid misrun value to 0.25 allows misruns to be predicted within 5 % range of the fraction solid value at which the alloy is immobilised. Figure 6.12 shows a casting without any misrun defect predicted. Figure 6.13 shows a casting cavity which has misrun predicted, primarily within the blade regions. For misrun analysis, the casting volumes were examined with a cut-off type of results plot. This type of plot allows only defects with a risk factor above the cut-off value to be shown. In this case, the cut-off risk value was set to ‘2’, meaning that only high risk areas are shown.

Figure 6.14 shows which of the numbered casting wheels were predicted to be high risk for misrun occurrence, for the given models that were run. These models had temperature distributions imported as the initial condition for the billet volume. The runs tested were

6.3. MODELLING VIM-IC: MOULD FILLING, SOLIDIFICATION AND DEFECT PREDICTION

a constant temperature of 1466 °C, the one-piece billet, and each of the DOE L9 array runs apart from Runs 6 and 8.

Run	Wheel No.																Total Misruns	Percentage of Total Castings with Misrun
	Tier 1				Tier 2				Tier 3				Tier 4					
	1	2	3	4	5	6	7	8	9	10	11	12	13	14	15	16		
Constant: 1466°C																	0	0
One-piece billet			1	1	1			1	1				1	1			7	43.75
1			1				1						1				3	18.75
2								1	1				1	1			4	25
3	1		1	1				1	1				1				6	37.5
4		1				1								1			4	25
5	1		1					1	1				1				5	31.25
7				1					1	1			1		1	1	7	43.75
9	1				1				1				1			1	6	37.5

Figure 6.14: Defect mapping: misrun

From this, it is evident that applying a constant temperature of 1466 °C throughout the billet volume as the initial condition does not allow for any instances of misrun to be predicted. Multi-tier investment casting tree moulds manufactured using the VIM-IC technique are known to be high risk for misrun defects, due to the variation in temperature throughout the length of the billet during VIM. In a multi-tier design, if multiple tiers are filling simultaneously, this can increase the total time taken to fill each tier completely. The filling of multiple tiers simultaneously could result in potentially random misrun locations by wheel position and tier. This can be attributed to misrun being a flow dependent defect, as it occurs when the alloy stops short of the extremities of the mould cavity geometry. Misrun occurring throughout the tiers could be caused by two different mechanisms. During pouring, there is simultaneous filling of all tiers, with more alloy being poured into the lower tiers. Therefore the lower tiers fill more quickly, primarily with cool alloy that is the first to pour from the molten billet. A comparatively smaller amount of this cool alloy still enters the upper tiers during this initial pouring. As filling continues, the bottom tiers fill completely first, and hotter alloy starts to pour, primarily filling the upper tiers as the lower tiers are already filled. The small volumes of initially cooler alloy filling the top tiers is prone to solidification mid pouring, which can block extremities of the mould geometry from filling entirely, resulting in misrun; small volumes of alloy can solidify more quickly than larger volumes. The bottom tiers initially fill with

6.3. MODELLING VIM-IC: MOULD FILLING, SOLIDIFICATION AND DEFECT PREDICTION

a greater volume of the initial cooler alloy. As the alloy that fills the bottom tiers is overall cooler than the alloy filling the higher tiers, the bottom tiers are likely to solidify quickly, potentially resulting in misrun in the bottom tiers too. Therefore, as there is cool alloy pouring into all of the tiers, this may explain why misrun is observed throughout all tiers and positions, with no obvious trend.

As slow pouring times is a known cause of misruns in castings, a number of misruns are to be expected. A pouring temperature of 1466 °C is the averaged value taken from the top billet face temperature measurement at the point of pouring in experiments. This outcome of no defects predicted for a constant alloy temperature of 1466 °C shows that in this case, measured billet temperatures from the top billet face during VIM-IC are not sufficient to predict misrun occurrence in castings. Conducting temperature measurement trials for alloy leaving the crucible outlet during pouring is necessary, for IN713C 3 kg billets and moulds preheated under the given conditions, to predict misrun occurrence.

For a one-piece billet, a total of seven castings were identified as high risk for misrun. This does not necessarily mean that this exact number of castings will experience misruns in this shell mould design. The misrun tool in ESI ProCAST software acts a risk indicator, and the unpredictable nature of induction melting in VIM-IC can result in varying levels of defect occurrence in reality. However, as the misrun prediction criteria is kept the same for all of the tested runs, it can be taken as an indicator of misrun prevalence relative to the other runs.

The casting tree in which the least number of misrun defects was predicted is that of 'Run 1'. This corresponds to the run in which a 15 mm 'penny' was tested, with no holes present in any of the positions. For misrun prevention, this result suggests that the introduction of a penny can decrease misrun occurrence by more than half compared to those from one-piece billets. For misruns, none of the runs tested resulted in a higher prevalence in castings than those of a one-piece billet.

Mould erosion occurs when refractory particles delaminate from the internal surface of the mould cavity. In investment casting shell moulds, mould erosion is most likely to occur in instances of alloy turbulence and high velocity flow. Velocities of metal during mould filling can be determined to predict the occurrence of inclusions due to mould erosion. Mould erosion prediction in ESI ProCAST Visual-Viewer post-processing software works on the basis that there is a critical alloy velocity in mould filling which would cause particles to delaminate from the internal mould surface. In this case, a critical velocity of 2.5 m/s was set. This was taken as an arbitrary velocity value, as the true critical velocity

6.3. MODELLING VIM-IC: MOULD FILLING, SOLIDIFICATION AND DEFECT PREDICTION

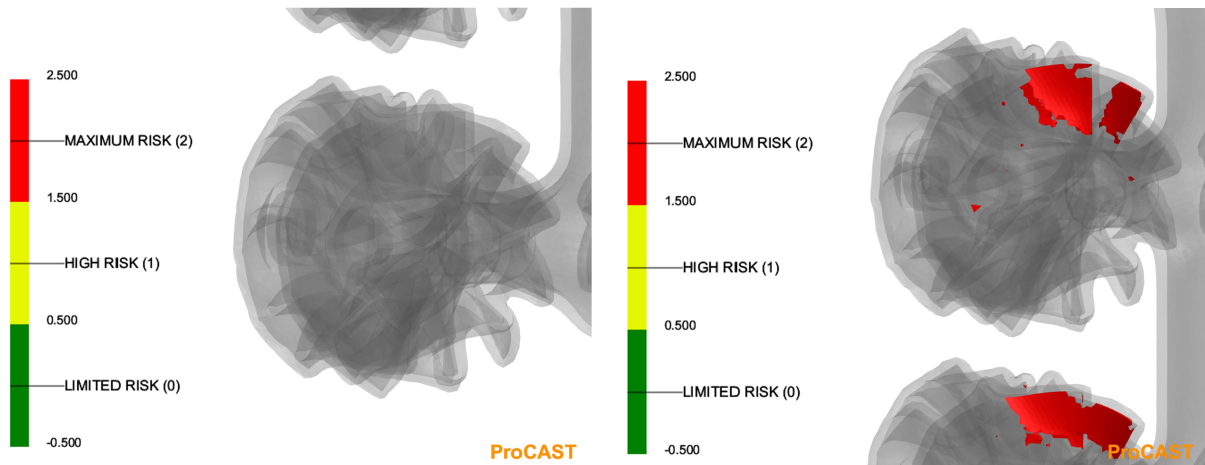


Figure 6.15: Shell region with no mould erosion predicted *Figure 6.16: Shell region with mould erosion predicted*

causing mould erosion can vary dependent on a number of factors. Although 2.5 m/s was an arbitrary value, it was selected as a result of empirical backfitting. This critical velocity value was validated by numerous industrial trials comparing the predicted rates of mould erosion from simulations with the rates observed in casting trials. Unfortunately, these studies could not be included in the body of this work due to commercial sensitivity.

Shelling room conditions, such as humidity, at the time of creating the investment casting shell mould can impact upon the ease of refractory particle delamination. This is due to the impact of environmental conditions, such as humidity, on the fidelity of the dried shell slurry. Quality of the supplied refractory material can also affect prevalence of mould erosion, alongside other factors such as shell drying time and the implementation of forced drying. For prediction of mould erosion, a cut-off plot was generated in which only regions of above risk value '2' were shown. This was considered to be a region of maximum risk on the scale. Figure 6.15 shows a region of shell mould for which no erosion was predicted, while Figure 6.16 shows a region of shell in which mould erosion was considered as high risk. It should be noted that the highlighted regions are the areas from which the refractory particles are likely to delaminate from, and do not indicate the regions in which these particles could potentially end up as inclusions in the finished castings. The defect mapping for the given mould erosion can be seen in Figure 6.17.

It is also important to note that any castings involving gravity filling are prone to the generation of high mould filling velocities during filling. This is due to the acceleration of the alloy due to gravity as it moves down the sprue. A value of 2.5 m/s for critical velocity was selected, as this allowed for variations in the prevalence of mould erosion

6.3. MODELLING VIM-IC: MOULD FILLING, SOLIDIFICATION AND DEFECT PREDICTION

Run	Wheel No.																Total Mould Erosion	Percentage of Total Castings with Mould Erosion
	Tier 1				Tier 2				Tier 3				Tier 4					
	1	2	3	4	5	6	7	8	9	10	11	12	13	14	15	16		
Constant: 1466°C	1	1	1	1	1	1	1		1	1		1		1	1		12	75
One-piece billet	1	1	1	1	1	1	1	1	1		1	1		1			12	75
1	1		1	1			1	1	1			1	1				8	50
2		1	1	1	1	1	1	1	1			1	1			1	11	68.75
3	1	1	1	1		1	1	1	1		1	1		1			11	68.75
4	1	1	1	1	1	1	1		1	1	1	1	1	1		1	14	87.5
5	1	1	1	1	1	1	1	1		1	1	1	1	1	1	1	15	93.75
7	1	1		1			1	1				1			1	1	8	50
9	1	1		1	1	1	1	1			1			1		1	10	62.5

Figure 6.17: Defect mapping: mould erosion

across the total number of castings for each run. Again, the number of casting regions for which mould erosion was deemed to be high risk is only a relative risk indicator, and does not necessarily equal the total number of castings which would experience mould erosion in reality. The design of the investment casting tree mould and wheel used are not designs which are used in reality, and were created for demonstration purposes only. Furthermore, a casting mould design which produced such a high number of instances of inclusions as seen Figure 6.17 would not be viable to manufacture in reality.

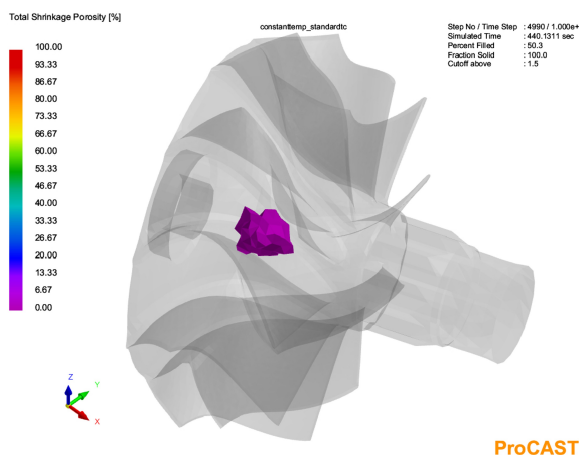


Figure 6.18: Casting with only internal shrinkage porosity predicted

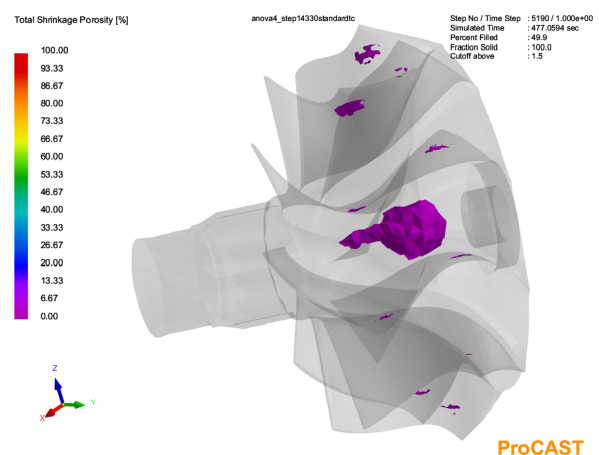


Figure 6.19: Casting with surface level porosity predicted on blades

Porosity occurs when the supply of molten alloy is insufficient to feed the casting geometry

6.3. MODELLING VIM-IC: MOULD FILLING, SOLIDIFICATION AND DEFECT PREDICTION

upon shrinkage, which takes place during solidification. Figure 6.18 shows a wheel casting with internal porosity the centre. Figure 6.19 shows a wheel casting with both internal porosity and porosity predicted on the blades. For turbocharger turbine wheels, the castings are not subject to X-rays and therefore internal porosity would not be detected. The type of porosity that would be flagged upon visual inspection is a surface level of porosity, such as those seen on the blades in Figure 6.19.

Run	Wheel No.																Total Surface Porosity	Percentage of Total Castings with Surface Porosity	
	Tier 1				Tier 2				Tier 3				Tier 4						
	1	2	3	4	5	6	7	8	9	10	11	12	13	14	15	16			
Constant: 1466°C																	0	0	
One-piece billet					1								1	1	1	1	1	6	37.5
1								1					1	1	1	1	1	6	37.5
2								1	1				1	1	1	1	1	7	43.75
3	1						1					1	1	1	1		1	7	43.75
4														1			1	2	12.5
5		1					1	1	1		1	1	1	1	1	1	1	10	62.5
7									1				1	1	1	1	1	6	37.5
9					1			1	1		1	1	1	1	1	1	1	9	56.25

Figure 6.20: Defect mapping: surface level porosity

Run	Wheel No.																Total Internal Porosity	Percentage of Total Castings with Internal Porosity	
	Tier 1				Tier 2				Tier 3				Tier 4						
	1	2	3	4	5	6	7	8	9	10	11	12	13	14	15	16			
Constant: 1466°C														1		1	1	3	18.75
One-piece billet						1			1	1	1	1	1	1	1	1	1	9	56.25
1						1		1	1	1	1	1	1	1	1	1	1	10	62.5
2					1	1			1	1	1	1	1	1	1	1	1	10	62.5
3					1		1	1	1	1	1	1	1	1	1	1	1	11	68.75
4					1				1	1	1	1	1	1	1	1	1	9	56.25
5									1	1	1	1	1	1	1	1	1	8	50
7					1		1	1	1	1	1	1	1	1	1	1	1	11	68.75
9									1	1	1	1	1	1	1	1	1	8	50

Figure 6.21: Defect mapping: internal porosity

Figure 6.20 shows a defect map of the wheels with a surface level of porosity from the

6.3. MODELLING VIM-IC: MOULD FILLING, SOLIDIFICATION AND DEFECT PREDICTION

mould filling runs. In ESI ProCAST Visual-Cast post-processing software, porosity is represented as a percentage. This value relates to the percentage of the region volume which is considered to be void. For example, a region of 100 % porosity would represent a total void volume. A region in which no porosity is detected, at 0 %, represents a region which is fully solid with no voids contained within the volume. Surface level porosity was examined using a cut-off results plot, which showed only porosity values of 1.5 % and above. Internal porosity was recorded for values of 50 % and above. Internal porosity prevalence has also been noted and mapped in Figure 6.21, as internal porosity may be considered detrimental in parts such as critical aerospace components.

As a greater volume of the cool alloy that pours from the bottom of the crucible fills the bottom tiers, the wheels in the bottom tiers are more likely to solidify quickly before sufficient feeding of the castings can take place. It is suspected that this may be what causes porosity to be more prevalent in the lower tiers. As filling continues, the higher tiers tend to fill with more of the hotter alloy, so are less prone to solidifying as quickly once filled. The cooler alloy leaving the crucible at the end of the pour ends up in the top of the sprue rather than in the wheels, as the wheels in the top tier are filled at this point.

By applying a constant billet temperature of 1466 °C, surface level porosity is not predicted in any of the castings. The lowest prevalence of surface level porosity, apart from this constant billet temperature run, is that of Run 4. However, Run 4 which consisted of no manufactured holes and a disc height of 35 mm for the bottom billet piece, was subject to crucible breakage during VIM-IC. This breakage was due to the rattling of the bottom billet piece during VIM. This could not be predicted from the VIM-IC models, and highlights the importance of running small scale physical trials alongside simulations before committing to changes in working instructions on a large scale. The runs which used imported billet temperature distributions from the EMAG models with the lowest prevalence of surface porosity were the one-piece billet, and Runs 1 and 7. This defect map of surface level porosity also draws attention to the importance of understanding alloy temperature throughout the billet, as no surface level porosity was predicted for the constant temperature condition.

As previously mentioned, internal porosity would not be detected by standard visual inspection of turbocharger turbine wheels. However, it is used in this case as a criteria for comparison between different runs. It is clear that much fewer instances of internal porosity are detected for wheels produced with a constant billet temperature, when using

6.3. MODELLING VIM-IC: MOULD FILLING, SOLIDIFICATION AND DEFECT PREDICTION

the 50% cut-off results plot as the criteria for internal porosity.

It is evident from these defect mapping figures that for the same mould design, prediction of defect prevalence varies depending upon the temperature profile of the billet used as the initial condition for a mould filling and solidification model. In turn, the pour time and flow characteristics such as flow width, angle and fluid velocity would also vary dependent upon the initial condition applied for the billet. Therefore, it is unlikely that the top billet face temperatures obtained from the pouring point in casting trials would be sufficient to accurately predict the severity and location of defects in a solidified casting tree. Modelling the billet temperature distribution in induction heating using the EMAG module is a useful tool for prediction of casting defect severity and location. However, it is also important to conduct a number of casting trials in which pouring temperatures are recorded for comparison.

As mentioned in Section 4.6, the alloy temperatures in induction heating and pouring could differ in a real life casting scenario. This difference could occur as in the VIM-IC process, the crucible and mould assembly is preheated prior to loading the crucible with alloy and performing VIM-IC. This could cause a lower rate of heat loss of the billet during induction melting. However, the effect of crucible and mould preheating in the mould filling stage was accounted for by running a mould preheat model.

It is also important to note that alloy pouring temperatures and flow characteristics are not the only factors which affect defect occurrence in castings. Mould design also has an impact on the prevalence of defects. The best approach is to ensure that the alloy pouring characteristics are favourable, while optimising mould design according to mitigate fluctuations in temperature and pouring characteristics which are not favourable in VIM-IC manufacturing. However, mould design optimisation is not part of the scope of this work. As previously mentioned, the investment casting tree and wheel design studied in this case were created for demonstration purposes only. Therefore, they have not been optimised for defect prevention.

6.3.7 Modelling Mould Filling and Solidification: Conclusion

Modelling mould filling with a uniform, constant alloy temperature throughout the billet taken from the top billet face temperature at pouring from experiments does not predict all possible casting defects. Run 1 could be considered the best overall option in mitigating defects. Run 1 produced the lowest risk levels of misrun and mould erosion within finished castings. Although Run 4 performed better with regards to surface level porosity, it fared

6.4. MODELLING VIM-IC MOULD FILLING AND SOLIDIFICATION: CONCLUSION

worse in mould erosion and misrun risk levels. It was also known to cause issues with crucible cracking from experiments. Therefore, Run 4 is not considered a viable option. Overall, these results suggest that the use of a 15 mm penny could contribute towards defect reduction in 3 kg multi-tier investment casting moulds using the VIM-IC process.

6.4 Modelling VIM-IC Mould Filling and Solidification: Conclusion

An effective mould preheating model was developed, with simplified boundary conditions applied to the mould surface to mimic the effects of wrapping insulation. The temperature distribution of volumes from the preheat model was imported as an initial condition for the mould filling simulations. The mould filling models also involved importing the initial temperature condition for the billet from the VIM-IC electromagnetics models. It was evident from conducting defect mapping that differences are observed in the defect prediction criteria for misrun, inclusions by mould erosion, and porosity between the different run configurations [OB6]. Defect mapping suggests that Run 1, which is effectively the use of a solid ‘penny’, reduces defect prevalence even compared to a one-piece billet with no piping [OB4]. Differences in defect prevalence between the runs are observed in defect mapping across all defect criteria types. However, defect prediction should not be considered as a guarantee of exact numbers, and defect risk for each run should be considered relative to the levels predicted for the other runs in the array.

Chapter 7

Conclusion and Further Work

Using a Design of Experiments approach, an L9 array of two-piece billets was devised to investigate the impact of piping presence, size, and location in flow characteristics and defect occurrence. Experiments and models corresponding to this L9 array were designed and conducted. Pouring velocities were obtained by implementing PIV technique via a MATLAB program. ANOVA analysis of the flow characteristics observed from high speed imaging allowed for trends to be understood, quantifying the effect of varying parameter levels [OB2, OB3].

Accurate temperature measurements were possible due to extensive calibration experiments. The appropriate input values for measuring IN713C were determined for non-contact temperature measurement equipment. Trends could not be observed in the variance of top billet face temperatures from the L9 array experiments. However, the pouring temperatures of IN713C billets were obtained in a similar set of experiments which tested the effect of varying process parameters such as power and billet mass [OB2]. This provided a reasonable guideline for the temperature ranges that could be expected for billet temperature gradients and alloy pouring temperatures in simulations. Computed billet temperature gradients and pouring temperatures were in reasonable agreement with the ranges observed in the additional experiments [OB1, OB2]. This was also achieved for a small scale induction model, based upon top billet face temperature comparisons [OB1]. Where necessary, thermophysical properties were measured of IN713C for application in computational models [OB1].

Differences were observed in pouring flow characteristics, which were also reflected in the trends observed in VIM-IC and pouring models [OB1, OB2, OB3]. This was

largely due to the ability to model piping and thermal contact resistance for thermal only VIM-IC models, using the application of different heat transfer coefficient values for the different interface surfaces [OB5]. Billet temperature distribution data from VIM-IC electromagnetics models was crucial for the accurate prediction of defects. Interrogation of defect criteria in post-processing showed differences in defect occurrence and mapping for the different runs [OB6]. Through modelling solidification and the resultant defects, the use of a 15 mm disc, or ‘penny’ results in an overall reduction in defect rates [OB4]. This appears to be caused by the reduction in maximum pouring temperature observed for this particular alloy configuration, which is Run 1.

Although model validation of predicted porosity location has been achieved for real parts, including subsequent riser design adjustments to eliminate the porosity, this could not be included in this work for commercial sensitivity reasons. Further work should aim to experimentally validate the differences in defect prevalence observed in Chapter 6. This could be achieved by running physical casting trials of mould filling and solidification for this demonstrative component and riser design. The trials should seek to validate and define the cut-off value for results criterion at which misrun, mould erosion and porosity is present in castings in reality. These criterion are critical fraction solid, critical velocity and total shrinkage porosity percentage respectively. The trials should also perform defect mapping to determine the locations of defects, which can be compared to the distributions obtained in the models. Priority in these trials should be given to investigating the impact on casting defect prevalence when using a 15 mm disc, the ‘penny’, compared to a standard one-piece billet.

As mould design optimisation was not covered in the scope of this project, further work could also seek to optimise mould designs based on this new knowledge of temperature distributions and flow characteristics observed in pouring. Future mould optimisation projects should focus on balancing the reduction of defects and minimisation of alloy wastage, to achieve the most cost effective result.

References

- [1] Rudnev V, Loveless D, Cook R. *Handbook of Induction Heating*. Second Edition. CRC Press; 2017. doi:10.1201/9781315117485-3
- [2] Zinn S. *Elements of Induction Heating: Design, Control, and Applications*. ASM International; 1988.
- [3] Reis M. *Fundamentals of Magnetism*. Oxford: Academic Press; 2013.
- [4] Fisk M. Validation of induction heating model for Inconel 718 component, *International Journal for Computational Methods in Engineering Science and Mechanics*. 2011;12: 161-167.
- [5] Sharon M, Oza G, Gupta A, Pandey S. Super-Paramagnetic Iron Oxide Nanoparticles (Spions) As Nano-Flotillas For Hyperthermia: A Paradigm For Cancer Theranostics. In: Thomas S, Kalarikkal N, Stephan A, Raneesh B. (eds.) *Advanced Nanomaterials: Synthesis, Properties and Applications*. New York: Apple Academic Press; 2014. p.307-328.
- [6] Osborn H, Brace P, Johnson W, Cable J, Eagan T. *Induction Heating*. Cleveland: American Society for Metals; 1946.
- [7] Rosenberg S J. *Nickel and Its Alloys*. Washington: National Bureau of Standards; 1968.
- [8] Campbell J. Entrainment, In: Gifford C (ed.) *Complete Casting Handbook: Metal Casting Processes, Metallurgy, Techniques and Design*. Second Edition. Oxford, United Kingdom: Elsevier Ltd; 2015. p.40-41.
- [9] Resendiz-Flores E O, Kuhnert J, Saucedo-Zendejo F R. Application of a generalized finite difference method to mould filling process. *European Journal of Applied Mathematics*. 2018;29(3): 450-469.

REFERENCES

- [10] Horr A M, Kronsteiner J. On Numerical Simulation of Casting in New Foundries: Dynamic Process Simulations. *Metals*. 2020;10(7): 886. doi:10.3390/met10070886
- [11] Malik I, Sani A A, Medi A. Study on using Casting Simulatoin Software for Design and Analysis of Riser Shapes in a Solidifying Casting Component. In: *Journal of Physics: Conference Series*. Bristol, England. IOP Publishing; 2020;1500: 012036. doi:10.1088/1742-6596/1500/1/012036
- [12] Zeneli M, Nikolopoulos N. Numerical methods for solid-liquid phase-change problems. In: Datas A (ed.) *Ultra-High Temperature Thermal Energy Storage, Transfer and Conversion*. Energy. Duxford, England: Woodhead Publishing, an imprint of Elsevier; 2020. p.165-199.
- [13] Vigmond E, Plank G. Mathematical Techniques in Biomedical Engineering: Cardiac Modeling. In: Narayan R, Krishnan S, Vadgama P (eds.) *Encyclopedia of Biomedical Engineering, Volume 3*. Amsterdam, Netherlands: Elsevier; 2019. p1-20.
- [14] Cao J, Zhou G, Wang C, Dong X. A hybrid adaptive finite difference method powered by a posteriori error estimation technique. *Journal of Computational and Applied Mathematics*. 2014;259: 117-128.
- [15] Si H-M, Cho C, Kwahk S-Y. A hybrid method for casting process simulation by combining FDM and FEM with an efficient data conversion algorithm. *Journal of Materials Processing Technology*. 2002;133(3): 311-321.
- [16] Rapp B E. Finite Volume Method. In: *Microfluidics: Modeling, Mechanics and Mathematics*. Micro and Nano Technologies. Oxford: William Andrew, an imprint of Elsevier; 2017.
- [17] Kolditz O. Finite Volume Method. In: *Computational Methods in Environmental Fluid Mechanics*. Berlin, Germany: Springer; 2002. p.173-190.
- [18] Ramirez W F. Solution of Partial Differential Equations. In: *Computational Methods in Process Simulation*. 2nd ed. Oxford, England: Butterworth-Heinemann; 1997. p.353-430.
- [19] Zienkiewicz O C, Taylor R L, Nithiarasu P. Introduction to the Equations of Fluid Dynamics and the Finite Element Approximation. In: *The Finite Element Method for Fluid Dynamics*. 7th ed. Oxford, England: Butterworth-Heinemann; 2014. p.1-28.
- [20] Calcom ESI SA. *ESI ProCAST*. Lausanne, Switzerland: ESI Group; 1990.

REFERENCES

- [21] Dughiero F, Forzan M, Pozza C, Sieni E. A Translational Coupled Electromagnetic and Thermal Innovative Model for Induction Welding of Tubes. *IEEE Transactions on Magnetics*. 2012;48(2): 483-486.
- [22] Fluent Inc. *FLUENT 6.3 - Magnetohydrodynamics (MHD) Module Manual*. Lebanon: Fluent Inc; 2006.
- [23] Wang S, Zhang L, Tian Y, Yanlong L, Ling H. Separation of Non-metallic Inclusions from Molten Steel Using High Frequency Electromagnetic Fields. *Metallurgical and Materials Transactions B*. 2014;45B(5): 1915-1935. doi:10.1007/s11663-014-0107-y
- [24] Yang Y H, Chen R R, Guo J J, Ding H S, Su Y Q. Numerical analysis for electromagnetic field influence on heat transfer. *International Journal of Heat and Mass Transfer*. 2018;122: 1128-1137.
- [25] Buliński P, Smolka J, Golak S, Pryzlucki R, Palacz M, Siwiec G et al. Numerical and experimental investigation of heat transfer process in electromagnetically driven flow within a vacuum induction furnace. *Applied Thermal Engineering*. 2017; 124: 1003-1013.
- [26] Spitans S, Baake E, Nacke B, Jakovics A. A numerical model for coupled free surface and liquid metal flow calculation in electromagnetic field. *International Journal of Applied Electromagnetics and Mechanics*. 2014; 44(2): 171-182.
- [27] Musaeva D, Ilin V, Baake E, Geza V. Numerical Simulation of the Melt Flow in an Induction Crucible Furnace Driven By a Lorentz Force Pulsed at Low Frequency. *Magnetohydrodynamics*. 2015;51(4): 771-783.
- [28] Pericleous K, Bojarevics V, Djambazov G. Magnetohydrodynamics Processing and Modeling. In: Eskin D G, Mi J (eds.) *Solidification Processing of Metallic Alloys Under External Fields*. Springer Series in Materials Science, 273. Cham, Switzerland: Springer Nature Switzerland AG; 2018. p.75-118.
- [29] Pericleous K, Bojarevics V, Harding R A, Wickins M. Experimental and Numerical Study of the Cold Crucible Melting Process. *Applied Mathematical Modelling*. 2006;30(11): 1262-1280.
- [30] Bojarevics V, Pericleous K. Cold Crucible Melting With Bottom Pouring Nozzle. To be published in *COMPEL International Journal of Computations and Mathematics in Electrical and Electronic Engineering*. [Preprint] 2019. doi:10.1108/COMPEL-05-2019-0208 [Accessed 29th December 2022].

REFERENCES

- [31] Buliński P, Smolka J, Golak S, Przlucki R. Coupled numerical model of metal melting in an induction furnace: sensitivity analysis and validation of model. *Przegląd Elektrotechniczny*. 2016;1(3): 51-54. doi:10.15199/48.2016.03.11.
- [32] Kermanpur A, Jafari M, Vaghayenegar M. Electromagnetic-thermal coupled simulation of levitation melting of metals. *Journal of Materials Processing Technology*. 2011;211(2): 222-229.
- [33] Kumar P, Huang Y, Toyserkani E, Khamesee M B. Development of a Magnetic Levitation System for Additive Manufacturing: Simulation Analyses. *IEEE Transactions on Magnetics*. 2020; 56(8): 8000407, doi: 10.1109/TMAG.2020.2997759
- [34] Bruyere V. *Tips and Tricks for Modeling Induction Furnaces*. Available from: <https://www.comsol.com/blogs/tips-and-tricks-for-modeling-induction-furnaces/> [Accessed 16th June 2017]
- [35] Kennedy M W, Akhtar S, Bakken J A, Aune R E. Analytical and Experimental Verification of Electromagnetic Simulations Using COMSOL, re Inductance, Induction Heating and Magnetic Fields. In: *Proceedings of the 2011 COMSOL Conference in Stuttgart, 26-28 October 2011*.
- [36] Hadad Y, Kochavi E, Levy A. Inductive heating with a stepped diameter crucible. *Applied Thermal Engineering*. 2016;102: 149-257.
- [37] Prasad A K, Kapil S, Bag S. Critical conditions for melting of metallic wire in induction heating system through numerical simulation and experiments. *Journal of Manufacturing Processes*. 2022;77: 678-693.
- [38] Umbrashko A, Baake E, Nacke B, Jakovics A. LES-Modelling and Experimental Investigation of the Melt Flow in Induction Furnaces. *Proceedings of International Scientific Colloquium on Modelling For Electromagnetic Processing, 24-26 March 2003, Hanover, Germany*. 2003. p.111-116.
- [39] Nardo G. Modelization of the Melt Flow and the Meniscus Shape in an Induction Furnace and Test of the Velocity Profile with the UDV Probe. Padova: Università degli Studi di Padova; 2015.
- [40] Sirrell B, Holliday M, Campbell J. Benchmark Testing the Flow and Solidification Modeling of Al Castings. *JOM: The Journal of the Minerals, Metals & Materials Society (TMS)*. 1996;48(3): 20-23.

REFERENCES

- [41] Hsu F-Y, Jolly M R, Campbell J. Vortex-gate design for gravity casting. *International Journal of Cast Metals Research*. 2013;19(1): 38-44. doi:10.1179/136404606225023318.
- [42] Zhao H, Ohnaka I, Zhu J. Modeling of mould filling of Al gravity casting and validation with X-ray in-situ observation. *Applied Mathematical Modelling*. 2008;32(2): 185-194.
- [43] Takahashi I, Anzai K, Niyama E. Simulation tools for practical die casting processes. *International Journal of Cast Metals Research*. 2002;15(4): 405-410.
- [44] Bounds S, Moran G, Pericleous K, Cross M, Croft T N. A computational model for defect prediction in shape castings based on the interaction of free surface flow, heat transfer, and solidification phenomena. *Metallurgical and Materials Transactions B*. 2000; 31B: 515-527.
- [45] Kumruoglu LC, Ozer A. Investigation of critical liquid fraction factor in nodular iron castings by computer simulation. *Journal of Materials Processing Technology*. 2008;197(1-3): 182-188.
- [46] Hajkowski J, Roquet P, Khamashta M, Codina E, Ignaszak Z. Validation Tests of Prediction Modules of Shrinkage Defects in Cast Iron Sample. *Archives of Foundry Engineering*. 2016;17(1): 57-66.
- [47] Mu K, Nikawa M, Yamashita M. Experimental Examination of Method for Estimating Solid Fraction at Flow Cessation from Flow Velocity of Molten Al–Si–Mg Alloy. In: *24th International Conference on Mechatronics Technology, Singapore*. New York, USA: IEEE; 2021. p.1-4. doi: 10.1109/ICMT53429.2021.9687259.
- [48] Barot R P, Ayar V S. Casting simulation and defect identification of geometry varied plates with experimental validation. *Materials Today: Proceedings*. 2020;26(2): 2754-2762.
- [49] Wang D, He B, Liu S, Liu C, Fei L. Dimensional shrinkage prediction based on displacement field in investment casting. *The International Journal of Advanced Manufacturing Technology*. 2016;85(1): 201-208. Available from: doi: 10.1007/s00170-015-7836-1 [Accessed 9th February 2017].
- [50] Gunasegaram D R, Farnsworth D J, Nguyen T T. Identification of critical factors affecting shrinkage porosity in permanent mold casting using numerical simulations

REFERENCES

- based on design of experiments. *Materials Processing Technology*. 2009;209(3): 1209-1219.
- [51] Hsu Q-C, Do A T. Minimum Porosity Formation in Pressure Die Casting by Taguchi Method. *Mathematical Problems in Engineering*. 2013;2013: 920865. doi: 10.1155/2013/920865.
- [52] Dabade U A, Bhedasgaonkar R C. Casting Defect Analysis using Design of Experiments (DoE) and Computer Aided Casting Simulation Technique. *Procedia CIRP*. 2013;7: 616-621.
- [53] Lei C, Yang Yi, Yang G, Huang Y. Magma software simulation assisted optimization of the casting system of turbocharger castings. *Procedia Manufacturing*. 2019; 37: 59-65.
- [54] Zhang L, Belblidia F, Davies H M, Lavery N P, Brown S G R, Davies D. Optimizing gate location to reduce metal wastage: Co–Cr–W alloy filling simulation. *Journal of Materials Processing Technology*. 2016;240: 249-254.
- [55] Jolly M. Prof. John Campbell's Ten Rules for Making Reliable Castings. *JOM: The Journal of the Minerals, Metals & Materials Society (TMS)*. 2005;57(5): 19-28.
- [56] CompuTherm LLC. *CompuTherm for Ni alloys*. Middleton, WI: CompuTherm LLC; 1996.
- [57] Guo J, Samonds M T. Alloy Thermal Physical Property Prediction Coupled Computational Thermodynamics with Back Diffusion Consideration. *Journal of Phase Equilibria and Diffusion*. 2006;28: 58-63.
- [58] Krajewski P K, Piwowarski G, Buras J, Krajewski W K, Rutowski P, Szeliga D. *Archives of Metallurgy and Materials*. 2014;59(3): 1055-1058.
- [59] Przeliorz R, Piatkoski J. Application of DSC Method in Studies on Phase Transitions of Ni Superalloys. *Archives of Foundry Engineering*. 2017;17(4): 133-136.
- [60] Nickel Institute. *Engineering Properties of ALLOY IN713C*. Nickel Institute.
- [61] NETZSCH. *Netzsch Proteus Thermal Analysis Manual*. NETZSCH.
- [62] Cullen J C T. High Throughput Methodologies and Materials Characterisation for the Optimisation and Discovery of New Alloys. Swansea, Wales: Swansea University; 2019.

REFERENCES

- [63] Boettinger W J, Kattner U R, Moon K -W, Perepezko J H. *DTA and Heat-flux DSC Measurements of Alloy Melting and Freezing*. Washington, USA: National Institute of Standards and Technology; 2006. p.35.
- [64] Mahendran K, Nagaraj S, Sridharan R, Gnanasekaran T. Differential scanning calorimetric studies on the phase diagram of the binary LiCl-CaCl₂ system, *Journal of Alloys and Compounds*. 2001;325: 78-83.
- [65] Mills K C. Measurement and estimation of physical properties of metals at high temperatures. In: Seetharaman S (ed.) *Fundamentals of metallurgy*. Cambridge, England: Woodhead Publishing Limited; 2005. p.145.
- [66] Davies E J. Through-heating by induction. In: Johns A T, Platts J R, Ratcliffe G. (eds.) *Conduction and induction heating*. IEEE Power Engineering Series 11. London, United Kingdom: Peter Peregrinus Ltd; 1990. p.211.
- [67] Raytek Corporation: A Fluke Company. *The Principles of Noncontact Temperature Measurement: Infrared Theory*. Fluke. 2012.
- [68] ISS Ltd. *Endurance 1R 2-Color Infrared Thermometer Operating Instructions*. Reference number: 59511; 2015.
- [69] Gopal V, Whiting M J, Chew J W, Mills S. Thermal contact conductance and its dependence on load cycling. *International Journal of Heat and Mass Transfer*. 2013;66: 444-450.
- [70] Parker W J, Jenkins R J, Butler C P, Abbott G L. Flash Method of Determining Thermal Diffusivity, Heat Capacity, and Thermal Conductivity. *Journal of Applied Physics*. 1961;32(9): 1679-1684.
- [71] Cheng B, Lane B, Whiting J, Chou K. A Combined Experimental-Numerical Method to Evaluate Powder Thermal Properties in Laser Powder Bed Fusion. *Journal of Manufacturing Science and Engineering*. 2018;140(11).
- [72] Dou R, Ge T, Liu X, Wen Z. Effects of contact pressure, interface temperature, and surface roughness on thermal contact conductance between stainless steel surfaces under atmosphere condition. *International Journal of Heat and Mass Transfer*. 2015;94: 156-163.
- [73] Grujicic M, Zhao C L, Dusel E C. The effect of thermal contact resistance on heat management in the electronic packaging. *Applied Surface Science*. 2005;246: 290-302.

REFERENCES

- [74] Thomas V U, Yar M A, Cullen J C T, Mehraban S, Brown S G R, Lavery N P. Numerical Modelling and Validation of Induction Melting of IN713C for Investment Casting. In: *Proceedings of COMSOL Conference 2020 Europe*. Online: 2020.
- [75] COMSOL Group. *AC/DC Module User's Guide*. COMSOL. 2018.
- [76] Wheeler H A, Formulas for the Skin Effect. *Proceedings of the I.R.E.* 1942;30: 412-424.
- [77] Voller V R, Prakash C. A fixed grid numerical modelling methodology for convection-diffusion mushy region phase-change problems, *International Journal of Heat and Mass Transfer*. 1987;30: 1709-1718.
- [78] Bruyere V. *COMSOL Blog: Tips and Tricks for Modeling Induction Furnaces*. Available from: <https://uk.comsol.com/blogs/tips-and-tricks-for-modeling-induction-furnaces/> [Accessed 30th September 2020].
- [79] Frei W. *COMSOL Blog: How to Choose Between Boundary Conditions for Coil Modeling*. Available from: <https://uk.comsol.com/blogs/how-to-choose-between-boundary-conditions-for-coil-modeling/> [Accessed 30th September 2020].
- [80] De A, DebRoy T. A smart model to estimate effective thermal conductivity and viscosity in the weld pool. *Journal of Applied Physics*. 2004;95: 5230-5240.
- [81] Charogiannis A, Zadrazil I, Markides C. Thermographic particle velocimetry (TPV) for simultaneous interfacial temperature and velocity measurements. *International Journal of Heat and Mass Transfer*. 2016;97: 589-595.
- [82] Qureshi M H, Tien W H, Lin Y J P. Performance comparison of particle tracking velocimetry (PTV) and particle image velocimetry (PIV) with long-exposure particle streaks. *Measurement Science and Technology*. 2020;32(2): 024008.
- [83] Mullis A M, McCarthy I N, Cochrane R F. High speed imaging of the flow during close-coupled gas atomisation: Effect of melt delivery nozzle geometry. *Journal of Materials Processing Technology*. 2011; 211(9): 1471-1477.
- [84] Campbell J. The 10 Rules for Good Castings, In: Gifford C (ed.) *Complete Casting Handbook: Metal Casting Processes, Metallurgy, Techniques and Design*. Second Edition. Oxford, United Kingdom: Elsevier Ltd; 2015. p.543.

REFERENCES

- [85] Tseng Q, Duchemin-Pelletier E, Deshiere A, Balland M, Guillou H, Filhol O et al. Spatial organization of the extracellular matrix regulates cell-cell junction positioning. *PNAS*. 2012;109(5): 1506-1511.
- [86] Lavery N P. *Optimisation by Design of Experiments*. [Lecture] Additive Manufacturing. Swansea University. 2019.
- [87] Rapp B E. *Microfluidics: Modeling, Mechanics and Mathematics*. Micro and Nano Technologies. Oxford: William Andrew, an imprint of Elsevier; 2017.
- [88] Oh Y S, Choi D Y, Son J Y, Kim B Y, Kang H W, Chang C B et al. Breakup behavior of a molten metal jet. *International Journal of Heat and Fluid Flow*. 2014;50: 27-37.
- [89] Speirs N B, Langley K R, Taborek P, Thoroddsen S T. Jet breakup in superfluid and normal liquid He. *Physical Review Fluids*. 2020;5: 0044001.
- [90] ESI Group. *Getting Started with ProCAST EMAG*. ESI Group. 2021.
- [91] Barton S, Weiss M K-B, Maier H J. In-Situ Characterization of Microstructural Changes in Alloy 718 during High-Temperature Low-Cycle Fatigue. *Metals*. 2022;12(11). 1871.
- [92] Paul C R. Introduction to Electromagnetic Compatibility. In: *Electromagnetic Compatibility*. 2nd ed. Hoboken, USA: John Wiley & Sons, Inc.; 2006. p.1-48.
- [93] COMSOL AB. *COMSOL Multiphysics*. Stockholm, Sweden: COMSOL AB; 1986.
- [94] Thomas V U, Koeser O, Leyland S P, Brown S G R, Lavery N P. Extension of Investment Casting Process Simulation By Electromagnetic Modelling of the Pre-Process Step of Billet Induction Melting. In: Krane M, Kharicha A, Ward M (eds.) *Proceedings of the Liquid Metal Processing & Casting Conference 2022, 18-21 September 2022, Philadelphia, USA*. Pittsburgh, USA: The Minerals, Metals & Materials Society (TMS). p.173-182.
- [95] Friedlander S. Stability of Flows. In: Francoise J-P, Naber G L, Tsun T S (eds.) *Encyclopedia of Mathematical Physics*. Elsevier Academic Press: 2006.
- [96] Calcom ESI SA. *ProCAST 2022.0 User's Guide*. Calcom ESI SA. 2022.
- [97] Lordan E, Zhang Y, Dou K, Jacot A, Tzileroglou C et al. High-Pressure Die Casting: A Review of Progress from the EPSRC Future LiME Hub. *Metals*. 2022; 12(10). 1575.

REFERENCES

- [98] Daugherty R L, Franzini J B, Finnemore E J. *FLUID MECHANICS with Engineering Applications*. McGraw Hill Metric Editions Mechanical Engineering Series, SI Metric Edition. Singapore: McGraw-Hill Book Company; 1989.
- [99] Song M, Kartawira K, Hillaire K D, Li C, Eaker C B, Kiani A et al. Overcoming Rayleigh-Plateau instabilities: Stabilizing and destabilizing liquid-metal streams via electrochemical oxidation. *Proceedings of the National Academy of Sciences of the United States of America*. 2020;117(32): 9026-19032.
- [100] Winterton R H S. Radiation. In: *Heat Transfer*. Oxford, England: Oxford University Press; 1997. p.62-82.
- [101] Buschgens D, Schubert C, Pfeifer H. Radiation modelling of arbitrary two-dimensional surfaces using the surface-to-surface approach extended with a blocking algorithm. *Heat Mass Transfer*. 2022;58: p.1637-1648.
- [102] Upadhya G K, Das S, Chandra U, Paul A J. Modelling the investment casting process: a novel approach for view factor calculations and defect prediction. *Applied Mathematical Modelling*. 1995;19(6): p.354-362.
- [103] Yener T, Yener S, Mutlu R. Convection Coefficient Estimation of Still Air Using An Infrared Thermometer and Curve-Fitting. *Journal of Engineering Technology and Applied Sciences*. 2019;4(2): p.95-103.
- [104] Mao Y, Yang M, Wang T, Wu F, Qian B. Influence of Vacuum Level on Heat Transfer Characteristics of Maglev Levitation Electromagnet Module. *Applied Sciences*. 2020;10(3): 1106.
- [105] Dantzig J A, Rappaz M. Porosity. In: *Solidification*. 2nd ed. Engineering Sciences, Materials 3. Lausanne, Switzerland: EPFL Press; 2016. p.543-586.
- [106] Carlson K D, Beckermann C. Prediction of Shrinkage Pore Volume Fraction Using a Dimensionless Niyama Criterion. *Metallurgical and Materials Transactions A*. 2009;50: 163-175.
- [107] ASM International. Classification of Casting Defects. In: *Casting design and performance*. Ohio, USA: ASM International; 2009. p.251-258.
- [108] Papanikolaou M, Saxena P. Sustainable casting processes through simulation-driven optimization. In: Gupta K, Saloni K (eds.) *Sustainable Manufacturing*. Handbooks in Advanced Manufacturing 4. Elsevier; 2021. p.165-198.